Heat transport through atomic and molecular contacts

Dissertation
submitted for the degree of a

Doctor of Natural Science
(Dr.rer.nat.)

by
Jan Christopher Klöckner

at the

Faculty of Sciences
Department of Physics

Date of oral examination:	April 8th, 2019
1. Referee	Prof. Dr. Fabian Pauly
2. Referee	Prof. Dr. Dvira Segal

Konstanz, 2019

Preface

This thesis was written under the supervision of Prof. Dr. Fabian Pauly in the Theory of Nanostructures Group at the University of Konstanz. All results presented here were obtained in collaboration with him. In addition, I interacted with Prof. Dr. Juan Carlos Cuevas from the Univesidad Autonóma de Madrid, during his stay as a Mercator fellow as part of the SFB767 at the University of Konstanz. Some chapters of this thesis are to a large extent copies of already published papers.

In particular, Chap. 2.4 is a revised version of the publication in Ref. [1]. Furthermore, part of Chap. 3 has been published in Refs. [2, 3]. The first part of Chap. 4.1 is an improved version of Ref. [4], written in collaboration with Dr. Marius Bürkle from the Institute of Advanced Industrial Science and Technology, in Tsukuba, Japan, as well as Chap. 4.2 an updated report of Ref. [5]. Chaps. 2.6, 2.7, and 4.3 are partially adaptions of the work in Ref. [6], where also M.Sc. Robert Siebler contributed to all the results.

Zusammenfassung in deutscher Sprache

Die hier vorliegende Arbeit handelt vom Ladungs- und Wärmetransport in einzel-atomaren sowie einzel-molekularen Kontakten. Diesbezüglich werden unterschiedliche Beiträge zu den jeweiligen Strömen berechnet, bestehend aus elektronischen, phononischen und photonischen Anteilen. Ein besonderer Fokus wird auf den Wärmetransport gelegt, insbesondere getragen von Phononen.

Nachdem in Kap. 1 eine allgemeine Einführung in das Gebiet gegeben wird, werden im ersten Teil der Arbeit die unterschiedlichen theoretischen Konzepte vorgestellt, die im weiteren Verlauf zur Berechnung oder Analyse benötigt werden. Insbesondere beinhaltet Kap. 2.1 eine kurze Herleitung der relevanten Formel für die Berechnung der phononischen Komponente des Wärmeflusses im phasenkohärenten Regime. Anschließend wird in Kap. 2.2 auf die verwendete theoretische Modellierung realistischer Geometrien eingegangen und ausgeführt, wie wir diese mittels Dichtefunktionaltheorie umsetzen. Eine dazu komplementäre Methode basierend auf Molekulardynamik, sowie Details hinsichtlich ihrer Realisierung im Rahmen dieser Arbeit, wird in Kap. 2.3 aufgezeigt. Im weiteren Verlauf erläutern wir in Kap. 2.4 ein Verfahren, mit dessen Hilfe sich Informationen über die phononische Transmission anhand einer Eigenkanalanalyse gewinnen lassen. Des Weiteren folgt in Kap. 2.5 eine Strategie, wie sich in einem auf Cluster basierendem Modell, die sogenannte "akustische Summenregel" an Systemen mit Oberflächen erzwingen lässt. Abschließend beinhalten Kap. 2.6 sowie Kap. 2.7, die theoretischen Grundlagen in Bezug auf elektronische und photonische Beiträge zu den jeweiligen Strömen.

Im zweiten Teil werden metallische Kontakte analysiert, in denen aufgrund ihrer leitenden Eigenschaften ein wesentlicher Anteil des Wärmestromes von deren elektronischem System herrührt. Eine wichtige Fragestellung lautet, wie groß der Einfluss des phononischen Systems im Vergleich zum elektronischen ist. Dies manifestiert sich unter anderem in der Frage bezüglich der Anwendbarkeit des Wiedemann-Franz Gesetzes, welches in makroskopischen metallischen Systemen gültig ist. Die in dieser Arbeit verwendeten Methoden erlauben, dessen Geltungsbereich in nanoskopischen Kontakten zu überprüfen. Darüber hinaus wird demonstriert, in welchen Systemen sich eine Quantisierung des thermischen Leitwertes beobachten lässt.

Diesbezüglich untersuchen wir mit unterschiedlichen Methoden Gold in Kap. 3.1, Platin in Kap. 3.2 und in Kap. 3.3 Aluminium, wobei Platin ausschließlich im phasenkohärenten Regime betrachtet wird. Es zeigt sich in der Analyse des phasenkohärenten Transportes, dass für Gold und Platin die phononischen Beiträge im wesentlichem unterhalb von 10% relativ zum elektronischen liegen, während für Aluminium größere Abweichungen bis hin zu 40% auftreten können. Darüber hinaus führen wir für Gold und Aluminium eine statistische Überprüfung der gewonnen Erkenntnisse durch, wobei bei der Berechnung des phononischen Beitrages auch anharmonische Prozesse in Betracht gezogen werden. Die wesentlichen Erkenntnisse sind die allgemeine Anwendbarkeit des Wiedemann-Franz Gesetzes in Gold und Platin und dessen teilweise Verletzung in speziellen Geometrien von Aluminium sowie die Quantisierung des thermischen Leitwertes in Gold. Alle Aussagen beziehen sich auf Ergebnisse bei Raumtemperatur.

Im dritten Teil dieser Arbeit werden molekulare Kontakte untersucht. Die ersten analysierten Moleküle in Kap. 4.1 sind Alkanketten. Hier wird primär die Längenabhänigkeit des ballistischem Transportes diskutiert. Dazu wird in Kap. 4.1.2 auf den Einfluss unterschiedlicher Ankergruppen sowie verschiedener Substituenten eingegangen. Kap. 4.1.3 verallgemeinert die Ergebnisse bezüglich der Variabilität in der Modellierung aufgrund von unterschiedlichen Kontaktgeometrien und Zuleitungsorientierungen und diskutiert die Veränderung des phononischen Beitrages durch geometrische Defekte. Eine letzte Untersuchung in Kap. 4.1.4 bestätigt die Erkenntnisse durch

molekulardynamische Simulationen.

In Kap. 4.2 werden benzolähnliche Moleküle verwendet, um die Möglichkeit zu untersuchen den phononischen Wärmestrom durch Interferenzeffekte zu beeinflussen. Es zeigt sich am Beispiel von Benzol in Kap. 4.2.2, dass durch die Einführung von Substituenten mit großer Masse im Vergleich zum Wasserstoffatom eine Reduzierung des Leitwertes möglich ist. Als Ursache können molekülinterne Resonanzen aufgezeigt werden, welche aufgrund von gewissen Symmetrieeigenschaften zu einer destruktiven Interferenz führen. Die Aussagen lassen sich sowohl auf mehrere Substituenten als auch auf das benzolähnliche Molekül OPE3 in Kap. 4.2.3 übertragen.

In Kap. 4.3 wird der Einfluss der elektronischen, phononischen, sowie photonischen Beiträge des thermischen Leitwertes auf die thermoelektrische Effizienz berechnet. Dies geschieht am Beispiel von C_{60}-Monomer, sowie C_{60}-Dimer Kontakten. Während im Monomer die elektronische Komponente überwiegt, zeigen wir, dass für die Dimere sowohl der phononische als auch der photonische Beitrag nicht zu vernachlässigen ist, sodass die Effizienz erheblich reduziert wird. Abschließend wird in Kap. 5 eine Zusammenfassung aller Ergebnisse präsentiert und ein Ausblick auf weiterführende Problemstellungen gegeben.

Contents

1 Introduction

Heat transport in the most general form can be classified into different contributions stemming from convection and conduction of particles. Neglecting convective terms, which normally applies to any condensed matter system, heat conduction can be attributed to three different carriers, namely photons, electrons, and phonons [7]. While transport between two bodies out of contact, with characteristic dimensions large compared to the thermal wavelength, is mediated by photons and based on Planck's law of heat radiation, heat conduction of macroscopic solids in contact is described by Fourier's law for heat conduction, stating that the heat current density is proportional to the thermal gradient with a proportionality constant κ being a material property $J = -\kappa \nabla T$. The microscopic origin of this property depends on the underlying system. In metals it is generally assumed that κ is dominated by electrons for most temperatures, however, for semiconductors and insulators this is in general not valid because phonons can contribute the biggest part to the thermal conductivity. Since the focus of this thesis is on the phonon transport, we concentrate on it in the following.

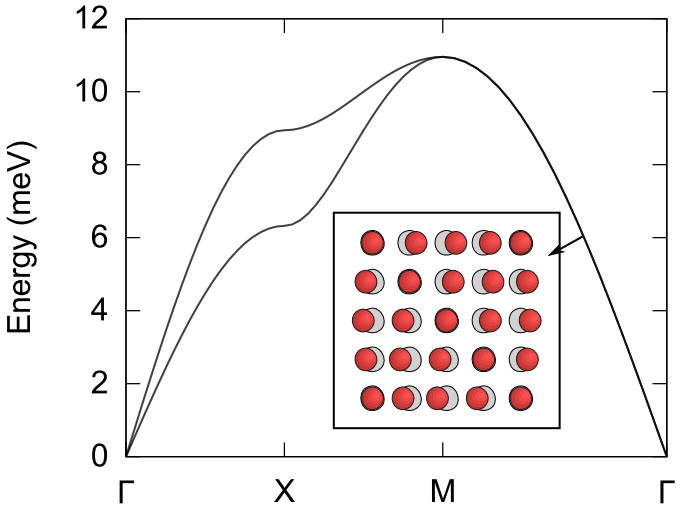

Figure 1. The dispersion relation of the phonons along the high symmetry lines determines the possible excitations of the atomic lattice. In the inset an example of a real-space representation of the phonon mode along the direction M→ Γ is shown.

The concept of a phonon appears in connection with an infinite translationally invariant atomic lattice. It represents the quasiparticle as quantized excitation of the collective atomic vibrations. In the harmonic approximation, they can be derived as small perturbations of the atoms around their equilibrium position and all possible modes are completely determined by the dispersion relation [8], see Fig. 1 as an example. Since such a system would have diverging conductivity, for a realistic description in bulk materials anharmonic effects are crucial. The historical idea that they are responsible for thermal currents is based on Debye who proposed these lattice waves as a medium for heat currents [9]. This concept has been refined by Peierls [10], who used statistical-mechanical arguments to derive an equation, which is known as the Boltzmann transport equation for phonons, that could provide a microscopic description of κ in these systems. Under the so-called relaxation time approximation, generally valid in solids dominated by Umklapp processes,

the thermal conductivity can be calculated as

$$\kappa = \frac{1}{V} \sum_{\lambda} C_{\lambda} v_{\lambda}^2 \tau_{\lambda}, \tag{1.1}$$

where $C_{\lambda} = \hbar\omega_{\lambda}\partial n/\partial T$ is the mode-specific heat capacity, $v_{\lambda} = \partial\omega_{\lambda}/\partial k$ the respective group velocity, λ denotes a phonon mode with wave vector k and polarization j and τ_{λ} is the scattering time or inverse scattering rate. This equation, although it was very successful in the description of the temperature-dependent heat conductivity in various materials, relies on the choice of different scattering rates. These rates can arise due to different processes, for instance phonon-phonon interaction, the presence of grain boundaries, point defects, or scattering with isotopes [11, 12]. In early days the energy-dependent rates had to be fitted to average values measured experimentally, so a predictive power was missing.

With the help of computer-assisted science those problems are overcome and a description of the scattering rates can be done from first principles. Today those rates can be calculated using either density functional theory (DFT) [13, 14, 15, 16], molecular dynamics (MD) simulations [17, 18, 19, 20] or even theories based on Green's function techniques [21, 22]. Supported by methods entirely based on molecular dynamics approaches [23], the thermal conductivity in bulk systems is well understood and successfully led to an understanding of materials with a low thermal conductivity [24, 25] as well as to predictions of materials with high thermal conductivity [26]. Together with the progress in nanoscience, which allows the precise control of matter at the atomic scale, these achievements have inspired scientists to look for new ways to control the thermal conductivity carried by phonons [27], for instance in terms of super-lattices [28, 29] or nanostructured holes.

In contrast to these bulk materials, where the transport is diffusive and to a large extent given by inelastic properties, the progress in nanoscale structuring also allowed to explore systems, where Fourier's law breaks down and the thermal conductance does not scale with system size as expected from macroscopic theories [30, 31]. In addition to the contribution of phonons which have mean free paths bigger than the system's size and thus conduct heat ballistically, there is an ongoing debate of whether or not Fourier's law should ever be fulfilled in low dimensional systems [32, 33]. Furthermore, interesting physical phenomena have been explored due to the coherent nature of phonons like the phonon thermal conductance quantization [34, 35], thermal lenses [36], thermal rectifiers [37], which all have in common that they have been measured at low temperatures and not all possible phonon modes contribute to the transport.

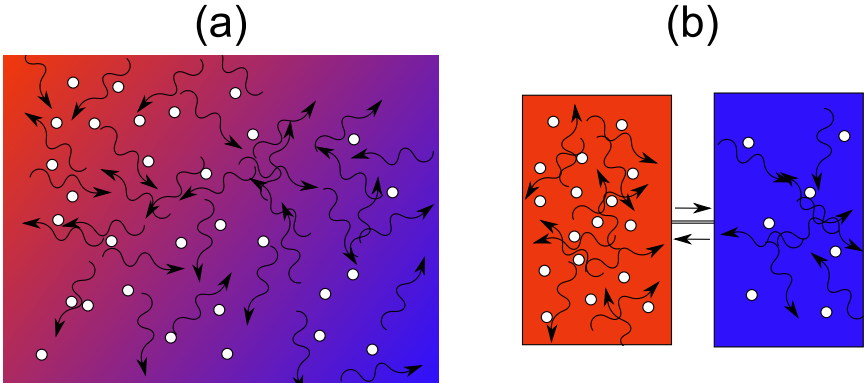

Figure 2. (a) The thermal transport in bulk samples occurs via a diffusive walk (curved arrows), while the phonons (white dots) are exposed to multiple scattering events. (b) In a phase-coherent transport regime (straight arrows) phonons are exchanged with a certain probability, while they thermalize inside the reservoirs.

In the extreme case when the characteristic dimensions of the system are comparable to the smallest coherence length of the phonons, inelastic scattering is negligible for all possible modes up to the material-specific cut-off frequency, and the view on phonon transport has to be revised.

Contrary to the diffusive transport of phonons in a bulk situation, similar to a random walk of a Brownian particle, in this regime their wave character becomes significant. It is important to notice that in principle a phonon is a solution to the infinitely extended translationally invariant system and therefore not well defined in regions that lack such symmetries. For this reason, it is customary to define a phonon bath in a certain semi-infinite space region and look at the transmission probability of the modes to be transmitted to an additional bath via an arbitrary bridge. Thermalization is supposed to occur inside these baths.

Experimentally thermal transport at room temperature in length scales comparable to the smallest mean free path of phonons is so far unexplored. Nevertheless, with the recent progress in experimental techniques like scanning thermal microscopy and the subsequent discovery of new interesting physics related to heat transport, like the quantization of thermal conductance for electrons at room temperature (see Chap. 3 for further discussion) or the near-field enhancement of radiative heat transport due to the tunneling of evanescent modes [38, 39], there is a chance that in the near future this regime will be accessible for phonon-dominated systems as well.

A big impact on the field of thermal transport is related to the hope that solution to the energy management in nanoscale systems, like nowadays CPU's where there is a significant amount of wasted leakage power, will be of thermoelectric nature [40]. Inspired by the fact that most of the best thermoelectric materials have a very low thermal conductance [41, 42], the need for an understanding of the phononic transport mechanism arises. Let us emphasize, that recent advances in conventional thermo-electrical elements can be traced back to an understanding of processes that reduce the phonon thermal conductance [43, 44, 45, 46, 38].

In this context, a different class of materials has been proposed based on molecular junctions, which due to their strongly energy-dependent transport properties and their high degree of structural flexibility, could lead to highly efficient thermoelectric materials [47]. Although basic properties like electrical conductance and Seebeck coefficient are well known, the thermal conductance due to phonons remains to a large extent unexplored in those kinds of systems and their contribution needs to be clarified in order to give a realistic estimation of their thermoelectric suitability. A more comprehensive overview of the state-of-the-art in these systems will be given in Chap. 4.

This thesis contributes to this large emerging field of thermal transport in nanoscale systems by exploring thermal transport in single-atom or single-molecule junctions, which offer a platform to probe thermal transport in the ultimate limit of heat currents entirely dominated by elastic processes for both electrons and phonons. The content is as follows.

In Sec. 2.1 we derive the basic formula, needed for the description of the coherent heat current for phonon transport. It is followed by a discussion in Sec. 2.2 on how we model this particular current with the help of ab-initio methods. Details about a complementary study based on molecular dynamics are given in Sec. 2.3. In Sec. 2.4 we develop a method to extract a spatial representation of eigenchannels, which paves the way for a better understanding of coherent thermal transport. Furthermore, we present in Sec. 2.5 a technical procedure to account for the acoustic sum rule in atomic-sized systems. The following Secs. 2.6 and 2.7 describe the calculation of the heat current due to electrons and photons.

We show in Chap. 3 the quantization of the thermal conductance in single-atom gold junctions in the coherent transport regime and discuss the differences related to other metals like platinum and aluminum. In addition, we will explore whether the Wiedemann-Franz law is still applicable down to the single-atomic level. Furthermore, in Chap. 4 we aim at an understanding of the coherent nature of phonon transport in molecular systems and discuss aspects like Fourier's law, interference effects and the impact of phononic as well as photonic processes on the thermoelectric efficiency. We close with a summary and an outlook in Chap. 5.

2 Theoretical formalism

In this chapter, we present the methods to calculate the various contributions to the thermal conductance in single-atom and single-molecule junctions. It starts with a brief derivation of the heat current in the phase-coherent regime in Sec. 2.1, followed by an explanation of the numerical implementation with DFT methods in Sec. 2.2. An alternative method based on non-equilibrium molecular dynamics (NEMD) will be presented in Sec. 2.3. These sections are followed by an introduction to the concept of transmission eigenchannels in Sec. 2.4, which provides a suitable method for analyzing a phononic transmission function. Furthermore, we illustrate the implications of the acoustic sum rule on the phonon transport in Sec. 2.5, while Secs. 2.6 and 2.7 are associated with the description of the transport coefficients of electrons and photons.

2.1 Phonon heat current

In the following, we will derive the main formula needed for the description of the heat current due to phonons in nanoscale systems. We start the derivation with the description of the phononic system in the harmonic approximation. To calculate the heat current, we look at phonons in an infinite spatial domain Ω, described by the following Hamiltonian

$$\hat{H} = \sum_{i\in\Omega,\alpha} \frac{\hat{p}_{i\alpha}^2}{2} + \frac{1}{2\hbar^2} \sum_{i,j\in\Omega,\alpha,\beta} \hat{q}_{i\alpha} K_{i\alpha,j\beta} \hat{q}_{j\beta} \tag{2.1}$$

Here, $\hat{q}_{i\alpha} = \hat{Q}_{i\alpha}\sqrt{m_i}$ is the mass-weighted displacement operator of atom i with mass m_i, $\hat{p}_{i\alpha} = \hat{P}_{i\alpha}/\sqrt{m_i}$ is the corresponding mass-scaled canonical momentum operator, and $K_{i\alpha,j\beta}$ couples the α coordinate of the i-th atom to the β coordinate of the j-th atom. Details about this matrix will be given in Sec. 2.2. Displacements of atoms i, j are assumed to be along the Cartesian axes $\alpha, \beta = \mathrm{x}, \mathrm{y}, \mathrm{z}$. The operators in Eq. (2.1) fulfill the standard commutation relations $[\hat{q}_{i\alpha}, \hat{q}_{j\beta}] = [\hat{p}_{i\alpha}, \hat{p}_{j\beta}] = 0$ and $[\hat{q}_{i\alpha}, \hat{p}_{j\beta}] = \mathrm{i}\hbar\delta_{i,j}\delta_{\alpha,\beta}$.

In a typical transport setup the domain Ω is divided into three parts: a semi-infinite left (L) lead, a finite central (C) part and a semi-infinite right (R) lead. A sketch of the setup can be seen in Fig. 3. The Hamilton operator takes the following form

$$\hat{H} = \hat{H}_\mathrm{L} + \hat{H}_\mathrm{C} + \hat{H}_\mathrm{R}, \tag{2.2}$$

with

$$\hat{H}_X = \sum_{i\in X,\alpha} \frac{\hat{p}_{i\alpha}^2}{2} + \frac{1}{2\hbar^2} \sum_{i\in X,j\in\Omega,\alpha,\beta} \hat{q}_{i\alpha} K_{i\alpha,j\beta} \hat{q}_{j\beta}, \tag{2.3}$$

where X=L,C,R. Since it is customary in the field of phonon transport to work in the Heisenberg picture, we shall consider the Heisenberg operator

$$\hat{q}_{i\alpha}(t) = e^{\mathrm{i}\hat{H}t/\hbar} \hat{q}_{i\alpha} e^{-\mathrm{i}\hat{H}t/\hbar}. \tag{2.4}$$

With this, we can define the heat current operator as the change in energy per time of the Hamilton operator of one of the leads. This quantity can be calculated using the Heisenberg

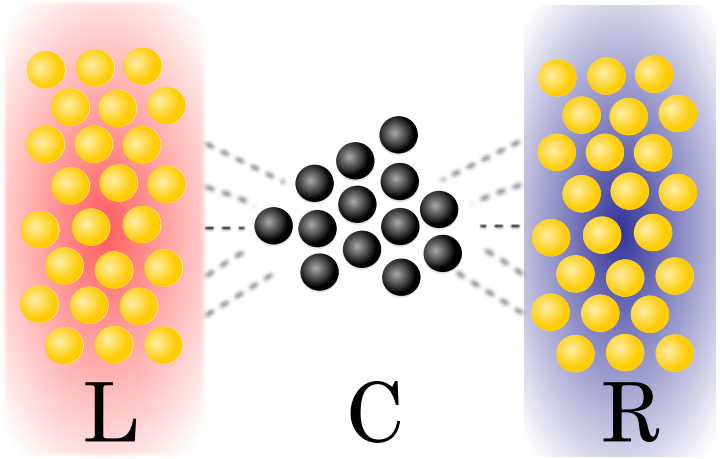

Figure 3. Sketch of the transport setup assumed for the calculation of the heat current. A semi-infinite left reservoir (L) with temperature T_L, is coupled via a finite central part (C) to a right reservoir (R) at temperature $T_R < T_L$. Due to the non-equilibrium condition in phonon population a heat current evolves.

equation of motion. Here, we consider the right heat current operator $\hat{J}_\mathrm{R}$, due to the changes in the right reservoir, nevertheless, the same considerations can be done for the left heat current operator $\hat{J}_L$. The heat current operator reads as

$$\hat{J}_\mathrm{R}(t) = \frac{d}{dt}\hat{H}_\mathrm{R}(t) = \frac{1}{i\hbar}\left[\hat{H}_\mathrm{R}(t), \hat{H}\right] = \frac{1}{i\hbar}\left[\hat{H}_\mathrm{R}(t), \hat{H}_\mathrm{C}(t)\right] \tag{2.5}$$

$$= \frac{1}{2\hbar^2}\sum_{i\in\mathrm{R}, j\in\mathrm{C},\alpha,\beta} -\hat{q}_{j\beta}(t)K_{j\beta,i\alpha}\partial_t\hat{q}_{i\alpha}(t) + \hat{q}_{i\alpha}(t)K_{i\alpha,j\beta}\partial_t\hat{q}_{j\beta}(t), \tag{2.6}$$

where we assumed the left and right leads to be uncoupled. This equation can be recast into the following form

$$= \frac{1}{2\hbar^2}\lim_{t\to t'}\sum_{i\in\mathrm{R}, j\in\mathrm{C},\alpha,\beta}\partial_{t'}\left(-\hat{q}_{j\beta}(t)K_{j\beta,i\alpha}\hat{q}_{i\alpha}(t') + \hat{q}_{i\alpha}(t)K_{i\alpha,j\beta}\hat{q}_{j\beta}(t')\right). \tag{2.7}$$

If we now seek for the physically measurable heat current we look at the expression

$$J = \left\langle\hat{J}_\mathrm{R}(t)\right\rangle = \frac{1}{2\hbar^2}\lim_{t\to t'}\sum_{i\in\mathrm{R}, j\in\mathrm{C},\alpha,\beta}\partial_{t'}\left(-K_{j\beta,i\alpha}\left\langle\hat{q}_{j\beta}(t)\hat{q}_{i\alpha}(t')\right\rangle + K_{i\alpha,j\beta}\left\langle\hat{q}_{i\alpha}(t)\hat{q}_{j\beta}(t')\right\rangle\right), \tag{2.8}$$

here the average is taken with respect to a non-equilibrium state, where the left and right leads are initially held at different temperatures. Note that with steady-state conditions, the heat current gets time independent. In this equation we can identify the lesser Green's function so we write the equation as

$$J = \frac{i}{2\hbar}\lim_{t\to t'}\partial_{t'}\mathrm{Tr}\left[-K_\mathrm{CR}D^<_\mathrm{RC}(t,t') + K_\mathrm{RC}D^<_\mathrm{CR}(t,t')\right]. \tag{2.9}$$

We refer to App. A.2 or Ref. [48, 49] for a complete set of definitions of various Greens functions. The next step is to go into the energy space (see App. A.2 for a definition), since we can assume a general Green's function to obey

$$D(t,t') = D(t-t'), \tag{2.10}$$

as the system is supposed to be in a stationary state. The current then becomes

$$J = \frac{1}{4\pi\hbar}\int_{-\infty}^{+\infty} E\,\mathrm{Tr}\left[-K_\mathrm{CR}D^<_\mathrm{RC}(E) + K_\mathrm{RC}D^<_\mathrm{CR}(E)\right]\mathrm{d}E. \tag{2.11}$$

Now the question arises how to calculate the lesser Greens function in Eq. 2.11 under non-equilibrium conditions. The answer is to use non-equilibrium Green's function (NEGF) techniques and evaluate the functions on a so-called Keldysh contour, which is equivalent to an adiabatic assumption [50]. Under appropriate boundary conditions we get a Dyson like equation similar to standard perturbation theory but with respect to variables which are defined on the contour [51, 49]. These equations can then be transformed to standard time arguments using Langreth rules [52]. Again, under the assumption of a stationary current, we can use the Fourier transformed quantities, to get the following set of equations

$$D^<_{\mathsf{CR}}(E) = D^<_{\mathsf{CC}}(E) K_{\mathsf{CR}} d^a_{\mathsf{RR}}(E) + D^r_{\mathsf{CC}}(E) K_{\mathsf{CR}} d^<_{\mathsf{RR}}(E) \tag{2.12}$$

$$D^<_{\mathsf{RC}}(E) = d^<_{\mathsf{RR}}(E) K_{\mathsf{RC}} D^a_{\mathsf{CC}}(E) + d^r_{\mathsf{RR}}(E) K_{\mathsf{RC}} D^<_{\mathsf{CC}}(E). \tag{2.13}$$

In this equation, a Green's function with small letter d refers to the isolated system, whereas a capital letter D corresponds to a Green's function of the coupled system. Inserting this into Eq. 2.11 we obtain

$$J = \frac{1}{4\pi\hbar}\int_{-\infty}^{+\infty} E \mathsf{Tr}\left[-K_{\mathsf{CR}}\left(d^<_{\mathsf{RR}} K_{\mathsf{RC}} D^a_{\mathsf{CC}} + d^r_{\mathsf{RR}} K_{\mathsf{RC}} D^<_{\mathsf{CC}}\right) + K_{\mathsf{RC}}\left(D^<_{\mathsf{CC}} K_{\mathsf{CR}} d^a_{\mathsf{RR}} + D^r_{\mathsf{CC}} K_{\mathsf{CR}} d^<_{\mathsf{RR}}\right)\right] \mathrm{d}E. \tag{2.14}$$

This can be further simplified by noting that

$$d^<_{XX}(E,T) = n(E,T_X)\left(d^r_{XX}(E) - d^a_{XX}(E)\right), \tag{2.15}$$

which is known as the fluctuation-dissipation theorem for systems in equilibrium [53, 50], and

$$D^<_{\mathsf{CC}}(E) = D^r_{\mathsf{CC}}(E)\left(\Lambda_{\mathsf{L}}(E) n(E,T_{\mathsf{L}}) + \Lambda_{\mathsf{R}}(E) n(E,T_{\mathsf{R}})\right) D^a_{\mathsf{CC}}(E), \tag{2.16}$$

with $n(E,T_X) = \left[1 - e^{E/k_{\mathsf{B}}T_X}\right]^{-1}$ and $\Lambda_X(E) = K_{\mathsf{CX}}\left(d^r_{XX}(E) - d^a_{XX}(E)\right) K_{\mathsf{XC}}$, which holds for a set of oscillators described by the Hamiltonian of Eq. 2.1 [54]. Finally, we get the expression for the heat current due to phonons in the harmonic approximation

$$J = \frac{1}{2\pi\hbar}\int_0^{\infty} E \mathsf{Tr}\left[D^r_{\mathsf{CC}}(E)\Lambda_{\mathsf{R}}(E) D^a_{\mathsf{CC}}(E)\Lambda_{\mathsf{L}}(E)\right]\left(n(E,T_{\mathsf{R}}) - n(E,T_{\mathsf{L}})\right)\mathrm{d}E, \tag{2.17}$$

by using the fact that $D^r_{\mathsf{CC}} - D^a_{\mathsf{CC}} = D^r_{\mathsf{CC}}\left(\Lambda_{\mathsf{L}} + \Lambda_{\mathsf{R}}\right) D^a_{\mathsf{CC}}$ and that the kernel is symmetric with respect to the integrand. This formula is similar to the Landau-Büttiker formula for electrons and has been derived in more detail in Refs. [55, 56, 57, 51, 58, 59, 60].

Eq. 2.17 determines the heat current in the coherent regime between two reservoirs held at an arbitrary temperature difference $\Delta T = T_{\mathsf{L}} - T_{\mathsf{R}}$. In practice, however, one is interested in the linear response of the system, the heat current which establishes when an infinitesimal temperature difference is applied. To this end, we expand the distribution function under the assumption $T_{\mathsf{L}} = T_{\mathsf{R}} + \Delta T$, with $\Delta T/T_{\mathsf{R}} \ll 1$, which leads to

$$J(T) = \kappa_{\mathsf{pn}}(T)\Delta T, \tag{2.18}$$

where $\kappa_{\mathsf{pn}}(\mathrm{T})$ is given by

$$\kappa_{\mathsf{pn}}(T) = \kappa_0 \int_0^{\infty} \mathrm{d}E W_{\mathsf{pn}}(E,T)\tau_{\mathsf{pn}}(E). \tag{2.19}$$

Here $\kappa_0 = \frac{\pi^2 k_{\mathsf{B}}^2 T}{3h}$ is the universal thermal conductance quantum, $W_{\mathsf{pn}}(E,T) = \frac{3}{\pi^2}\left(\frac{E}{k_{\mathsf{B}}T}\right)^2\left(-\frac{\partial n(E,T)}{\partial E}\right)$ is the phonon window function and $\tau_{\mathsf{pn}}(E) = \mathsf{Tr}\left[D^r_{\mathsf{CC}}(E)\Lambda_{\mathsf{R}}(E) D^a_{\mathsf{CC}}(E)\Lambda_{\mathsf{L}}(E)\right]$ is the phononic transmission. Notice that since $W_{\mathsf{pn}}(E)$ is a universal function, the transmission function uniquely defines the thermal conductance and thus plays a crucial role in the context of phononic thermal conductance.

For some cases it is useful to investigate the so-called cumulative thermal conductance

$$\kappa_{\mathsf{pn}}^{\mathsf{c}}(E,T) = \kappa_0 \int_0^E dE' W_{\mathsf{pn}}(E',T)\tau_{\mathsf{pn}}(E') \tag{2.20}$$

defined as the thermal conductance due to phonon modes up to a given energy E. This quantity can provide more detailed information on how the individual modes contribute to the total thermal conductance for a given energy.

2.2 Ab-initio description of phonon transport

In this section, we will show how we model the phonon transport in realistic nanoscale systems using DFT and the NEGF formalism presented in chapter. 2.1. In principle, this formalism requires the couplings between an infinite set of atoms, which is not suitable for DFT calculations. However, we will explain in the following how we can restrict the computation to a reasonable subset of atoms.

DFT is a method in the field of electronic structure theory, which allows for an efficient description of the electronic system based on the geometrical configuration of different atoms. Besides computation specific parameters, like basis sets or pseudopotentials, in this method, there is only a choice in the use of different density functionals which affects the results. More important, DFT offers within the framework of density functional perturbation theory a convenient way to account for the phononic system, since the coupling elements can be extracted as the second derivative of the Born-Oppenheimer energy surface with respect to the atomic position

$$K_{i\alpha,j\beta} = \frac{\hbar^2}{\sqrt{M_i M_j}} \frac{\partial^2 E_{\mathrm{BO}}}{\partial R_{i\alpha} \partial R_{j\beta}}. \tag{2.21}$$

For an overview of DFT-related topics we refer to Ref. [61, 62] .

In practice, however, using DFT the description is limited to a few hundreds of atoms in the simulation box, due to the tremendous computational effort inherited to this method. This is in clear contrast to experimental geometry variations which can reach several μm. To overcome these limitations, the main assumption made in ab-initio transport simulations of atomic or molecular contacts can be attributed to the expectation, that in nanoscale systems the most resistive part can be described by a finite geometry of the size of a few atoms. Thus, only the geometrical variations at the interface between the smallest part and the macroscopic heat reservoirs must be described microscopically.

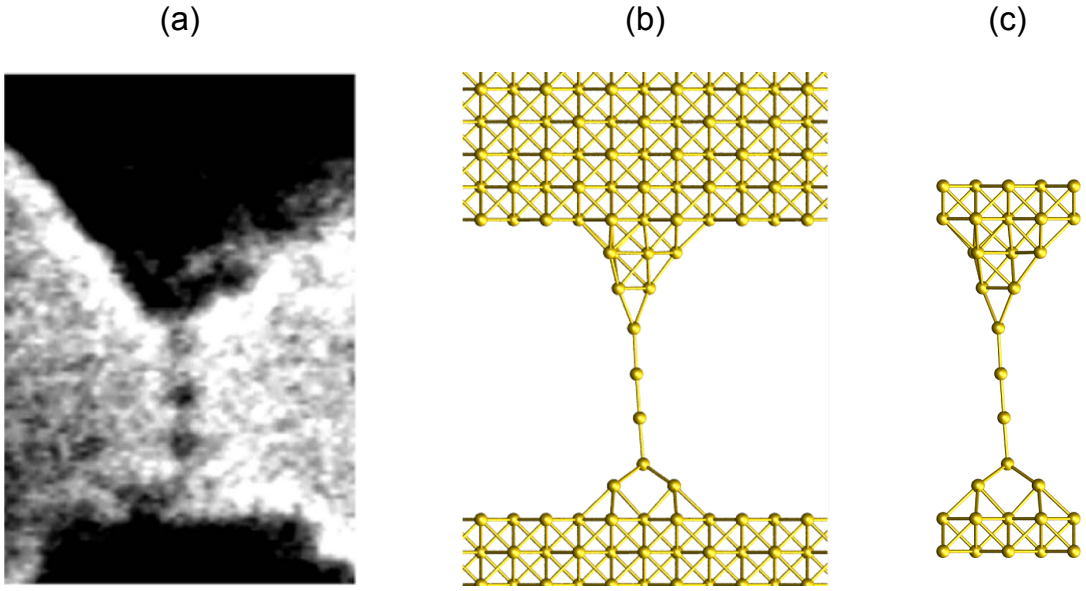

Figure 4. Comparison of an experimental geometry in (a) taken from Ref. [63], consisting of at least 3 gold atoms forming a gold chain, with the geometry in (b) considered in the theoretical calculation of a comparable contact both showing approximately a conductance of 1 G_0. In (c) we show the corresponding ECC.

In our approach, this finite region is simulated in a so-called extended central cluster (ECC) calculation. There, only a finite number of reservoir atoms, which are characterized by fixed

atom positions on the ideal lattice sites of the perfect crystal, are coupled to a central part. In the center, however, the atoms are free to adjust their position and will be optimized such that stress effects are minimized. Within the ECC we can extract the coupling elements from the central part, as well as the coupling to the leads. The semi-infinite heat reservoirs, on the other hand, are assumed to have perfect, defect-free, translational symmetry. This allows the use of bulk parameters, which can be obtained in an independent simulation of a perfect crystal, or with a cluster-based approach [64]. Thus, using this approach we limit the computation to a reasonable number of atoms, treatable within DFT. Let us emphasize, that the same concept is also successfully applied to the electronic description of meso- and nanoscale systems [65, 54].

A comparison of an experimental geometry of a gold chain produced with a scanning electron microscope at room temperature and taken from Ref. [63] with a geometry used in our simulation is shown in Fig. 4. While in Fig. 4(a) the experiment (atoms colored in black) reveals variations of the surface and clear deviations from the ideal fcc-lattice for both sides of the contact in (b) these variations are neglected in theory and instead the surface is assumed to be symmetric and of perfect fcc type. The coupling to the leads, as well as the information on the central part is taken from the ECC calculation shown in Fig. 4(c). Here, only a finite number of surface atoms are sufficient to get the relevant parameters (For tests of convergence with respect to the size of the ECC see Apps. C and D).

In our calculations we always use the functional proposed by Perdew-Burke and Ernzerhof (PBE) [66, 67], which can be grouped in the class of generalized gradient approximated functionals. If not explicitly stated we use the program TURBOMOLE [68], which is an all-electron code based on Gaussian orbitals, the default2 basis set of split-valence-plus-polarization quality def2-SV(P) [69], and the corresponding Coulomb fitting basis [70]. Details about the implementation of the force constants based on Gaussian orbitals can be found in Ref. [71, 72]. In general, we use very tight convergence criteria of scfconv 9 and gcart 5 which corresponds to a convergence of the total energy better then 10^{-9} a.u. and the maximum norm of the component of the gradient smaller then 10^{-5} a.u., to avoid imaginary modes in the central part. The surface Greens function, which enters the transmission through the linewidth-broadening matrix $\Lambda_X(E)$, will be calculated using a decimation technique proposed by Guinea et al. [73], with parameters obtained in a separate bulk calculation, see App. C.

2.3 NEMD description of phonon transport

As an alternative to the calculation of the thermal conductance based on DFT+NEGF, molecular dynamics offers several possibilities to predict the heat current at an atomistic level. Generally speaking, those methods can be classified into two different subgroups, namely equilibrium and non-equilibrium molecular dynamics. Whereas in equilibrium one looks at certain correlation functions, using the Green-Kubo formalism, in non-equilibrium the system is driven out of equilibrium and the response is measured directly. In principle, with either methods both bulk [23, 74, 75] and interface [76, 77, 78, 79] conductivities can be calculated, however, all of them suffer from different finite size effects [80, 81, 82].

In comparison to the ab-initio approach described in Sec. 2.2 those methods offer several advantages. Whereas the former one is limited to a few hundreds of atoms, with MD simulations atom numbers in the order of 10^6 are theoretically computable. Furthermore, temperature effects like lattice expansion and geometrical phase space sampling are implicitly included. The most important benefit, however, is that the inclusion of anharmonic effects takes place in a non-perturbative manner.

The major drawback can be attributed to the need for empirical interatomic potentials, which are not universal and often optimized for special purposes. This becomes most evident when systems with interfaces on the size of nanometers are considered. Here, due to lack of chemical information conventional potentials fail to describe geometries at the single atomic scale or rely on the harmonic approximation. Although there are potentials which incorporate this, these go hand-in-hand with higher computational costs. In contrast, DFT-based methods are known to give reliable geometries at these length scales. Moreover, the avoidance of finite size effects in the heat baths is crucial for a calculation of the thermal conductance and effectively limits the number of interface atoms. Since MD performs simulations using classical statistics, another disadvantage is that quantum effects are not considered, which can be decisive especially for low temperatures in comparison to the material-specific cut-off energy.

In short, both approaches complement each other and therefore both will be used in this work. To be precise, we use a direct NEMD approach, where the non-equilibrium situation is set by maintaining two regions separated in space at a constant temperature difference, using a thermostat. The thermal conductance is calculated according to

$$\kappa_{\mathrm{pn}} = \frac{J}{\Delta T} = \frac{\Delta E}{\Delta t \Delta T}, \tag{2.22}$$

where $J = \frac{\Delta E}{\Delta t}$ is the steady-state heat current, which is calculated as the energy fed into the system by the thermostats per timestep Δt divided by the temperature difference ΔT. In practice, we monitor the output of the thermostats over a measurement time τ and calculate the heat current as the slope of a linear fit to this dataset.

A typical geometry can be seen in Fig. 5. The outermost atoms at each side, indicated in black, are fixed, to avoid a collapse of the system. These regions are followed by several atom rows colored in red and blue, where a thermostat is applied. The largest part of the simulation box consists of the left (L) and right (R) lead, which is colored in orange here. To avoid finite size effects, their precise number of atoms has to be chosen depending on the interatomic potential and the average temperature. Similar to the NEGF formalism we define a central part (C) as all atoms in between the leads.

In all simulations, we apply periodic boundary conditions perpendicular to the direction of transport and fixed boundary conditions parallel to it. Since we are looking at a non-equilibrium situation one has to take care of the lattice mismatch due to the temperature difference. Therefore, to minimize strain effects we take the following effective lattice constant

$$a_{\mathrm{eff}} = \sqrt[3]{\frac{a(T_{\mathrm{L}})^3 + a(T_{\mathrm{R}})^3}{2}}, \tag{2.23}$$

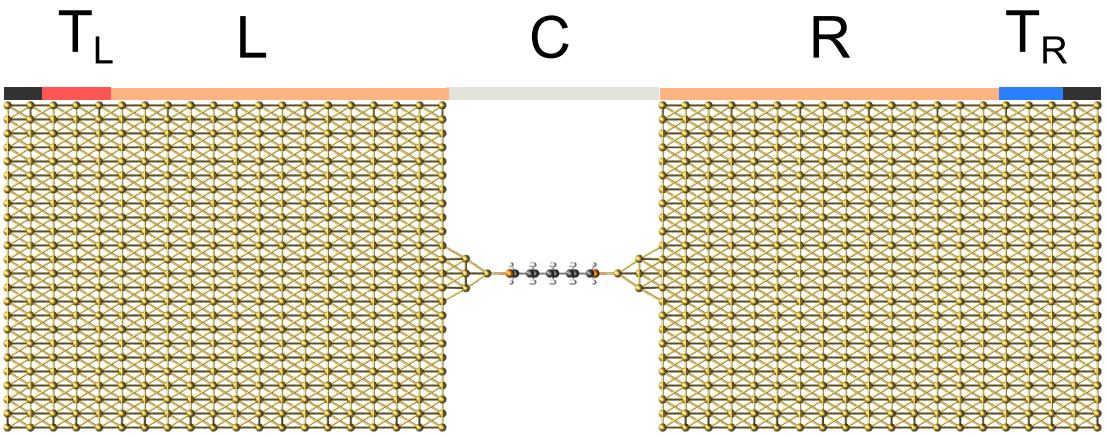

Figure 5. Typical geometry used in NEMD calculations of the thermal conductance.

which determines the volume of the simulation box. The simulations are done with the LAMMPS software code [83], for the integration of Newton's equation of motion we use the velocity-Verlet algorithm [84].

To analyze the phononic spectrum it is useful to look at the phonon density of states (DOS), calculated according to

$$D(\omega) = \frac{1}{3Nk_B T} \int \langle v_i(t) v_i(0) \rangle e^{i\omega t} \mathrm{d}t, \tag{2.24}$$

with N the total number of atoms and T the temperature. This is the Fourier transformed velocity autocorrelation function [85].

In this work, we consider two different types of atomic potentials. The first one relies on the embedded atom method (EAM) potential. This potential is defined as follows

$$E_{\mathrm{tot}} = \sum_i F_i(n_i) + \frac{1}{2} \sum_{i \neq j} V_{ij}(R_{ij}) \tag{2.25}$$

and

$$n_i = \sum_{j \neq i} \varrho_j(R_{ij}), \tag{2.26}$$

with $F_i(n_i)$ the embedding energy, $V_{ij}(R_{ij})$ the pair potential and $\varrho_j(R_{ij})$ the electron density function. In most cases, each function is described as a set of points that are connected by splines of a specific degree, trained to a certain data set. This kind of many-body potential is especially successful in the description of crystal related properties. The second potential used in this work is a reactive force field (REAXFF), which is based on the concept of a bond order to model interactions within a chemical system. With it a dynamic breaking and forming of bonds are possible, thus it does not rely on predefined reactive sites within harmonic interactions. The total potential is given as

$$E_{\mathrm{system}} = E_{\mathrm{bond}} + E_{\mathrm{over}} + E_{\mathrm{under}} + E_{\mathrm{lp}} + E_{\mathrm{val}} + E_{\mathrm{angle}} + E_{\mathrm{tor}} + E_{\mathrm{vdWaals}} + E_{\mathrm{Coulomb}}, \tag{2.27}$$

where the contributions are due to bonding order, over-coordination penalty and under-coordination stability,lone-pair energy, valence angle and torsion, and non-bonding van der Waals and Coulomb interaction [86, 87]. For the non-bonded interaction REAXFF calculates the polarization of charges inside the molecule based on the EEM and Qeq methods developed by Mortier and Rappe [88, 89, 90]. A detailed description of each term can be found in the supplementary material of Ref. [91].

2.4 Transmission eigenchannels

We have seen in Sec. 2.1, that the phononic transmission function uniquely determines the thermal conductance in the phase-coherent limit. To get an idea about the physical modes involved in the transport, methods are needed to extract information from this function. In systems with translational symmetry, an analysis which relates the transmission of a certain ingoing to a respective outgoing bulk mode exists, which can be naturally performed with mode-matching-based approaches [92, 93, 94] or with the help of NEGF techniques [95, 96]. However, mode-dependent transmission studies do not actually provide information on the modes of the central device part, thus such a kind of analysis is not suitable for atomic and molecular junctions that lack spatial symmetry.

For this reason, the calculations in these systems are often interpreted with the help of the local density of states (LDOS) [97, 98, 99, 100]. Such analyses are certainly useful, but they do not establish a direct connection to the key quantity for coherent phonon transport, namely the transmission function. Moreover, in those calculations the information about the phase gets lost, which is important, for instance, for the interpretation of interference effects. Instead, the concept of transmission eigenchannels resolves the total transmission $\tau = \sum_\mu \tau_\mu$ into contributions of eigenchannels, which are particular scattering states with transmission coefficients $0 \leq \tau_\mu \leq 1$. More important, those eigenstates are clearly connected to the transmission, they are closely related to the local vibrational modes, and they preserve the phase information. In the case of electronic transport, Paulsson and Brandbyge [101] were able to establish a method to obtain the eigenchannels from information about the subspace of the central part of the device only, i.e., from data that is readily available in NEGF-based approaches. In the following we extend those ideas and transfer them to coherent phonon transport. In particular, we present a general procedure to extract these eigenchannels in NEGF-based calculations.

2.4.1 Scattering states

In mesoscopic systems, the theoretical description of the transport of electrons can be related to a quantum mechanical scattering problem [102, 103, 65]. There, the concept of scattering states is introduced, which are solutions of the scattering problem under certain boundary conditions. More important, these scattering states offer a spatial representation of the current carrying modes. Additionally, in Ref. [101] they were shown to give a profound basis for the transmission eigenchannels in the central part and it was demonstrated how to obtain them from NEGF-based methods. As we will need the concept of scattering states for the phononic transmission eigenchannels, they will be introduced in this section.

Consider the displacement operator in the Heisenberg picture

$$\hat{q}_{i\alpha}(t) = e^{\mathrm{i}\hat{H}t/\hbar}\,\hat{q}_{i\alpha}\,e^{-\mathrm{i}\hat{H}t/\hbar}. \tag{2.28}$$

It is straightforward to show that this operator, with the Hamiltonian defined in Eq. 2.2, fulfills the following equation of motion (see App. A.1)

$$\hbar^2 \frac{d^2\hat{q}_{i\alpha}(t)}{dt^2} = -\sum_{j\in\Omega,\beta} K_{i\alpha,j\beta}\,\hat{q}_{j\beta}(t). \tag{2.29}$$

The full solution to this equation of motion is formed from two sets of states [104, 102]. One set includes propagating states with a continuous energy spectrum. It is generated from the electrodes, which we assume to be perfect semi-infinite crystals without defects. The upper cutoff energy E_c of the spectrum is determined by the highest phonon energy of the left or right electrode material and is set to the maximum of the two values. The other set is formed by bound states with a discrete energy spectrum, originating from the finite central region. For

coherent transport these bound states are not important, because they do not contribute to the transmission. Nevertheless, we take them into account in our considerations, since they are important for the normalization of the states, as we will discuss below.

The solution of Eq. (2.29) can then be expressed in terms of the normal modes of the propagating and bound sets as

$$\begin{aligned}\hat{q}_{i\alpha}(t) &= \int_0^{E_c} \mathrm{d}E \sum_m \frac{\hbar}{\sqrt{2E}} \left(b_m^\dagger(E) \Phi_{m,i\alpha}^*(E) e^{\mathrm{i}Et/\hbar} + \mathrm{h.c.} \right) \\ &\quad + \sum_m \frac{\hbar}{\sqrt{2E_m}} \left(\bar{b}_m^\dagger \bar{\Phi}_{m,i\alpha}^* e^{\mathrm{i}E_m t/\hbar} + \mathrm{h.c.} \right), \end{aligned} \tag{2.30}$$

where h.c. denotes Hermitian conjugation. The normal mode operators fulfill standard commutation relations with the only nonvanishing commutators being $[b_m(E), b_n^\dagger(E')] = \delta_{mn}\delta(E-E')$ and $[\bar{b}_m, \bar{b}_n^\dagger] = \delta_{mn}$. In these expressions, $\Phi_{m,i\alpha}(E)$ is the component of the normal mode vector $\Phi_m(E)$ on atom i for the displacement along α, which solves the following eigenvalue problem

$$K\Phi_m(E) = E^2 \Phi_m(E) \tag{2.31}$$

for a given energy E. Here, m runs over all degenerate states with energy E. Similar relations hold for the bound states, where $\bar{\Phi}_m$ is the normal mode vector m, which is a solution to

$$K\bar{\Phi}_m = E_m^2 \bar{\Phi}_m. \tag{2.32}$$

In this case, the index m enumerates all bound states. Overall, the normal mode vectors are normalized such that

$$\begin{aligned}\int_0^{E_c} \mathrm{d}E \sum_m \Phi_{m,i\alpha}^*(E) \Phi_{m,j\beta}(E) \\ + \sum_m \bar{\Phi}_{m,i\alpha}^* \bar{\Phi}_{m,j\beta} &= \delta_{ij}\delta_{\alpha\beta}. \end{aligned} \tag{2.33}$$

Since we are interested in the formulation of transport as a scattering problem, we solve Eq. (2.31) for the propagating set of states by starting from the solutions of the uncoupled subsystems X and treat the coupling between the different parts, K_{XY} with $Y \neq X$, as a perturbation K_1. For this reason we write $K = K_0 + K_1$ with

$$K_0 = \begin{pmatrix} K_{\mathrm{LL}} & 0 & 0 \\ 0 & K_{\mathrm{CC}} & 0 \\ 0 & 0 & K_{\mathrm{RR}} \end{pmatrix} \tag{2.34}$$

and

$$K_1 = \begin{pmatrix} 0 & K_{\mathrm{LC}} & 0 \\ K_{\mathrm{CL}} & 0 & K_{\mathrm{CR}} \\ 0 & K_{\mathrm{RC}} & 0 \end{pmatrix}. \tag{2.35}$$

Note that we assume here and henceforth that left and right parts are decoupled, meaning that $K_{\mathrm{LR}} = K_{\mathrm{RL}}^\dagger = 0$. For the eigenvalue E^2, we arrive in this way at a general solution $\Phi_m(E) = (\Phi_{m,\mathrm{L}}(E), \Phi_{m,\mathrm{C}}(E), \Phi_{m,\mathrm{R}}(E))^T$, which can be expressed by using the Green's function formalism as follows

$$\Phi_{m,X}(E) = \boldsymbol{\varphi}_{m,X}(E) + \sum_{Y \neq X} d_{XX}^{\mathrm{r}}(E) K_{XY} \Phi_{m,Y}(E). \tag{2.36}$$

Here $\boldsymbol{\varphi}_{m,X}(E)$ is the solution of the unperturbed system, i.e., $\left(E^2 - K_{XX}\right)\boldsymbol{\varphi}_{m,X}(E) = 0$, and

$$d_{XX}^{\mathrm{r}}(E) = \left[(E+\mathrm{i}\eta)^2 - K_{XX}\right]^{-1} \tag{2.37}$$

is the retarded Green's function of the unperturbed solution with an infinitesimal parameter $\eta > 0$. The states in Eq. (2.36) can also be written in terms of the retarded Green's function of the full system

$$D^{\mathrm{r}}(E) = \left[(E + \mathrm{i}\eta)^2 - K\right]^{-1} \tag{2.38}$$

as

$$\Phi_{m,X}(E) = \boldsymbol{\varphi}_{m,X}(E) + \sum_{Z} \sum_{Y \neq Z} D^{\mathrm{r}}_{XZ}(E) K_{ZY} \boldsymbol{\varphi}_{m,Y}(E). \tag{2.39}$$

From this equation, we define the scattering states $\Phi^{\mathrm{L}}_m(E)$ $[\Phi^{\mathrm{R}}_m(E)]$ generated from unperturbed states that enter the junction region from the left [right] lead, which are special solutions with the boundary conditions $\boldsymbol{\varphi}_{m,\mathrm{C}}(E) = 0$ and simultaneously $\boldsymbol{\varphi}_{m,\mathrm{R}}(E) = 0$ $[\boldsymbol{\varphi}_{m,\mathrm{L}}(E) = 0]$. We will show in the next section that, apart from contributions due to bound states, these left- and right-incoming states give rise to the spectral function of the central part.

2.4.2 Spectral function

The phonon spectral function plays a central role in the determination of the transmission eigenchannels. This function is defined in terms of the phonon Green's functions as follows

$$A(E) = \mathrm{i}\{D^{\mathrm{r}}(E) - [D^{\mathrm{r}}(E)]^{\dagger}\}. \tag{2.40}$$

Making use of the propagating and bound sets of solutions to Eqs. (2.31) and (2.32), the spectral function can be rewritten as

$$\begin{aligned} A(E) &= -2 \int_0^{E_{\mathrm{c}}} \mathrm{d}E' \sum_m \mathrm{Im} \left[\frac{\Phi_m(E') \Phi^{\dagger}_m(E')}{(E + \mathrm{i}\eta)^2 - E'^2} \right] \\ &\quad -2 \sum_m \mathrm{Im} \left[\frac{\bar{\Phi}_m \bar{\Phi}^{\dagger}_m}{(E + \mathrm{i}\eta)^2 - E_m^2} \right]. \end{aligned} \tag{2.41}$$

We note that this form of the spectral function is consistent with the standard definition of the Green's functions used for the derivation of the Landauer formula [105]. Those Green's functions are defined in terms of the operators $\hat{q}_{i\alpha}(t)$ of Eq. (2.30), and such a starting point also leads to Eq. (2.41). Now, using that $\lim_{\eta \to 0} \mathrm{Im}\,[1/(E + \mathrm{i}\eta)] = -\pi\delta(E)$, we can express the spectral function as follows

$$\begin{aligned} A(E) &= \frac{\pi}{E} \sum_m \Phi_m(E) \Phi^{\dagger}_m(E) \\ &\quad + \sum_m \frac{\pi}{E_m} \delta(E - E_m) \bar{\Phi}_m \bar{\Phi}^{\dagger}_m \\ &= \frac{\pi}{E} \rho(E), \end{aligned} \tag{2.42}$$

where

$$\rho(E) = \sum_m \Phi_m(E) \Phi^{\dagger}_m(E) + \sum_m \delta(E - E_m) \bar{\Phi}_m \bar{\Phi}^{\dagger}_m \tag{2.43}$$

is the phonon density matrix. This means that the sets of states $\Phi_m(E)$ and $\bar{\Phi}_m$, respectively, form the density matrix at a given energy. From this expression, the density of states of a given subset can be obtained by a projection on this subset and an additional trace over the respective degrees of freedom.

After these general considerations, we now address the spectral function of our scattering problem. We obtain the retarded Green's function in the central region from Eq. (2.38), and it is given by the Dyson equation

$$D^{\mathrm{r}}_{\mathrm{CC}}(E) = \left[(E + \mathrm{i}\eta)^2 - K_{\mathrm{CC}} - \Pi^{\mathrm{r}}_{\mathrm{L}}(E) - \Pi^{\mathrm{r}}_{\mathrm{R}}(E)\right]^{-1}, \tag{2.44}$$

where $\Pi^{\mathrm{r}}_Z(E) = K_{CZ}\, d^{\mathrm{r}}_{ZZ}(E) K_{ZC}$ with Z=L,R is the embedding self-energy due to the coupling to the leads. The spectral function of the central part can then be expressed using Eq. (2.40) as

$$\begin{aligned} A_{\mathrm{C}}(E) &= \mathrm{i} D^{\mathrm{r}}_{\mathrm{CC}}(E) \left\{ \left[D^{\mathrm{r}}_{\mathrm{CC}}(E)^\dagger \right]^{-1} - D^{\mathrm{r}}_{\mathrm{CC}}(E)^{-1} \right\} D^{\mathrm{r}}_{\mathrm{CC}}(E)^\dagger \\ &= \sum_{Z=\mathrm{L},\mathrm{R}} D^{\mathrm{r}}_{\mathrm{CC}}(E) \Lambda_Z(E) D^{\mathrm{r}}_{\mathrm{CC}}(E)^\dagger - 4\mathrm{i}\eta E D^{\mathrm{r}}_{\mathrm{CC}}(E) D^{\mathrm{r}}_{\mathrm{CC}}(E)^\dagger \end{aligned} \tag{2.45}$$

with $\Lambda_Z(E) = \mathrm{i}\left[\Pi^{\mathrm{r}}_Z(E) - \Pi^{\mathrm{r}}_Z(E)^\dagger\right] = K_{CZ} a_Z(E) K_{ZC}$ and $a_Z(E) = (\pi/E)\sum_m \boldsymbol{\varphi}_{m,Z}(E)\boldsymbol{\varphi}^\dagger_{m,Z}(E)$. While the last term $-4\mathrm{i}\eta E D^{\mathrm{r}}_{\mathrm{CC}}(E) D^{\mathrm{r}}_{\mathrm{CC}}(E)^\dagger$ in Eq. (2.45) corresponds to the bound-state contributions, one can show that the two terms $D^{\mathrm{r}}_{\mathrm{CC}}(E)\Lambda_Z(E)D^{\mathrm{r}}_{\mathrm{CC}}(E)^\dagger$ for $Z = \mathrm{L}, \mathrm{R}$ are related to the scattering states $\Phi^{\mathrm{L}}_m(E)$ and $\Phi^{\mathrm{R}}_m(E)$. This can be demonstrated as follows

$$\begin{aligned} A^Z_{\mathrm{C}}(E) &= \frac{\pi}{E} \sum_m P_{\mathrm{C}} \Phi^Z_m(E) \Phi^Z_m(E)^\dagger P_{\mathrm{C}} \\ &= \frac{\pi}{E} \sum_m P_{\mathrm{C}} \left[\boldsymbol{\varphi}^Z_m(E) + D^{\mathrm{r}}(E) K_1 \boldsymbol{\varphi}^Z_m(E) \right] \left[\boldsymbol{\varphi}^Z_m(E)^\dagger + \boldsymbol{\varphi}^Z_m(E)^\dagger K_1^\dagger D^{\mathrm{r}}(E)^\dagger \right] P_{\mathrm{C}} \\ &= D^{\mathrm{r}}_{\mathrm{CC}}(E) \Lambda_Z(E) D^{\mathrm{r}}_{\mathrm{CC}}(E)^\dagger, \end{aligned} \tag{2.46}$$

where we have used Eq. (2.39) for the scattering states, $\boldsymbol{\varphi}^{\mathrm{L}}_m(E) = \left(\boldsymbol{\varphi}_{m,\mathrm{L}}(E), 0, 0\right)^T$, $\boldsymbol{\varphi}^{\mathrm{R}}_m(E) = \left(0, 0, \boldsymbol{\varphi}_{m,\mathrm{R}}(E)\right)^T$ and the projection operator

$$P_{\mathrm{C}} = \sum_{i\in \mathrm{C},\alpha} \boldsymbol{e}_{i\alpha} \boldsymbol{e}^\dagger_{i\alpha}. \tag{2.47}$$

In this expression, $\boldsymbol{e}_{i\alpha}$ is a unit vector of the same dimension as the $\Phi_m(E)$, and its entries are given by $e_{i\alpha,j\beta} = \delta_{ij}\delta_{\alpha\beta}$. We have thus shown that the spectral function of the central part $A_{\mathrm{C}}(E) = A^{\mathrm{L}}_{\mathrm{C}}(E) + A^{\mathrm{R}}_{\mathrm{C}}(E) + A^{\mathrm{B}}_{\mathrm{C}}(E)$ consists of two spectral functions $A^{\mathrm{L}}_{\mathrm{C}}(E)$ and $A^{\mathrm{R}}_{\mathrm{C}}(E)$, which can be attributed to scattering states $\Phi^{\mathrm{L}}_m(E)$ and $\Phi^{\mathrm{R}}_m(E)$ that enter the central device region from the left and right leads, respectively, and a part $A^{\mathrm{B}}_{\mathrm{C}}(E)$ due to bound states.

2.4.3 Transmission eigenchannel from NEGF

We are now in the position to finally describe the procedure to determine the transmission eigenchannels. Let us first recall that we assume that the left and right parts are decoupled [see Eqs. (2.34) and (2.35)]. Under these conditions and using the NEGF formalism, one can show that the phononic heat current is given by a Landauer-like formula (see Sec. 2.1) where the main quantity to be determined

$$\tau(E) = \mathrm{Tr}\left[D^{\mathrm{r}}_{\mathrm{CC}}(E) \Lambda_{\mathrm{L}}(E) D^{\mathrm{r}}_{\mathrm{CC}}(E)^\dagger \Lambda_{\mathrm{R}}(E) \right], \tag{2.48}$$

is the total phonon transmission.

In order to obtain eigenchannels as linear combinations of projections of scattering states onto the central junction part simultaneously with the corresponding transmission eigenvalues, we express the transmission using Eq. (2.46) with $Z = \mathrm{L}$ as

$$\begin{aligned} \tau(E) &= \mathrm{Tr}\left[A^{\mathrm{L}}_{\mathrm{C}}(E) \Lambda_{\mathrm{R}}(E) \right] \\ &= \frac{\pi}{E} \sum_m \Phi^{\mathrm{L}}_m(E)^\dagger P_{\mathrm{C}} \Lambda_{\mathrm{R}}(E) P_{\mathrm{C}} \Phi^{\mathrm{L}}_m(E). \end{aligned} \tag{2.49}$$

Inspired by this expression, we define the transmission probability matrix

$$\tau^{(1)}_{mn}(E) = \frac{\pi}{E} \Phi^{\mathrm{L}}_m(E)^\dagger P_{\mathrm{C}} \Lambda_{\mathrm{R}}(E) P_{\mathrm{C}} \Phi^{\mathrm{L}}_n(E), \tag{2.50}$$

which is actually the matrix that we shall diagonalize to obtain the eigenchannels.

In order to diagonalize this transmission matrix, we follow the procedure for the electronic problem, as described in Refs. [101, 106], and perform a spectral decomposition for the central part of the spectral function

$$\begin{aligned} A_{\mathsf{C}}^{\mathsf{L}}(E) &= \sum_m \tilde{\boldsymbol{\chi}}_m(E)\lambda_m(E)\tilde{\boldsymbol{\chi}}_m^\dagger(E) \\ &= \frac{\pi}{E}\sum_m \tilde{\boldsymbol{\xi}}_m(E)\tilde{\boldsymbol{\xi}}_m^\dagger(E). \end{aligned} \tag{2.51}$$

Here, $\tilde{\boldsymbol{\xi}}_m(E) = \sqrt{E\lambda_m(E)/\pi}\tilde{\boldsymbol{\chi}}_m(E)$ and $\tilde{\boldsymbol{\chi}}_m^\dagger(E)\tilde{\boldsymbol{\chi}}_n(E) = \delta_{mn}$. As can be seen from a comparison of Eqs. (2.46) and (2.51), the vectors $\tilde{\boldsymbol{\xi}}_m(E) = P_{\mathsf{C}}\Phi_m^{\mathsf{L}}(E)$ originate from the scattering states that arrive from the left lead via projections onto the central part and are therefore normalized through the $\Phi_m^{\mathsf{L}}(E)$ [see also Eq. (2.33)]. Then, we transform $\pi\Lambda_{\mathsf{R}}(E)/E$ into the new basis of the $\tilde{\boldsymbol{\xi}}_m(E)$ through

$$\begin{aligned} \tau_{mn}^{(1)}(E) &= \frac{\pi}{E}\tilde{\boldsymbol{\xi}}_m^\dagger(E)\Lambda_{\mathsf{R}}(E)\tilde{\boldsymbol{\xi}}_n(E) \\ &= \frac{\pi}{E}\left[\tilde{U}^\dagger(E)\Lambda_{\mathsf{R}}(E)\tilde{U}(E)\right]_{mn}, \end{aligned} \tag{2.52}$$

where $\tilde{U}(E) = \left(\tilde{\boldsymbol{\xi}}_1(E), \ldots, \tilde{\boldsymbol{\xi}}_{3N_{\mathsf{C}}}(E)\right)$ and N_{C} is the number of atoms in the central part. The eigenvectors are solutions of the equation

$$\sum_n \tau_{mn}^{(1)}(E)c_{n\mu}(E) = \tau_\mu(E)c_{m\mu}(E) \tag{2.53}$$

with $\sum_m c_{m\mu}^*(E)c_{m\nu}(E) = \delta_{\mu\nu}$, and the eigenchannel μ in the central region is given by

$$\begin{aligned} \tilde{\Psi}_\mu(E) &= \sum_m c_{m\mu}(E)\tilde{\boldsymbol{\xi}}_m(E) \\ &= \sum_{i\in\mathsf{C},\alpha} a_{i\alpha,\mu}(E)\boldsymbol{e}_{i\alpha}. \end{aligned} \tag{2.54}$$

with $a_{i\alpha,\mu}(E) = \sum_m \tilde{U}_{i\alpha,m}(E)c_{m\mu}(E)$. The eigenchannels thus arise from a unitary transformation of the states $\tilde{\boldsymbol{\xi}}_m(E)$.

Let us note that the eigenchannels of Eq. (2.54) are right eigenvectors of the transmission probability matrix $\tau^{(2)}(E) = A_{\mathsf{C}}^{\mathsf{L}}(E)\Lambda_{\mathsf{R}}(E)$ that appears in the trace of Eq. (2.49), i.e.,

$$\tau^{(2)}(E)\tilde{\Psi}_\mu(E) = \tau_\mu(E)\tilde{\Psi}_\mu(E). \tag{2.55}$$

This is evident, if the relations in Eqs. (2.51)–(2.54) are used. It is worth pointing out that apart from $\tau^{(1)}(E)$ or $\tau^{(2)}(E)$, one could eventually consider other forms for the transmission probability matrix. For instance, we might want to use $\tau^{(3)}(E) = t(E)t^\dagger(E)$ with $t(E) = \Lambda_{\mathsf{R}}^{1/2}(E)D_{\mathsf{CC}}^{\mathsf{r}}(E)\Lambda_{\mathsf{L}}^{1/2}(E)$. Given an eigenchannel $\tilde{\Psi}_\mu(E)$ with eigenvalue $\tau_\mu(E)$ of $\tau^{(2)}(E)$ [see Eq. (2.55)], we find that $\Lambda_{\mathsf{R}}^{1/2}(E)\tilde{\Psi}_\mu(E)$ is an eigenvector of $\tau^{(3)}(E)$ with the same eigenvalue $\tau_\mu(E)$. Similar to the electronic case [106], we thus observe that the eigenvectors of $\tau^{(3)}(E)$ do no longer result from a unitary transformation of scattering states that are projected onto the center via P_{C} [see Eq. (2.47)], as it was the case when using $\tau^{(2)}(E)$ [see Eq. (2.54)]. Instead, the matrix $\Lambda_{\mathsf{R}}^{1/2}(E)$ destroys simultaneously the P_{C} projection property as well as the normalization [see Eq. (2.33)], and a comparison of the amplitudes of eigenchannels of $\tau^{(3)}(E)$ would thus not be meaningful.

As it is obvious from the relation $\tilde{\boldsymbol{\xi}}_m(E) = P_{\mathsf{C}}\Phi_m^{\mathsf{L}}(E)$, Eqs. (2.50)–(2.54) yield left-incoming eigenchannels originating from the scattering states $\Phi_m^{\mathsf{L}}(E)$. This means that the lattice vibrations arrive at the scattering region from the left lead and are subsequently transmitted

to the right lead or scattered back to the left one. In order to obtain right-incoming eigenchannels, it is sufficient to start from $\tau^{(4)}_{mn}(E) = \pi\Phi^{\mathsf{R}}_m(E)^\dagger P_{\mathsf{C}}\Lambda_{\mathsf{L}}(E)P_{\mathsf{C}}\Phi^{\mathsf{R}}_n(E)/E$ in Eq. (2.50) or $\tau^{(5)}(E) = A^{\mathsf{R}}_{\mathsf{C}}(E)\Lambda_{\mathsf{L}}(E)$ in Eq. (2.55). The corresponding transmission probability matrices are obtained by rearranging the expression in the trace of Eq. (2.48) through cyclic permutation, by exploiting the definition of $A^{\mathsf{R}}_{\mathsf{C}}(E)$ in Eq. (2.46), and by noting that it can also be written in the form $A^{\mathsf{R}}_{\mathsf{C}}(E) = D^{\mathsf{r}}_{\mathsf{CC}}(E)^\dagger\Lambda_Z(E)D^{\mathsf{r}}_{\mathsf{CC}}(E)$ through the relations given in Eqs. (2.40) and (2.45).

The eigenchannels in the complete system space $\Psi_\mu(E) = \sum_m c_{m\mu}(E)\Phi^{\mathsf{L}}_m(E)$ can be obtained from the $\tilde{\Psi}_\mu(E)$ in Eq. (2.54) by omitting the projection P_{C} on the central device part. We will, however, focus in the following on device-projected eigenchannels. The $\tilde{\Psi}_\mu(E)$ are normalized according to Eq. (2.33), because they are constructed through a unitary transformation with the $c_{m\mu}$ from the $\tilde{\boldsymbol{\xi}}_m(E)$. Consequently, they are measured in units of $\mathrm{J}^{-1/2}$. There is also a global phase factor that needs to be fixed for every eigenchannel $\tilde{\Psi}_\mu(E)$. In the examples shown below, we will simply set the component of a certain atom to a real value for the one-dimensional chain. In the ab-initio calculations, the numerical routines used for computing the eigenvectors determine the phase factor, which may thus vary both with E and μ.

We want to transform now the $\tilde{\Psi}_m(E)$ to displacement vectors measured in units of m, in analogy to what is done when normal modes of finite systems are calculated classically from the eigenvalue equation (2.32). For this reason, we divide $\tilde{\Psi}_\mu(E)$ by $\sqrt{m_i}$ [see also the mass factor in Eq. (2.30)] and multiply in addition with an energy-dependent scaling factor $s(E)$ of unit $\mathrm{J}^{1/2}\mathrm{m}$. In this way the complex displacements of the central part of the eigenchannels are obtained as

$$\begin{aligned}\tilde{\boldsymbol{Q}}_\mu(E) &= \sum_{i\in\mathsf{C},\alpha}\frac{s(E)}{\sqrt{m_i}}a_{i\alpha,\mu}(E)\boldsymbol{e}_{i\alpha} \\ &= \sum_{i\in\mathsf{C},\alpha}\frac{s(E)}{\sqrt{m_i}}|a_{i\alpha,\mu}(E)|e^{\mathrm{i}\theta_{i\alpha,\mu}(E)}\boldsymbol{e}_{i\alpha}. \qquad (2.56)\end{aligned}$$

Equation (2.56) shows that each atomic displacement acquires a phase factor due to the incident wave from the left lead. Note that the displacements of the eigenchannels $\tilde{\boldsymbol{Q}}_\mu(E)$ in Eq. (2.56) are proportional to the eigenchannels $\tilde{\Psi}_\mu(E)$ in Eq. (2.54), if all of the m_i are the same, as it is the case in mono-atomic junctions. In contrast, the proportionality is broken for hetero-atomic junctions. We have furthermore introduced a real-valued scaling factor $s(E)$ in Eq. (2.56), which we may adjust for optimized visualization of displacements at each energy E. In this way, eigenchannel displacements $\tilde{\boldsymbol{Q}}_\mu(E)$ at different energies should only be compared on qualitative grounds, while they are fully comparable at a certain fixed energy.

The full solution for a wave moving from left to right at an energy E is

$$\tilde{\boldsymbol{Q}}_\mu(t, E) = \tilde{\boldsymbol{Q}}_\mu(E)e^{-\mathrm{i}Et/\hbar}. \qquad (2.57)$$

Obviously, $\tilde{\boldsymbol{Q}}_\mu(t = 0, E) = \tilde{\boldsymbol{Q}}_\mu(E)$. The time dependence of the real part of the eigenchannel displacement vector $\mathrm{Re}\tilde{\boldsymbol{Q}}_\mu(t, E)$ can be shown in a movie. However, for illustrative purposes we shall often restrict ourselves to the representation of the real part of the eigenchannel displacements at time $t = 0$, i.e., $\mathrm{Re}\tilde{\boldsymbol{Q}}_\mu(t = 0, E) = \mathrm{Re}\tilde{\boldsymbol{Q}}_\mu(E)$.

2.4.4 1D chain

We now consider the case of a one-dimensional (1D) atomic chain, where the whole procedure for the determination of phonon transmission eigenchannels can be carried out analytically. The system that we are interested in is depicted in Fig. 6(a). In this model junction, the C part consists of two atoms, labeled -1 and 0 and colored in black. These two atoms are coupled through a spring with force constant k_{C}. The leads are described by two semi-infinite chains of coupled harmonic oscillators with nearest-neighbor coupling constant k_{l}. The left (right) lead is connected to atom -1 (0) in the central region with a coupling constant k_{l}. Since the

atomic movements are assumed to happen along the direction of the chain, α reduces to a single component, and the compound index $i\alpha$ simplifies to just the atom index i in the following. Furthermore, we assume that all atoms in the L, C and R parts have the same mass $m_i = m$.

The Green's function of the central part $D^{\mathrm{r}}_{\mathrm{CC}}(E)$ can be obtained from Eq. (2.44) using

$$K_{\mathrm{CC}} = \begin{pmatrix} k_{\mathrm{c}} + k_{\mathrm{l}} & -k_{\mathrm{c}} \\ -k_{\mathrm{c}} & k_{\mathrm{c}} + k_{\mathrm{l}} \end{pmatrix} \tag{2.58}$$

together with the self-energies

$$\Pi^{\mathrm{r}}_{\mathrm{L}}(E) = f(E) \begin{pmatrix} 1 & 0 \\ 0 & 0 \end{pmatrix}, \quad \Pi^{\mathrm{r}}_{\mathrm{R}}(E) = f(E) \begin{pmatrix} 0 & 0 \\ 0 & 1 \end{pmatrix}, \tag{2.59}$$

where $f(E) = (E^2 - 2k_{\mathrm{l}} - E\sqrt{E^2 - 4k_{\mathrm{l}}})/2$. Thus, the corresponding linewidth-broadening matrices can be written as

$$\Lambda_{\mathrm{L}}(E) = g(E) \begin{pmatrix} 1 & 0 \\ 0 & 0 \end{pmatrix}, \quad \Lambda_{\mathrm{R}}(E) = g(E) \begin{pmatrix} 0 & 0 \\ 0 & 1 \end{pmatrix}, \tag{2.60}$$

with

$$g(E) = \begin{cases} E\sqrt{4k_{\mathrm{l}} - E^2} & \text{if } E^2 < 4k_{\mathrm{l}}, \\ 0 & \text{if } E^2 \geq 4k_{\mathrm{l}}. \end{cases} \tag{2.61}$$

From these expressions, the spectral function $A^{\mathrm{L}}_{\mathrm{C}}(E)$ in Eqs. (2.46) and (2.51) is computed. For $E^2 < 4k_{\mathrm{l}}$, the eigenvalues of this matrix are given by

$$\lambda_1(E) = \frac{\sqrt{4k_{\mathrm{l}} - E^2}[2k_{\mathrm{c}}^2 + E^2(k_{\mathrm{l}} - k_{\mathrm{c}})]}{k_{\mathrm{l}} E[4k_{\mathrm{c}}^2 + E^2(k_{\mathrm{l}} - 2k_{\mathrm{c}})]}, \quad \lambda_2(E) = 0 \tag{2.62}$$

with the corresponding eigenvectors

$$\begin{aligned} \tilde{\boldsymbol{\chi}}_1(E) &= \begin{pmatrix} \frac{-E^2 + 2k_{\mathrm{c}} - \mathrm{i}E\sqrt{4k_{\mathrm{l}} - E^2}}{\sqrt{8k_{\mathrm{c}}^2 + 4E^2(k_{\mathrm{l}} - k_{\mathrm{c}})}} \\ \frac{k_{\mathrm{c}}}{\sqrt{2k_{\mathrm{c}}^2 + E^2(k_{\mathrm{l}} - k_{\mathrm{c}})}} \end{pmatrix}, \\ \tilde{\boldsymbol{\chi}}_2(E) &= \begin{pmatrix} \frac{k_c(E^2 - 2k_c + iE\sqrt{4k_l - E^2})}{2\sqrt{(k_c^2 + E^2(k_l - k_c))(2k_c^2 + E^2(k_l - k_c))}} \\ \frac{\sqrt{k_c^2 + E^2(k_l - k_c)}}{\sqrt{2k_c^2 + E^2(k_l - k_c)}} \end{pmatrix}, \end{aligned} \tag{2.63}$$

which are orthonormal, i.e., $\tilde{\boldsymbol{\chi}}^{\dagger}_m(E)\tilde{\boldsymbol{\chi}}_n(E) = \delta_{mn}$. From the $\tilde{\boldsymbol{\chi}}_m(E)$ we obtain the C projections of left-incoming scattering states $\tilde{\boldsymbol{\xi}}_m(E)$ by multiplying with $\sqrt{E\lambda_m(E)/\pi}$ [see the discussion of Eq. (2.51)]. Constructing $\tilde{U}(E) = \big(\tilde{\boldsymbol{\xi}}_1(E), \tilde{\boldsymbol{\xi}}_2(E)\big)$, we determine $\tau^{(1)}(E)$ via Eq. (2.52). Diagonalizing the resulting transmission probability matrix [see Eq. (2.53)], we obtain the transmission eigenvalues

$$\tau_1(E) = \frac{k_{\mathrm{c}}^2(4k_{\mathrm{l}} - E^2)}{k_{\mathrm{l}}[4k_{\mathrm{c}}^2 + E^2(k_{\mathrm{l}} - 2k_{\mathrm{c}})]}, \quad \tau_2(E) = 0 \tag{2.64}$$

and eigenvectors

$$\boldsymbol{c}_1(E) = \begin{pmatrix} 1 \\ 0 \end{pmatrix}, \quad \boldsymbol{c}_2(E) = \begin{pmatrix} 0 \\ 1 \end{pmatrix}. \tag{2.65}$$

These coefficients determine the eigenchannels $\tilde{\Psi}_\mu(E)$ via Eq. (2.54). The time-dependent eigenchannel displacements can now be computed through Eqs. (2.56) and (2.57) by transforming the eigenchannels to the eigenchannel displacement vectors and by multiplying with a time-dependent phase factor.

Since we assume that the masses of all atoms $m_i = m$ are identical in the 1D chain, eigenchannels and eigenchannel displacements are proportional $\tilde{\boldsymbol{Q}}_\mu(E) = s(E)\tilde{\Psi}_\mu(E)/\sqrt{m}$ to each

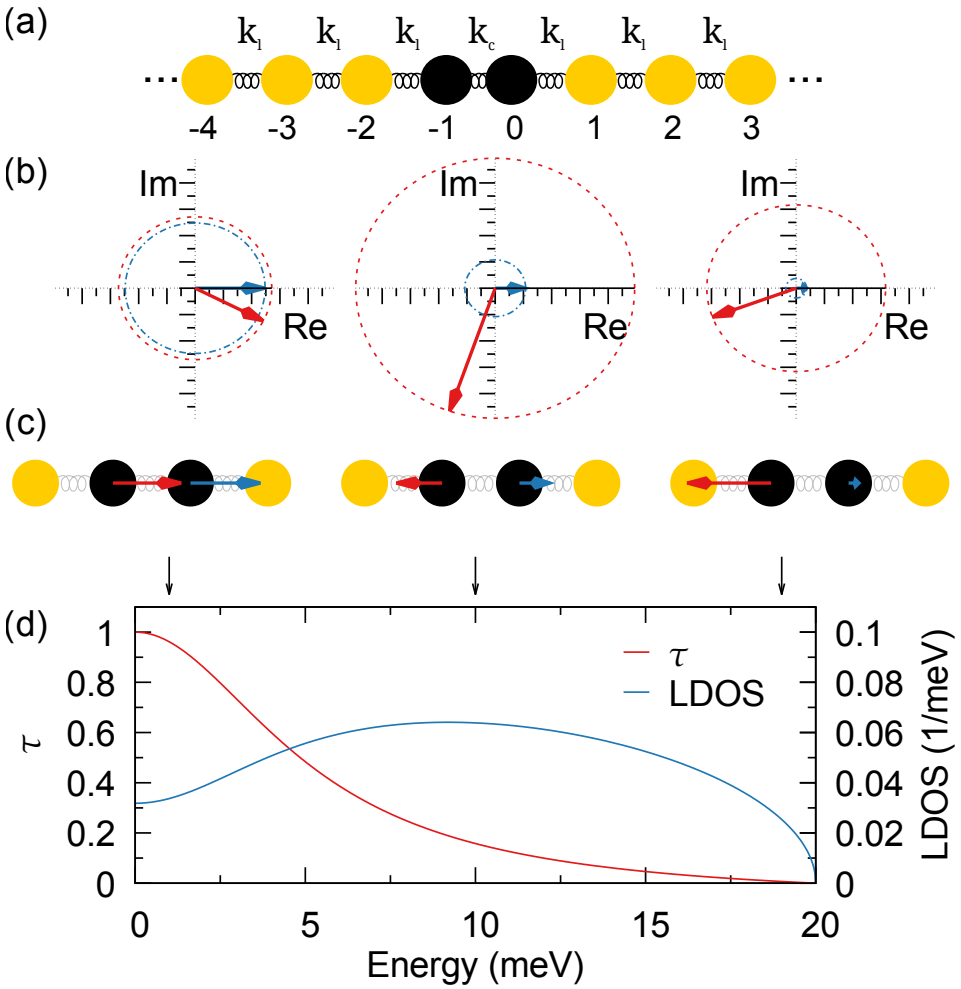

Figure 6. (a) Sketch of the 1D junction. Two semi-infinite leads with nearest-neighbor coupling constants k_l are connected at sites -1 and 0 with the coupling constant k_c. The region $(-\infty,-2]$ is considered as the L part, the region $[-1,0]$ as the C part and $[1,\infty)$ as the R part. (b) Transmission eigenchannel $\tilde{Q}_1(E,t=0)$ for the 1D chain represented in the complex plane for energies of $E=1$ meV, 10 meV, and 19 meV. The red arrow shows the complex number $\tilde{Q}_{1,-1}(E,t=0)$ for the atom -1, the blue one $\tilde{Q}_{1,0}(E,t=0)$ for atom 0. (c) The same as in panel (b), but now we display only the real part of the solution $\mathrm{Re}\tilde{Q}_1(E,t=0)$. (d) The corresponding transmission eigenvalue $\tau_1(E)$ as a function of energy together with the LDOS of one of the atoms (-1 or 0) in the central part. The energies of those eigenchannels, which are studied in panels (b) and (c), are indicated with arrows. For panels (b)–(d), we assumed spring constants of $k_l = 100$ meV^2 and $k_c = 20$ meV^2.

other. We therefore define $\tilde{\Psi}_\mu(E,t) = \sqrt{m}\tilde{\boldsymbol{Q}}_\mu(t,E)/s(E)$ and use both quantities interchangeably. Choosing the global phase factor of the eigenchannel such that the component of the atom 0 is real and positive at $t = 0$, the time-dependent eigenchannels read

$$\tilde{\Psi}_1(t,E) = \sqrt{\frac{\sqrt{4k_l - E^2}k_c^2}{\pi k_l\,(E^2(k_l - 2k_c) + 4k_c^2)}} \begin{pmatrix} \frac{-E^2+2k_c-iE\sqrt{4k_l-E^2}}{2k_c} \\ 1 \end{pmatrix} e^{-iEt/\hbar}, \quad \tilde{\Psi}_2(t,E) = 0. \quad (2.66)$$

Let us discuss several points at this stage. We note that there is only a single eigenchannel with nonvanishing transmission. This is due to the fact that in our 1D model there is only nearest-neighbor coupling. Displacements, which we assume to be along the chain direction, thus need to spread sequentially from atom to atom. The leads provide a cutoff energy of $E_c = 2\sqrt{k_l}$, above which no propagating states exist. If $0 \le k_c \le k_l$ the whole junction shows no bound states, while they arise if $k_c > k_l \ge 0$. Due to the particular left-right symmetry of our problem, the following relations hold for $k_c \le k_l$: $\rho_{ii}(E) = E[A^L_{ii}(E) + A^R_{ii}(E)]/\pi = E\mathrm{Tr}[A^L_C(E)]/\pi = E\lambda_1(E)/\pi = |\tilde{\Psi}_1(E)|^2$ with $i = -1, 0$. The expressions imply that the square of the norm of the transmission eigenchannel 1 follows the LDOS of one of the atoms in the C part. Integration yields $\int_0^{E_c} \mathrm{d}E\,\rho_{ii}(E) = \int_0^{E_c} \mathrm{d}E|\tilde{\Psi}_1(E)|^2 = 1$, which is consistent with the normalization condition in Eq. (2.33), since there are no bound states present. For the case $k_c > k_l$, we get $\int_0^{E_c} \mathrm{d}E|\tilde{\Psi}_1(E)|^2 < 1$, and bound-state contributions need to be taken into account in the C part to fulfill the normalization condition in Eq. (2.33).

If we now consider the perfect chain with $k_c = k_l$, the previous results reduce to

$$\tau_1(E) = 1, \quad \tau_2(E) = 0 \quad (2.67)$$

with

$$\tilde{\Psi}_1(t,E) = \frac{1}{\sqrt{\pi\sqrt{4k_l - E^2}}} \begin{pmatrix} u_{-1}(t,E) \\ u_0(t,E) \end{pmatrix}, \quad \tilde{\Psi}_2(t,E) = 0, \quad (2.68)$$

where $u_n(t,E) = \exp[ik(E)nd - iEt/\hbar]$. The $u_n(t,E)$ appear as solutions for the equation of motion of atoms arranged in an infinite chain and coupled by the same nearest-neighbor spring constants [107]. Here, we have introduced the wave vector $k(E) = (2/d)\sin^{-1}(E/E_c)$ and neighboring atoms are assumed to be separated by the distance d. Note that the interatomic distance d is not relevant for our transport problem, which is entirely determined by the force constant matrix K [see Eqs. (2.34) and (2.35)], where force constants will of course be functions of interatomic distances in realistic systems. As discussed in the previous paragraph, we find that $\rho_{ii}(E) = |\tilde{\Psi}_1(E)|^2 = 2/(\pi\sqrt{4k_l - E^2})$ with $\int_0^{E_c} \mathrm{d}E\,\rho_{ii}(E) = 1$.

We want to use now the analytical expressions to examine different representations of the transmission eigenchannel displacements. For this purpose we choose the global scaling factor $s/\sqrt{m}$ in Eq. (2.56) to be real, energy-independent and of units $\mathrm{J}^{1/2}\mathrm{m}/\mathrm{kg}^{1/2}$. In Fig. 6(b)–(d) we study the transmission, LDOS and eigenchannel displacements for the 1D chain with $k_l = 100$ meV^2 and $k_c = 20$ meV^2, i.e., in the situation where there are only propagating states in the junction system. Corresponding figures for the perfect chain with $k_c = k_l = 100$ meV^2 and with bound states contributions, $k_l = 100$ meV^2 and $k_c = 2000$ meV^2, can be found in Appendix B. The transmission $\tau(E)$ in Fig. 6(d) shows a monotonically decreasing behavior with increasing energy and vanishes above the cutoff energy of $E_c = 20$ meV. At the same time, we plot the LDOS $\rho_{ii}(E)$ of the atom $i = -1, 0$ in the central part, which starts from a finite value at $E = 0$, increases to a maximum around 9 meV and drops to zero beyond E_c. The transmission eigenchannel displacements $\tilde{\boldsymbol{Q}}_1(t = 0, E)$ are shown in Fig. 6(b) for the energies $E = 1$ meV, 10 meV, and 19 meV, indicated by arrows in Fig. 6(d). The two complex components are indicated by two arrows in the complex plane. Notice that while the norm of the eigenvector $\tilde{\boldsymbol{Q}}_1(t,E)$ is proportional to $\sqrt{\rho_{ii}(E)}$ for the energy-independent s chosen here, the relative magnitude at the atom $i = 0$ as compared to the atom $i = -1$, i.e., $|\tilde{Q}_{1,0}(t,E)|/|\tilde{Q}_{1,-1}(t,E)|$, decreases with increasing energy because a larger portion of the left-incoming wave gets reflected at the

constriction. We also note that the phase difference $\theta_{0,1}(E) - \theta_{-1,1}(E)$ [see Eq. (2.56)] between the two components increases from 0 at $E = 0$ to π at $E = 20$ meV. With increasing time the arrows precess around the origin at a constant angular velocity of $\omega = E/\hbar$, spanning the circle indicated by the dashed lines in the plot. Since the two atoms typically do not swing in phase, the real parts of $\tilde{Q}_{1,-1}(t, E)$ and $\tilde{Q}_{1,0}(t, E)$ take maximum amplitudes at different times.

In Fig. 6(c) we present another way to visualize the eigenchannel displacements by simply plotting $\mathrm{Re}\tilde{Q}_{1,-1}(t, E)$ and $\mathrm{Re}\tilde{Q}_{1,0}(t, E)$ at $t = 0$ as arrows attached to the respective atoms. This is actually the representation that we will use in all the figures shown in the rest of this work. Notice that due to our choice of the global phase factor, we get $\theta_{0,1}(E) = 0$ and $\mathrm{Re}\tilde{Q}_{1,0}(t = 0, E)$ is hence maximal at $t = 0$. In contrast $\mathrm{Re}\tilde{Q}_{1,-1}(t, E)$ depends both on the absolute value $|\tilde{Q}_{1,-1}(E)|$ and the phase $\theta_{-1,1}(E)$, as it is visible from Fig. 6(b). Despite the large $|\tilde{Q}_{1,-1}(E)|$ at $E = 10$ meV, $\mathrm{Re}\tilde{Q}_{1,-1}(t, E)$ is rather small, because $\theta_{-1,1}(E) \approx -0.6\pi$. In spite of such shortcomings, one gets an impression of the nature of the atomic motions involved in the eigenchannel. Indeed, we observe that the eigenchannel displacements at low energy $E = 1$ meV resemble a translational mode of the two atoms, while they are basically vibrating against each other at 19 meV, as it is clear from the evolution of the phase difference $\theta_{0,1}(E) - \theta_{-1,1}(E)$ with energy, discussed in the previous paragraph. Videos could be used to examine the full time-dependent dynamics of $\mathrm{Re}\tilde{\boldsymbol{Q}}_1(t, E)$, but we refrain from this here, since the simple 1D case is well characterized with the help of Fig. 6(b).

In total, we have established a method to obtain useful representations of the transmission eigenchannels with quantities available in standard NEGF-based calculations. This method allows for a detailed analysis of the vibrational modes involved in the transport of heat.

2.5 Acoustic sum rule

The acoustic sum rule enforces a relation on a general force constant matrix. Rooted in the translational invariance of the system, it leads to zero energy or massless modes in the energy-momentum relation. Models which obey this relation are called momentum conserving, while momentum non-conserving approaches violate the condition. In the context of heat transport in systems with reduced dimensionality, especially 1D systems, this rule is important since it has been shown that momentum conserving models violate Fourier's law, which states that the thermal conductivity is independent of conductor's length, whereas if the momentum is not conserved for some models Fourier's law is recovered in the thermodynamic limit [32]. Experimentally this deviation has been measured for 1D[30, 108] and two-dimensional (2D) systems [31].

The sum rule can be derived by noting that an arbitrary translation of the whole system along a direction $\delta\vec{r}$, will not lead to a force on it. In a harmonic lattice, this reads as

$$0 = \vec{F} = H\delta\vec{r}, \tag{2.69}$$

where $H_{i\alpha,j\beta} = \frac{\partial^2 E}{\partial R_{i\alpha} R_{j\beta}}$ is the Hessian matrix. Since $\delta\vec{r}$ is arbitrary we get a relation, for each direction $\alpha = \mathrm{x}, \mathrm{y}, \mathrm{z}$

$$\sum_j H_{i\alpha,j\beta} = 0, \tag{2.70}$$

which has to be fulfilled for any physical harmonic system. This equation can be rewritten in a more familiar form, using the dynamical matrix $K = \sqrt{M^{-1}} H \sqrt{M^{-1}}$, with the inverse mass matrix M and by separating the diagonal elements from the rest

$$\sum_{j\neq i} \sqrt{\frac{m_j}{m_i}} K_{i\alpha,j\beta} = -K_{i\alpha,i\beta}. \tag{2.71}$$

Since the Hessian matrix is symmetric this implies that $K_{i\alpha,i\beta} = K_{i\beta,i\alpha}$ and

$$\sum_{j\neq i} \sqrt{\frac{m_j}{m_i}} K_{i\alpha,j\beta} = \sum_{j\neq i} \sqrt{\frac{m_j}{m_i}} K_{i\beta,j\alpha} \tag{2.72}$$

Let us mention that although breaking of the translational invariance is in general unphysical, in low dimensional systems an on-site pinning which violates Eq. 2.71, could be physically motivated by an additional coupling to a substrate.

2.5.1 Acoustic sum rule in phonon transport

In a typical transport setup, one studies the amount of energy transmitted from one reservoir at temperature T_L to a reservoir at temperature T_R via a central bridge. Therefore, one divides the system into three parts, the left lead L, the central part C, and the right lead R, see Sec. 2.1. If one neglects the coupling between the left and the right lead, the force constant matrix will look as follows

$$K = \begin{pmatrix} K_{\mathrm{LL}} & K_{\mathrm{LC}} & 0 \\ K_{\mathrm{LC}} & K_{\mathrm{CC}} & K_{\mathrm{RC}} \\ 0 & K_{\mathrm{CR}} & K_{\mathrm{RR}} \end{pmatrix}. \tag{2.73}$$

In most cases, the calculation of the coupling elements is divided into two separate calculations, namely one for the semi-infinite leads (K_{LL} and K_{RR}) and the other one for a finite scattering region (K_{CC} and K_{XY}, with $X, Y \in \mathrm{C}, \mathrm{L}, \mathrm{R}$ and $X \neq Y$). In our case, the finite region is calculated by means of the ECC, see Ref. [109]. Whereas each individual computation can be easily forced to obey the sum rule, this does not necessarily hold for the combined system. In a system with equal dimensions in the individual parts, a violation could come from a different number of

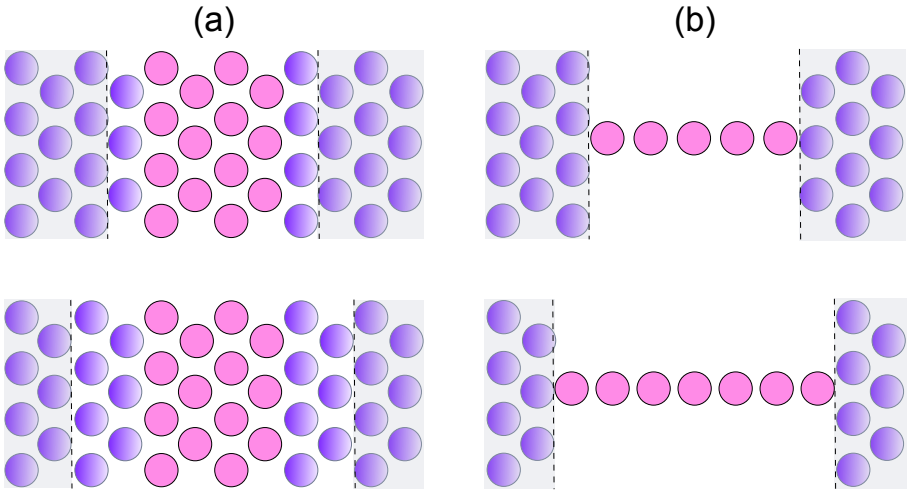

Figure 7. (a) System with equal dimensions in each part. Upon increasing the central part (indicated with the dashed line) from top to bottom the geometry does not change. (b)A System with a different dimension in the lead with respect to the central part. A change in the partitioning leads to a different geometry of the central part.

neighbors considered in each calculation or differences in the simulation-dependent parameters, like electronic k-points, smearing or different density grids, just to name a few. However, these parameters can be controlled in principle and for a large enough scattering region, such that the physical boundary is far away from the cut, Eq. 2.71 should hold. This situation is sketched in Fig. 7(a). A change in the partitioning does not lead to a different geometry. At some point, the coupling elements of the outermost lead atoms in the central part should converge to the bulk values. Nevertheless, in efficient simulations, a simple correction scheme as, for instance, proposed in Ref. [110] can be used to fulfill the sum rule without converging to the bulk limit.

In contrast, if we consider a system with different dimensionality of the lead with respect to the central part, like in our ECC calculation, a straightforward implementation of the sum rule is not possible. The reason for this can be seen in Fig. 7(b). A change in the partitioning of the system is now accompanied by a change of the geometry in the central part since a former layer which was infinite perpendicular to the transport direction now becomes finite. More importantly, with respect to the acoustic sum rule, there will always be a physical surface layer at the boundary between leads and central part. In this layer, atoms with a different coordination number in comparison to the bulk situation exist, and since Eq. 2.71 is a sum over all neighbors, it is clear that the sum rule can't be fulfilled with bulk parameters in any calculation. Additionally, the diagonal elements of the surface atoms which are coupled to the central part, have to be corrected since they have a different environment compared to the bare surface. In what follows we present a two-step scheme to resolve these issues.

Let us start with the construction of the supercells for the semi-infinite lead. For simplicity, we chose the transport direction to be along the z-direction and we focus on the left lead, the results, however, hold for arbitrary directions and can be done similar for the right lead. If we take the coupling elements from a separate bulk calculation K_i, where i labels the neighbor in

the z-direction, the corresponding matrix will take the following form

$$K_{\mathrm{LL}}^{\mathrm{bulk}} = \begin{pmatrix} \ddots & \vdots & \vdots & \vdots & \vdots & \vdots & \vdots & \vdots \\ \vdots & \ddots & \vdots & \vdots & K_{n_z-2} & K_{n_z-1} & K_{n_z} & 0 \\ \vdots & \vdots & \ddots & \vdots & K_{n_z-3} & K_{n_z-2} & K_{n_z-1} & K_{n_z} \\ \vdots & \vdots & \vdots & \ddots & \vdots & \vdots & \vdots & \vdots \\ \dots & K_{n_z-2} & K_{n_z-3} & \dots & K_0 & K_1 & K_2 & K_3 \\ \dots & K_{n_z-1} & K_{n_z-2} & \dots & K_1 & K_0 & K_1 & K_2 \\ \dots & K_{n_z} & K_{n_z-1} & \dots & K_2 & K_1 & K_0 & K_1 \\ \dots & 0 & K_{n_z} & \dots & K_3 & K_2 & K_1 & K_0 \end{pmatrix}, \tag{2.74}$$

where each block K_i is of dimension $n_x \times n_y \times 3 \times 3$, consisting of 3x3 blocks K_i^{jk}, where i, j, k labels the relative distance of atom in x,y,z-direction, n_x, n_y, n_z are the respective total number of neighbors used in the bulk calculation and we assumed the symmetry $K_i = K_{-i}$. One can group this matrix into blocks, such that we get a block diagonal structure

$$K_{\mathrm{LL}}^{\mathrm{bulk}} = \begin{pmatrix} \ddots & \vdots & \vdots & \vdots & \vdots \\ \dots & \tilde{K}_0 & \tilde{K}_1 & 0 & 0 \\ \dots & \tilde{K}_1 & \tilde{K}_0 & \tilde{K}_1 & 0 \\ \dots & 0 & \tilde{K}_1 & \tilde{K}_0 & \tilde{K}_1 \\ \dots & 0 & 0 & \tilde{K}_1 & \tilde{K}_0 \end{pmatrix}. \tag{2.75}$$

To account for the missing neighbors in the surface layer we now change the corresponding surface block, to get a matrix of the form

$$K_{\mathrm{LL}} = \begin{pmatrix} \ddots & \vdots & \vdots & \vdots & \vdots \\ \dots & \tilde{K}_0 & \tilde{K}_1 & 0 & 0 \\ \dots & \tilde{K}_1 & \tilde{K}_0 & H_1 & 0 \\ \dots & 0 & \tilde{K}_1 & \tilde{K}_0 & \tilde{K}_1 \\ \dots & 0 & 0 & \tilde{K}_1 & \tilde{K}_{\mathrm{S}} \end{pmatrix}. \tag{2.76}$$

Here $\tilde{K}_{\mathrm{S}}$ represents the surface layer and for $\tilde{K}_{\mathrm{S}} = \tilde{K}_0$ follows $K_{\mathrm{LL}} = K_{\mathrm{LL}}^{\mathrm{bulk}}$. If we use the bulk parameters, the diagonal elements of $\tilde{K}_S$ read $K_0^{00} = -\sum_{(ijk)\neq(000)} K_i^{jk} - \sum_{i>0} K_i^{jk}$, where $0 \leq i \leq n_z$, $-n_y \leq j \leq n_y$, $-n_x \leq k \leq n_x$. To fulfill the sum rule one has to adjust these diagonal elements according to Eq. 2.71. This leads to

$$\tilde{K}_S = \begin{pmatrix} K_0^{n_z} & \vdots & K_{n_z-3} & K_{n_z-2} & K_{n_z-1} & K_{n_z} \\ \vdots & \vdots & \vdots & \vdots & \vdots & \vdots \\ K_{n_z-3} & \dots & K_0^3 & K_1 & K_2 & K_3 \\ K_{n_z-2} & \dots & K_1 & K_0^2 & K_1 & K_2 \\ K_{n_z-1} & \dots & K_2 & K_1 & K_0^1 & K_1 \\ K_{n_z} & \dots & K_3 & K_2 & K_1 & K_0^0 \end{pmatrix}, \tag{2.77}$$

where the matrices K_0^m differ in their diagonal element K_0^{00} given by

$$(K_0^{00})^m = -\sum_{(ijk)\neq(000)} K_i^{jk} - \sum_{i\leq m, i\neq 0, jk} K_i^{jk}, \tag{2.78}$$

and m labels the different surface layers in z-direction. The surface atoms are supposed to have equal masses, so the mass term in Eq. 2.71 vanishes. This matrix includes the renormalization of the diagonal elements due to the missing neighbours in the surface planes. Note, within different z-layers the atoms are exposed to distinct couplings.

The next step is to include the couplings from the central part on the diagonal of Eq. 2.77. If $\tilde{d}_{\mathsf{LL}}$ is the solution to the problem of the bare surface

$$\tilde{d}_{\mathsf{LL}} = \left[\omega^2 - K_{LL}\right]^{-1}, \tag{2.79}$$

then d_{LL} is the solution of the problem where the renormalization of the diagonal elements due to the coupling to the central part has been included. This Greens function can be calculated using Dyson equation

$$d_{\mathsf{LL}} = \left[\omega^2 - K_{LL} - \delta\right]^{-1} = \tilde{d}_{\mathsf{LL}} + \tilde{d}_{\mathsf{LL}}\delta d_{\mathsf{LL}}, \tag{2.80}$$

which leads to

$$d_{\mathsf{LL}} = \left(1 - \tilde{d}_{\mathsf{LL}}\delta\right)^{-1} \tilde{d}_{\mathsf{LL}}. \tag{2.81}$$

Here

$$\delta_{i\alpha,i\beta} = -\sum_{j\in C} \sqrt{\frac{m_j}{m_i}} K^{\mathsf{ECC}}_{i\alpha,j\beta}, \tag{2.82}$$

with $i \in \mathsf{L}$ is the missing term of the diagonal elements and K^{ECC} indicates that these parameters are taken from the ECC. In the implementation one problem arises with the symmetry condition Eq. 2.72 since in general it is not fulfilled when two different calculations are considered. One can think of two different solutions to overcome this problem. The first is to force in the ECC calculation every coupling element to fulfill $K^{\mathsf{ECC}}_{i\alpha,j\beta} = K^{\mathsf{ECC}}_{i\beta,j\alpha}$, which would lead to a modification of the eigenmodes of the central part. The second possibility is to still violate the acoustic sum rule and only force the diagonal elements of the corrected lead atoms to be symmetric with

$$K_{i\alpha,i\beta} = \frac{1}{2}\left(K_{i\alpha,i\beta} + K_{i\beta,i\alpha}\right) \quad i \in \mathsf{L},\mathsf{R}. \tag{2.83}$$

Let us close with a remark that in principle more advanced correction schemes exists in literature to account for the acoustic sum rule [111, 112]. However, since all of these would lead to a modification of the coupling elements between different atoms, we restrict ourselves to the simple form proposed above.

2.5.2 1D lead

To test the method and to get an idea of how translational invariance influences the phonon transmission, we apply the method to a 1D system where two semi-infinite leads with coupling elements k_l are coupled to one atom with coupling k_c. For simplicity, we assume all atoms to have identical masses $m_l = m_c = m$. Since the dimension of the leads and the central part are identical the correction scheme would not be necessary, nevertheless, we take this as a pedagogical example. The matrices of the system without the coupling to the central parts are

$$K_{\mathsf{LL}} = \begin{pmatrix} \vdots & \vdots & 0 \\ \vdots & 2k_l & -k_l \\ 0 & -k_l & k_l \end{pmatrix} \quad \text{and} \quad K_{\mathsf{RR}} = \begin{pmatrix} k_l & -k_l & 0 \\ -k_l & 2k_l & \vdots \\ 0 & \vdots & \vdots \end{pmatrix}. \tag{2.84}$$

Here the surface element has already been corrected according to Eq. 2.78, although, due to only nearest neighbor coupling this is somehow trivial. Using these we get a surface Green's function of the following form

$$\tilde{d}_s(E) = \frac{1}{2k_l E}\left(E - \sqrt{E^2 - 4k_l}\right). \tag{2.85}$$

In a next step we correct this function, due to the coupling to a central part with the coupling k_c, using Eq. 2.80, which yields the following equation

$$d_s = \tilde{d}_s + \tilde{d}_s k_c d_s \rightarrow d_s = \frac{1}{2}\frac{E^2 - 2k_c - E\sqrt{E^2 - 4k_l}}{E^2(k_l - k_c) + k_c^2}. \tag{2.86}$$

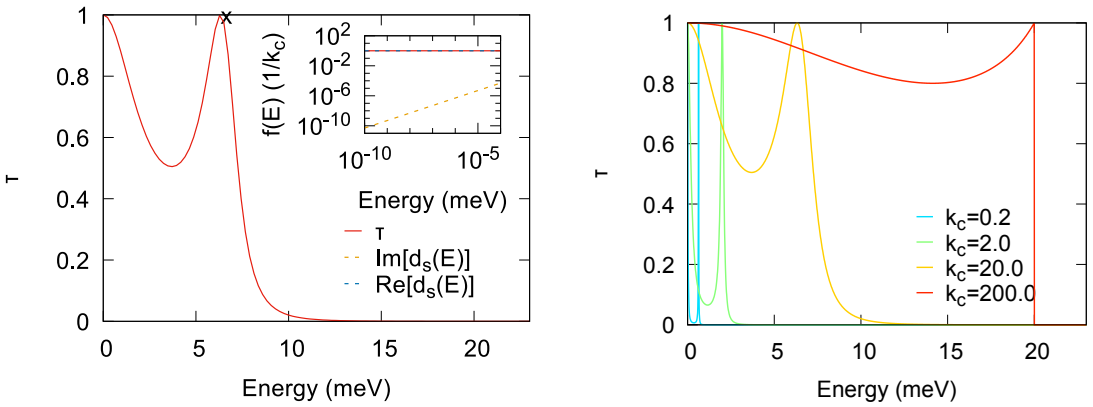

Figure 8. (Left) Transmission, real and Imaginary part of the surface Greens function for a 1d chain with 1 site. The real part of the Green's function has the value -1/kc at E=0 so Gcc gets a resonance at this Energy. (Right) Evolution of the zero energy peak with changing of the mode in the central part. As the mode of the central part shifts to lower energies the zero energy peak gets narrower.

Note that this function is identical to the surface Green's function obtained by directly fulfilling the sum rule in the matrix of the full system.

To see the effect of the sum rule on the transport, we show in Fig. 8(a) the transmission for a system with $k_c = 20\text{meV}^2$ and $k_l = 100\text{meV}^2$, together with the real and the imaginary part of the surface Green's function $d_s(E)$. The eigenmode of the central part is indicated with a cross. While there is a resonance in the transmission at the position of the eigenmode, another resonance shows up at zero energy. We want to use the following expression for the transmission of this simple model

$$\tau = \frac{4k_c^4 \text{Im}[d_s(E)]^2}{(E^2 - 2k_c - 2k_c^2 \text{Re}[d_s(E)])^2 + 4k_c^4(\text{Im}[d_s(E)])^2} = \frac{2\pi k_c^2}{E}\text{Im}[d_s(E)]\varrho_C(E), \tag{2.87}$$

to discuss the tranmission at zero energy. One can see that mathematically the transmission gets 1 at zero energy, if the real part of $d_s(E)$ goes faster to $1/k_c$ for $E \to 0$ leading to a resonance in $D_{CC}(E = 0)$, then the imaginary part of $d_s(E)$ going to zero. As we will show later in more detail, the sum rule leads to a resonance at zero energy, or

$$\text{Det}\,|K| = 0, \tag{2.88}$$

for the infinite matrix K. Next, we want to study the relation of the zero energy peak with the position of the central resonance. For this we depict in Fig. 8(b) the transmission for different k_c ranging from 0.2 $(\text{meV})^2$ to 200 $(\text{meV})^2$. One can see that while the mode in the central part shifts to lower energies, the zero energy peak gets narrower. This gives us a very intuitive physical interpretation of the sum rule. If the wavelength of the incoming phonon is much larger compared to the wavelength of the lowest central mode, the phonon doesn't see the central part as an impurity and gets transmitted without being scattered.

To close this section and to show the connection between zero energy peak and sum rule we study how a violation of this condition influences the transmission. For this purpose, we use the following matrices for the system

$$K_{\text{LL}} = \begin{pmatrix} \ddots & \vdots & \vdots \\ \dots & 2k_l & -k_l \\ \dots & -k_l & (k_l + k_c + \delta) \end{pmatrix} K^n_{\text{CC}} = \begin{pmatrix} 2k_c & -k_c & \dots & 0 \\ -k_c & 2k_c & \dots & 0 \\ \vdots & \vdots & \ddots & \vdots \\ 0 & 0 & \dots & 2k_c \end{pmatrix}, \tag{2.89}$$

where K^n_C is of size $n \times n$. First, we pick one n, here n=2 and check the transmission for different δ. In Fig. 9(a) one can see the results. For δ=0 there are transmission peaks at the energies

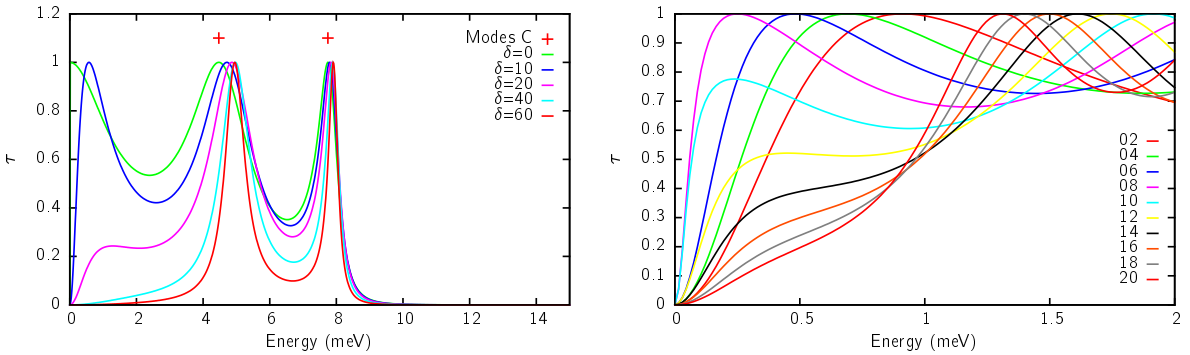

Figure 9. (Left)Transmission of 1D system violating the sum rule for different δ with n=2. (Right) Same but for fixed $\delta = 10\text{meV}^2$ and varying n.

of the center modes whereas a third peak arises at zero energy. As already discussed this peak is a consequence of translational invariance. With increasing δ this zero energy peak shifts to higher energies and decreases in amplitude, while the resonances of the system only slightly shift but decrease in width. At deviations $\delta > 20$ meV^2 the transmission curve shows only the two resonances of the center.

Next, we fix $\delta = 10$ meV^2 and vary n between 2-20 in steps of two to see how the zero energy peak shifts for different lengths of the central system. A consequence of the increasing length is a shift of the lowest resonance in the system to lower energies since the maximum possible wavelength in the system increases. This also modifies the peak around zero energy, as can be seen in Fig. 9(b). While it first decreases in energy and width, it is nearly absent for $n > 18$.

2.5.3 2D lead

In the previous section, the 1D model was studied to verify the proposed correction scheme analytically, although it was not necessary since the dimension of the lead was equal to the dimension of the center. Now we construct a toy model, where a 2D lead is coupled to a 1D chain, so the correction scheme is necessary. Furthermore, we assume the vibrational modes of the y- and x-direction to be decoupled, which will further simplify our analysis and restrict the transport to be only along x-direction. For the 2D semi-infinite left/right lead this gives us the following Hamiltonian

$$H_L = H_R = \frac{1}{2}\sum_{i,j} p_{i,j}^2 + k_x \left(x_{i+1,j} - x_{i,j}\right)^2 + k_y \left(x_{i,j+1} - x_{i,j}\right)^2 \quad i \in x, j \in y, \tag{2.90}$$

where k_x is the coupling of the x-coordinates of two atoms in x-direction, while k_y is the coupling of the x-coordinates between atoms in y-direction. A sketch of the system can be seen in Fig. 10. The central part is assumed to couple only with a single surface atom at each side. With this,

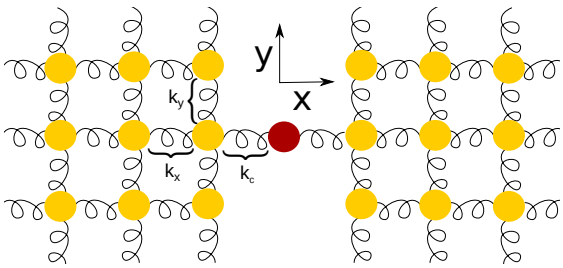

Figure 10. Sketch of the model with 2D leads.

we get two equations of motion for mathematically distinct layers

$$E^2 x_{00} = 2k_y x_{00} - k_y x_{01} - k_y x_{0-1} + k_x x_{00} - k_x x_{10} \tag{2.91}$$

and

$$E^2 x_{10} = 2k_y x_{10} - k_y x_{11} - k_y x_{1-1} + 2k_x x_{10} - k_x x_{20} - k_x x_{00}. \tag{2.92}$$

Since the problem is translational invariant in y-direction with respect to a lattice vector we can go in reciprocal space, by assuming

$$x_{lm} = x_l e^{iqma}, \tag{2.93}$$

where a is the distance between two atoms and q is a reciprocal vector in y-direction. The equations now read

$$E^2 x_0 = 2k_y x_0 - k_y e^{iqa} x_0 - k_y e^{-iqa} x_0 + k_x x_0 - k_x x_1 \tag{2.94}$$

and

$$E^2 x_1 = 2k_y x_1 - k_y x_1 e^{iqa} - k_y x_1 e^{-iqa} + 2k_x x_1 - k_x x_2 - k_x x_0. \tag{2.95}$$

We can write this in matrix form as follows

$$\begin{pmatrix} k_x + 4k_y(sin^2(\frac{qa}{2})) & -k_x & 0 & \dots \\ -k_x & 2k_x + 4k_y(sin^2(\frac{qa}{2})) & -k_x & \ddots \\ \vdots & \ddots & \ddots & \ddots \end{pmatrix} x = \begin{pmatrix} E^2 & 0 & 0 & \dots \\ 0 & E^2 & 0 & \ddots \\ \vdots & \ddots & \ddots & \ddots \end{pmatrix} x. \tag{2.96}$$

The Green's function element $d_{00} = d_s$ of this problem can be calculated in q-space in analogy to the 1D chain and is given by

$$\tilde{d_s}(q) = 2\left[E^2 - 4k_y \sin^2(qa/2) + \sqrt{\left(E^2 - 4k_y \sin^2(qa/2)\right)\left(E^2 - 4k_x - 4k_y \sin^2(qa/2)\right)}\right]^{-1}. \tag{2.97}$$

The surface Green's function in real space is then calculated according to

$$\tilde{d_s}(0) = \frac{1}{2\pi}\int \tilde{d_s}(q)\mathrm{d}q, \tag{2.98}$$

which can't be solved analytically, so one has to use numerical methods to evaluate it. After the calculation of this integral, the Dyson equation Eq. 2.80 can be used to account for the coupling to the center.

In Fig. 11 the transmission for a single atom with $k_x = 100$ meV^2, $k_y = 2$ meV^2 and $k_c = 19$ meV^2 is depicted. One can see that instead of a peak at zero energy a peak at the highest energy of a transversal mode in y-direction arises, namely at $2\sqrt{k_y}$. The inset shows the real and imaginary part of the surface Green's function for $E \to 0$ in units of $(1/k_c)$. Similar to the 1D lead, the real part of $d_s(E)$ goes towards a resonance ($\to 1/k_c$) but this time the imaginary part of $d_s(E)$ drops faster, which is the reason for the absence of the zero energy transmission peak. Let us emphasize that these findings are in accordance with the one proposed in Ref. [113], where they find the transmission of systems with dimensions greater than 1 to go to zero for $E \to 0$.

2.5.4 3D lead

In this section we apply the method to realistic junctions, consisting of a metallic gold and a molecular junction. The first system contains only atoms of one type such that the sum rule is valid for both the dynamical matrix and the Hessian, whereas in the second system the sum rule is only fulfilled for the Hessian matrix due to the mass difference of the different atom types.

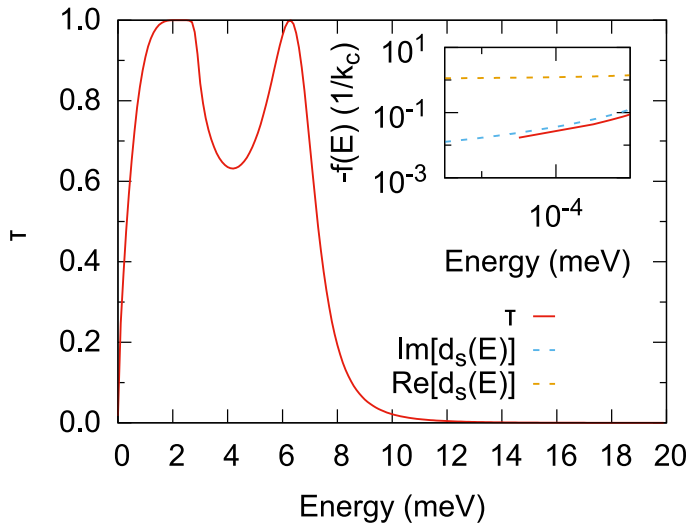

Figure 11. Transmission for the 2D infinite chain coupled to a single atom, with k_x=100 meV^2 k_y=2 meV^2 k_c=20 meV^2. The zero energy peak disappears while a second peak arises at the maximum energy of the transverse mode ($\hbar\omega_{max} = 2\sqrt{2\text{meV}^2} \approx 2.83\text{meV}$).

In Fig. 12(a) we compare the phonon transmission for a metallic nanowire, with and without the correction scheme, where without correction means using the bulk parameters for the surface layers. First of all notice that the position of the resonance peaks are quite unaffected and are very similar for both calculations. The most striking difference is the behavior in the low energy range, especially the width of the resonances increases while using the correction scheme. Overall the thermal conductance is greater in the whole temperature range upon using the modified parameters with an increased conductance of $\approx$ 11 % at 300 K in comparison to the calculation with the bulk ones. As already seen for the 2D lead in Sec. 2.5.3 there is no transmission peak around zero energy, which can be explained with the low energy behavior of the phonon density of states.

Finally in Fig. 12(b) the phonon transmission for a single-molecular junction containing a dithiolated alkane chain is shown. Once again the high energy behavior is nearly un-effected by the correction, whereas the width of the transmission peaks at low energies in general increases, leading to a higher total transmission in this energy range. The inset displays the total thermal conductance and again we find an enhanced conductance of $\approx$ 22 % at 300 K.

Let us emphasize that the low energy behavior gets effected by the definition of the Green's function which reads as

$$D = \left[(E + i\eta)^2 - K\right]^{-1}. \tag{2.99}$$

Here one adds a small imaginary part to shift the pole in the imaginary plane. Using the form of Eq. (2.99) the imaginary part gets energy dependent thus one adds a shift of $-\eta^2$ on the resonance. For the transmission this η should be small enough such that this shift is negligible and big enough to avoid numerical problems. Nevertheless, an influence especially at low energies can not be excluded.

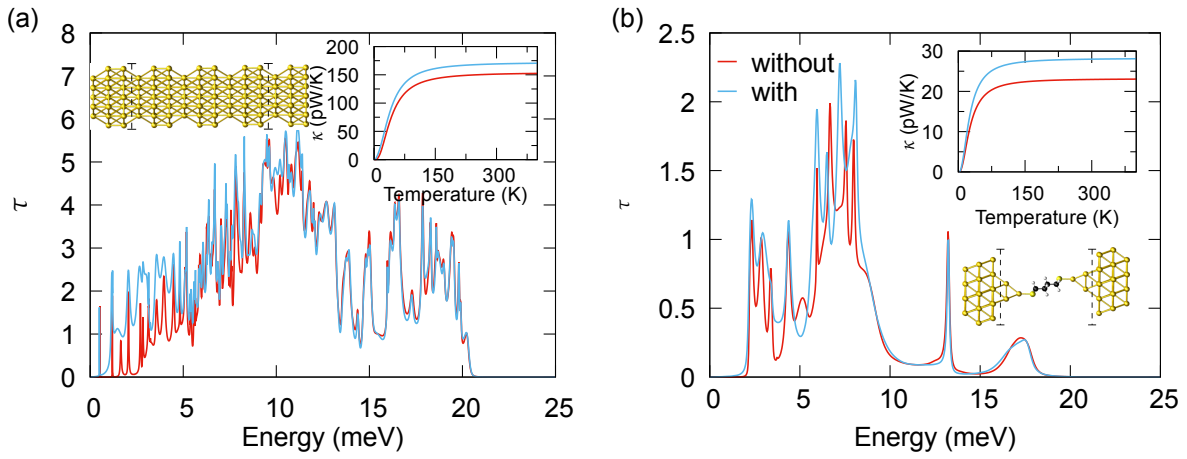

Figure 12. (a) Transmission function of a gold nanowire attached to a 3D surface, without (red) and with (blue) the corrected surface elements. The partitioning is as indicated in the picture. In the inset the temperate dependence of both calculations is shown. (b) Same comparison for a single-molecule junction.

2.6 Electrons

Besides the thermal conductance due to phonons, we are also interested in the thermal conductance carried by electrons, since the relative contributions from both are important for experimental measurements. Within the Landauer-Büttiker picture, their contribution to the different transport properties is determined by the energy-dependent electronic transmission $\tau_{\mathrm{el}}(E)$. In particular, in the linear response regime, in which we are interested in, the electrical conductance G, thermopower S, and the electronic thermal conductance κ_{el} are given by [114, 54]

$$G = G_0 K_0, \tag{2.100}$$

$$S = -\frac{K_1}{eTK_0}, \tag{2.101}$$

$$\kappa_{\mathrm{el}} = \frac{2}{hT}\left(K_2 - \frac{K_1^2}{K_0}\right), \tag{2.102}$$

where $e = |e|$ is the absolute value of the electron charge, h is Planck's constant, k_{B} is Boltzmann's constant, T is the average junction temperature, and $G_0 = 2e^2/h$ is the conductance quantum. The coefficients K_n in Eqs. (2.100)-(2.102) are given by

$$K_n = \int_{-\infty}^{\infty} dE\, \tau_{\mathrm{el}}(E)\left(-\tfrac{\partial f(E)}{\partial E}\right)(E-\mu)^n, \tag{2.103}$$

where $f(E) = \{\exp[(E-\mu)/k_{\mathrm{B}}T]+1\}^{-1}$ is the Fermi function. Here, the chemical potential $\mu \approx E_{\mathrm{F}}$ is approximately given by the Fermi energy E_{F} of the Au electrodes. Dependences of transport quantities, the coefficients K_n and the Fermi function on temperature and chemical potential have been suppressed.

Let us emphasize that we have used the exact Eqs. (2.100)-(2.102) in all calculations, but it is instructive to have in mind the corresponding low-temperature expansions, which turn out to be very good approximations in almost all cases. They read

$$G \approx G_0 \tau_{\mathrm{el}}(E_{\mathrm{F}}), \tag{2.104}$$

$$S \approx -\frac{\pi^2 k_{\mathrm{B}}^2 T}{3e}\left.\frac{\partial_E \tau_{\mathrm{el}}(E)}{\tau_{\mathrm{el}}(E)}\right|_{E=E_{\mathrm{F}}}, \tag{2.105}$$

$$\kappa_{\mathrm{el}} \approx L_0 G T. \tag{2.106}$$

The latter expression for κ_{el} is known as the Wiedemann-Franz law [54] and $L_0 = (k_B/e)^2\pi^2/3$ is the Lorentz number.

We remark, that all system dependent parameters are inherently taken into account in the electron transmission which we compute making use of our DFT-NEGF formalism, implemented in TURBOMOLE and explained in detail in Ref. [64]. A key advantage of our approach is that for a given junction we can compute both contributions stemming from electrons and phonons on the same level of theory, thus we can correlate both values. Additionally, an analysis in terms of transmission eigenchannels, where the transmission is resolved in terms of individual contributions from eigensolutions to the transmission matrix, is possible and reads

$$\tau_{el} = \sum_i \tau_{el,i}. \tag{2.107}$$

This concept is similar to the one introduced in Sec.2.4 for phonons, and details about our implementation can be found in Ref. [106].

To account for the deficits in the description of the molecular orbital alignment related to DFT and associated with many-electron self-energy effects on the carrier energies, we apply a method known as DFT+Σ which tries to heuristically account for the quasiparticle energies based on a physically motivated model [115, 116, 117]. In this, the molecular orbitals attain a self-energy correction term of the following form

$$\hat{\Sigma} = \sum_n \Sigma_n |\Psi_n^{mol}\rangle\langle\Psi_n^{mol}|, \tag{2.108}$$

where n runs over the molecular orbitals. The self-energy correction Σ_n is calculated in the following manner. First, the highest occupied molecular orbital (HOMO) and lowest unoccupied molecular orbital (LUMO) obtained from DFT are connected with the ionization energy and electron affinity of the gas-phase molecule, derived from the total energy difference on a DFT-level. The resulting band gap is further reduced, due to polarizations in the electrode induced by adding an electron (LUMO) or hole (HOMO) to the system, which are calculated using classical image-charge potentials caused by the charge distribution of the respective molecular orbital in the presence of two metallic leads. Since the electronic transmission is supposed to be dominated by the HOMO and LUMO resonances, it is sufficient to calculate only Σ_{HOMO} (Σ_{LUMO}) and apply the shift to all occupied (unoccupied) orbitals. Details about the calculation of these terms can be found in Ref. [118]. As pointed out by Ref. [119], this method neglects the internal screening response of the molecular orbitals due to the polarization of the metal surface and depends only on a choice of the image-charge plane. In our calculations, this image plane is chosen to be 1.47 Å away from the first unrelaxed layer.

2.7 Photons

A last contribution to the thermal conductance arises due to the presence of a photonic flux, driven by thermal excitations. A theory which determines these contributions, namely κ_{pt}, is the fluctuational electrodynamics [120]. This formulation of photonic heat transport was indeed employed recently to study the radiative heat transfer between a gold surface and a gold tip in the extreme near-field regime and shown to work nicely all the way down to gaps of a few nanometers [38].

Our calculation of the radiative thermal conductance κ_{pt} proceeds in two steps. First, we calculate the so-called heat transfer coefficient, i.e. the linear radiative thermal conductance per unit area, for two infinite parallel Au plates, and then we use this result together with the so-called proximity approximation (see below) to compute κ_{pt} for two arbitrary geometries.

Within the framework of fluctuational electrodynamics [120] the heat transfer coefficient ζ for two infinite parallel plates separated by a distance Δ is given by [121]

$$\zeta(\Delta) = \int_0^\infty \frac{d\omega}{2\pi} \frac{\partial \Theta(\omega, T)}{\partial T} \int \frac{d^2 k_\parallel}{(2\pi)^2} \tau_{\mathrm{pt}}(\omega, \boldsymbol{k}_\parallel), \tag{2.109}$$

where $\Theta(\omega, T) = \hbar\omega n(E, T)$, ω is the radiation frequency, $\boldsymbol{k} = (k_\perp, \boldsymbol{k}_\parallel)$ is the wave vector expressed in terms of components perpendicular and parallel to the surface planes with $k_\perp = k_{\mathrm{x}}$ and $\boldsymbol{k}_\parallel = (k_{\mathrm{y}}, k_{\mathrm{z}})$, $\tau_{\mathrm{pt}}(\omega, \boldsymbol{k}_\parallel)$ is the total transmission probability of the electromagnetic waves, and we have omitted the temperature dependence of ζ. Notice that the second integral in Eq. (2.109) is carried out over all possible directions of $\boldsymbol{k}_\parallel$, and it includes the contribution of both propagating waves with $k_\parallel < \omega/c$ and evanescent waves with $k_\parallel > \omega/c$, where $k_\parallel = |\boldsymbol{k}_\parallel|$ and c is the velocity of light in vacuum. The total transmission can be written as $\tau_{\mathrm{pt}}(\omega, \boldsymbol{k}_\parallel) = \tau_{\mathrm{s}}(\omega, \boldsymbol{k}_\parallel) + \tau_{\mathrm{p}}(\omega, \boldsymbol{k}_\parallel)$, where the contributions of s- and p-polarized waves are given by [121]

$$\tau_\alpha(\omega, \boldsymbol{k}_\parallel) = \tag{2.110}$$
$$\begin{cases} (1 - |r_{\alpha,21}|^2)(1 - |r_{\alpha,23}|^2)/|D_\alpha|^2, & k_\parallel < \omega/c \\ 4\mathrm{Im}\{r_{\alpha,21}\}\mathrm{Im}\{r_{\alpha,23}\} e^{-2|k_{\perp,2}|\Delta}/|D_\alpha|^2, & k_\parallel > \omega/c \end{cases}.$$

Here, $\alpha = \mathrm{s}, \mathrm{p}$ and index 1 refers to the left plate, 2 to the vacuum gap, and 3 to the right plate. The coefficients $r_{\alpha,ij}$ are reflection (or Fresnel) coefficients of the two interfaces between gold and the vacuum gap and are given by

$$r_{\mathrm{s},ij} = \frac{k_{\perp,i} - k_{\perp,j}}{k_{\perp,i} + k_{\perp,j}} \quad \text{and} \quad r_{\mathrm{p},ij} = \frac{\epsilon_j k_{\perp,i} - \epsilon_i k_{\perp,j}}{\epsilon_j k_{\perp,i} + \epsilon_i k_{\perp,j}}, \tag{2.111}$$

where the component of the wave vector in system i perpendicular to the plates may also be expressed as $k_{\perp,i} = \sqrt{\epsilon_i \omega^2/c^2 - k_\parallel^2}$ and $\epsilon_i(\omega)$ is the corresponding dielectric function. Finally, $D_\alpha = 1 - r_{\alpha,21} r_{\alpha,23} e^{2ik_{\perp,2}\Delta}$ is a Fabry-Pérot-like denominator, resulting from multiple scattering events between the two interfaces.

To compute the heat transfer coefficient, we have employed the experimental dielectric function for Au reported in Ref. [122]. Our results basically coincide with those reported in Ref. [123], with minor differences due to the different Au dielectric function employed here. We also find for small gaps in the near-field regime that the contribution of s-polarized evanescent waves, resulting from total internal reflection, completely dominates the radiative heat transfer all the way down to separations of about 1 Å. Let us remark that in the formalism detailed above, we make use of a local approximation, in which the dielectric function is assumed to depend only on frequency. In fact, non-local contributions due to the momentum dependence of the dielectric function have been shown to be negligible for gaps larger than 1 Å [123], as the ones studied in this work.

We can use the results for the heat transfer coefficient ζ to estimate the radiative thermal conductance in a junction with Au electrodes. For this purpose, we need to know the macroscopic shape of the electrodes. In scanning tunneling microscope (STM)-based experiments, the electrodes are a tip and planar surface. Thus, and since we are interested in the extreme near-field regime (with gaps in the order of nanometers), it is reasonable to model this situation with a finite sphere of a given radius R and an infinite planar surface. We shall refer to this geometry as tip-surface geometry. On the other hand, in the case of mechanically controllable break junctions, it is more appropriate to model the electrodes as two spherical tips. For simplicity we assume two spheres of the same radius R. We shall refer to this geometry as tip-tip geometry.

In principle, one can carry out a very accurate analysis of the radiative heat transfer in these two types of geometries along the lines of Ref. [38], but for our purposes here it suffices to make use of the so-called proximity approximation, sometimes referred to as Derjaguin approximation [124]. It has been shown to provide a very good approximation for the two geometries considered

here in the limit in which the tip radius is much larger than the gap size [125, 126, 127, 38]. In particular, Kim *et al.* [38] showed that microscopic details like surface roughness (either at the tip or at the surface) do not significantly change the results for Au. Within the proximity approximation the radiative heat conductance between a sphere and a plane and between two spheres can be computed as

$$\kappa_{\mathrm{pt}}(\Delta) = \int_0^R \zeta(h(r)) 2\pi r \, dr, \tag{2.112}$$

where Δ is the gap, ζ is the heat transfer coefficient calculated as described above, R is the sphere radius, and $h(r) = \Delta + R - \sqrt{R^2 - r^2}$ for the tip-surface geometry and $h(r) = \Delta + 2R - 2\sqrt{R^2 - r^2}$ for the tip-tip geometry.

Finally, let us point out that we do not take the presence of molecules into account in the calculation of the photonic thermal conductance. In the single-molecule junctions considered in this work, the molecules only modify the refractive index of the gap in a very tiny region. Due to the long-wavelength nature of the electromagnetic waves that dominate the near-field radiative heat transfer (NFRHT), this region is orders of magnitude smaller than the portion of the electrodes that contribute to the radiative heat transfer [38]. Therefore, the role of the molecules in the photonic transport is expected to be negligible.

3 Metallic atomic-size contacts

The invention of experimental techniques like the scanning tunneling microscope and the mechanically controllable break junction made it possible to fabricate stable metallic atomic-size contacts all the way down to single-atom junctions and even atomic chains. A single-atom contact is the ultimate limit of miniaturization in the context of electronic devices. Since the mean free path of electrons and phonons is much longer then the characteristic dimension of such systems, transport is dominated by quantum mechanical effects. A lot of interesting properties related to charge and energy transport, like electrical conductance [128, 129], shot noise [130, 131, 132, 133], photocurrent [134, 135, 136, 137], thermopower [138, 139, 140, 141], and Joule heating [142, 118], just to mention a few, have already been theoretically investigated and experimentally measured in such junctions. Overall these systems have been an ideal test platform to probe scattering theory for coherent quantum transport.

Only recently, a basic property, the thermal conductance, which was unexplored in this kind of junction up to this point, has been obtained experimentally [143, 144]. Making use of picowatt resolution calorimetry our experimental colleagues have been able to measure quantum effects on the thermal conductance, in particular they could show that for some metals the thermal conductance is quantized in units of $\kappa_0 = \pi^2 k_B^2 T/(3h)$, where T is the absolute temperature. A schematic picture of the experimental setup can be seen in Fig. 13(a). A gold-coated SThM tip suspended on a platform at temperature T_0 is brought into contact with a planar surface at temperature T_s. While the junction forms, a temperature change can be monitored via the resistance of the platinum thermometer at the tip. This can be further linked to the thermal conductance of these single-atom contacts with a resistance network model. If simultaneously an ac-current is supplied to the junctions, both quantities, the thermal and electrical conductance can be measured at the same time. An example of a measured conductance vs. displacement curve can be seen in Fig. 13(b), obtained while withdrawing the tip from the surface at a constant velocity of approx. 0.5 nm/s. The units are normalized such that they correspond to the quantized values of $2\kappa_0$[1] ($T = 300$) and G_0 respectively. In these examples, both signals follow each other very closely and the conductance signals decrease in discrete steps. Many of the curves show preferential conductance values at integer multiples of $2\kappa_0$ or G_0. This measurement has been repeated to perform a statistical analysis over a larger dataset of about 2000 traces and the corresponding 2D histogram of the electrical and thermal conductance can be seen in Fig. 13(c). It has a prominent peak at the crossing point of $1G_0$-$2\kappa_0$ which reveals the first measurement of the quantization of the thermal conductance at room temperature for gold contacts. Further analysis with platinum has demonstrated that this is not a universal feature and the underlying chemical valence has to be considered in order to explain the results.

Another interesting question which has arisen in these studies concerns the proportionality of the ratio of thermal and electric conductance to the temperature, with the constant $L_0 = \pi^2 k_B^2/(3e^2) = 2.44 \times 10^{-8}$ WΩK^{-2}, which is well known as the Wiedemann-Franz law for macroscopic systems. As can be seen in Fig. 13(d) they have found the law to be approximately valid also for single-atom contacts. An additional measurement on a platinum contact suggests that this could be true for any metal contact with only small deviations and a statistical spreading related to the electronic structure of the metal. As they have already pointed out, these

[1] Note that spin degeneracy, unlike the electrical conductance quantum, is not included in the definition of the thermal conductance quantum because historically this expression was first defined in the context of phonon transport.

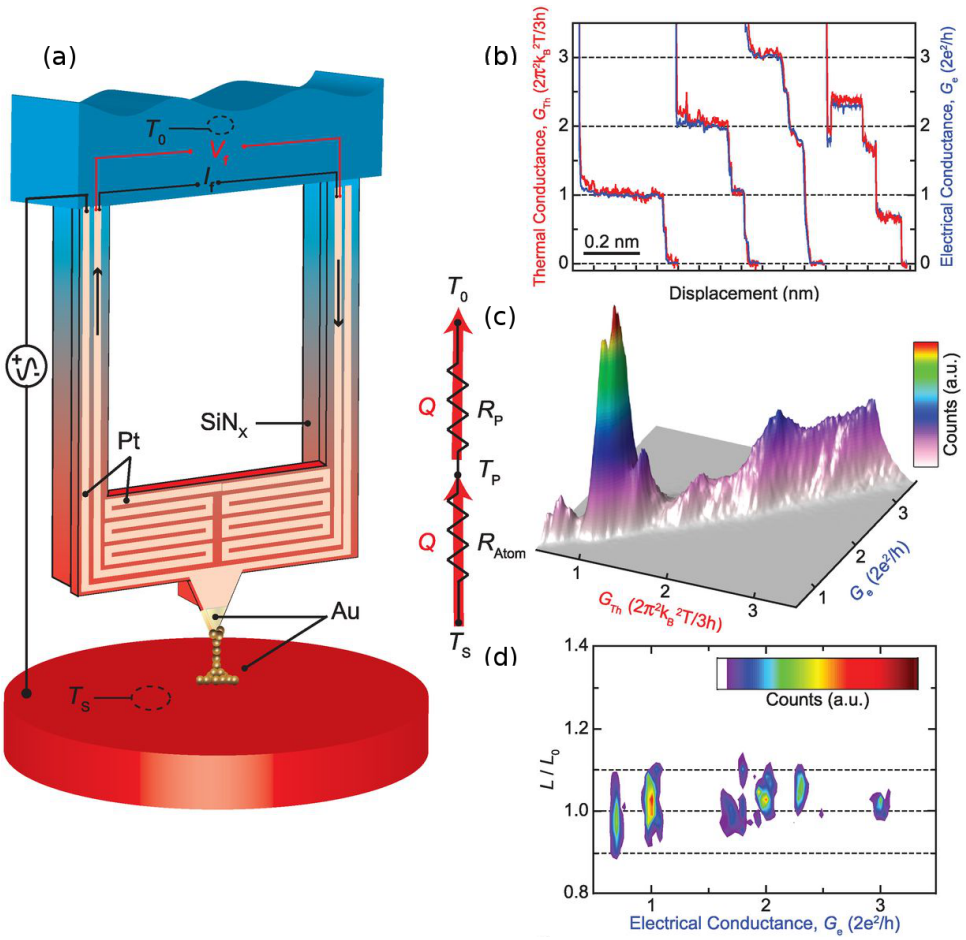

Figure 13. (a) Experimental setup to study the thermal conductance in single-atomic junctions. A gold-coated SThM tip initially at temperature T_0 is brought into contact with a planar substrate at temperature T_s, while an ac-current is supplied. When the contact forms, a temperature change in the platinum wire can be measured, which can be linked with a network model to the thermal conductance of these nano contacts. (b) Typical thermal (red) and electrical (blue) conductance signals, obtained while the tip is displaced with a constant velocity away from the surface. (c) Histogram of the thermal conductance versus the electrical conductance reveals the quantization of the thermal conductance at room temperature for single-atom gold contacts. (d) Histogram of the Lorentz ratio, which verifies the Wiedemann-Franz law down to the single-atom contact. All Pictures are taken from Ref. [2].

discoveries are generally only possible if in this transport regime the electronic contribution is still dominating the thermal properties as it is in bulk systems.

On this background we now want to explore the theoretical principles underlying these experiments and investigate metallic contacts of Au in Sec. 3.1 and Pt in Sec. 3.2. In addition, we consider Al in Sec. 3.3, which is interesting because of its lower mass compared to the former metals and hence the possible greater influence of phonons. In particular, we calculate the electronic and phononic contribution to the heat conduction using different techniques, to compare with the experimental results and estimate the expected influence of phonons. With the help of a combination of DFT and NEGF techniques we first explore an ideal geometry, represented by a dimer configuration, and look at the different contributions coming from electrons and phonons in a harmonic approximation. Additionally, we study stretching and pulling curves in close analogy to the measurements. Furthermore, we combine NEMD simulations with a tight-binding parametrization for the electronic system to justify the transport regime and discuss the influence of anharmonic effects on the phonon thermal conductance. At last, we show a statistical analysis, to allow for a direct comparison to the experiments. The DFT studies are carried out

for all metals, while the NEMD calculations exclude Pt since a similar behavior to Au can be expected.

Simple estimation in the phase-coherent transport regime

Before we present our detailed calculations using realistic electronic and phononic structure parameters, we want to estimate, in a simplified picture, under which circumstances the experimental observations can be understood in the context of phase-coherent transport. In particular, we want to highlight in which cases we expect the Wiedemann-Franz law to hold for the metalic contacts. As outlined in Sec. 2 the system dependent parameter, for the electronic as well as for the phononic response, is given by the corresponding transmission function and therefore this quantity uniquely determines the respective transport coefficient. With this in mind we first focus on the electronic system, neglecting any phononic influence, by looking at three generic electronic transmission functions as depicted in Fig. 14(a).

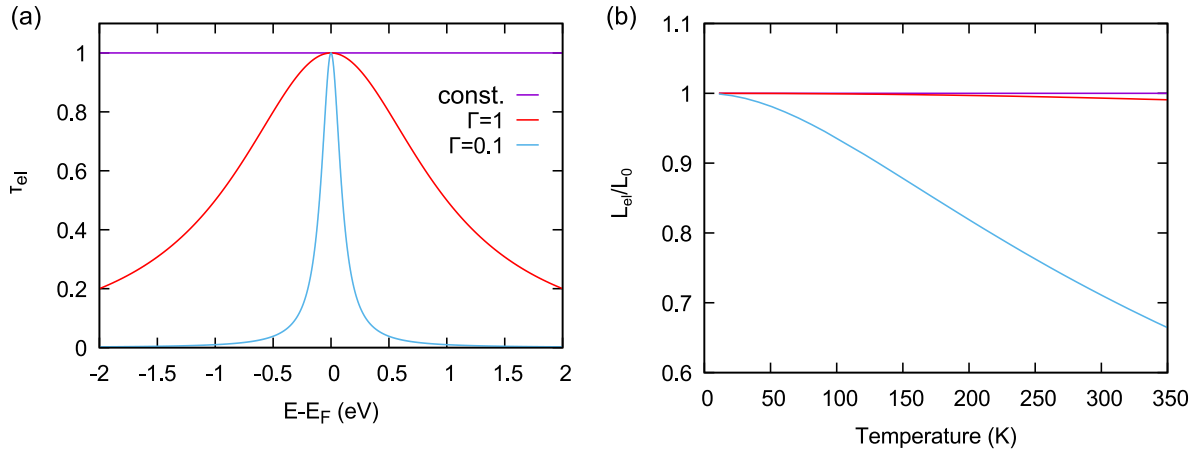

Figure 14. (a) Three electronic transmission functions which differ in their energy dependence. (b) Corresponding electronic Lorentz ratio as defined in Eq. 3.2.

The first one is constant in energy E while the others are choosen to have a Lorentzian shape given by

$$\tau_{el} = \frac{\Gamma^2}{\Gamma^2 + (E - E_F)^2} \tag{3.1}$$

with varying width Γ. Important for our considerations, they differ in their energy dependence. Since we are interested in the validity of the Wiedemann-Franz law we can define the so called electronic Lorentz ratio

$$\frac{L_{el}}{L_0} = \frac{\kappa_{el}}{L_0 T G} \tag{3.2}$$

which is a measure for deviations from the theoretical Lortenz constant L_0. In Fig. 14(b) this quantity can be seen for the respective transmission function for a temperature range from $0 - 350$ K. For the constant transmission it is equal to one irrespective of the temperatures, meaning the proportionality between thermal and electronic conductance divided by temperature is L_0 for the whole range. In contrast, we see small deviations from one for the transmission with a larger width which gets even more pronounced for $\Gamma = 0.1$. These results can be understood by inspecting Eq. 2.102. Without an energy dependence K_1 will vanish and κ_{el} will be given by the low temperature limit 2.106. In other words, a small or negligble energy dependece leads to the validity of the Wiedmann-Franz law for the eletronic ratio.

After we have discussed the neccesary conditions for the electrons, we now turn to the phonon thermal conductance at room temperature. To get an estimate for an upper bound, we assume that there are three phonon conduction channels. We choose the number of three, since one

expects one channel for each spatial dimension. They might also be seen as a longitudinal and two transverse eigenchannels. Let us furthermore assume that the channels exhibit a perfect transparency for energies up to the corresponding Debye energy E_D of the metal: 20 meV for Au, 25 meV for Pt, and 40 meV for Al. Thus, if we use $\tau_{ph}(E) = 3$ for $E \in [0, E_D]$, we obtain a room temperature phononic thermal conductance of 0.199 nW/K $= 0.7\kappa_0$ for Au, 0.244 nW/K $= 0.86\kappa_0$ for Pt, and 0.378 nW/K $= 1.33\kappa_0$ for Al. Notice that the largest value arises for Al, which is simply due to its higher Debye energy as compared to Au and Pt. These estimates need to be put into relation to the electronic contribution to the thermal conductance. If we assume for instance electronic values of $1G_0/2\kappa_0$, we see that the phononic and electronic contributions could in principle be of similar order, and it is by no means obvious that phonons can be ignored in the analysis of the heat conduction in metallic atomic contacts. The quantitative determination of the relative contributions of electrons and phonons to the thermal conductance will be a central issue of the rest of this chapter.

3.1 Gold

3.1.1 DFT-NEGF

The gold contact is known from the experiment as well as classical MD and DFT simulation to exhibit a plateau corresponding to a one-atom-thick geometry that is usually formed by an atomic dimer configuration before breaking of the contact [145]. For this reason, we study first an ideal dimer configuration as shown in Fig. 15(a) as a representative example of such single-atom contacts.

The crystallographic direction of the contact is assumed to be in (111) direction. If we look at the electronic transmission in Fig. 15(b), we see that at the Fermi energy transport is dominated by one single channel, which is fully open, meaning a transmission of ≈ 1. The number of channels is well known to be determined by the chemical valence of the metal which is of s-type for gold [129, 146, 147]. The corresponding transmission eigenchannel is visualized in Fig. 15(a). Although on the pyramid a contribution from the d-orbitals is visible, at the constriction, a σ-bond evolves. Additionally, we see that the transmission is nearly energy independent around the Fermi energy. In this particular case, we find that the electrical conductance is $1.01G_0$, while the corresponding result for the electric conductance at room temperature is $\kappa_{el} = 0.577\text{nW/K} \approx 2\kappa_0$. This value agrees very well with the expectation from the Wiedemann-Franz law, which can be explained by the flat transmission around the Fermi energy. If we next look at the phononic transmission in Fig. 15(c), we see that the transmission is nonzero only for values below the cut-off energy which is here $\approx 20\text{meV}$. Furthermore, we see that the transport is dominated approximately by a maximum of 3 transmission channels over the whole energy range, except for a short interval around 5 meV, corresponding to the three different polarizations. This can be illustrated for instance if we look at the three most transmissive phonon eigenchannels, at the lowest possible energy which exhibits a resonance at 1.5 meV, depicted in Fig. 15(b). There, one can see the transversal character of the two channels highest in transmission, which have perpendicular polarization to each other, depicted in the inset, while the third one exhibits longitudinal character. Note that due to a lower transmission, the decay of the phonon mode for the third channel is clearly visible, since the amplitude on the right is reduced compared to the left side. For completeness, we show in Fig. 15(d) the temperature dependence of the thermal conductance, including the electronic and the phononic contributions, as well as the total one. As one can see, the thermal conductance of this Au dimer contact is clearly dominated by electrons for most temperatures. On the other hand, the room temperature thermal conductance quantization, as observed in Ref. [143], is a consequence of the fact that, in addition, the Wiedemann-Franz law is fulfilled for the electronic contribution.

To further study the relative contributions of electrons and phonons to the thermal conductance

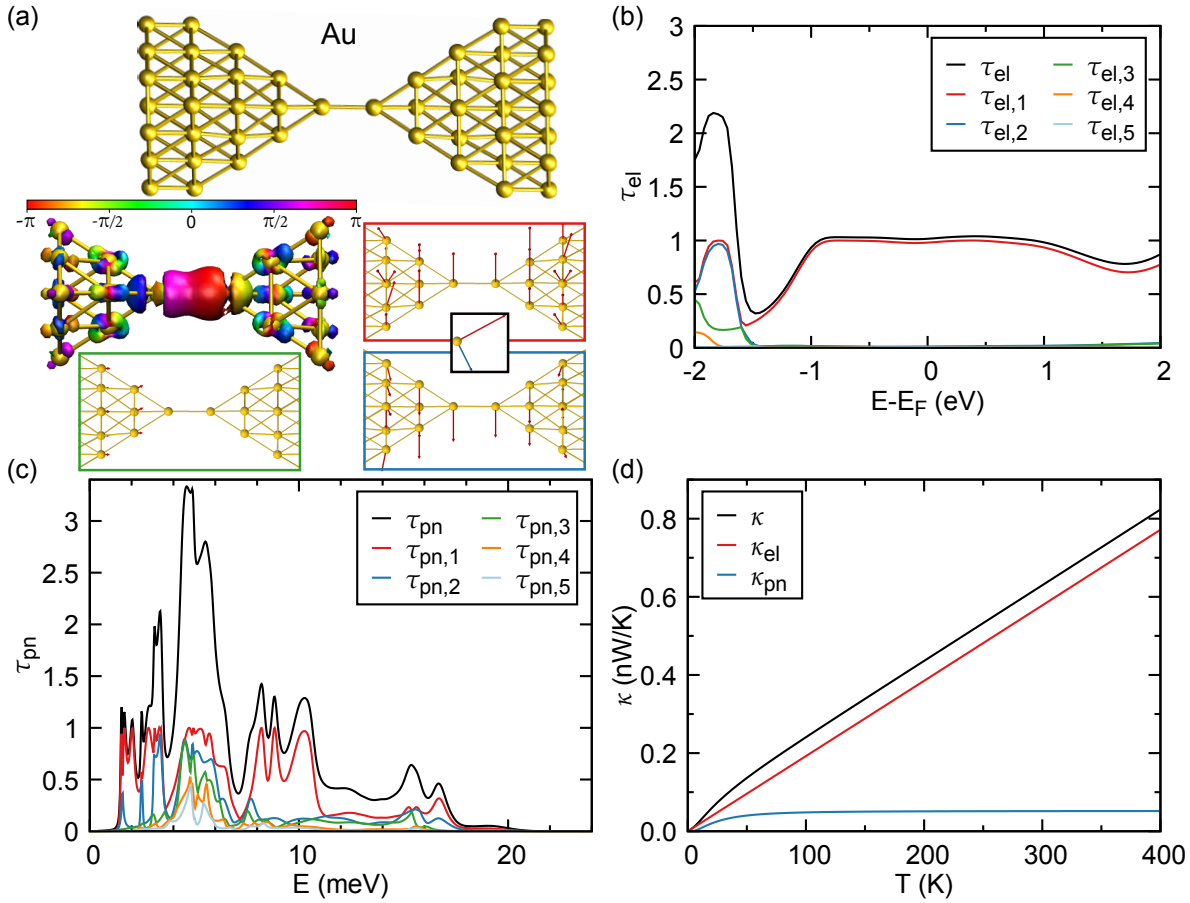

Figure 15. (a) Picture of the studied geometry with the highest electronic transmission eigenchannel at the Fermi energy where the color code represents the phase of the channel. In addition, the three highest phononic ones at an energy of 1.5 meV are shown. There the color corresponds to the respective color in the transmission plot. (b) Electronic transmission τ_{el} as a function of energy (measured with respect to the Fermi energy E_F). We display the total transmission as well as the five largest transmission coefficients, as indicated in the legend. (c) The corresponding phononic transmission as a function of energy. Similar to the electronic transmission we show both the total one and the largest five individual transmission coefficients. (d) Thermal conductance as a function of temperature for the Au single-atom contact with the total thermal conductance κ resolved into electronic and phononic contributions, κ_{el} and κ_{pn}, respectively. The arrows indicate the energy of the respective transmission eigenchannel in (a).

and to model the experiments more closely, we have used our DFT-based approach to simulate the contact formation and to compute the corresponding conductance traces. This is done by separating or by approaching the electrodes in a step-like manner and by subsequent re-optimization of the junction geometry. As displacement step, we use 0.26 Å and compute G, κ_{el}, κ_{pn} and κ with our DFT-based transport method for the obtained equilibrium geometries.

In Fig. 16(a) we show the results of such a simulation for the Au contact of Fig. 15 that is grown along the (111)-direction of the fcc lattice. We started with the dimer contact represented by the second geometry in that panel, counting from the right. This geometry was compressed to obtain thicker cross-sections as well as stretched to simulate the breaking of the contact. In Fig. 16(a) we show the results for G and κ at room temperature for the series of contacts, obtained following our protocol. The electrical conductance in this plot is normalized by the electrical conductance quantum, G_0, while the thermal conductance is normalized by $2\kappa_0$ with $T = 300$ K. As one can see, both conductances proceed in a step-like manner in a succession of plateaus and abrupt jumps, related to elastic stages, where bonds are stretched and forces build up, and plastic stages, where bonds break and the accumulated tension is released. This

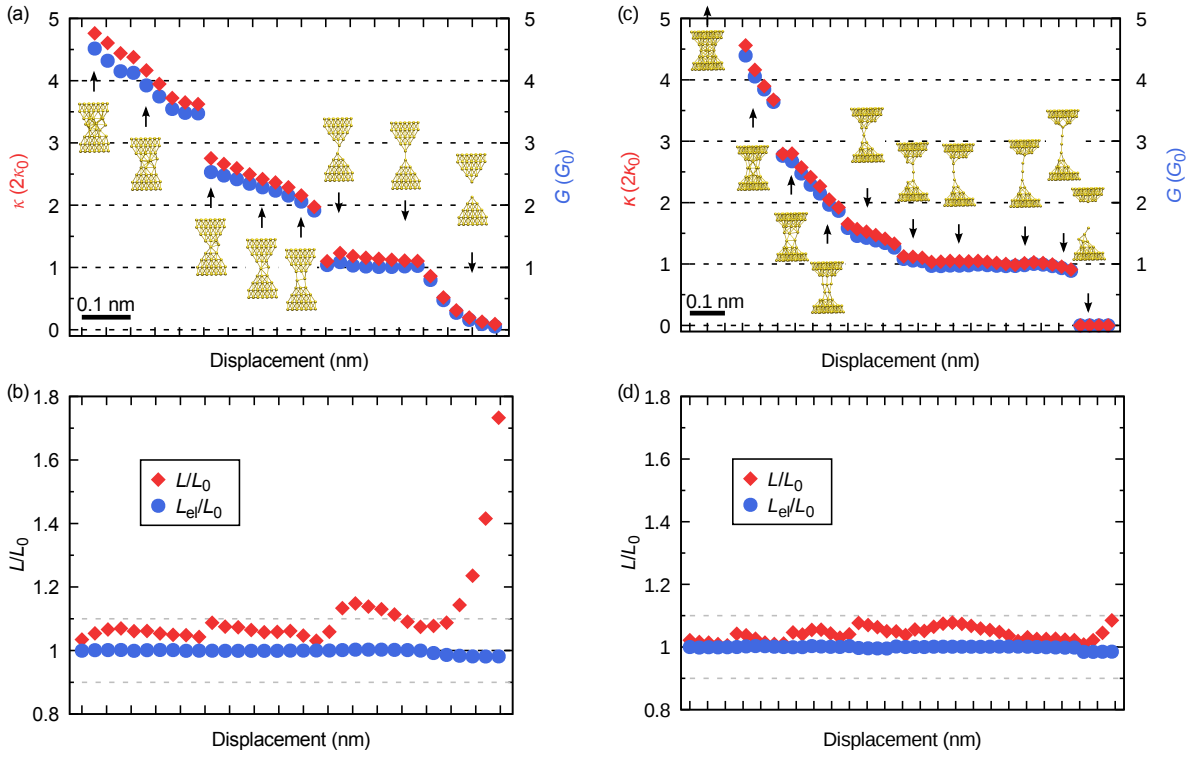

Figure 16. (a) Electrical and thermal conductance at room temperature as a function of electrode displacement for an Au contact, oriented along the fcc (111) crystallographic direction. The blue dots correspond to the results for the electrical conductance (right vertical scale), which is normalized by the electrical conductance quantum G_0. The red diamonds correspond to the total thermal conductance (left vertical scale), taking into account both the electronic and phononic contributions, and it is normalized by twice the thermal conductance quantum κ_0. The different geometries, shown in this panel, correspond to snapshots taken during the elongation and compression processes. (b) The corresponding Lorentz ratios, defined via Eq. (3.3). The red diamonds show the full ratio computed with the total thermal conductance, while the blue dots show the electronic Lorentz ratio, if the thermal conductance consists only of the electronic contribution. Panels (c) and (d) show the corresponding plots for an Au contact grown along the fcc (100) crystallographic direction. The contact was elongated, starting with the geometry shown in the upper left part of panel (c).

behavior resembles the experiments [143]. In addition, both conductances follow each other very closely. With the normalization used here, this means that the Wiedemann-Franz law is well obeyed. Notice also that both G and κ feature a plateau at $1G_0$ and $2\kappa_0$, respectively, which illustrates the tendency of Au single-atom contacts to exhibit quantized electronic and thermal transport, even at room temperature [143].

To quantitatively assess the validity of the Wiedemann-Franz law, it is customary to define the so-called Lorentz ratio as follows

$$\frac{L}{L_0} = \frac{\kappa}{L_0 T G}. \tag{3.3}$$

Here, $\kappa = \kappa_{\rm el} + \kappa_{\rm pn}$ is the total thermal conductance due to both electrons and phonons, L_0 is the Lorentz number, and G is the electrical conductance. A Lorentz ratio equal to 1 means that the measured thermal conductance agrees exactly with the expectations from the Wiedemann-Franz law, while deviations from 1 signal that this relation is violated. Such violations could be due to the contribution of phonons or they can have an electronic origin. In Fig. 16(b) we show the Lorentz ratio (red diamonds), using the results of panel (a). As one can see, there are small deviations from 1 on the order of 5-10% in the contact regime, depending on the exact junction geometry. These observations are in good agreement with the measurement of Ref. [143].

In order to better understand the origin of these deviations, we also show in Fig. 16(b) (blue dots) the electronic Lorentz ratio $L_{\mathrm{el}}/L_0 = \kappa_{\mathrm{el}}/(L_0 T G)$, constructed by replacing κ with κ_{el} in Eq. (3.3). As one can see, this electronic Lorentz ratio is very close to 1, irrespectively of the electrode displacement. This means that the deviations from the Wiedemann-Franz law are mainly due to phonons. It is also worthwhile to consider in detail the behavior of L/L_0 with the electrode displacement in Fig. 16(b). Deviations from the Wiedemann-Franz law tend to increase with larger displacements, i.e. towards smaller minimal contact cross sections. Furthermore, L/L_0 exhibits a sawtooth-like shape, typically decreasing within each elastic stage. Taking into account that $L_{\mathrm{el}}/L_0 \approx 1$ implies $L/L_0 \approx \kappa/\kappa_{\mathrm{el}} = 1 + \kappa_{\mathrm{pn}}/\kappa_{\mathrm{el}}$, this means that the relative weight of κ_{pn} in κ tends to reduce with increasing stress in the Au single-atom contacts. We attribute this to overall decreasing force constants with pulling or, in other words, a softening of interatomic bonds. Revivals of L/L_0 are seen at the points, where bonds break and the atomic contact reconfigures.

It is worth stressing that we have checked that the conclusions above are not an artifact of the protocol used to simulate the contact formation or the choice of the crystallographic direction of the contact geometries. On the right side of Fig. 16 we show an example of such tests, where we have simulated the contact formation of another Au atomic wire. In this case, the contact is grown along the fcc (100)-direction, and we started the simulation with the geometry shown in the upper left part of Fig. 16(c). As before, we then stretched the contact progressively in steps of 0.26 Å. We find that all the basic observations made above about the Au contacts are reproduced here. Notably, this Au wire forms a chain with up to four atoms in length in the last stages before breaking. During the formation of this atomic chain, G and κ remain approximately quantized with values of $1G_0$ and $2\kappa_0$, respectively. The formation of such Au atomic chains has been reported in numerous experiments [148, 149, 150, 151], and their electronic transport properties have been amply discussed in the literature [152, 54]. As for the Au contact before, the plots of the Lorentz ratio show that the relative contribution of phonons to the total thermal conductance tends to decrease with increasing tension in the contact.

3.1.2 NEMD

The former approach based on a combination of DFT and NEGF techniques allows for a nearly parameter-free approach, which captures all the details of a specific geometry and incorporates all the quantum mechanical effects, although relying on the harmonic approximation. Ideally, to get a better comparison with experiments, one would like to generate a set of independent geometrical realizations on this level of theory to analyze statistics over a large set of reasonable configurations. However, these simulations are very time-consuming, and a study of conductance histograms with DFT-based methods is presently not feasible. It is therefore customary to use alternative methods based on for instance classical molecular dynamics, to create such large sets of geometries. Those studies rely on a choice of the interaction potential and are therefore not a priori parameter free. Nevertheless, it has been demonstrated in a lot of theoretical studies that this kind of approach, combined with appropriate interaction potentials and a tight-binding parametrization for the electrons, reproduces the experimental findings regarding the electronic properties well [143, 153, 140, 145]. To look at the phononic contribution in such systems non-equilibrium molecular dynamics can be used as has been done for instance in Ref. [154, 155] on molecular junctions, using a reversed non-equilibrium method. A major advantage over the previous study is the inclusion of the full anharmonicity of the potential into the simulation, thus allowing for phonon-phonon interaction up to arbitrary order and direct access to differences related to the harmonic approximation.

We start this section with the first obvious difference due to temperature effects not captured in the former approach, the expansion of the lattice at finite temperature, leading to an equilibrium lattice constant as a function of the temperature. Since this crucially depends on the used

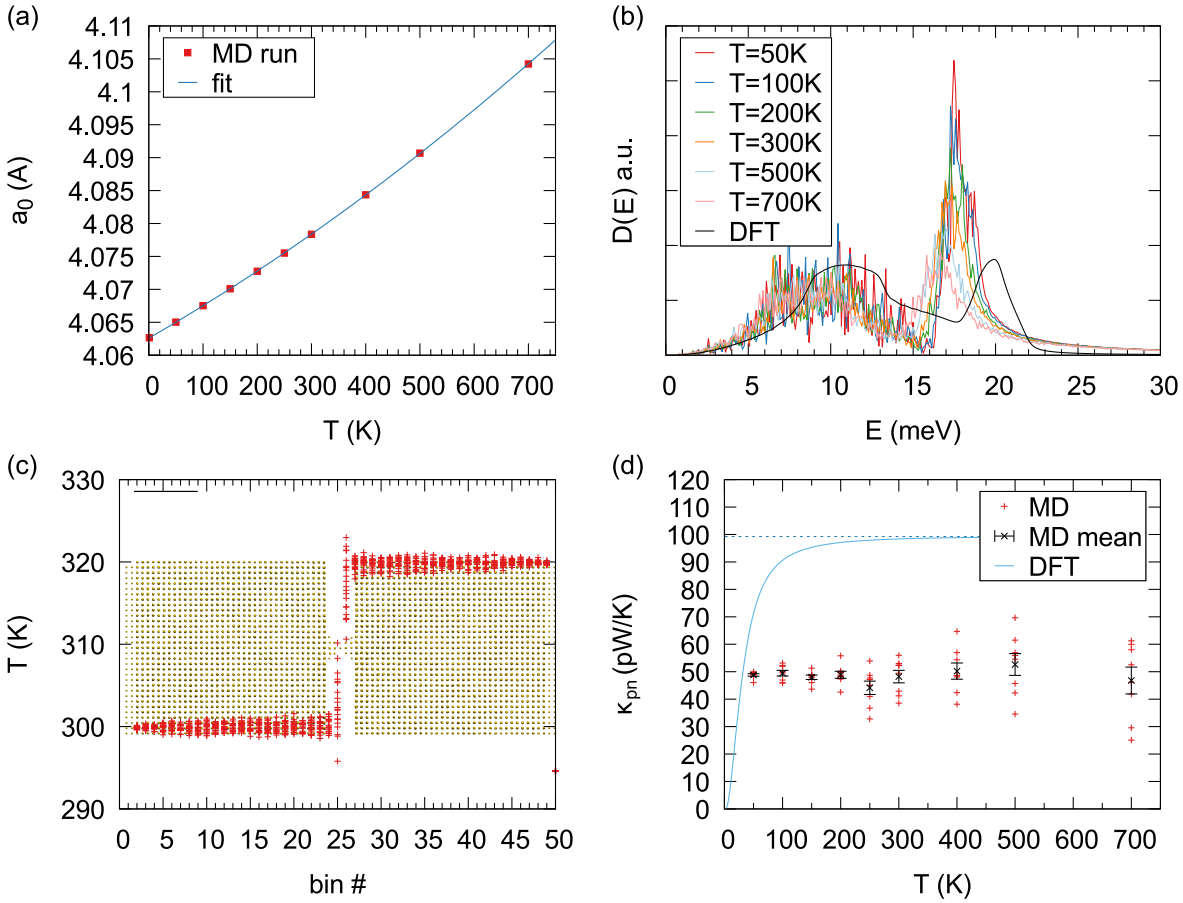

Figure 17. In panel (a) we show the temperature dependence of the bulk equilibrium lattice constant, exhibiting thermal expansion with increasing temperature. The fit is done with a polynomial of second order. In (b) we display the evolution of the phonon DOS at various temperatures. Additionally, the phonon DOS used for the DFT part is plotted. Panel (c) shows a temperature profile of a geometry as depicted in the inset and (d) depicts the temperature dependency of this geometry at various temperatures. In addition, we show results for the same initial geometry using DFT-NEGF method. The dashed line indicates the classical limit.

interacting potential, these parameters have to be calculated in a separate reference calculation. For this, we run MD calculations in the NPT ensemble, with a timestep of 1 fs at constant temperate and zero pressure using a Nose-Hoover thermostat for 10 ns with damping constants of 100 (500) timesteps for temperature (pressure) and drag of 1.2. The final volume will be extracted at the last 2 ns. Using the EAM potential of Ref. [156] we get the following temperature dependence for the equilibrium lattice constant of gold

$$a_{\mathrm{Au}}(T) = 4.06262 + 4.70275 \times 10^{-5} T + 1.81318 \times 10^{-8} T^2, \tag{3.4}$$

which is plotted in Fig. 17(a). As a consequence of this expansion, the phonon density of states from the bulk material also gets a function of temperature. In Fig. 17(b) we show this temperature dependence for various temperatures in the range of 50 K -700 K. First of all, notice that the cut-off energy is in all cases roughly below 20 meV. The most obvious influence of temperature is the reduced peak at energies around 15-20 meV, accompanied by a softening of the phonon modes, meaning a shift of the modes to lower energies. In analogy to the DFT studies, this means that the highest possible frequency shifts to lower energies, giving a first hint regarding the influence of anharmonicity on the thermal conductance, although being very low. We want to emphasize that common approaches to treat anharmonic effects based on a perturbative treatment using NEGF-techniques, like Ref. [157, 48, 49, 105, 158, 159] neglect such effects, since the anharmonic interaction in this cases is restricted to the central part, whereas the

bulk modes are used unperturbed. In consideration to compare both approaches, we also show in Fig.17(b) the phonon DOS for the DFT calculations. In spite of that the overall shape looks quite similar, we see a shift to higher energies, which is larger than the shift due to temperature effects. This has to be kept in mind when we, later on, show a direct comparison of both approaches.

Having established the differences with respect to the bulk parameters, we now want to use NEMD to calculate the thermal conductance in a single-atom junction. For this, we use a direct NEMD approach, where we control the temperature of two reservoirs using a velocity-rescaling thermostat in an NVT-ensemble. Time integration is done using the Velocity-Verlet algorithm, as before we use a timestep of 1 fs and the initial velocity distribution is chosen randomly to fulfill a Maxwell-Boltzmann distribution at the applied temperature. The measurement protocol is as follows. First, we equilibrate the junction at the respective temperature for 1 ns, then we establish the temperature difference of 20 K for an additional ns to run the simulation at the applied temperature gradient for further 10 ns. The thermal conductance can then be calculated, by fitting the amount of energy added/subtracted in the reservoir over time with an assumed linear dependency. To make sure that our system reaches a steady-state condition, we start the fitting procedure after 4 ns. The output from the thermostats is written every ps.

A sketch of the junction geometry can be seen in the inset of Fig. 17(c). The transport direction is assumed to be along the fcc (100) plane. In this setup, in both leads, the two outermost atom rows are kept fixed to avoid a collapse of the junction, followed by four rows on which the thermostat is applied and additional 32 rows mimicking the phonon bath. Perpendicular to the transport axis additional 32 atom rows are used in each direction. The size of the bath has been chosen such that they minimize finite size effects on the bulk phonon DOS. The central part consists of two (100) pyramids facing each other in one atom. In total, the simulation includes 38939 atoms. Initially, we start with an ideal geometry based on the lattice constant of roughly $a_{\mathsf{Au}}(T + \Delta T/2)$.

In Fig. 17(c) we see as an example a temperature profile of a considered junction at 300 K calculated as the average kinetic energy with an arbitrary binning of N=50 along the transport direction. Interestingly, and in accordance with interpretations of transport measurements in the harmonic regime, the temperature drop occurs at the narrowest constriction, whereas the two heat baths are at their respective constant temperature. Let us point out that, in contrast to the former one, a finite temperature gradient exists. Fig. 17(d) finally shows the thermal conductance calculated within NEMD formalism at temperatures ranging from 50-700 K, each sampled by 8 independent runs. Considering the use of classical statistics, when using MD simulations, one would expect, in a harmonic limit, the thermal conductance to be constant over temperature. And indeed we find the mean value of thermal conductance, except for T=700 K to be roughly the same. However, as an effect of temperature the variance increases. This can be understood in terms of the increased phase space of geometrical configurations due to higher temperatures. As a consequence, and opposite to the DFT approach, thermal conductance calculations are an average over multiple configurations within the measurement time, consistent with the boundary condition. Let us stress that at higher temperatures than 700 K the initial geometry was not stable, and at 700 K some runs revealed a minimum cross-section of 2 atoms within the smallest part during measurement time. For completeness, we compare the thermal conductance to results from DFT with the same initial geometry, where for DFT the experimental lattice constant of 4.08 Å has been used.

As mentioned earlier, the difference in the limit $T \to 0$ comes from the use of classical statistics in the case of MD, whereas DFT uses the right quantum statistics. However, for a better comparison, we show also the classical limit of the DFT results using a dashed curve, which is, due to the harmonic approximation, independent of temperature. In this limit the thermal conductance from DFT $\kappa_{\mathsf{pn}}^{\mathsf{DFT}} = 100\mathsf{pW/K}$ is almost twice the thermal conductance obtained from NEMD calculations. Different reasons can explain this discrepancy. First, the MD potential, optimized for bulk properties, could fail in the description of these single-atom contacts. Secondly, the slightly higher cut-off frequency used in the DFT calculations could partially lead to this

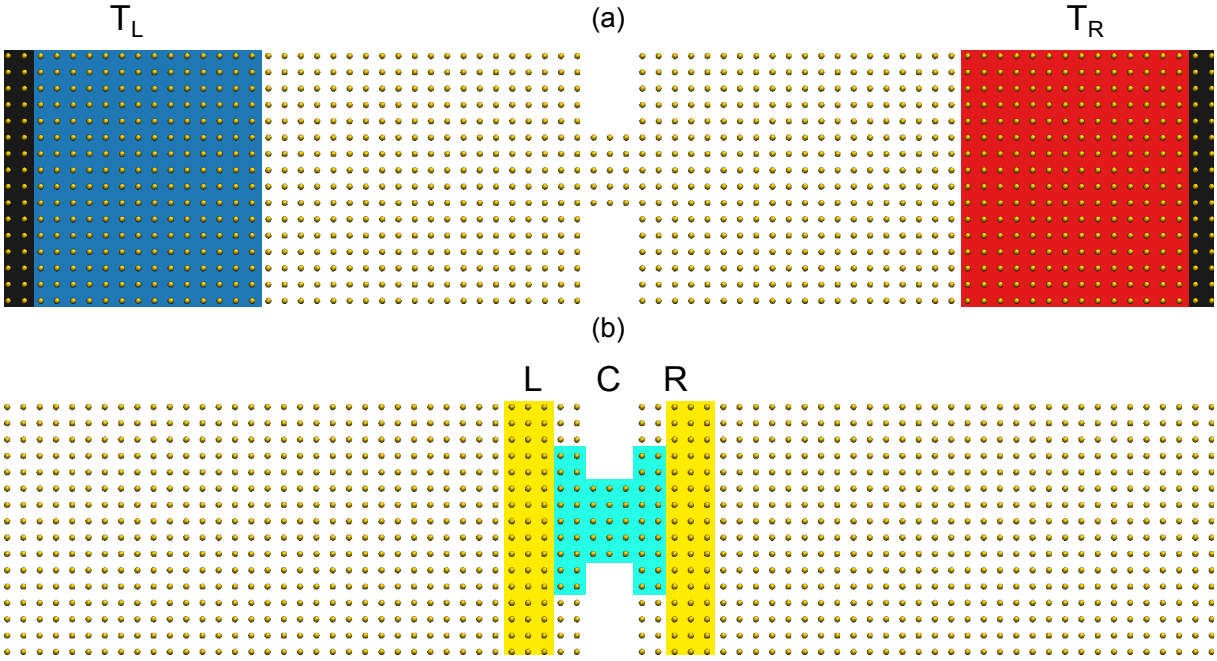

Figure 18. (a) Initial geometry used for the statistical analysis. The black rows are fixed during the measurement, whereas on the red (blue) area a thermostat is applied at T_L (T_R). (b) Partitioning of the system to calculate the electronic transport.

higher value and as a last point, different stress conditions, due to unequal boundary conditions used in NEMD and DFT, could be the origin of this discrepancy. Whereas in the NEMD approach the lattice constant of the unstrained bulk is used, in DFT we use the experimental lattice constant of 4.08 Å which is smaller than the bulk equilibrium lattice constant of ≈ 4.2 Å for a reference calculation with the same parameter set (see App. C).

Now we are in the position to perform a statistical analysis over different geometrical configurations in analogy to what has been done for purely electronic transport, for instance in [6], however, with a slightly different simulation protocol to be compatible with measurements on phonon thermal conductance. We start with an initial geometry shown in Fig. 18(a) and equilibrate the system as before for 1 ns at the initial temperature of 300 K, followed by an increased temperature of 20 K for the left reservoir over an additional nanosecond. After this, we stretch the junction by $\approx 0.26\mathring{A}$ over 1 ns to let the configuration run for further 3 ns. These stretching steps are repeated for a maximum of 35 times. The phononic thermal conductance is obtained for every stretching step with a fit over the last 2 ns.

For the electronic contribution, we take the geometries obtained from the MD simulations and compute their transport properties within the Landauer-Büttiker formalism. In this case, the electronic transmission that determines both the electrical conductance and the electronic contribution to the thermal conductance is computed with the help of a tight-binding model. To be precise, we employ a non-orthogonal Slater-Koster tight-binding parameterization, which has been constructed by fitting DFT-based results for the electronic band structure and total energies of metals across the periodic table, see Refs. [160, 161] for details. In this parameterization, we take into account the relevant valence orbitals, which include for Au the $5d$, $6s$ and $6p$ orbitals. Moreover, the hopping and overlap matrix elements in this tight-binding model are functions of the distance between the atoms, which enables us to use it with our MD simulations.

To compute the electronic transmission, we combine this model with NEGF techniques and the formulas detailed in section 2.6, very much like in the DFT-based calculations. Details can be found in Refs. [145, 153]. Briefly, as in the MD simulations, the system is divided into three regions for the transport calculations, i.e., the two electrodes and the central wire, see Fig. 18(b). Because the local environment of the atoms in the central part is very different from

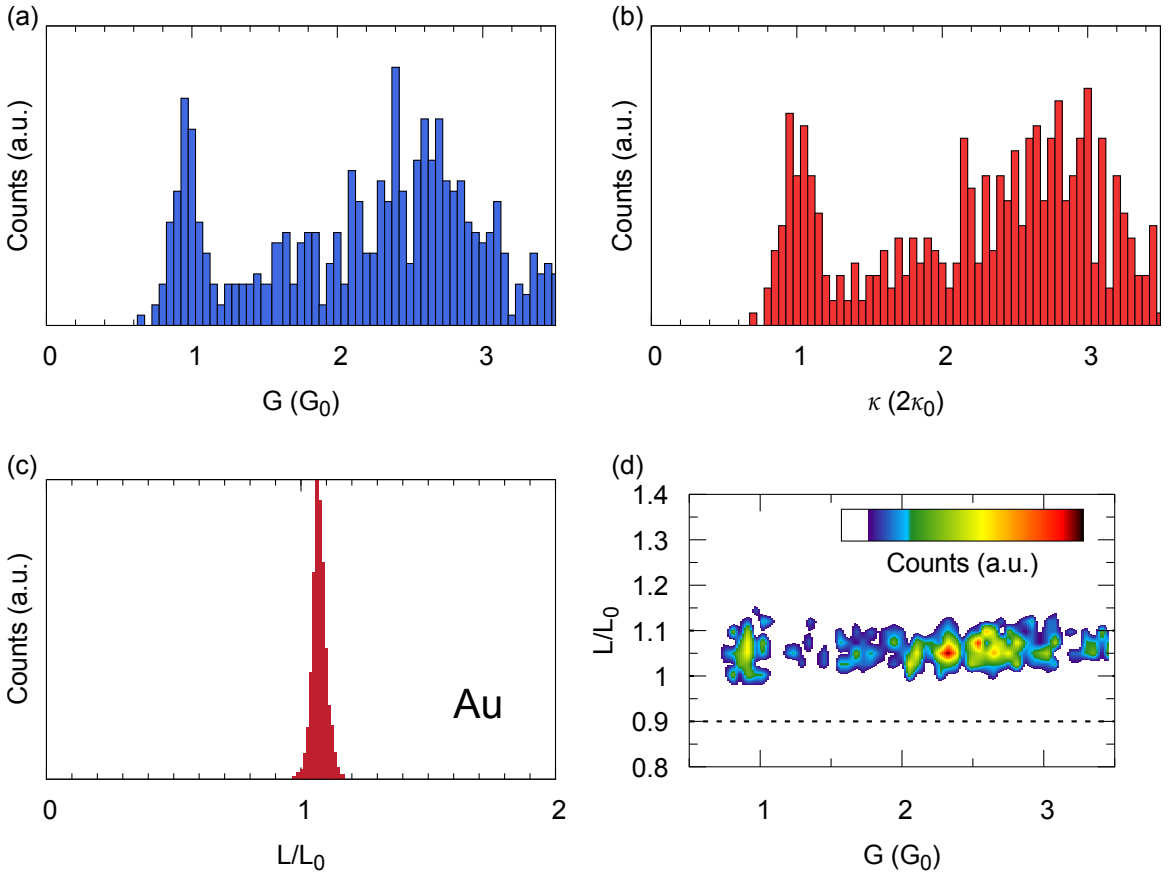

Figure 19. (a) Electric conductance histogram for the Au contact, revealing the quantization of the electric conductance. (b) Corresponding histogram for the total thermal conductance including both contributions from electrons and phonons. (c) Histogram for the ratio of L/L_0 for the contacts up to a conductance value of $3.5G_0$. The peak position is at 1.07%. (d) Two-dimensional heat map of the correlation between deviations from the Wiedemann-Franz law and the electric conductance.

that in the bulk-crystal, we impose a charge neutrality condition for all the atoms of the central wire [145, 153], which is known to be approximately fulfilled in metallic systems. As in the DFT case, the electrodes are considered to be semi-infinite perfect crystals, and their surface Green's functions are computed with the help of a decimation technique [64, 73].

Since the phononic measurement is an average over a timespan of 2 ns, we also calculate the electronic contribution as the mean value of the conductance for 8 geometrical configurations within these 2 ns with a difference in time of 250 ps. This kind of quasi-static measurement is justified by the experimental timescales for electronic conductance measurements of roughly $1\mu s$ and stretching velocities of 0.05 nm/s [2], which is by far longer than the total measurement time considered in our calculations. Fig. 19(a) shows the histogram of the electric conductance over 60 independent runs, whereas in Fig. 19(b) the corresponding total thermal conductance, including both contributions from electrons and phonons, is depicted. Both histograms reveal a prominent peak around $1G_0/2\kappa_0$, which explains the experimental observation of the thermal conductance quantum [143]. As already discussed in the DFT part, this peak can be traced back to a single-atom contact, which is dominated by one fully open channel. At last, we show in Fig. 19(c) a histogram of the ratio L/L_0 for all geometrical configurations, which is a measure of the deviation from the Wiedemann-Franz law, whereas in Fig. 19(d) a histogram of this ratio over the electronic conductance of the particular geometry is shown. Overall, and in accordance to the experimental findings, the influence of the phonons on the thermal conductance is less than 10%

and the mean influence is approximately 6-7%, which confirms the validity of the Wiedemann-Franz law down the single-atom contact regime for gold. Let us stress out the excellent agreement between the DFT and the NEMD results which reveals elastical events to be the dominant source of scattering mechanism in these systems.

3.2 Platinum

3.2.1 DFT-NEGF

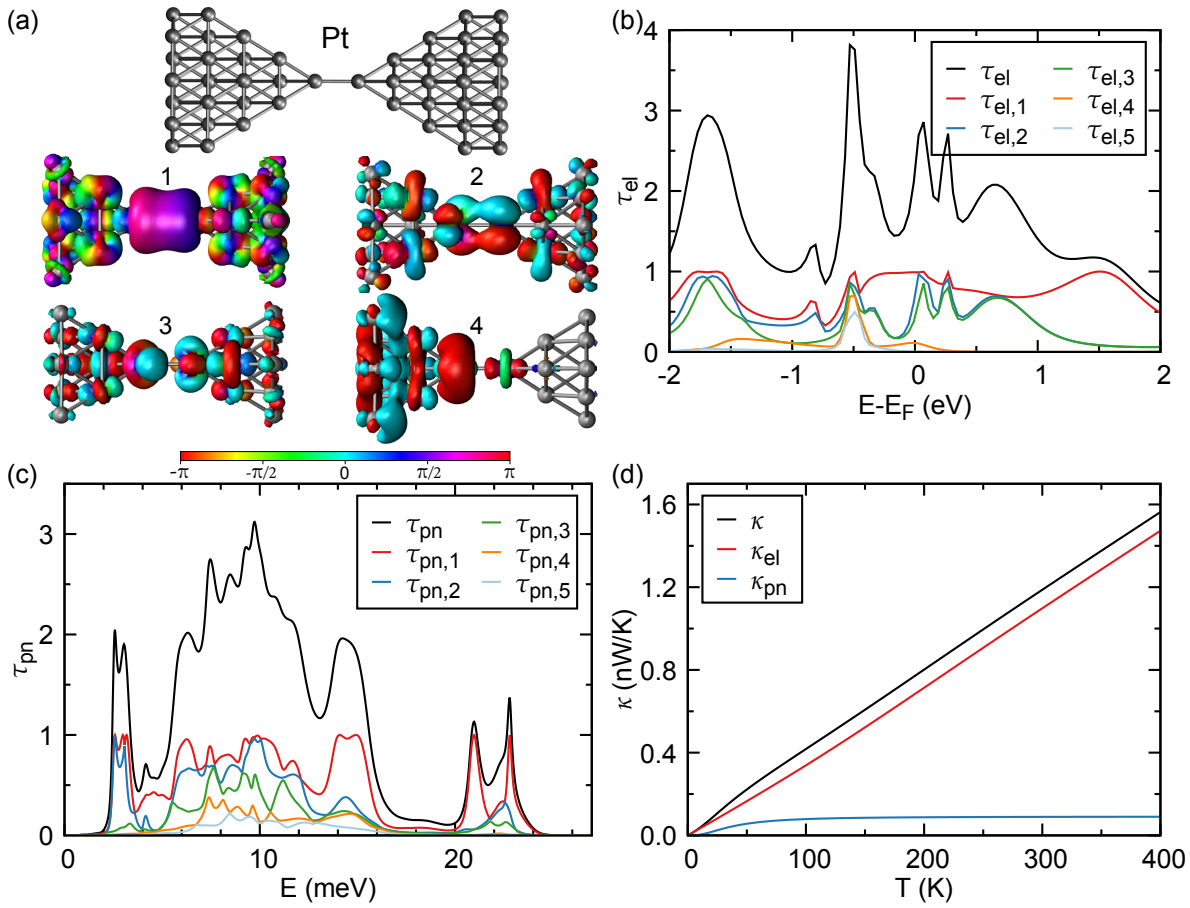

Figure 20. The same as in Fig. 15 for a platinum contact, representing a dimer configuration. (a) The four highest electronic transmission eigenfunctions are visualized.

As a next example, we will now discuss the second material studied in Ref. [143], which is platinum. Contrary to Au, no quantization of the electronic thermal conductance was found, although the Wiedemann-Franz law was still fulfilled with a mean deviation of roughly 3 % stemming from phonons. To proof this, we start our discussion again with a Pt single-atom contact as shown in Fig. 20(a). The corresponding total electronic transmission function is displayed in Fig. 20(b) along with the five most relevant transmission coefficients. There are four conduction channels that provide a sizable contribution to the transport at the Fermi energy, which is in strong contrast with the Au case. This is due to the fact that apart from the *s*-valence orbitals, the *d*-valence orbitals of Pt atoms also contribute to the electronic transport [162, 153, 140], which can be seen, for instance by looking a the 4 most transmissive transmission eigenfunctions in Fig. 20(a). Moreover these orbitals yield conduction channels that are partially open, which naturally explains the lack of electrical conductance quantization in this metal [163, 148, 140]. The transmission function results in electrical conductance of $1.83G_0$, while

the corresponding electronic contribution to the thermal conductance at room temperature is 1.098 nW/K = $3.87\kappa_0$. This is close to the value of 1.041 nW/K = $3.67\kappa_0$ suggested by the Wiedemann-Franz law. The larger deviation from this law, as compared to Au, arises from the more pronounced energy dependence of the electronic transmission function of Pt around the Fermi energy, caused by the d bands [153, 164, 140].

In contrast to the electronic transport, the shape of the phonon transmission of this Pt contact is similar to that of the Au contact, as visible from Fig. 20(c). This originates from the similar masses of Au and Pt atoms, leading to comparable Debye energies. As in the case of Au, three to four conduction channels dominate the phonon transport in the Pt dimer contact, leading to a phonon thermal conductance of 0.098 nW/K = $0.35\kappa_0$. This value almost doubles κ_{pn} of the Au contact, but is comparable in relative terms: It also constitutes about 8% of the total thermal conductance κ .

Fig. 20(d) shows that, very much like in the case of Au, the thermal conductance is largely dominated by the electrons at all relevant temperatures. The lack of electrical conductance quantization results in the absence of thermal conductance quantization for single-atom contacts of Pt, as was confirmed experimentally in Ref. [143]. We omit the analysis based on NEMD for this type of metal since we expect the phononic behavior to be very similar to the case of gold due to the comparable atomic mass. Note that the electronic properties have already been studied in [1].

3.3 Aluminum

3.3.1 DFT-NEGF

Let us now address the Al single-atom contact displayed in Fig. 21(a). We remark that the thermal transport in Al contacts has not been investigated experimentally so far. Aluminum is a reactive metal that is not easy to handle at room temperature, but the electronic transport through Al atomic contacts has been thoroughly explored at low temperatures. It is a very good example of light metal with a Debye energy that is significantly larger than those of Au and Pt. The total electronic transmission around the Fermi energy stems from two to three partially open channels, as one can see in Fig. 21(b) and has been reported both theoretically and experimentally in numerous occasions [165, 129, 166, 167, 168, 169]. These observations can be understood by the contribution of both s and p valence orbitals of Al atoms [129, 166], as can be seen in the transmission eigenchannels in Fig. 21(a). The electrical conductance in this example is $0.49G_0$, while the room temperature electronic thermal conductance is 0.277 nW/K = $0.98\kappa_0$, in very good agreement with the value of 0.271 nW/K = $0.95\kappa_0$ from the Wiedemann-Franz law. As it is visible at the phonon transmission function, displayed in Fig. 21(c), the phonon transport is also dominated by three to four conduction channels, like in the Au and Pt cases, but now phonon modes up to 40 meV participate. These additional phonon modes give rise to a phonon thermal conductance of 0.130 nW/K = $0.46\kappa_0$. This value is clearly larger than those of Au and Pt. Together with the lower electrical conductance, κ_{pn} yields now about to 32% of κ. Figure 21(d) shows the corresponding temperature dependence of the thermal conductance for the Al dimer contact. Notice that contrary to the cases of Au and Pt the phonon contribution is now of the same size as the electronic one in a broad range of temperatures up to $T = 100$ K and at room temperature it still constitutes a very significant contribution. These results suggest that a clear violation of the Wiedemann-Franz law should be observable in Al single-atom contacts, a prediction that yet awaits experimental verification.

In Fig. 22(a) we show the results of the simulation for an Al atomic wire that was performed following exactly the same protocol as in the Au simulation of Fig. 16, where we use the Al dimer contact of Fig. 21 as starting geometry. As in the Au case, the electrical and thermal conductances proceed in a step-like manner with the peculiarity that most plateaus exhibit a positive slope at

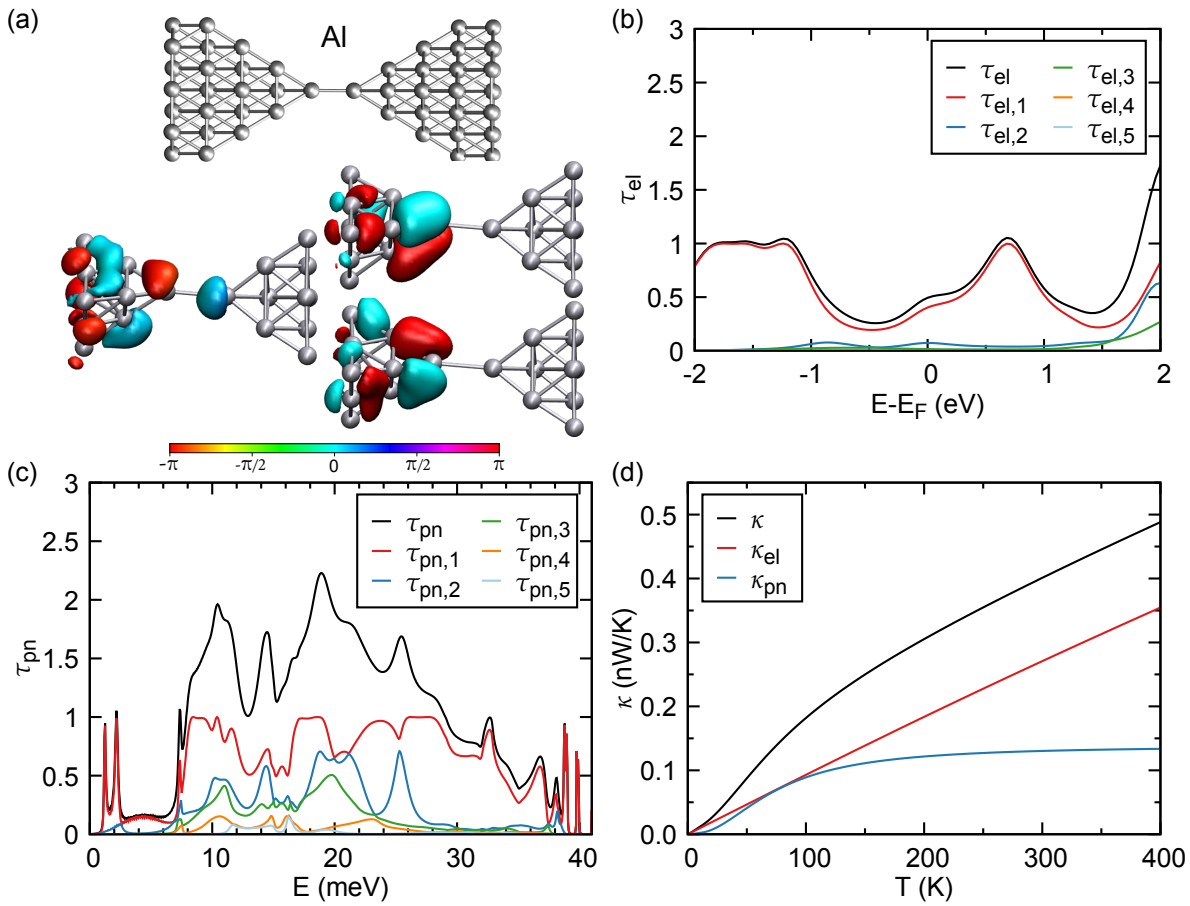

Figure 21. The same as in Fig. 15 for an aluminum contact, representing a dimer configuration. (a) The three highest electronic transmission eigenfunctions are visualized.

the end of each plateau, i.e., the conductance increases upon stretching before bonds break. This unique behavior of Al contacts is well-known, and it has been observed in different experiments and convincingly explained [165, 129, 167, 170, 168]. The electrical and thermal conductance are correlated, but larger deviations as compared to Au are visible. This is well apparent in the Lorentz ratio, shown in Fig. 22(b), which features deviations from the Wiedemann-Franz law as large as 40% and even above. Notice also that the electronic contribution to the thermal conductance follows closely the prediction of the Wiedemann-Franz law, with deviations that are at most about 5%, as can be inferred from the electronic Lorentz ratio L_{el}/L_0. Thus, the larger violations of the Wiedemann-Franz relation that we find for Al are mainly due to the phonon contribution to the thermal transport.

Let us emphasize that the high relative contributions from phonons are intrinsically coupled to the positive slope of the electronic conductance upon stretching of the contact since the phonon conductance behaves inverse to it. Henceforth, the largest deviations from the Wiedemann-Franz are seen at dips in the electronic conductance. Our results illustrate that the phonon thermal conductance cannot always be neglected when analyzing the thermal transport of metallic atomic-size contacts. The sawtooth-like behavior of L/L_0, discussed for Au before, is not so apparent for this Al contact. In any case, the Lorentz ratio exhibits minima close to the displacement values, at which atomic bonds break.

As the last example, we briefly discuss the stretching simulation for the Al contact depicted in Fig. 22(c). As in the Au case of Fig. 16(c), this Al contact is grown along the fcc (100)-direction and the stretching simulations were initiated with the geometry displayed in the upper left part of Fig. 22(c). There are two features of the results that we want to highlight. First of all, the last plateau before the breaking of the wire exhibits an electrical conductance of about $2G_0$.

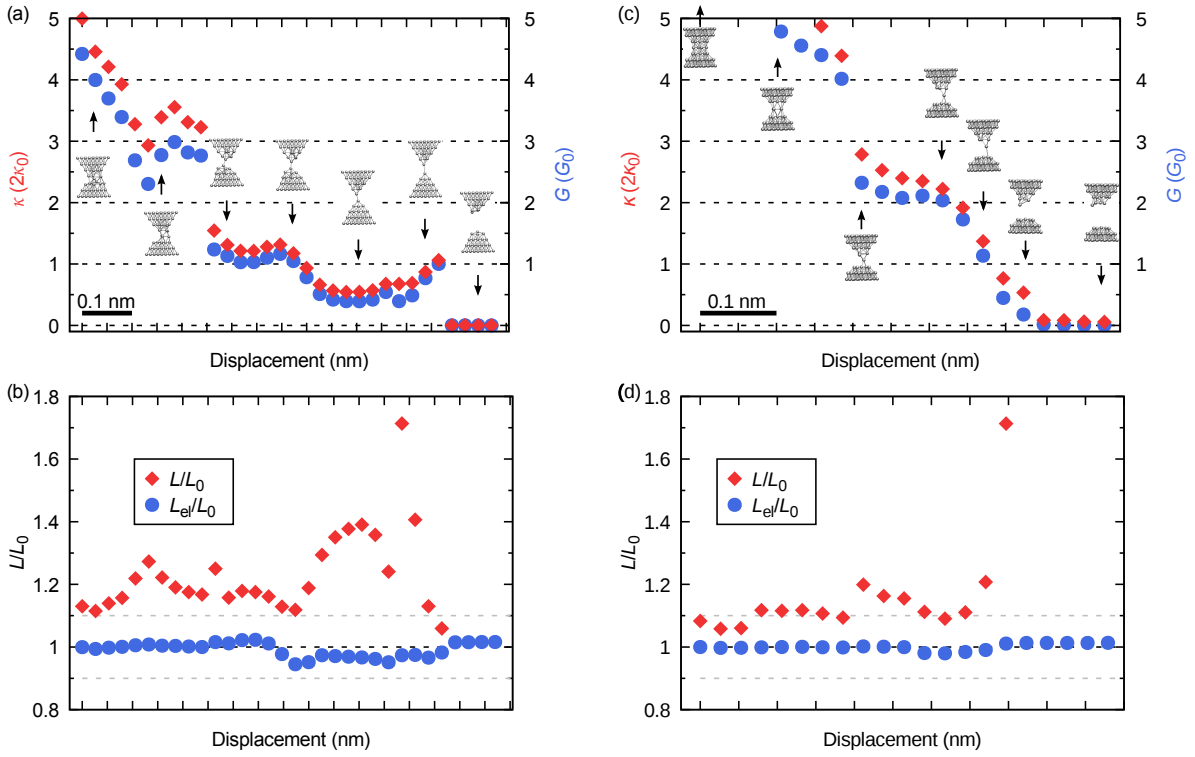

Figure 22. The same as in Fig. 16, but for an Al contact.

It originates from a one-thick contact, where there is a monomer in the narrowest region, as opposed to the dimer realized before breaking in the previous Al simulation of Fig. 22(a). This type of geometry is responsible for a second peak in the electrical conductance histogram of this metal close to $2G_0$. The second feature worth remarking is that, as one can see in Fig. 22(d), the phonons give a slightly smaller contribution to the total thermal conductance, as compared with the example of Fig. 22(b), but still clearly larger than in the Au case. This is mostly due to the fact that, in this type of geometry the anomalous slope of the electronic conductance upon elongation is typically not observed [171, 172]. On the other hand, the sawtooth-like shape of L/L_0 as a function of electrode displacement in Fig. 22(d) is much more pronounced than in Fig. 22(b)

3.3.2 NEMD

To complete the analysis of the thermal conductance in single-atom aluminum contacts, we want to use NEMD to generate a statistical set of geometries and furthermore look at the influence of anharmonicity in these type of junctions. If not stated otherwise, the simulation details are identical to the one used in Sec. 3.1.2. The EAM potential is taken from Ref. [173], which has been generated by fitting the potential apart from bulk properties also to ab-initio forces of Al cluster and (100) surfaces. In Fig. 23(a) we show the temperature dependence of the lattice constant which reads

$$a_{\mathrm{Al}}(T) = 4.03209 + 9.49545 \times 10^{-5} T - 1.37243 \times 10^{-7} T^2 + 1.58162 \times 10^{-10} T^3. \qquad (3.5)$$

Opposite to gold, a polynomial of second degree was unable to capture the data calculated in the MD run, so we used the next higher one. Fig. 23(b) shows the density of states as a function of temperature and energy. In accordance with the density of states obtained within our DFT calculation, the cut-off energy of Al is roughly at 40 meV which is almost twice the value of Au. As a consequence of thermal expansion, the phonon modes soften, leading to a shift of the whole

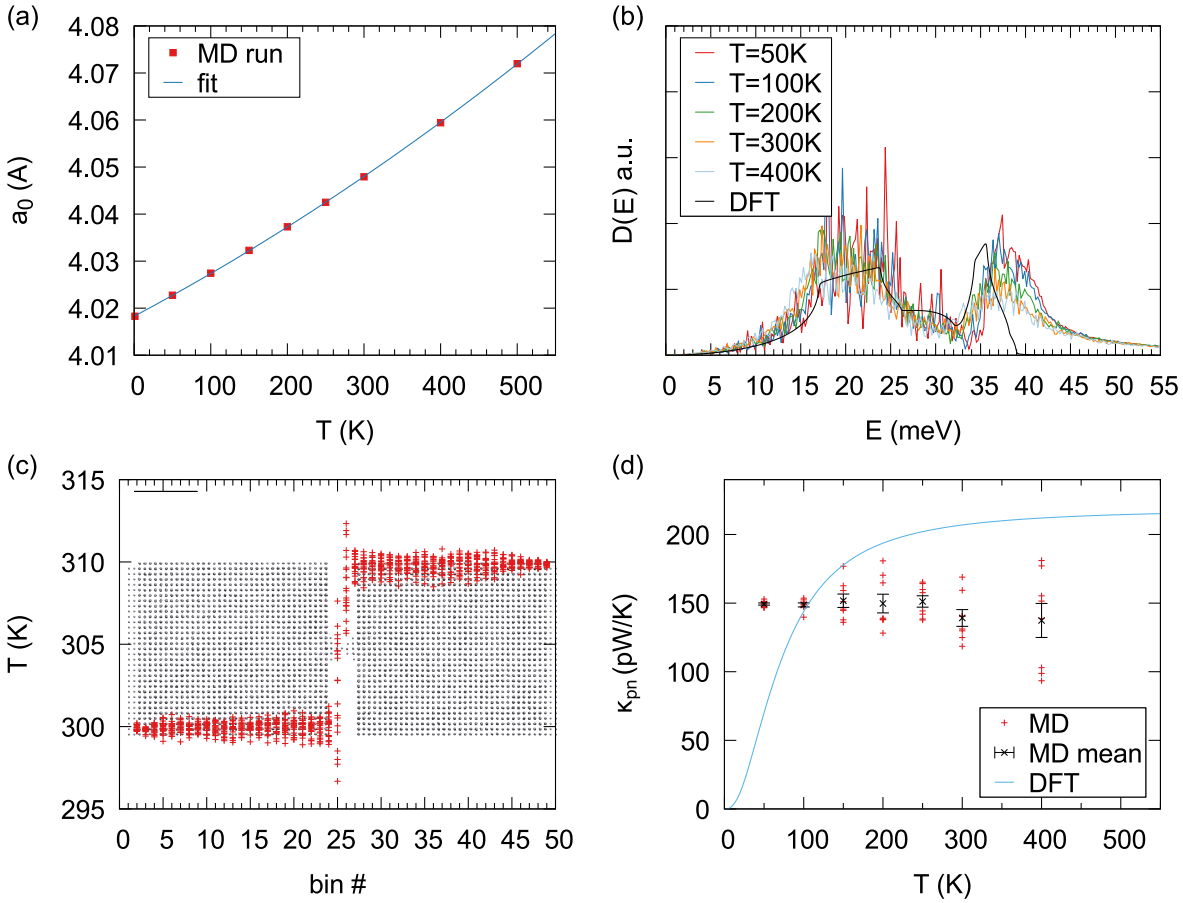

Figure 23. The same as in Fig. 17, but for aluminum.

density of states to lower energies. However, similar to the case of Au this effect is rather low. Let us mention that for T=50 K finite size effects are most pronounced in terms of a peaked DOS, especially at energies around 15-30 meV, which could be avoided by further increasing the size of the bath.

After the discussion related to bulk properties, we now want to study a single-atom contact as depicted in Fig. 23(c), together with a temperature profile for an example at $T = 300$ K. Again, as assumed by the NEGF approach, both phonon baths are almost decoupled and at their respective temperature, whereas the temperature drop occurs at the smallest part containing the single-atom contact. We repeat the calculation for this geometry using the simulation protocol of Sec. 3.1.2, with a smaller temperature difference of $\Delta T = 10$ K, since the heat transport due to phonons is much larger in this material. The results for $N = 8$ independent runs for each temperature can be seen in Fig. 23(d). The mean value is almost energy-independent, apart from the T=700 K results, whereas the variance increases with temperature. As already stated for gold, this is due to an enhanced phase space of geometrical configurations, with increasing temperature. In all runs for $T < 700$ K, the single-atom contact persist over the measurement time. At $T = 700$ K, the junction breaks at some point for some junctions, leading to a very small thermal conductance in those cases.

The higher conductance for this material compared to gold can be explained by the higher phonon energies occuring for aluminum. For completeness, we also compare to DFT calculations for this monomer, with the same boundary conditions. The results are in good agreement with each other, nevertheless, differences could be associated to, poor description of the MD potential for this type of geometry, differences related to the bulk DOS, and the different stress conditions stemming from the use of the experimental lattice constant in the DFT part. The influence of the latter one is less important compared to Au since here the deviation from the equilibrium

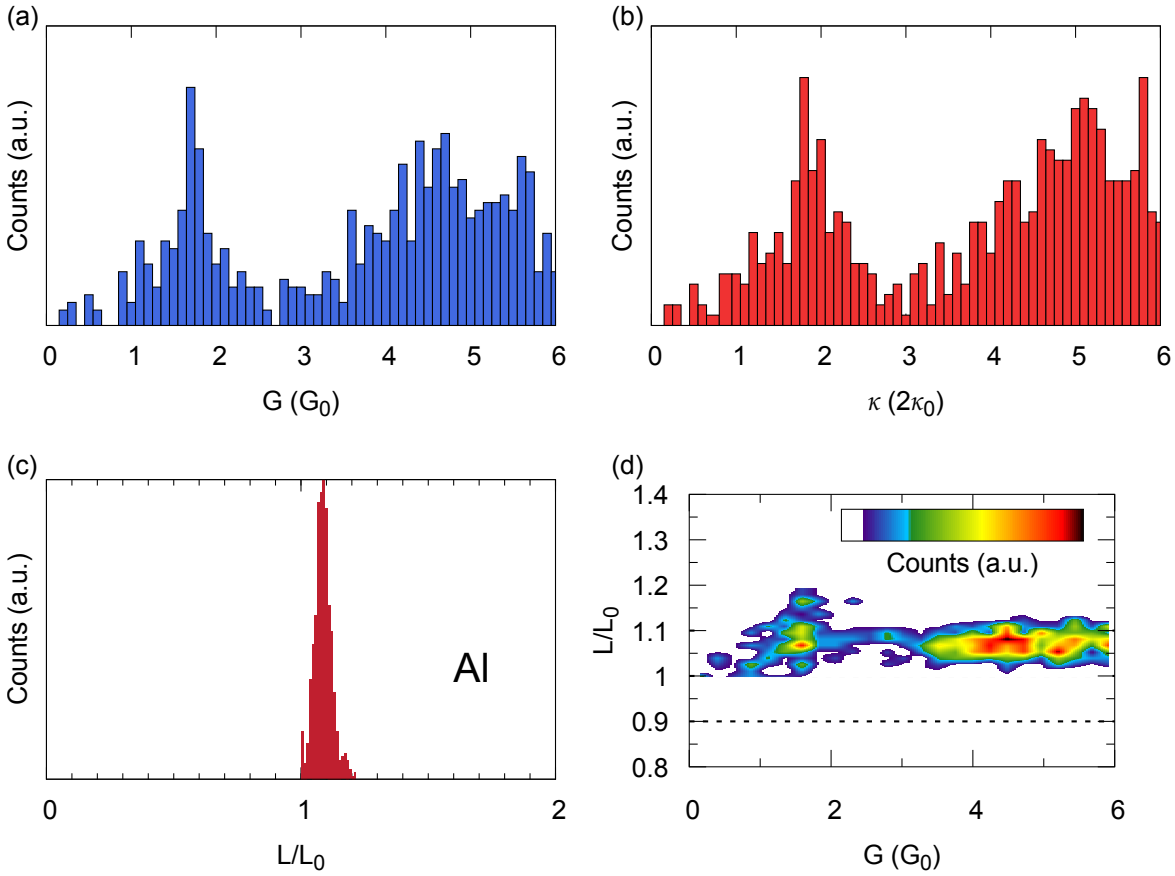

Figure 24. The same as in Fig. 19, but for aluminum. The peak position in (c) is at 1.09 %.

lattice constant to the experimental one is smaller (see App. C).

Finally, we present a statistical analysis for the aluminum atomic contact, starting with the initial geometry as depicted for gold in Fig. 18. For the electronic contribution we employ, similar to the gold simulation, a tight-binding parametrization of the electronic structure, including the $3s$, $3p$ and $3d$ orbitals of Al. The details about the calculation are identical to Sec. 3.1.2. The histograms for the electronic and the thermal conductance can be seen in Fig. 24(a) and 24(b). At low temperatures, these are experimentally known to exhibit two peaks in the electronic histogram at values around 1.3 G_0 and 1.8 G_0 [174], which corresponds to dimer- and monomer-contacts, similar to those studied in Fig. 22. However, our histogram at 300 K only shows the second peak. This raises the question of whether the dimer configuration is stable, or if the used MD potential is just incapable of describing this kind of geometry at room temperature. Furthermore, as explained in Sec. 3.3.1 the lack of conductance quantization can be related to the valence structure of Al with contributions from s and p orbitals. As a consequence, also the histogram of the thermal conductance does not show peaks at quantized values. To test the validity of the Wiedemann-Franz law we plot in Fig. 24(c) the histogram of the ratio L/L_0 for all geometries with conductance values up to 6 G_0. Clearly visible is that the deviations are larger compared to gold with a peak at almost 10 %. In accordance with the DFT results, this can be attributed to the higher Debye energy of Al. The heat map in Fig. 24(d) reveals the correlation between the electronic conductance value and the Lorenz ratio. The largest deviations are observed for single atom contacts with a conductance value around 1-2 G_0, with up to 20%, in accordance with the DFT results. Interestingly, we do not see higher deviations in contrast to Sec. 3.3.1. As already pointed out, the large deviations there could be explained by the anomalous slope of Al upon elongation. However, this effect is not observed within our set of geometries. In addition, the dimer configuration with a lower electronic conductance and

a relatively high phonon contribution is not stable in our MD simulations.

4 Single-molecule junctions

In the last chapter fundamental properties of heat conduction at the nanoscale in monoatomic metal junctions have been investigated. Due to their electrically conducting nature, it has been shown that in most cases phonons play a minor role in the total thermal conductance. In this chapter we now come to systems consisting of molecules connected to metallic leads, so-called molecular junctions, which are generally insulating and henceforth the thermal conductance is expected to be determined by phonons.

The field of molecular electronics has gained a lot of attention due to the appealing idea of building electrical components based on single molecules as the ultimate limit of miniaturized electronic devices [175, 176]. Experimental studies have commenced with advances in the control of subnanometer distances, such as in platforms based on molecular break compounds [177] or STM-based methods [178], which revealed the broad facets of transport through single molecules at the fundametal level of quantum theory. It turned out, that those systems offer a large tunability in terms of conjugation [179], anchoring groups [180, 181], chemical substituents [182] or structural changes induced mechanically [183, 184] or due to photo-active processes [185]. Additionally, they provided a deeper understanding about the nature of metal-molecule interfaces [186, 187] and the role of interference effects on the electronic transport properties [188]. Although, from a technological point of view, it is widely believed that they will not be competitive with silicon based technology, all these works contributed significantly to our current understanding of charge transport at the shortest length scales [54].

In recent years, these nanojunctions were additionally studied in the context of quantum theories that describe energy transport in nanoscale devices [47]. In particular, recent experimental advances have made it possible to investigate different aspects of energy and heat conduction in molecular junctions such as thermoelectricity [189, 190, 191], Joule heating [142] and Peltier cooling [192]. All these studies focused on the electronic properties in these kinds of systems and only recently the phononic contribution or the thermal conductance has been started to be analyzed [193, 143].

A lot of work is related to phonon transport in multi-molecular systems so called self-assembled monolayers [194, 195, 57, 196] or ideal infinite molecular wires [197]. From an experimental point of view most studies up to date differed from the conventional approaches used in molecular electronics, for instance, with time domain thermal reflectance measurements, which are restricted to multi-molecular systems [198, 199, 200, 201]. The ultimate limit of a single-molecule junction, seemed so far experimentally not accessible. Nevertheless, with the recent progress in experimental measurements at the single-atom scale [143, 144], the realization of such an experiment has come within reach.

From the theoretical side, a few groups studied the thermal conductance in contacts, where only a single molecule contributes to the heat transport, but either with simplified models [202, 56, 203, 60, 204], with 2D leads, or semiconducting leads [205, 206, 207, 208, 154]. Only few works are done with gold electrodes [209, 109], although these are experimentally the most relevant systems.

In this work we fill this gap from a theoretical point of view and study systematically various aspects related to phonon thermal conductance in single-molecule systems attached to gold electrodes, by taking advantage of the structural flexibilities which is intrinsic to molecular systems. More precisely, in Sec. 4.1 we study one of the most fundamental questions related to heat conduction in nanoscale system, namely the length dependence of the thermal conductance. The

molecular system we are considering are alkane chains of varying length and different anchoring groups as well as alternating substituents. Furthermore, we look at the expected variance in these systems due to variations in the metal-molecule bonding, lead orientation and geometrical defects on the basis of ab-initio as well as NEMD methods.

Sec. 4.2 is referring to the question, whether one could take advantage of the coherent transport regime and use interference effects in the phononic system to manipulate the thermal properties of a molecular junction. Here we use amine anchored benzene derivatives. Upon inclusion of substituents with different masses, we analyze if it is possible to tune interference effects, such that they vary the thermal conductance significantly.

At last, we study in Sec. 4.3 the possible influence of the phononic as well as the electronic contribution to the thermal conductance on the thermoelectric efficiency. Therefore we consider the single-C_{60} junction and a C_{60}-dimer junction. In addition, we estimate the importance of a further contribution coming from photons, to give a realistic device efficiency.

4.1 Alkanes

In this section we will study one of the most fundamental questions in the context of phonon transport in atomic-scale systems, namely the length dependence of the thermal conductance of a molecular chain.

It starts with a comparison of distinct classes of molecules in Sec. 4.1.2. The classes are divided into different groups of anchoring groups and variations upon substituents (alkanes vs fluoroalkanes). Here, we investigate equally constructed geometries with a lead orientation in (111) direction. In Sec. 4.1.2.2 we develop a simple 1D model for these kinds of systems to rationalize the effect of binding group in terms of scalar coupling constants. In addition, in Sec. 4.1.2 we compare the influence of electronic contributions to the thermal conductance among all subsets of molecules and relate them to existing experimental as well as theoretical works.

To estimate the variations of the thermal conductance, we furthermore compare different geometries in Sec. 4.1.3.1, based on different lead orientations and alternating gold-sulfur bonding positions. Here, we restrict the analysis to a subset of dithiolated molecule from 2-10 units, since those are known to form various kind of contact structures. As a further variation we look in Sec. 4.1.3.2 at the influence of structural defects upon elongation of the junction. We close in Sec. 4.1.4 with a comparison to NEMD calculations.

4.1.1 Length dependence - introduction

The theoretical discussion of the thermal conductance of a linear 1D chain has a long history [210, 32, 55]. The general conclusion is that in long ideal chains (of more than 100 identical units) exhibiting nonlinear interactions, momentum conservation and no disorder, the thermal conductance decays algebraically as $\kappa_{\mathsf{pn}} \propto L^{\alpha-1}$, where L is the chain length and the exponent α is found to be $\alpha = 1/3$. Although these results are of fundamental interest, it is not clear that they are very relevant for actual experiments on nanoscale systems due to the long chain lengths required.

In the context of molecular junctions, the issue of the length dependence of the thermal conductance has already been addressed both experimentally and theoretically. Often the molecules of choice have been alkane chains [198, 196], which are saturated molecules, whose electrical properties have been widely studied in the context of molecular electronics [211, 212, 213, 214, 215, 216, 217, 218, 179, 180, 219, 220, 221, 222]. From the experimental side, the length dependence of the thermal conductance of alkane-based molecular junctions was investigated by Wang *et al.* [57] making use of alkanedithiol self-assembled monolayers (SAMs) that were sandwiched between Au and GaAs electrodes. It was found that the thermal conductance of junctions with 8, 9, and 10 CH_2 units did not depend significantly on the molecule length. More recently, Meier *et al.* [201] reported thermal conductance measurements of monothiolated alkane monolayers, self-assembled on Au(111) surfaces as a function of their length (ranging from 2 to 18 methylene units). Making use of a scanning thermal microscope with a Si tip, it was found that the thermal conductance first increases for short chains, reaching a maximum for 4 units, and then it exhibits an (arguable) slow decay for lengths above 8 units. From the theory side, Segal *et al.* [202] made use of semi-empirical methods to predict that the thermal conductance of alkane chains approaches a constant value for more than 20 CH_2 units for a weakly coupled junction, while it decreases inversely proportional to the length for the strongly coupled case. On the other hand, Duda *et al.* [195], using a diffusive transport model combined with Hartree-Fock calculations of the vibrational modes of alkane chains, suggested that the thermal conductance should be fairly length-independent for chains with more than 5 CH_2 units. In the only ab-initio study of this issue that we are aware of, Sadeghi *et al.* [209] explored the phonon transport in alkane-based single-molecule junctions with 2, 4, 8, and 16 CH_2 units and found a very pronounced decay of the thermal conductance for the longest molecular length. These seemingly contradictory

theoretical results call for new inspections of the fundamental issue of the length dependence of the thermal conductance of molecular junctions.

4.1.2 Comparison of anchoring groups and substituents

4.1.2.1 DFT-NEGF

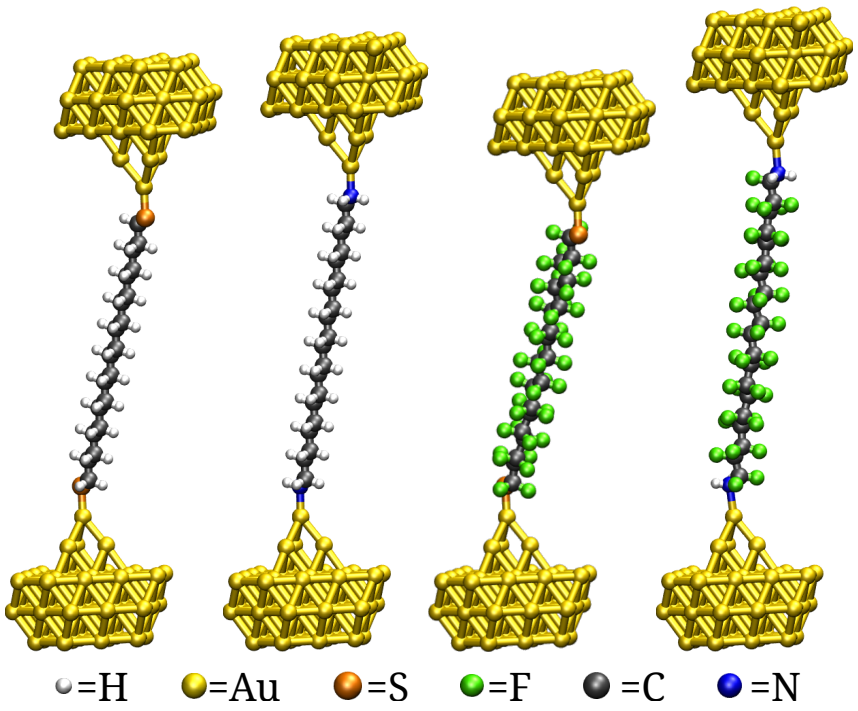

Figure 25. Examples of the four types of molecular junctions studied in this work. The four molecules have the structure X-$(CY_2)_n$-X, where the terminal or anchoring group X is either S or NH_2, while the Y atom in the repeated unit is either H or F. The integer number n denotes the number of CY_2 segments in the molecules. In all cases, the electrodes are made of gold and the contact geometries are such that molecules are bonded to the electrodes in an atop position via the anchoring groups.

To investigate the length dependence of the thermal conductance of single-molecule junctions, we study alkanes chains of different length with an even number n of methylene (CH_2) units ranging between 2 and 30, using the ab-intio approach as explained in Sec. 2.2. These saturated molecules are electrically rather insulating, which ensures that the thermal transport is dominated by phonons (see below). To elucidate the role of the anchoring or terminal group in the length dependence of the phonon transport, we analyze two standard groups in molecular electronics, namely thiol (S) and amine (NH_2) groups. Moreover, we study the impact of the substitution of the H atoms in the alkane chains by heavier F atoms to investigate polytetrafluoroethylenes (PTFEs) with both thiol and amine groups. Thus, in an attempt to draw general conclusions, we investigate four different families of molecules attached in all cases to gold electrodes.

In what follows, we shall focus on the binding geometries illustrated in Fig. 25, where the molecules are bonded to the electrodes in an atop position via the corresponding anchoring group. Let us stress that in all cases the molecular junctions were optimized, such that the maximum gradient is below 10^{-5}a.u. . Moreover, in order to establish a meaningful comparison between the different compounds, special care was taken to avoid both strain effects and the appearance of defects in the molecular chains. In this sense, the alkane chains remain linear in our case, while the introduction of F atoms causes the carbon atoms to deviate from this linear

structure, leading to more disordered PTFE chains. Independent of this, the distance between the carbon atoms stays nearly constant in all chains with a value of around 1.5 Å.

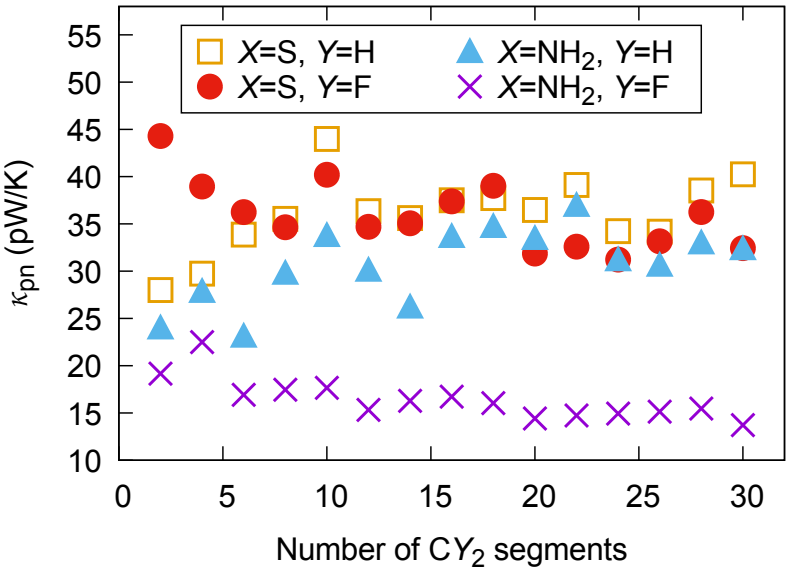

Figure 26. Room-temperature ($T = 300$ K) phonon thermal conductance as a function of the number of CY_2 units ($Y = H, F$) in the molecule for both anchoring groups, thiol and amine. The distance between neighboring C atoms in the chains of around 1.5 allows to translate the number of units to a corresponding distance.

We summarize in Fig. 26 the main result of this part, namely the room-temperature phononic thermal conductance for the four types of molecular junctions as a function of the number of CY_2 segments ($Y = H, F$) ranging from 2 to 30, which corresponds to a maximum length of around 4.5 nm. The first thing to mention is that the conductance values range from 15 to 45 pW/K. Second, for chains with more than 5 segments the conductance exhibits small variations, but it is basically length-independent, irrespective of the molecular family. Third, the molecules with amine anchoring groups typically exhibit a lower conductance than the corresponding dithiolated ones. This is particularly evident in the case of the PTFE-diamine molecules, which exhibit thermal conductances that are about a factor of 2 smaller than those of the other families. Overall, these results show that the phononic thermal conductance of alkane-based single-molecule junctions is rather insensitive to the molecular length for up to 30 segments, which is a signature of ballistic phonon transport.

To understand these results, let us first analyze the energy dependence of the phonon transmission. An example for the four types of molecules with $n = 10$ CY_2 segments is shown in Fig. 27. First of all, notice that the transmission is different from zero only in an energy region between 0 and 20 meV, which is determined by the phonon density of states of the gold electrodes (see Ref. [109]). Second, the most obvious feature in these results is the fact that for the molecules with the amine group the transmission spectra exhibit narrower peaks, which explains the lower conductance obtained for these molecules. (This is particularly well pronounced for the PTFE-diamine ones.) This strongly suggests that the phononic metal-molecule coupling for the amine group is weaker than for thiol. On the other hand, although the fluorinated molecules are expected to exhibit more vibrational modes in the transport window than the alkane chains due to the larger mass of the F atoms, one does not observe significant differences.

To further clarify how the elastic phonon transport takes place, we show in Fig. 28 the largest individual phonon transmission coefficients for molecular junctions with alkanedithiols of three different lengths ($n = 10$, 20, and 30 methylene units). The first thing to notice is that the

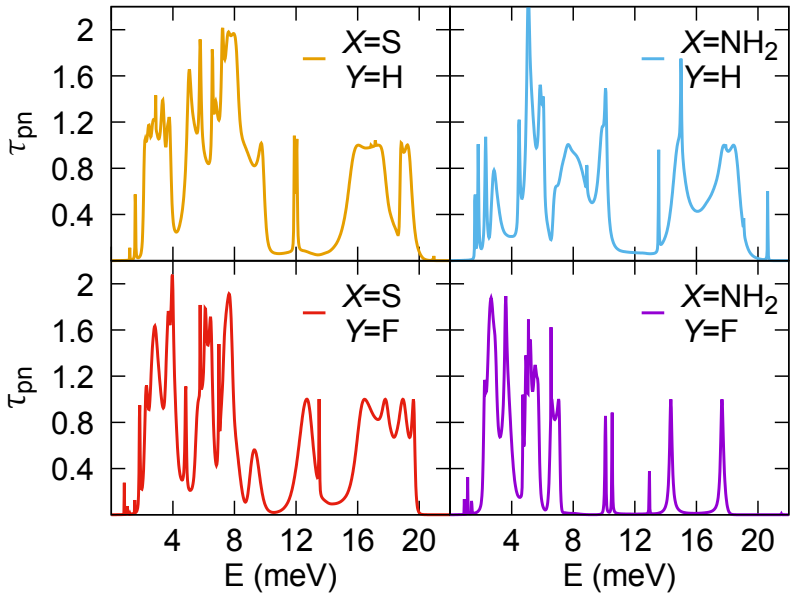

Figure 27. Phonon transmission as a function of energy for junctions containing molecules with 10 CY_2 units.

total transmission is dominated by a single or two phonon channels, with a third one giving only a small contribution. The number of channels is controlled in this case by the rather linear molecules, and the three channels correspond to the three polarizations of the vibrational modes. It is important to realize that this number of channels cannot be altered by the number of vibrational modes in the molecular chains, which only determine the actual values of the transmission coefficients. More important for our discussion of the length dependence is the fact that the dominant channel is fully open (transmission equal to 1) over a wide range of energies, irrespective of the length of the molecule. This is indeed the true signature of ballistic phonon transport, which is realized here with alkane and alkane-related molecular chains.

4.1.2.2 1D model

To gain further insight into our ab-initio results, we have developed a simple 1D model that is schematically represented in Fig. 29(a). In the following we will use the notation k_{ij} for elements of the dynamical matrix coupling atoms i and j in the toy model as compared to K_{ij} in the full ab-initio results. In the model we consider only nearest-neighbor couplings between segments in the molecular chain, k_{CC}, and the leads are modeled as 1D Au chains with an analogous nearest-neighbor coupling, k_{AuAu}. Finally, the metal-molecule coupling is described by a single constant, $k_{AuC} = k_{AuX}\sqrt{M_X/M_C}$ with $X = \mathrm{S, N}$. We extracted these parameters from the DFT calculations as the highest eigenvalue of K_{ij}, see Eq. (2.21). These parameters depend on the molecular species, but not on the molecular length, and we summarize their values in Table 3.

Using these parameters, we computed the corresponding thermal conductance with the Green's function method described in Sec. 2.1 and the results are displayed in Fig. 29(b). As one can see, this simple model is able to reproduce all the salient features of our ab-initio results in Fig. 26. In particular, it nicely reproduces the fact that the amine-terminated molecules exhibit a lower thermal conductance, which is especially evident in the case of the PTFE-diamine chains. Now we can confirm that this lower thermal conductance is due to a weaker coupling to the leads (see values of k_{AuX} in Table 3). The strongly reduced coupling for PTFE-diamine chains as compared to their alkane-diamine counterparts results in practice from the larger distance (about 0.15 Å)

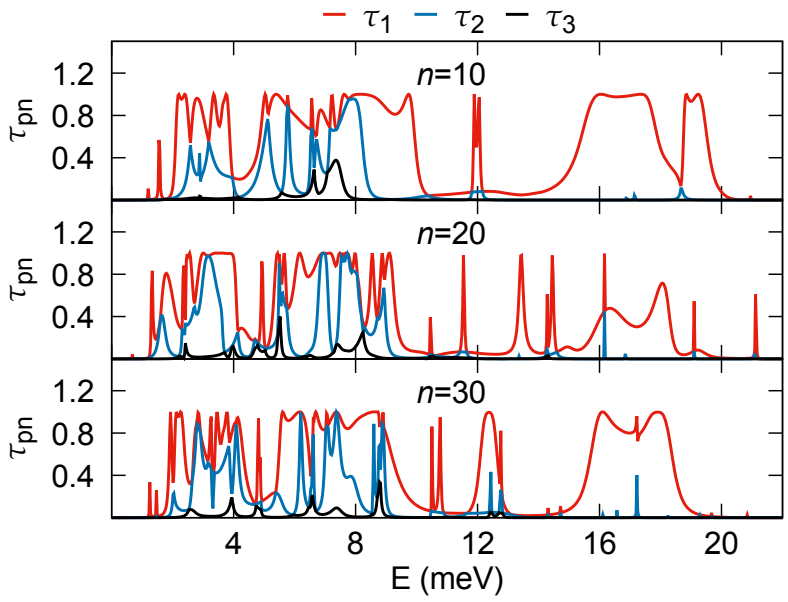

Figure 28. Individual phonon transmission coefficients as a function of the energy for three alkanedithiols with different lengths (10, 20, and 30 methylene units). We show the coefficients of the three most transmissive channels.

X	Y	k_{AuX}	k_{CC}	k_{AuAu}
S	H	485	6150	100
S	F	426	4850	100
N	H	218	6150	100
N	F	55	4850	100

Table 1. Parameters for the 1D model schematically represented in Fig. 29(a). All elements k_{ij} of the dynamical matrix are given in units of meV^2. Notice that the same value of k_{AuAu} was used in all cases.

between the Au electrodes and the N atoms in these molecular junctions. Let us also mention that we attribute the higher conductance values obtained with the 1D model as compared to the ab-initio results to the fact that we extract the parameters k_{ij} from the largest eigenvalues of the dynamical submatrices K_{ij} and the contrasting behavior of $\tau(E)$ for $E \to 0$ due to different lead dimensions. This can be seen in Fig. 30, where the transmission for the alkane chains for 3 different length of n=8,14,20 is shown. In opposite to the DFT results with 3D lead, for the 1D leads the transmission goes to 1 as the energy approaches zero.

Another aspect we want to highlight in this simple model is the oscillatory behavior in the thermal conductance as seen for all sets of molecules in Fig. 29(b). To explain this behavior let us look at the different transmissions in Fig. 30 for X=NH_2 and Y=H. The values for n have been chosen, such that they show the evolution of one maxima to the next following. At n=8, which corresponds to the first peak in the thermal conductance for this molecule, a transmission peak is located just next to the cut off energy of 20 meV. Upon increasing of the chain length this resonance shifts to lower energies which lowers the total thermal conductance (exemplified at n=14), until the next resonance shifts in the energy window set by the Debye energy (n=20), which leads to another maximum in κ_{pn}. The value at which the maxima occur depends on the respective coupling constants, which gets obvious, for instance, in the second example with X=S and Y=H, where the maximum occurs at n=14. The general behavior however is identical within one set of molecules, irrespective of the chosen parameters. Comparing to the DFT results in

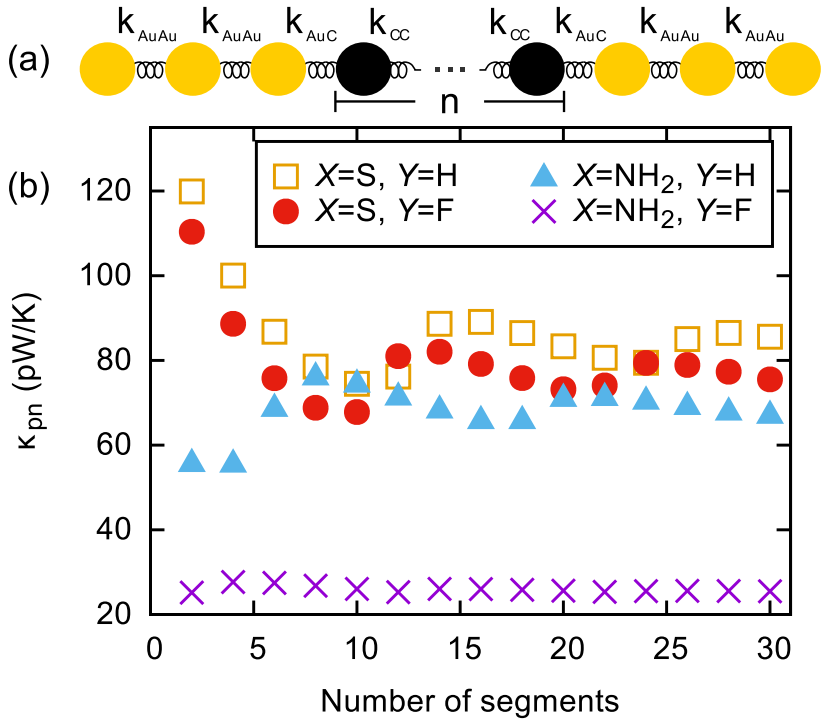

Figure 29. (a) Schematic representation of the 1D model used to understand our findings. The meaning of the different parameters is explained in the text. (b) Results obtained with the 1D model for the room-temperature phonon thermal conductance as a function of the number of CY_2 units ($Y = H, F$) in the molecule for both anchoring groups, thiol and amine.

Fig. 26, we can also identify this kind of behavior, although being less pronounced compared to the simple model. In fact, we observe that specific modes shift inside the energy window first and then to lower ones, especially in the range around 10-20 meV. However, the phonon density of states of a 3D material has a much more complex energy dependence then the simple 1D model, and different polarizations of the molecule can couple differently to the leads. So in order to interpret the DFT transmission generally one need to take into account additional features, beyond this simple shift of resonances due to increasing chain lengths. Nevertheless, we want to point out that the "maxima" there could be influenced by variations in the contact geometries, as well as by different stress conditions, since all of these influences the position of the molecular resonances slightly.

4.1.2.3 Further discussion

So far we have focused on the phononic contribution to the thermal conductance but for experiments it is important to analyze whether the electrons play any role. Alkanes are known to be poor electrical conductors [211, 212, 213, 214, 215, 216, 217, 218, 179, 180, 219, 220, 221, 222]. Thus, on the basis of the Wiedemann-Franz law [54, 109], therefore one does not expect the electrons to give a significant contribution to the thermal conductance. To check this, we have studied the electronic contribution to the thermal conductance, κ_{el}, in all of our molecular junctions using the ab-initio methodology briefly described in Sec. 2.6. Using $T = 300$ K, we show in Fig. 31 the results for the ratio between the electronic and phononic thermal conductances as a function of the molecular length for the four families of molecules investigated here. As one can see, when molecular chains have more than 4 segments, the electronic contribution is negligible. Notice that the exponential decay of the conductance ratio is a simple consequence

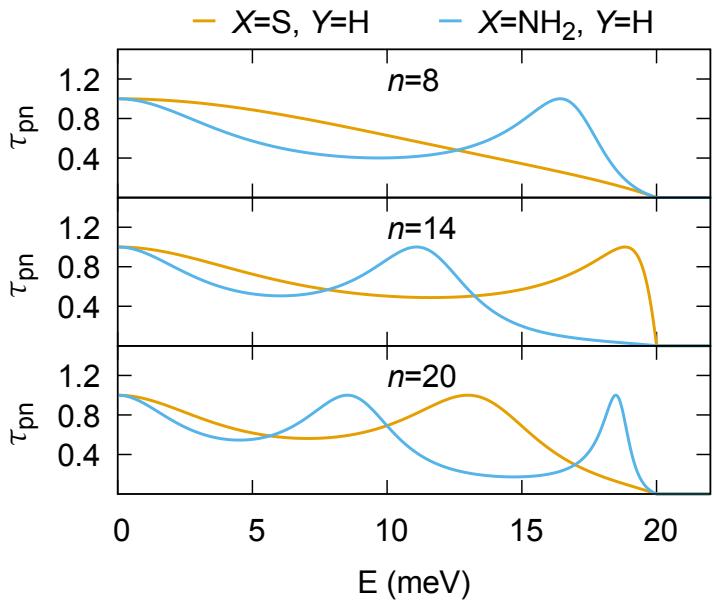

Figure 30. Transmission function of the 1D model for 3 different values of n=8,14,20, shown only for the alkane chains.

of the exponential decay of the electrical conductance with length in the off-resonant transport situation. It follows from the proportionality of κ_{el} and the electrical conductance and a rather length-independent κ_{pn}.

In the previous section we discussed the results for the thermal conductance at room temperature. For completeness, we now briefly address the issue of the temperature dependence of the phonon transport. Fig. 32 displays the temperature dependence from 0 to 300 K of the phonon thermal conductance for junctions with the four molecular species and featuring $n = 10$ CY_2 segments. This temperature dependence is relatively insensitive to the molecular length and thus, the results of Fig. 32 are representative for the four molecular species studied in this work. As one can see, the thermal conductance raises abruptly at low temperatures, it tends to saturate, depending on the molecule, above approximately 100 to 200 K, and around room temperature it is fairly constant. This overall behavior simply reflects the fact that for temperatures above the Debye temperature of gold, all the phonons of the metal electrodes as well as the vibrational modes of the molecule with energies within the transport window are thermally occupied, while below this temperature the higher-lying modes are only partially occupied and the thermal conductance hence becomes sensitive to the temperature.

Let us now discuss the comparison with existent results. From the theory side our results, showing a thermal conductance relatively insensitive of the molecular length, are qualitatively compatible with the insights of Segal *et al.* [202] for weakly coupled alkane chains. This also applies to the results of Duda *et al.* [195]. Our results are also in agreement with the molecular dynamics calculations performed by Luo and Lloyd [194], which studied octanedithiol SAMs sandwiched between gold electrodes and estimated a thermal conductance per molecule of 43 pW/K. However, our results are clearly at variance with the strong decay for the longest molecule reported by Sadeghi *et al.* [209], which indeed is the only ab-initio study published to date on the length dependence of the thermal conductance of alkane single-molecule junctions. The reason for the discrepancy is unclear to us, but it is worth pointing out that those authors only analyzed a very limited number of molecules (with 2, 4, 8, and 16 methylene units) and they used a different anchoring group (hydrobenzothiophene).

With respect to existent experiments on the length dependence, we cannot establish a direct comparison, but our length independence is compatible with the experiments of Wang *et al.* [57]

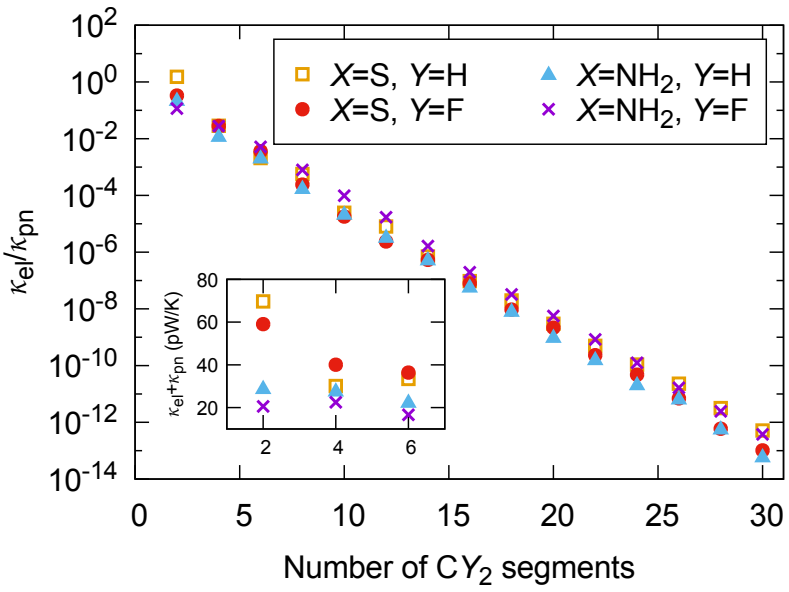

Figure 31. Ratio of the electronic (κ_{el}) and phononic (κ_{pn}) room-temperature thermal conductance as a function of the molecular length for the 4 different types of molecules studied in this work. In the inset the thermal conductance due to both electronic and phononic contributions is displayed for short chain lengths.

in junctions based on alkanedithiol SAMs sandwiched between Au and GaAs electrodes. On the other hand, the experiments of Meier *et al.* [201], which represent the most systematic study of the length dependence of the thermal conductance of alkane junctions to date, exhibit some basic differences with the junctions studied in this work. First, their tip electrode has been made of Si. Second, the alkanes have been monothiolated. Third, the temperature difference used in the experiment has been between 200 and 300 °C, which is most likely beyond the linear response regime addressed in our work. Finally, in this experiment the number of contacted molecules is not directly determined, and it is only inferred with the help of tip models. Furthermore, the estimated conductance values per molecule lie in the range of our calculated values and a careful inspection of the experimental data shows that the conductance is indeed fairly independent of the molecular length for chains with more than 8 methylene units. Anyway, a rigorous comparison with experiments to settle the issue of the length dependence of the thermal conductance requires true single-molecule experimental techniques, and our results provide clear predictions that we hope will be tested experimentally in the near future.

Related to the role of the anchoring group, let us mention that Losego *et al.* [223] investigated experimentally with the time-domain thermoreflectance technique its impact on heat transport in SAMs of alkanes contacted to quartz and gold films. They observed that the replacement of amines as the binding group to the Au film by thiols led to a 60% increase of the thermal conductance per unit area for chains with 11 methylene units. This is consistent with the general trend found here in the sense that the amine-terminated molecules exhibit in general a lower thermal conductance than their thiolated counterparts.

Let us conclude this section by stressing that in spite of the fact that we are using an approach, where anharmonic effects are not taken into account, the finding of a length-independent thermal conductance, as reported, here is by no means trivial. The intrinsic disorder in the molecular chains, which is present e.g. in the PTFE chains, can in principle lead to a diffusive transport regime, where the conductance decays linearly with length, or ultimately to an Anderson-localized regime, where the conductance is exponentially suppressed with length. In our study we see that for chains of up to 30 segments (with a length of up to 4.5 nm) the conductance exhibits a weak

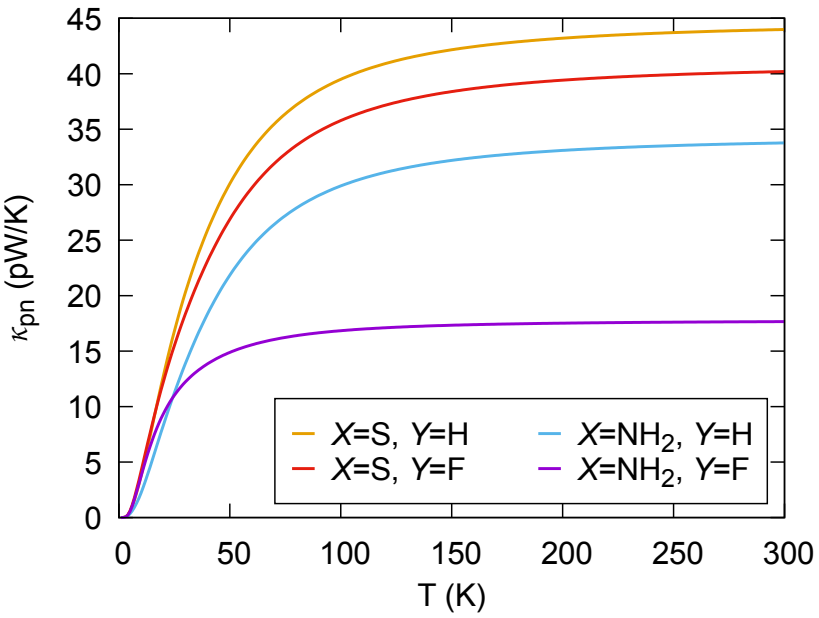

Figure 32. Phonon thermal conductance as a function of the temperature for junctions containing molecules with 10 CY_2 units.

length dependence, indicating that the elastic mean free path is larger than the system size. It would be interesting to study the limits of this quasi-ballistic transport. Let us also emphasize that Segal *et al.* [202] showed that anharmonicity in the alkane chains is rather weak and it is not expected to play a crucial role in the range of lengths studied in this work. Therefore, our approach is well justified.

4.1.3 Variations of the thermal conductance

In the previous section we compared different types of molecules within a set of similar geometries. We now want to estimate the variation in the thermal conductance due to a different binding to the lead, different lead orientations and the influence of geometrical defects, within one class of molecules. For this we use dithiolated alkanes and restrict our analysis to chain lengths of 2-10 CH_2 units, hereafter named C2-C10.

4.1.3.1 Contact geometry

To better understand the variability of the thermal conductance in single-molecule junctions, we have determined the thermal conductance of different junction types. These junctions have been created by varying the binding position as well as the lead orientation. The lead orientations are (111) for junction type 1 (JT1) and JT2, (100) for JT3 and (110) for junction type JT4. A picture of the various geometries can be seen in Fig. 33(a) shown here for an alkane with 6 CH_2 units. The contacts have been constructed such that within one junction type, all the alkanes of different length show a comparable geometry. Let us first look at the electronic conductance for each junctions, calculated using DFT+Σ as explained in Sec. 2.6. For all junctions types the electronic conductance shows an exponential decay, with a variation which can reach up to 80% of the average value. Together with the phononic contribution, this gives the total thermal conductance depicted in Fig. 33(c). Here, the thermal conductance is nearly length independent, apart from a reduced thermal conductance, when going from 2 CH_2 units to 4 CH_2 units. Typical

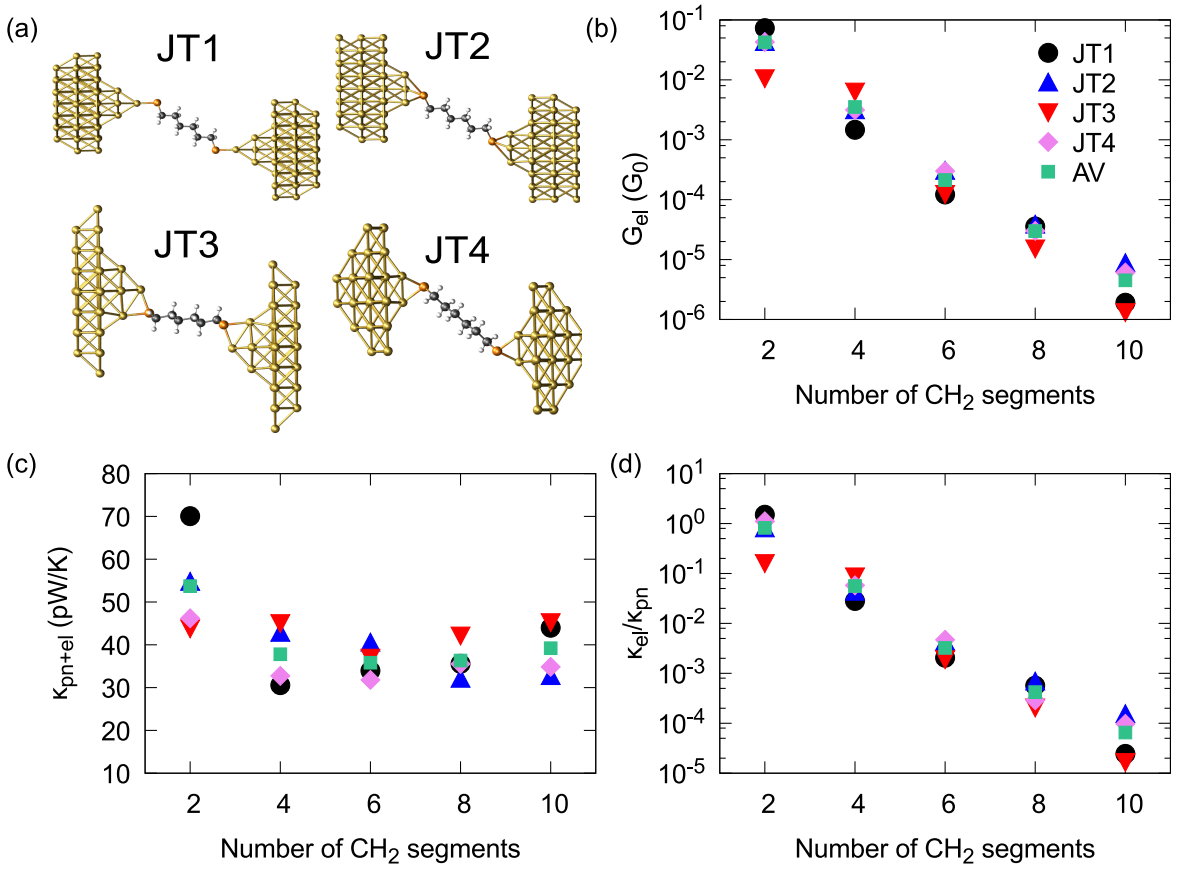

Figure 33. (a) Different types of junction geometries (JT1-JT4) used for the calculation of thermal and electrical conductances, as shown for an alkane with 6 CH2 units. (b) Calculated electrical conductance as a function of molecular length. (c) Total thermal conductance and (d) ratio between electronic and phononic contribution to the thermal conductance as a function of molecular length.

variances are on the order of 5 pW/K for C4-C10, whereas the variance for C2 differs and is on the order of 10 pW/K. The origin of this can be explained by looking at the relative contributions κ_{el}/κ_{pn} plotted in Fig. 33(d). Consistent with the previous results, the thermal conductance is dominated by phonons for C4-C10 and both contribute equal for a chain length of 2. Thus, the variance as well as the total thermal conductance of the smallest chain length is influenced by the electronic contribution, whereas the variance and the total conductance for the other molecules is dominated by the phononic system.

4.1.3.2 Defects and pulling curves

The former results focused on the thermal conductance of alkane chains in a straight configuration. However, alkane chains are known to exhibit geometrical defects, which can be thermally activated. In a recent study with graphene leads [205], these defects have been shown to reduce the thermal conductance in comparison to straight chains, where the authors suggested a mechanically driven thermal switch, based on this effect. In a study related to the electronic conductance, using ab-initio MD simulation [224], the authors could relate a low conductance peak in the electronic conductance histogram of a gold-alkane-gold junction to these defects. Furthermore, they pointed out that upon stretching of the system all defects vanish and before breaking of the contact, it inhibits a straight configuration.

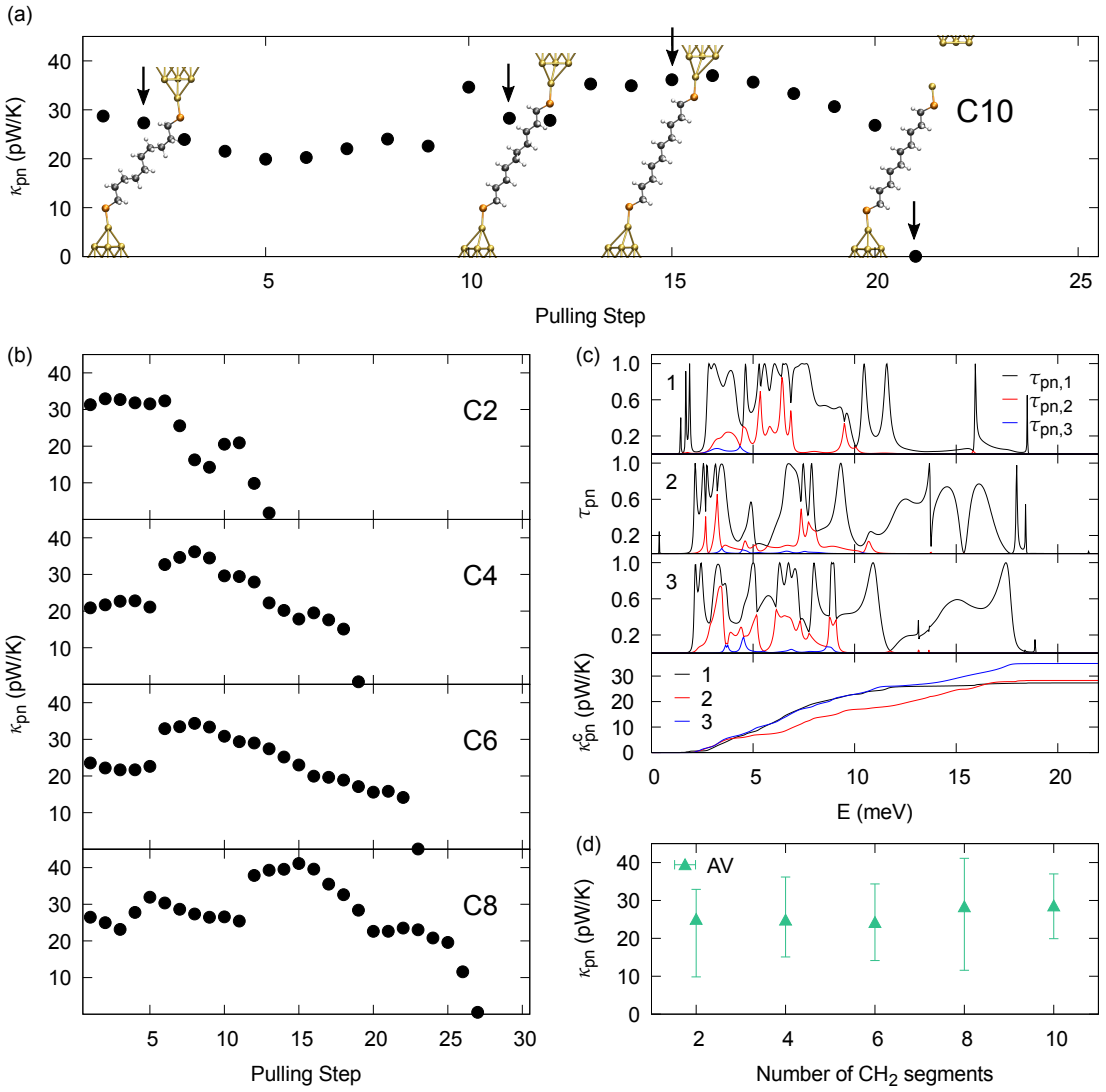

Figure 34. (a) Pulling curve for the C10 chain with defects. The thermal conductance of the visualized geometries are indicated with arrows. (b) Corresponding pulling curves for the chain C2-C8. (c) Eigenchannel resolved transmission for the three geometries of (a) in contact, together with the cumulative thermal conductance. (d) Average thermal conductance for C2-C10.

To test the influence of these defects on the phonon thermal conductance, we generate defective chains by arbitrary varying the torsional angle in the alkanes. In this way, we produce four different geometries for each length. Then we pick one geometry for each molecule and construct the junction in the usual way, by first relaxing the chain on top of one lead and afterwards attaching the second lead by applying a point mirror symmetry operation at the free thiol group. These geometries are then stretched to look at their response to different strain conditions. The displacement is done along the gold atop-atop distance vector with an increment of approximately 0.26 Å. Since C2 can not host any geometrical defect, the defective chains are restricted to the set of C4-C10.

Let us first look at the example of an alkane chain with 10 CH_2 segments, depicted in Fig. 34(a). Initially this chain inhibits various defects and the thermal conductance varies smoothly around 20-30 pW/K. In this stage the response of the junction to the elongation is just a variation of the bonding distances to adopt for the new strain condition. This stage ends with a certain jump in the thermal conductance at a pulling step of 10. There, the geometry of the alkane chain changes

and all but one defect vanishes. After 2 additional points with a decreased thermal conductance due to the induced strain, an additional jump occurs, and the chain is now defect free. At this point a further pulling only smoothly varies the conductance. Before breaking of the contact, the thermal conductance decreases, and finally breaks at an Au-Au bond. This behavior is similar for the other molecules (C2-C8), which are depicted in Fig. 34(b). Whereas C2 does not contain a defect and is just shown for completeness, the single defect in C4 and C6 and the two defects in C8 dissapear upon pulling, visible in a jump of the thermal conductance. In all cases, the thermal conductance of the straight configuration is consistently larger then the one with defects.

To gain more insight into the origin of these reductions, we show in Fig. 34(c) the eigenchannel resolved transmission of the three examples indicated with an arrow in Fig. 34(a), which have non-negligible conductance values. In the two examples with defects, named 1 and 2, phonons within a different energy range are responsible for the reduced conductance as compared to the chain without defects (example 3). In 1 this energy range is about 10-20 meV, for 2 the reduced transmission is in the opposite region of 0-10 meV. This gets evident by looking at their cumulative thermal conductance, as defined in Eq. 2.20. Here, the curves 1 and 3 almost coincide up to an energy of around 15 meV, and deviate above this energy. However, a comparison of 2 and 3 reveals the main difference to occur around 5 meV, whereas after this energy the difference stays nearly constant.

At last we show in Fig. 34(d) a mean thermal conductance of all junctions, calculated by averaging over the conductance values > 0.1 pW/K, together with the highest and lowest contribution within this range plotted as an arrow bar. The so calculated thermal conductance is an average over several strain conditions and geometrical configurations and thus, is likely to represent experimental results at ambient temperature, as we will point out in Sec. 4.1.4. Consistent with the previous results in Sec. 4.1.2 the thermal conductance is nearly length independent and ranges from 20-30 pW/K. In comparison to the straight chain configuration, however, the inclusion of defects into the alkane chain generally leads to a lower thermal conductance.

4.1.4 NEMD

To close the analysis of the alkane chains, we want to look at temperature effects in this type of molecular junction, in terms of NEMD simulations. Since those simulations rely on a choice of the interaction potential, we need a parametrization which is able to express the geometry and the vibrational modes of the molecule as well as the ones of the metallic lead and at the same time is capable to describe the metal-molecule interaction.

In the literature several calculations exist with different force fields, which have in common that the sulfur-gold bond is described with a Morse potential [194, 225]. This kind of parametrization is useful to characterize the binding situation in a self-assembled monolayer [194, 226, 196]. If we go to single-molecular contacts, however, these potentials are incapable to describe the correct chemical bond and therefore lead to an overcoordination of the sulfur atom. Additionally, within this parametrization the intra-molecular interactions are usually described in a harmonic approximation. In contrast, reactive force fields are able to describe chemical bonds and therefore lead to more reliable geometries. Furthermore, they contain anharmonic interactions in the overall system [87].

In our study we use the REAXFF from Ref. [227, 228] which has a preferable bonding of the sulfur atom to a gold surface in an atop position. Similar to the calculation in Chap. 3, we first look at the parametrization of a gold bulk within REAXFF. In Fig. 35(a) the lattice constant as a function of temperature is depicted. In comparison to the EAM potential used in Sec. 3.1.2, this potential shows less anharmonicity for gold, so the lattice expansion with temperature is smaller. The vibrational density of states at 300 K, plotted in Fig. 35(b) for various dimensions of the cubic simulation cell $L_{x,y,z}=2Na_0(T)$, shows a slight blue shift, nevertheless, the qualitative agreement is sufficiently. Consistent with the smaller lattice expansion (less anharmonicity),

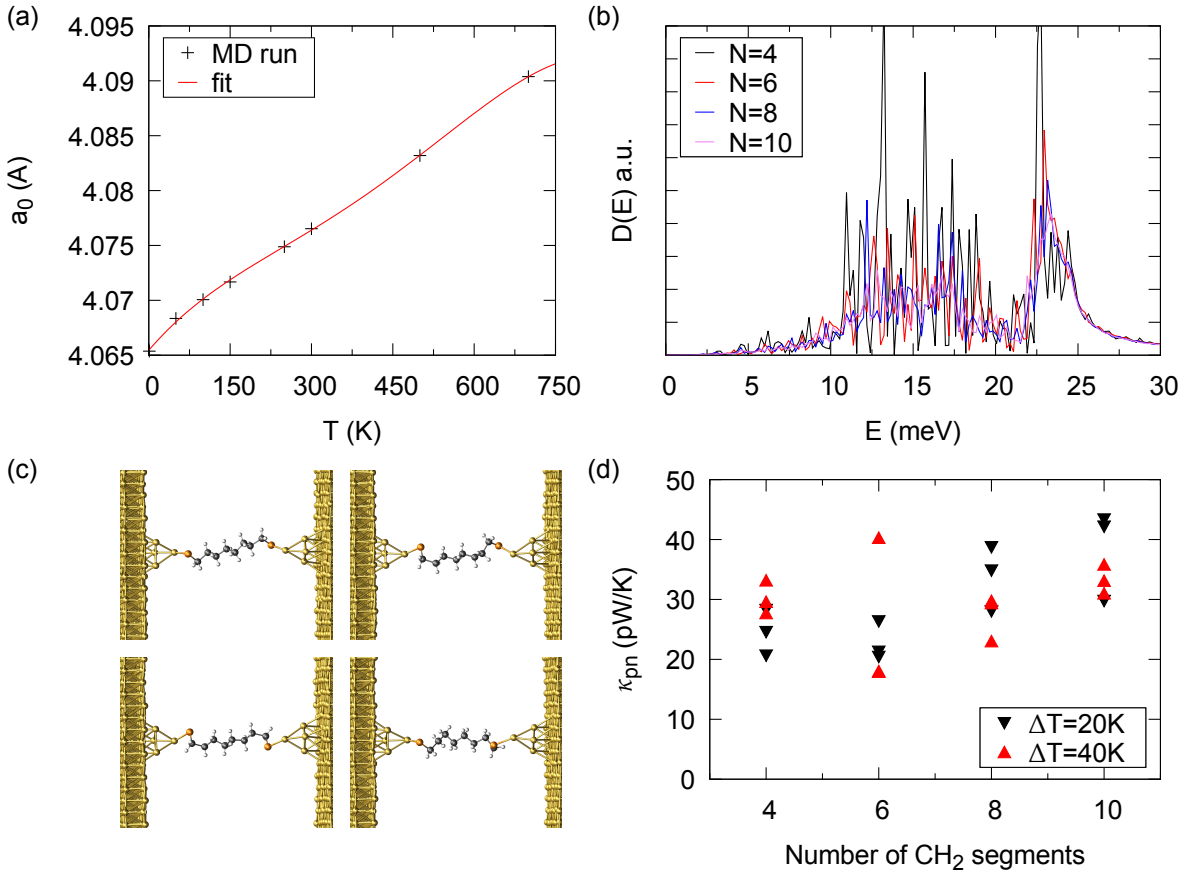

Figure 35. (a) Gold bulk lattice constant of the REAXFF potential as a function of the temperature. (b) Phonon density of states for different dimension $L = 2a_0(T)N$ of the simulation box. (c) Different geometrical configurations during the measurement are depicted for C8. (d) Thermal conductance as a function of the number of CH_2 segments for two different applied temperature gradients $\Delta T = 20$K (black) and 40K (red).

bigger finite size effects are observed in terms of a more "peaked" density of states for smaller simulation boxes.

In order to calculate the thermal conductance comparable to the ab-initio method, we use the central part of the DFT geometries as the starting point and attach the leads oriented along the (111) direction, such that the initial surface layers coincide. In this way we get similar geometries, nevertheless, due to temperature effects the junction is likely to be in a different strain condition. In transport direction, we consider six unit cells for the baths on each side, followed by one unit cell in which the thermostat is applied. These are enclosed by two rows of fixed atoms. Transverse to this direction we use 6 unit cells, oriented along the (-1-12) plane for the x-direction and along the (1-10) plane for the y-direction. In total the geometry consists of around 8000 atoms. The measurement is similar to that of the metallic contacts. We start by 1 ns of equilibration at 300 K, then increase the temperature for 1 ns in one lead to the applied temperature difference. After an additional equilibration for 1 ns, we start measuring for 5 ns. The timestep for C4 is 0.5 fs and 1 fs for C6-C10.

In Fig. 35(c) four representative snapshots of geometries during the measurement time are visualized for an alkane chain with 8 CH_2 segments. As an effect of temperature the alkane chain can exhibit different geometrical defects. Henceforth, the calculation of the thermal conductance at ambient temperatures is an average of several geometrical configurations, including chains with as well as without defects. Although here only shown for C8, this holds also for the other

molecules. The corresponding thermal conductance for two different temperature differences $\Delta T = 20, 40\mathrm{K}$ is plotted in Fig. 35(d) for C4-C10. First of all, notice that there is no significant difference related to the applied temperature gradient, so the linear response regime is justified. Overall the conductance ranges from 20-40 pW/K. This is smaller then the conductance ranges of the straight chain in different geometrical configurations studied in Sec. 4.1.2 but perfectly agrees with the results obtained for the defective chains in Sec. 4.1.3.2, especially for C4-C8. For C10 we noticed that, due to the mentioned inconsistencies in the boundary conditions and the expansion at finite temperatures, the geometry of one side of the lead changes from a tip or pyramid, to a blunt shape. This would correspond to a higher stress configuration for the alkane chain, or in analogy to the DFT studies to a lower probability of a geometrical defect. Indeed, the value for C10 is in closer correspondence to the DFT results of the straight chain. To conclude, we have pointed out the influence of geometrical variations upon the thermal conductance at room temperature. Furthermore, we find an excellent agreement between both methods, which confirms the phase-coherent nature of heat transport in this kind of system.

4.2 Benzene derivatives

In this section we study the impact of interference effects on the thermal conductance in molecular junctions. In particular we explore benzene- and OPE3-related molecules connected to Au electrodes, which is often the material of choice for the leads in such systems, and use amine anchoring groups. After a general introduction related to interfence effects in Sec. 4.2.1, we start with the benzene derivatives in Sec. 4.2.2 and analyze the influence of connecting the molecule in para and meta position. Moreover, we investigate the effect of single halogenides with different masses (F, Cl, Br, I), the variation related to additional substituents (Br), as well as the influence of alternating strain conditions. To understand the principles behind the occuring interferrence patterns we look at a simplified model. In Sec. 4.2.3 we additionally investigate similar topics in OPE3-based molecules.

4.2.1 Interference effects - introduction

While conventional attempts to perform manipulation of phonon heat conduction in bulk systems focused on incoherent transport mechanisms, due to the possibility to fabricate nanoscale devices and nanostructured materials, the interest to control heat currents in the coherent regime by making use of interference effects is growing [28]. Thus for instance, in the context of phononic structures the so-called superlattices have been introduced. Here one can tune the phonon band structure, phonon group velocity, and the related phonon density of states by means of wave interference effects [29, 229]. This strategy is limited by the quality of interfaces in terms of interface roughness and by the mean free path of the heat carriers. Due to these constraints the strategy is in general better applicable to systems, in which heat is carried by low-energy or equivalently long-wavelength phonons. However, if one assumes that atomically thin, single crystal planes can be manipulated at will, also higher-energy or short-wavelength phonons can in principle be affected, since structural length scales are of interatomic distance. Thus, Han *et al.* [230] theoretically proposed the suppression of heat transport using defect atom arrays embedded in a single crystal plane. To inhibit the heat flow, the authors exploited the destructive interference between two phonon paths. Resulting line shapes of the energy-dependent phonon transmission are indeed reminiscent of Fano resonances. Such Fano resonances are, in fact, a very general concept in nanostructured materials and occur in every system, in which a narrow discrete mode couples to a broad continuous spectrum [231]. Indeed, they have been reported in a great variety of systems ranging from quantum dots to photonic structures [232, 233, 234].

As compared to the inorganic materials discussed above, molecules offer an ideal platform to tailor structures at the single-atom level, and single-molecule junctions can be used to probe the coherent transport through the molecules [54]. In the field of molecular electronics interference effects have been studied with a special emphasis on their impact on the electronic transport properties of such junctions. Theoretically this topic has been explored extensively in the last two decades [235, 236, 237, 238, 239, 240, 241, 242, 243, 244, 245, 246, 247, 248, 249, 250, 251]. In particular, special attention has been devoted to the role of destructive interference [252, 253, 254, 255, 256] and to the determination of general rules governing the appearance of quantum interference effects in molecules with extended π-electron systems [257, 258, 259, 260]. Also different experimental reports in recent years have convincingly shown the influence of the quantum interference on electronic transport of molecular junctions, as illustrated by measurements of linear conductances and current-voltage characteristics [261, 262, 263, 264, 265, 266, 267, 268, 269, 270, 271, 272, 188]. When comparing electron and phonon transport, it needs to be kept in mind that for electrons the interference has to occur within some $k_\mathrm{B}T$ around $\mu \approx E_\mathrm{F}$, with the Fermi energy E_F, to get a measurable effect on the linear conductance. For phonons instead, Debye energies of typical metal electrodes are in the range of several ten meV so that already a sizable window of phonon energies contributes to thermal transport at room

temperature.

In the case of coherent phonon transport in molecular junctions the impact of interference effects is starting to be analyzed theoretically [273, 274]. For instance, Markussen [273] investigated the role of phonon interference in molecular junctions made of benzene and oligo-phenylene-ethynylene (OPE3) molecules attached to Si and graphene nanoribbon electrodes. Combining *ab initio* calculations for vibrational properties of the molecules with a phenomenological description of the leads and the molecule-lead couplings, Markussen found that the phonon transmission function for cross-conjugated molecules, like meta-connected benzene, exhibits destructive interference features very similar to those found for the corresponding electronic transport, which cause a reduction of the phononic thermal conductance with respect to the linearly conjugated analogues. On the other hand, Famili *et al.* [274] studied the phonon transport in alkane chains by means of a first-principles method based on DFT. In particular, they investigated the appearance of Fano resonances, when the alkanes are modified by the inclusion of certain side groups, so-called "Christmas trees". These resonances led to a reduction of the corresponding thermal conductance by a factor 2. However, alkanes are known to exhibit geometrical gauche defects that result in the localization of vibrational modes. These defects have been reported to reduce the thermal conductance by a similar magnitude [205], making it presumably difficult to discriminate between the effects of side-groups and gauche defects. In this sense, the study of stiff molecules like benzene derivatives may provide more conclusive results about the existence of interference effects.

4.2.2 Benzene

We start our discussion of the results with an analysis of single-molecule junctions based on the unsubstituted benzenediamine molecule. As shown in the upper part of Fig. 36(a), we consider contacts, where the amino (NH_2) group is attached to a single tip atom of the gold electrodes on each side both in the para and in the meta configuration. We will refer to this amino binding site on the gold also as "atop position" and note that these geometries are similar to those used in previous studies of electronic transport, mimicking typical binding geometries [115]. In Fig. 36(a) we show the results for the phononic transmission of these two binding configurations, computed with our ab-initio method, described in Sec. 2.2. The first thing to notice is that the transmission is only finite below approximately 20 meV, which corresponds to the maximum phonon energy possible in the gold electrode material. On the other hand, notice that although both transmission curves are different, which is reasonable due to the different geometrical configurations, we do not find any signature of destructive interference in the form of antiresonances. This is further confirmed by the results for the temperature dependence of the phononic thermal conductance, which we show in Fig. 36(b). In fact, both molecules exhibit similar thermal conductance values over the whole temperature range explored here.

The reason for the lack of destructive interference effects in these benzene-based junctions can be understood with the help of the work of Markussen [273]. Considering his semi-empirical results for phonon transport in benzene junctions with Si electrodes, he found that the lowest observable destructive interference features appear at energies around 40 meV. Since this energy is above the cut-off energy of gold, no effects are visible in our case.

These results raise the question, whether it is possible to observe interference effects in the phonon transport in junctions based on benzene derivatives with the standard Au leads. In the context of electronic transport it is known that interference features can be shifted in energy by introducing side groups [246], which have either electron-withdrawing or electron-donating character. The inclusion of such side groups moves the resonance features to lower or higher energies, respectively. Furthermore, the substituents can also break the symmetry of the molecule, leading to destructive interference in benzene junctions even for the para configuration of anchoring groups. Inspired by this idea, we shall analyze in what follows the effect of substituting a H

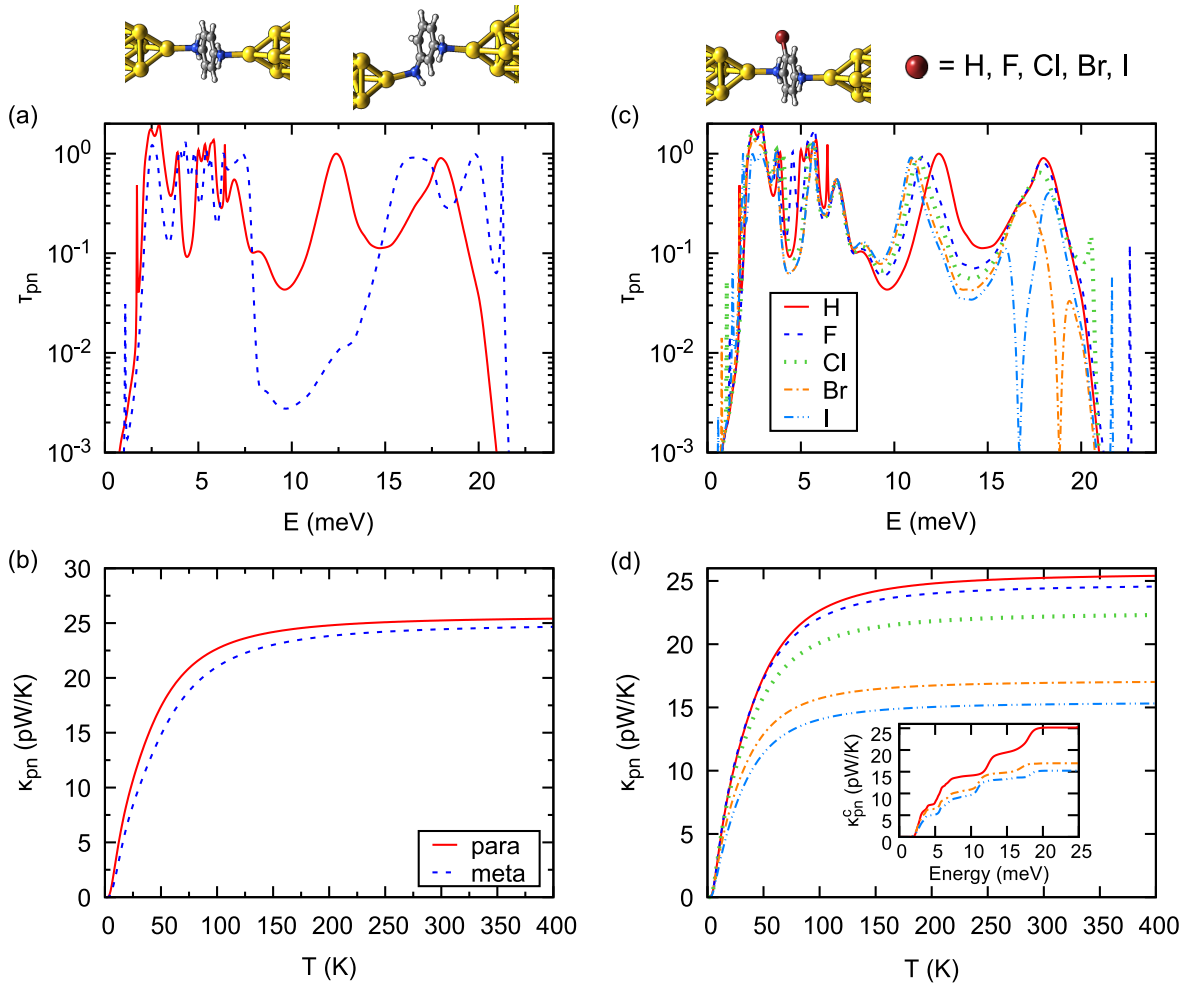

Figure 36. (a) Phonon transmission as a function of energy for the Au-benzenediamine-Au junctions shown above this panel for both para (left) and meta (right) binding configurations. (b) The corresponding phononic thermal conductance as a function of temperature. (c) Phonon transmission as a function of energy for Au-benzenediamine-Au junctions, where a H atom of the benzene molecule has been substituted by a halogen atom (X=F, Cl, Br, I), see upper part of the figure. (d) The corresponding phononic thermal conductance as a function of temperature for the different benzenediamine derivatives. The inset shows the room-temperature cumulative thermal conductance as a function of energy for the junctions with X=H, Br, I.

atom in the benzenediamine molecule by a heavier atom of mass m to tune the position of the resonance features. The basic idea is to try to shift the destructive resonances below the Debye energy of gold to observe a measurable effect on the thermal conductance.

With this idea in mind we consider the phonon transport in Au-benzenediamine-Au single-molecule junctions, where one of the H atoms of the benzene has been substituted by a halogen atom X=F, Cl, Br, I, as depicted in the upper part of Fig. 36(c). The naive expectation is that since the energy of a harmonic oscillator scales as $E \propto \sqrt{k/m}$, with k being the force constant, the resonance features should decrease in energy with increasing mass m of the substituent from F to I. This simple view is indeed confirmed by our ab-initio calculations of the phononic transmission, which are summarized in Fig. 36(c) for the substituted benzenediamine molecule in the para configuration. As one can see, there is a clear destructive interference feature for X=Br at an energy of around 19 meV. It is further shifted to lower energies for X=I, where it appears at around 16 meV. Additionally, we see that the peak at around 13 meV for the unsubstituted benzenediamine shifts to lower energies as the mass of the substituent increases, while the transmission for energies lower than 10 meV remains nearly unaffected. These results for the transmission have a clear impact on the phononic thermal conductance, see Fig. 36(d).

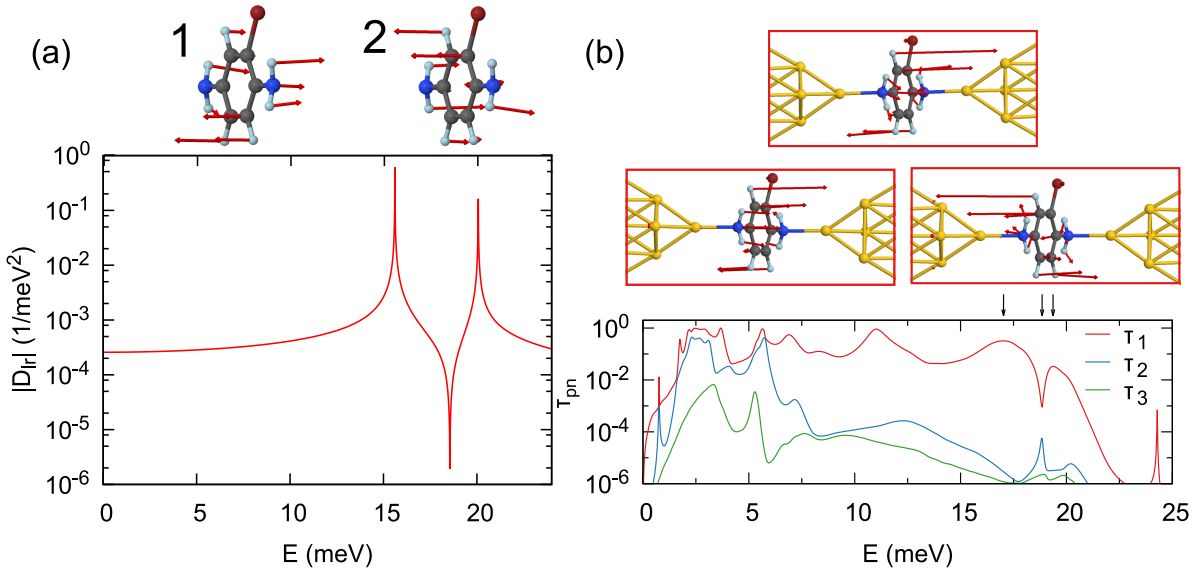

Figure 37. (a) In the upper part we visualize the two modes 1 and 2 that are responsible for the destructive interference feature at 19 meV in the benzenediamine molecule, substituted with X=Br. The first mode is at an energy of 15.61 meV and the second one at 20.07 meV. Since for both modes the arrows on the N atoms on the left and right sides point in the same direction, they interfere destructively. The graph below shows the calculated absolute value of the relevant Green's function element of the isolated molecule, taking into account in Eq. (4.2) only the modes 1 and 2 and using $\eta = 10^{-3}$ meV. (b) The three highest eigenchannel transmissions as a function of energy for a Au-2-bromo-1,4-diaminobenzene-Au junction. Above the graph, one can see the eigenchannels with the highest transmission for the three different energies from left to right of 17.03 meV, 18.85 meV, and 19.37 meV. The energies are selected by peaks of τ_1 in the transmission plot and are indicated by corresponding arrows.

Notice, in particular, that the thermal conductance decreases monotonically with the mass of the substituent, reaching in the case of X=I a reduction factor of 1.7 at room temperature, as compared with the unsubstituted benzene molecule.

To assess in a quantitative manner the impact of the antiresonances on the reduction of the thermal conductance upon the introduction of substituents, we show in the inset of Fig. 36(d) the room-temperature cumulative thermal conductance as a function of energy as defined in Eq. 2.20 for the Au-benzenediamine-Au junctions with X=H, Br, I. As one can see, the introduction of substituents actually modifies the phonon transport at all energies, but the change is particularly drastic at the energies at which the antiresonances occur. This illustrates that the destructive interference effects, induced by substituent atoms, play a key role in the reduction of the heat transport and can be used as a strategy to modify the thermal conductance.

In order to understand the origin of the destructive interference effect, discussed above for Br and I, we follow an argument based on the symmetry of the molecular orbitals developed for electron transport [257]. Since the structure of the transport formalism is almost identical for electrons and phonons, with the only difference arising from the equations of motion, this argument can be straightforwardly adapted to phonon transport. Assuming for simplicity only nearest neighbor couplings, the idea is as follows. If the molecule is attached to the left lead at position l with coupling constant k_{lL} and at position r with coupling constant k_{rR} to the right lead, then the transmission function can be expressed as

$$\tau_{\mathrm{pn}}(E) = \frac{\pi^2}{E^2} k_{\mathrm{lL}}^2 k_{\mathrm{rR}}^2 \rho_{\mathrm{L}}(E) \rho_{\mathrm{R}}(E) \left| D_{\mathrm{lr}}(E) \right|^2 . \tag{4.1}$$

Here $\rho_\alpha(E)$ is the local density of states at the lead atom $\alpha = \mathrm{L}, \mathrm{R}$ that is connected to the atom l, r of the molecule, respectively, and $D_{\mathrm{lr}}(E)$ is the lr-matrix element of the Green's function at

energy E. Let us assume that the typical embedding self-energies $\Pi_\alpha(E)$, which describe the coupling of the central junction part to the left and right electrodes[109, 4] and appear in the full expression for $D_{\rm lr}(E)$, can be neglected, which is for instance the case if molecule-lead couplings are not too strong. In this situation the Green's function entering in the previous equation can be approximated by the corresponding Green's function of the isolated molecule. It is given by the following spectral representation

$$D_{\rm lr}(E) = \sum_j \frac{C_{{\rm l}j} C^*_{{\rm r}j}}{(E+i\eta)^2 - E_j^2}, \tag{4.2}$$

where C_{nj} is the n-th component of the j-th eigenfunction or vibrational mode. Given the dynamical matrix $\boldsymbol{K}$, the eigenfunctions C_{nj} and angular momentum frequencies ω_j are obtained by solving the secular equation

$$\boldsymbol{K}\boldsymbol{C}_j = \omega_j^2 \boldsymbol{C}_j. \tag{4.3}$$

In the spectral representation in Eq. (4.2), η is a small imaginary part that prevents $D_{\rm lr}(E)$ from diverging at $E \to E_j$, and $E_j = \hbar\omega_j$ is the energy of the j-th vibrational mode of the isolated molecule. As discussed in Ref. [257] for molecular junctions and in Ref. [275] for mesoscopic systems, a destructive interference occurs between vibrational modes j that exhibit the same sign of the product $C_{{\rm l}j}C^*_{{\rm r}j}$, or more pictorially, the same parity of vibrational modes at the lead-connecting molecular sites. This conclusion is obvious from the general form of the Green's function in Eq. (4.2). If the embedding self-energies $\Pi_\alpha(E)$ are taken into account, they may lead to renormalizations of level positions and hence antiresonance peaks. They are also important to describe level broadenings, which are mimicked in Eq. (4.2) by η, and hence to avoid any divergences of the transmission in Eq. (4.1) at resonance positions $E = E_j$.

Let us now apply these ideas to understand the antiresonance that appears at around 19 meV in the transmission function for the benzenediamine junction with the substituent X=Br, see Fig. 36(c). For this purpose we first analyzed the vibrational modes of the isolated molecule within DFT and identified the two modes at 15.61 meV and 20.07 meV, which are shown in the upper part of Fig. 37(a). Taking into account only these two modes in the sum over j in Eq. (4.2), we display in this figure also the corresponding absolute value of $D_{\rm lr}(E)$. Here the connection to the leads has been assumed to be established only at the N atoms and the coefficients C_{nj} have been taken from the calculations of the isolated molecule. Since these two modes exhibit the same oscillation direction on the N atoms, the products $C_{{\rm l}1}C^*_{{\rm r}1}$ and $C_{{\rm l}2}C^*_{{\rm r}2}$ have the same sign, and the modes 1 and 2 are expected to interfere destructively. This is confirmed by the behavior of $|D_{\rm lr}(E)|$ in Fig. 37(a), which exhibits two peaks at the energies of the two modes and a minimum at around 19 meV, energetically located between these two modes. The position of the minimum is in good agreement with the minimum in the transmission curve in Fig. 36(c). Let us mention that the same considerations apply for the molecule with X=I, where we find two modes of similar characteristics at energies around 14.7 and 19.5 meV.

To complete the analysis we show in Fig. 37(b) the energy dependence of the three largest eigenchannel transmissions for this molecule. In this figure the most transmissive eigenchannel are displayed for three different energies. These dominate the phonon transport in this energy range. Clearly visible all the eigenchannels exhibit indeed a character that resembles the out-of-plane character (with respect to the molecular plane) of the two vibrational modes of the free molecule. Below the interference, one would naively expect the eigenchannel to resemble the first eigenmode of the free molecule, while above it could be related to the second mode of the free molecule. However, and in spite of the fact that the second mode of the free molecule and the highest eigenmode are similar, a simple one-to-one correspondence cannot be established, especially for the first eigenmode. This is partially due to the perturbation of the molecular modes due to the presence of the metal atoms. In addition, since both molecular vibrations are close in energy, the eigenchannel is actually a mixture of both them with different, non-negligible weights. Moreover, in the static picture of the eigenchannel shown in Fig. 37(b), one can see

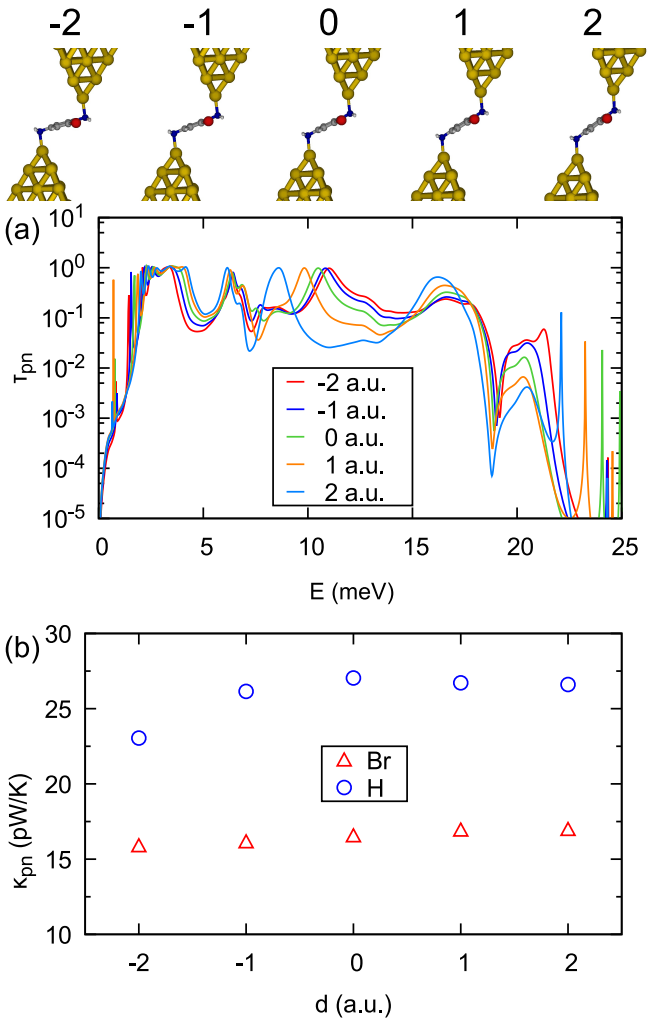

Figure 38. (a) Phonon transmission as a function of energy for the molecular junctions shown above this panel, which have been created by compression and stretching of the junction with "0 a.u.". (b) Comparison of the thermal conductance between the junction shown in (a) and the unsubstituted benzene junction upon elongation.

a jump of π in the phase of molecular motion as compared to the Au reference atoms, which is reflected by the fact that the arrows on the molecule point in opposite directions at energies above and below the antiresonance. This jump in the phase is a well-known phenomenon that accompanies destructive interference of various properties in the electronic transport [248, 244] and, in general, in the Fano model [276].

One may wonder whether the antiresonances, resulting from destructive interference, survive upon the elongation of the molecular junctions. We have investigated this aspect for the junctions with the benzene derivatives studied in Fig. 36(c) and found that the appearance of antiresonances is quite robust against stretching or compression, outlined in Fig. 38(a). The junctions were realized by stretching and compressing the original one up to 2 a.u.. Whereas we see small shifts in the resonance peaks due to geometrical variations, the interference pattern persists in all cases. This is indeed expected since, as we have already mentioned, the antiresonance is caused by the interaction of two vibrational modes within the molecule, and is therefore not strongly influenced by variations of the distance between the electrodes. For a complete story, the thermal conductance of the various strain conditions for the benzene bromide have to be compared to the one without substituent, which is shown in Fig. 38(b). Although the different boundary conditions influences the absolute value of κ_{pn} slightly, for all considered configurations the effect of the anti-resonance dominates the thermal conductance.

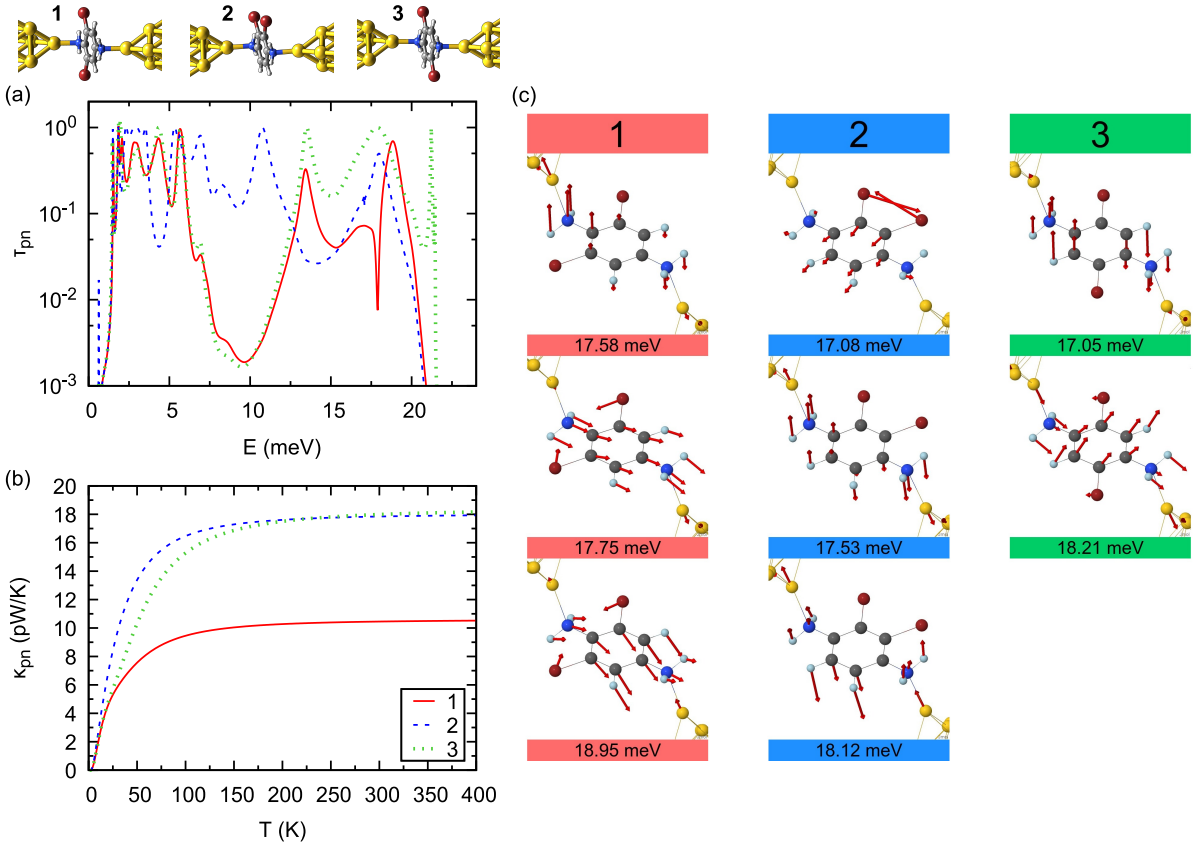

Figure 39. (a) Phonon transmission as a function of energy for the three molecular junctions shown above this panel, where two H atoms of the benzenediamine molecule have been replaced by two Br atoms. (b) The corresponding temperature dependence of the phononic thermal conductance. (c) All vibrational modes in the central region of the three molecular junctions in the energy range between 15 and 20 meV

Following the analogy with electronic systems, we analyze now, how the inclusion of additional substituents modifies the interference patterns [260]. For this purpose we investigate the phonon transport through benzenediamine junctions, if two H atoms are replaced by two Br atoms. Moreover we study the influence of the exact position, where these Br atoms are incorporated, and examine the three molecular junctions shown in the upper part of Fig. 39. All vibrational modes between 15 and 20 meV in the central region of the corresponding junctions are shown in Fig. 39(c).

The results for the phonon transmission are displayed in Fig. 39(a). As one can see, for molecule 1 a destructive interference antiresonance appears at about 17 meV. The origin of this feature is, as for the previous compounds, the interference between two modes that lie close in energy. These are the modes with energies of 17.75 and 18.95 meV in the left column of Fig. 39(c) that show the same parity on the terminal N atoms of the molecule. The difference with respect to the singly-substituted molecules discussed above is that these modes have no analogues in the isolated molecule. Instead they are hybrid modes in the sense that they also involve vibrations of the gold atoms in the electrodes. Additionally, a reduced transmission peak at 12.5 meV arises, which is due to a localized mode that is asymmetrically coupled to the electrodes. Interestingly, the other two molecules 2 and 3 do not exhibit any pronounced antiresonance, resulting from destructive interference, see Fig. 39(a), which we attribute to the lack of the necessary symmetry of the vibrational modes on the terminal N atoms, see Fig. 39(c). This shows that not only the masses of the substituents play a role, but also the exact position, where they are introduced. The changes in the transmission are reflected in the corresponding thermal conductance results. As we see in Fig. 39(b), while molecule 1 exhibits a largely reduced

thermal conductance at room temperature as compared to both the singly substituted case and the unsubstituted benzenediamine, molecules 2 and 3 exhibit conductance values that are similar to those of the singly substituted case.

4.2.3 OPE3

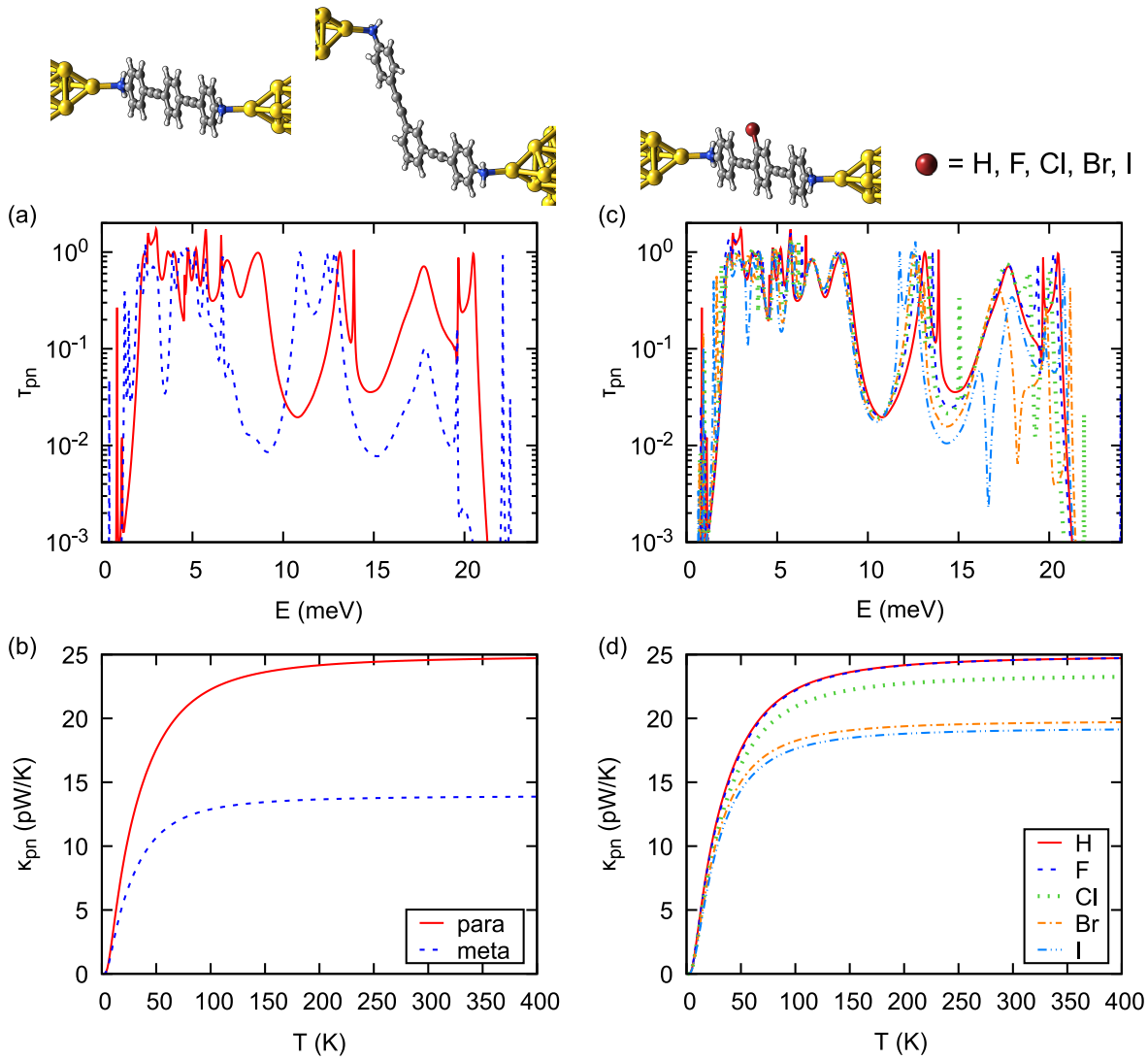

Figure 40. (a) Phonon transmission as a function of energy for the Au-OPE3-Au junctions shown above this panel for both para (left) and meta (right) binding configurations at the central benzene ring. (b) The corresponding phononic thermal conductance as a function of temperature. (c) Phonon transmission as a function of energy for Au-para-OPE3-Au junctions, where a H atom of the central benzene ring has been substituted by a halogen atom (X=F, Cl, Br, I), see plot above this panel. (d) The corresponding phononic thermal conductance as a function of temperature for the different para-OPE3 derivatives.

Now we show that the basic concepts discussed above also apply to other, more complex molecules. For this purpose, we consider OPE3. This molecule has been analyzed in the context of phonon transport in Ref. [273] with the help of semi-empirical methods and considering Si as well as graphene-nanoribbon electrodes. First we discuss the influence of the binding configuration, by examining para- vs. meta-OPE3, as shown in the upper part of Fig. 40(a). In this case our ab-initio results for the phonon transmission, which are displayed in Fig. 40(a), show that for meta-OPE3 several resonance peaks at energies below 15 meV appear shifted to lower

energies as compared to para-OPE3, while there is a pronounced decrease of the transmission for the meta-OPE3 above. The strong suppression of the transmission at around 18 meV is due to an interference effect, in which two quasi-degenerate modes are involved, as explained in Ref. [273]. In total the meta-OPE3 thermal conductance is reduced by a factor of 2, as compared to para-OPE3.

As in the case of benzene, the thermal conductance of Au-OPE3-Au junctions can be tuned by substituting one H atom in the central benzene ring with a halogen atom, as sketched in the upper part of Fig. 40(c). Similar to benzenediamine in Fig. 36(c), one can see in Fig. 40(c) that the phonon transmission exhibits an antiresonance at energies around 15-20 meV for the substituents Br and I, but now this feature also appears for Cl. Again the occurrence of destructive interferences below the Debye energy of gold leads to a suppression of the corresponding thermal conductance, as we show in Fig. 40(d). We find a monotonically decreasing thermal conductance with increasing mass of the substituent. As in the case of the benzene derivatives this behavior is due to the fact that, upon introducing the substituents, the energies of the vibrational modes decrease and the antiresonances, resulting from the interference effects, are redshifted at the same time. Thus, since the contribution of a vibrational mode scales with its energy, see Eq. 2.17, κ_{pn} is reduced upon increasing mass of the substituents.

Let us mention that we are not aware that the exact OPE3 compounds, shown in Fig. 40(c), have been synthesized. But closely related molecules exist, in which the central ring of an OPE3-diamine has been modified, among others, by the inclusion of several fluorine atoms and which have been studied in the context of single-molecule junction experiments [277]. So, we think that there should not be any fundamental problem to synthesize the compounds discussed in this work. In this respect, it is also worth stressing that our DFT calculations demonstrate that these molecules are indeed stable.

To complete the discussion of our results on phonon heat transport, it is important to emphasize that in all the molecular junctions investigated in this work, the room-temperature thermal conductance is dominated by the contribution of phonons. Therefore the impact of the interference effects discussed here should be, in principle, amenable to measurement. This point is discussed in detail in Appendix E, where we present our results for the electronic contribution to the thermal conductance.

4.3 C_{60}

The goal of this section is to critically evaluate the thermoelectric device efficiency of a single-molecule junction. For this purpose, we present here a detailed study of the role of different heat carriers in both the thermal conductance and the figure of merit of monomer and dimer C_{60} molecular junctions. In particular, we compute the contribution of both electrons and phonons to the different transport properties in Sec. 4.3.2., whereas in Sec. 2.7 the effect of a thermally driven photonic flux is additionally considered.

4.3.1 Thermoelectric figure of merit - introduction

The phonon contribution to the thermal conductance plays a fundamental role, when assessing the performance of molecular junctions as thermoelectric devices. This performance is characterized by the so-called figure of merit ZT, which is given by a combination of several transport quantities as follows [278]

$$ZT = \frac{GS^2T}{\kappa} = \frac{Z_{\mathrm{el}}T}{1 + \kappa_{\mathrm{other}}/\kappa_{\mathrm{el}}}. \tag{4.4}$$

Here, G is the electrical conductance, S the thermopower, T the absolute temperature, and κ the thermal conductance. Strictly speaking, this thermal conductance should include all possible contributions, and it can be written as $\kappa = \kappa_{\mathrm{el}} + \kappa_{\mathrm{other}}$, where κ_{el} is the electronic contribution and κ_{other} includes the contributions of other heat carriers like that of phonons and photons. By bringing Eq. (4.4) into the form on the right hand side using $Z_{\mathrm{el}}T = GS^2T/\kappa_{\mathrm{el}}$, it is obvious that any additional heat transport contribution (beyond electrons) will be detrimental for the thermoelectric performance, since ZT needs to be maximized. Therefore, the experimental and theoretical determination of κ_{other} is crucial to critically evaluate, whether molecular junctions can potentially operate as efficient nanoscale thermoelectric devices.

The most obvious additional contribution to the heat conductance in molecular junctions is that of phonons, a topic that is currently attracting a lot of attention. For a recent review, we recommend Ref. [193]. However, photons can also give a significant contribution to the total heat conductance. Molecular junctions actually constitute nano-scale gaps between metal surfaces, bridged by few or single molecules. Thus, even if the experiments are carried out in ultra-high vacuum conditions, one should also consider the contribution of thermal radiation or photon tunneling. It has been understood that when two bodies are brought sufficiently close together (with a separation below the thermal wavelength, which is 9.6 μm at room temperature), near-field contributions in the form of evanescent waves dominate the radiative heat transfer and lead to a huge enhancement of the radiative thermal conductance [121]. This NFRHT can exceed by orders of magnitude the limit set by the Stefan-Boltzmann law for black bodies, see Ref. [279] for a recent review. These ideas have been experimentally verified in recent years, and advances in nanothermometry have even made possible to explore thermal radiation in the extreme near-field regime, where objects are separated by gaps of a few nanometers and even below [280, 281, 38, 282, 283]. This aspect of photonic heat conduction has traditionally been ignored thus far in the field of molecular electronics.

The main goal of this work is to rigorously compute the contribution κ_{pn} of phonons to both the thermal conductance and the figure of merit in C_{60}-based single-molecule junctions using parameter-free ab-initio electronic structure methods. But also the photonic part κ_{pt} will be estimated using simple models for the molecular junction geometries within the framework of fluctuational electrodynamics. We will thus ultimately consider $\kappa = \kappa_{\mathrm{el}} + \kappa_{\mathrm{pn}} + \kappa_{\mathrm{pt}}$ in the following, i.e., a thermal conductance κ consisting of electronic (el), phononic (pn), and photonic (pt) parts.

The fullerene C_{60} is a test-bed molecule for molecular electronics and its electrical transport properties have been extensively investigated both experimentally [284, 285, 286, 287, 288,

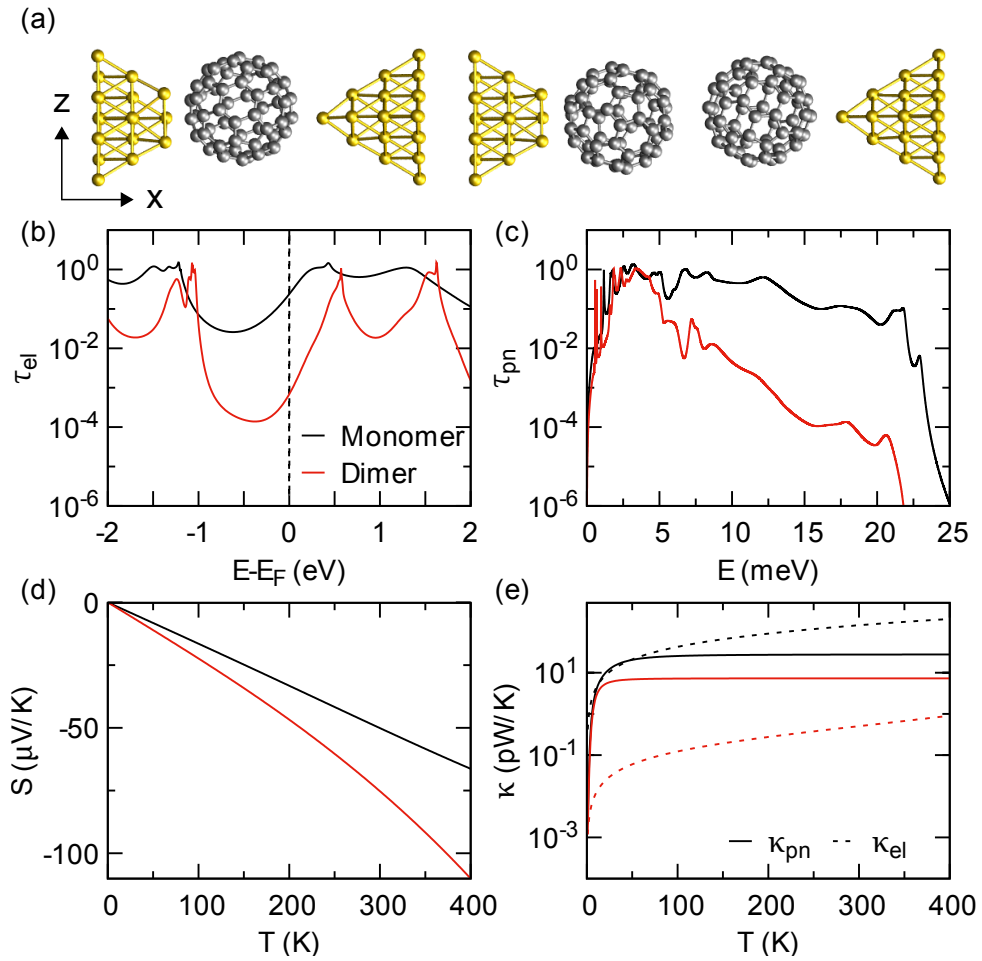

Figure 41. (a) Equilibrium geometries of C_{60} monomer and C_{60} dimer junctions. The molecules are bonded to blunt and sharp Au electrodes on the left and right. These geometries correspond to the minimum of the total energy with respect to the distance d between the electrodes. We call this particular separation for the equilibrium geometry d_0, see illustration in Fig. 43(a). (b) Electronic transmission as a function of energy, measured with respect to the Fermi level, for the two geometries shown in panel (a). (c) Phonon transmissions as a function of energy. (d) Thermopower of the two junctions as a function of temperature. (e) Electronic and phononic contributions to the heat conductance as a function of temperature for both junctions. Data referring to the monomer is shown in black, those of the dimer in red.

289, 290, 291, 292] and theoretically [288, 290, 291, 292, 293, 294, 295, 296, 297, 298, 299, 300, 301, 250]. Also in the context of thermoelectricity, C_{60}-based single-molecule junctions have been analyzed and several groups have reported room-temperature thermopower measurements [302, 303, 304]. In particular, Evangeli *et al.* [303] employed a STM setup to report simultaneous measurements of the conductance and thermopower in "single-C_{60}" or monomer molecular junctions with Au electrodes. They showed that these junctions can exhibit thermopower values ranging from -40 to 0 μV/K, depending of the contact details, with a mean value of -18 μV/K. The findings agree well with theoretical expectations that predict that these negative values are due to charge transport that is dominated by the lowest unoccupied molecular orbital (LUMO) [301]. Moreover, these authors were able to pick up C_{60} molecules with the STM tip and subsequently use them to contact another individual C_{60} molecule, forming in this way molecular junctions with a C_{60} dimer bridging the gap between the Au electrodes. These "two-C_{60}" or dimer molecular junctions were shown to exhibit negative thermopower values of up to -72 μV/K with an average value of -33 μV/K. This almost doubles the magnitude observed in the

monomer junctions, as it is generally expected for increasing molecular length in the off-resonant transport regime [305]. These results, together with first-principles transport calculations, led the authors to suggest that stacks of C_{60} molecules could provide a way to achieve high ZT values (even above 1), making fullerene-based junctions very promising for thermoelectric applications. However, it is worth stressing that this appealing suggestion was made without taking into account the phonon contribution in the ab-initio calculations and without measuring the thermal conductance. Indeed experimental setups were until recently not sensitive enough to measure κ at the atomic scale, and single-molecule junctions have yet to be examined with newly developed tools [2]. Thus, this interesting suggestion still has to stand careful theoretical and experimental tests with access to all the major quantities determining the figure of merit. In this work we try to fill this gap from the theoretical point of view.

4.3.2 Electron + phonon transport

We start our discussion of the results by considering the geometries shown in Fig. 41(a) for an Au-C_{60}-Au and an Au-C_{60}-C_{60}-Au junction, which will be hereafter referred to as monomer and dimer junctions, respectively. In these particular geometries, the molecules make contact to three Au atoms of a blunt tip on the left, while they are bonded to a single Au atom of an atomically sharp tip at the right Au electrode. This asymmetric situation is meant to mimic the geometries realized in the STM experiments of Ref. [303], in which one of the electrodes is an Au surface and the other one an Au STM tip. Let us stress that these geometries were obtained by minimizing the total energy of the junctions as a function of the electrode separation d, yielding the distance d_0. The distances d and d_0 are also visualized in Fig. 43(a). Using a coordinate system, oriented as depicted in Fig. 41, we find that the closest Au-C separation along the x-axis is roughly 1.8 Å from the blunt tip and 2.2 Å from the sharp tip. The x-axis separation between the two C_{60} molecules in the dimer junction is approximately 3.0 Å. In Fig. 41(b)-(e) we summarize the thermoelectric transport properties for these two junctions by showing the electronic transmission as a function of energy, the corresponding phononic transmission, the thermopower as a function of temperature, and the electronic and phononic contributions to the heat conductance as a function of temperature.

For these blunt-sharp junctions, the electrical conductance is $0.23G_0$ for the monomer and $7.1\times10^{-4}G_0$ for the dimer. These values are close to the experimental values found in Ref. [303], where mean values of $0.1G_0$ and $1.8\times10^{-3}G_0$ were reported for the monomer and dimer junctions, respectively. Notice that in both cases the electronic transmission at the Fermi energy is determined by the LUMO of the molecules, as it has been reported in numerous studies, see for instance Ref. [301] and references therein.

With respect to the phononic transmission, one can see in Fig. 41(c) that the phonon conduction is dominated by low-lying vibrational modes with energies $E < 10$ meV. Let us recall that the Debye energy of the metal electrodes sets an upper limit for the energy of the vibrational modes that can contribute to the transport, which in our case is around 20 meV [109]. However, in the range between 10 and 20 meV there are no significant contributions to the phonon thermal conductance, which we attribute to the weak metal-molecule coupling for the modes in this energy range.

Turning now to the thermopower, we see in Fig. 41(d) that it approximately follows a linear dependence on temperature, as expected from the low-temperature expression in Eq. (2.105). In particular, the room-temperature thermopower has a value of -49.6 μV/K for the monomer and -75.3 μV/K for the dimer junction. The negative values are due to the fact that the electronic transport is dominated in both cases by the LUMO, meaning that electric conduction is electron-like. Notice also that the thermopower value for the dimer junction almost doubles that of the monomer, similar to what was observed in Ref. [303], while the absolute values are somewhat larger than those reported experimentally.

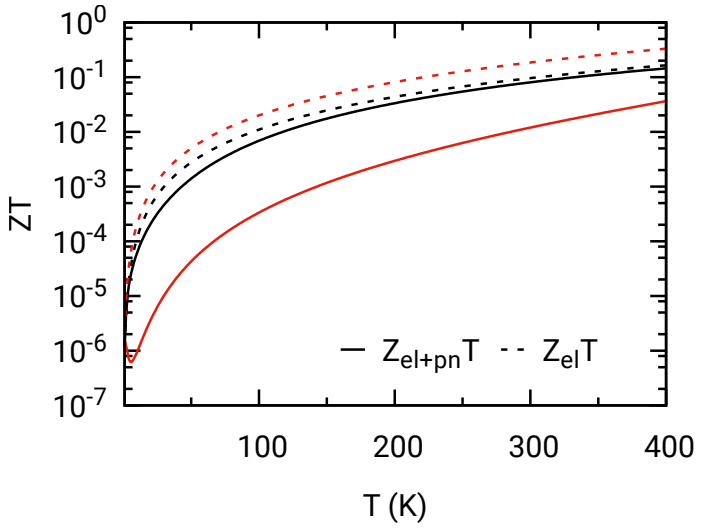

Figure 42. Figure of merit ZT as a function of temperature for the two geometries shown in Fig. 41(a). Black curves are for the monomer junction, while red ones are for the dimer. The solid lines correspond to $Z_{\mathrm{el+pn}}T$, including both the electronic and phononic contributions to the heat conductance, $\kappa = \kappa_{\mathrm{el}} + \kappa_{\mathrm{pn}}$, while the dashed lines correspond to $Z_{\mathrm{el}}T$, including only the electronic one, $\kappa = \kappa_{\mathrm{el}}$.

The temperature dependence of the different contributions to the heat conductance, displayed in Fig. 41(e), shows that both junctions behave qualitatively different, especially at room temperature. In the monomer junction the room-temperature electronic thermal conductance $\kappa_{\mathrm{el}} = 142.0$ pW/K, which is very close to the value expected from the Wiedemann-Franz law, dominates over the phononic one, $\kappa_{\mathrm{pn}} = 25.5$ pW/K. At the contrary, for the dimer junction the phononic contribution $\kappa_{\mathrm{pn}} = 7.3$ pW/K dominates the thermal conductance and the electrons give an insignificant contribution of $\kappa_{\mathrm{el}} = 0.5$ pW/K. Notice also that the total thermal conductance at room temperature is about 20 times larger for the monomer case than for the dimer case, which is mainly due to a dramatic decrease in the electronic contribution for the latter. For the sake of comparison, it is worth mentioning that we found in Ref. [4] that alkane-based chains of varying length exhibit phononic thermal conductance values ranging from 15 to 45 pW/K. Our results for these blunt-sharp C_{60} junctions show that there is a change in the dominant heat carriers as a function of the number of C_{60} molecules. This has a crucial impact on the figure of merit, as we proceed to discuss.

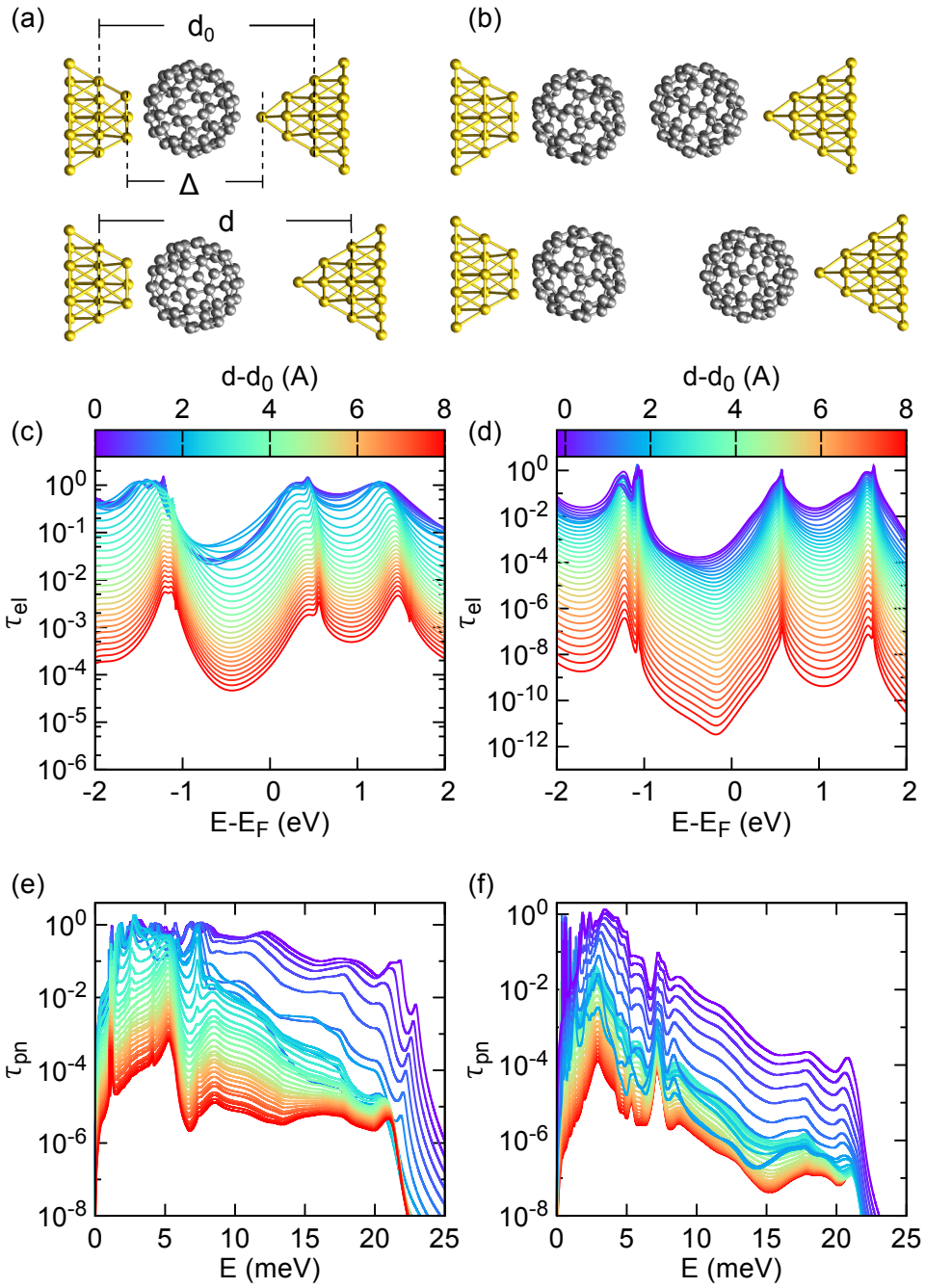

Figure 43. Evolution of the electronic and phononic transmissions with the elongation of the junctions in Fig. 41. (a) Geometries of the monomer junction. The upper geometry is the equilibrium geometry, already displayed in Fig. 41, while the lower junction is stretched. The distance d is measured between Au layers of the electrodes that are held fixed in the geometry optimization process, and d_0 is the separation for the equilibrium geometry. The gap distance Δ between the outer atoms of the Au electrodes that contact the molecules is somewhat shorter. (b) Same as in (a) but for the dimer junction. (c) Evolution of the electronic transmission of the monomer contact upon stretching as a function of the energy that is measured with respect to the Fermi energy. (d) The same as in panel (c) but for the dimer junction. (e) The corresponding evolution of the phononic transmission for the monomer junction. (f) The same as in panel (e) but for the dimer junction. We determine elongations as $d - d_0$, and plot the corresponding energy-dependent transmission curves in different colors as indicated by the color scale bar.

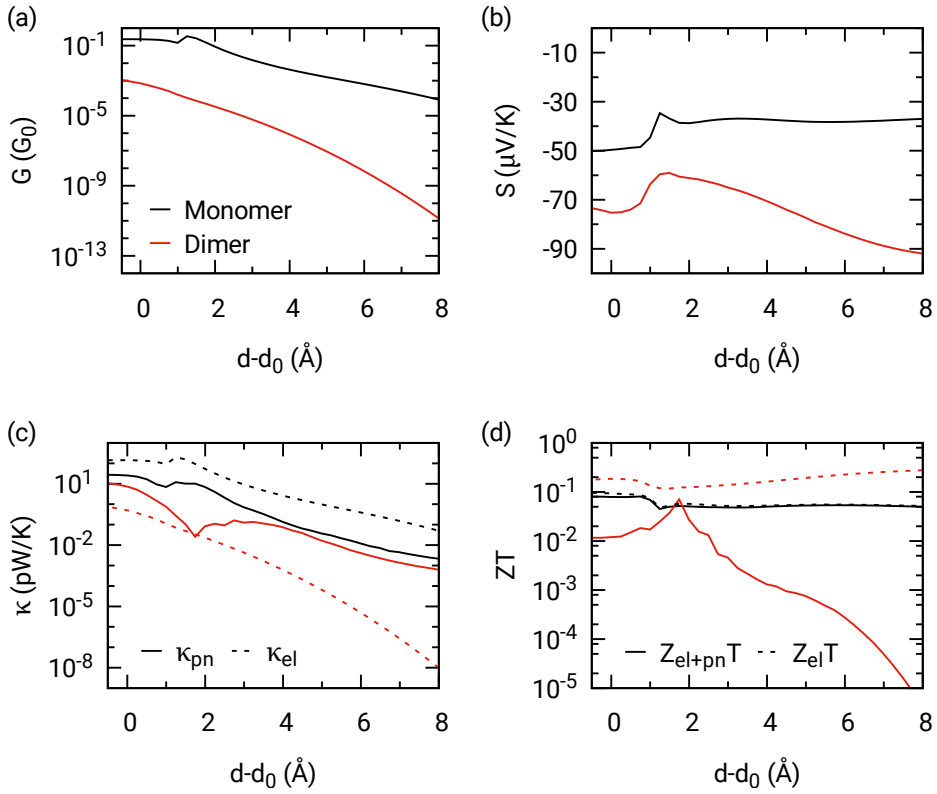

Figure 44. Transport coefficients at $T = 300$ K as a function of the distance $d-d_0$. The results are obtained from the transmission functions shown in Fig. 43. (a) Electrical conductance, (b) thermopower, (c) electronic and phononic thermal conductance, and (d) the corresponding figures of merit $Z_{\mathrm{el+pn}}T$ and $Z_{\mathrm{el}}T$. In all panels, black lines correspond to the monomer junction and red lines to the dimer junction.

Results for the figure of merit ZT, see Eq. (4.4), are shown in Fig. 42. There we depict the evolution of $Z_{\mathrm{el+pn}}T$ with temperature, taking into account both the electronic and phononic contributions to the thermal conductance, and $Z_{\mathrm{el}}T$, taking into account only the electronic contribution. The first thing to notice is that at room temperature the monomer junction reaches a value of $Z_{\mathrm{el}}T = 0.093$, which is only slightly reduced to $Z_{\mathrm{el+pn}}T = 0.079$ by the phononic contribution to the thermal transport. However, in the dimer case the room-temperature value $Z_{\mathrm{el}}T = 0.18$ is strongly reduced by the phonon heat conduction to $Z_{\mathrm{el+pn}}T = 0.012$. Exploiting the Wiedemann-Franz law in Eq. (2.106), which we find to be well obeyed, we can write $ZT \approx S^2/[L_0(1+\kappa_{\mathrm{other}}/\kappa_{\mathrm{el}})]$. With this relation the ZT values of the dimer junction can be interpreted as follows. Neglecting κ_{other}, the increase in $Z_{\mathrm{el}}T$ for the dimer junction is due to the increase of the thermopower as compared with the monomer. Setting $\kappa_{\mathrm{other}} = \kappa_{\mathrm{pn}}$, we see from Fig. 41 that the phonon thermal conductance of the dimer is slightly lower than those of the monomer. But due to the much stronger decrease of the electrical conductance for two C_{60} as compared to a single one, leading to a corresponding reduction of κ_{el} via the Wiedemann-Franz law, the ratio $\kappa_{\mathrm{pn}}/\kappa_{\mathrm{el}}$ and the denominator $L_0(1+\kappa_{\mathrm{pn}}/\kappa_{\mathrm{el}})$ get large, resulting in a pronounced suppression of $Z_{\mathrm{el+pn}}T$ for the dimer. Thus, this first example of blunt-sharp monomer and dimer junctions indicates that because of the important contribution of phonon conduction to the thermal transport, the appealing suggestion of Ref. [303] that high ZT values may be achieved by stacking C_{60} molecules, as discussed in the introduction, is not backed up by our calculations.

To test the robustness of the main conclusions so far, especially the strong reduction of $Z_{\mathrm{el+pn}}T$ as compared to $Z_{\mathrm{el}}T$ for the dimer junction, we have studied the role of strain in the different transport properties. For this purpose, and in order to mimic the STM experiments of Ref. [303],

Table 2. Gap between the gold electrodes Δ and room temperature values of the different transport properties for the three types of monomer and dimer equilibrium geometries with $d = d_0$ of Figs. 41, 45, 47. The distances d, d_0, Δ are defined in Fig. 43.

junction	Δ (nm)	G (G_0)	S (μV/K)	κ_{el} (pW/K)	κ_{ph} (pW/K)	$Z_{el}T$	$Z_{el+pn}T$
m, b-s	1.12	0.23	-49.6	142.0	25.5	0.093	0.079
d, b-s	2.12	7.1×10^{-4}	-75.3	0.5	7.3	0.185	0.012
m, s-s	1.18	0.11	-57.4	68.6	20.0	0.129	0.100
d, s-s	2.18	1.3×10^{-4}	-189.2	0.1	7.4	0.963	0.014
m, b-b	1.11	1.08	-41.9	572.7	46.3	0.077	0.071
d, b-b	1.91	2.3×10^{-3}	-96.9	1.8	7.0	0.273	0.057

we simulated the stretching and compression of the junctions shown in Fig. 41. The evolutions of the electronic and phononic transmissions for the monomer and dimer junctions are shown in Fig. 43. Here, the different curves correspond to different distances d between the electrodes, measured with respect to the distance in the equilibrium geometries d_0, as defined in Fig. 43(a). The thermoelectric transport properties G, S, κ and ZT are shown in Fig. 44 as a function of $d - d_0$. As one can see in Fig. 44(a), the electrical conductance exhibits an exponential decay both for the monomer and the dimer, as expected, when the junctions break and enter the tunneling regime. At all distances, G is much lower for the dimer than for the monomer, as expected for off-resonant transport (see for instance the electronic transmissions in Fig. 43(c,d)). In this regime the thermopower remains relatively constant, see Fig. 44(b), and for any distance the value for the dimer junction roughly doubles that of the monomer junction. With respect to the thermal conductance, both electronic and phononic contributions decay monotonically in the tunneling regime. And, like in the equilibrium geometry, we find that while for the monomer the electrons determine the thermal transport, in the dimer case the phonons dominate at almost all distances due to the largely reduced electronic thermal conductance of the dimer junctions. This fact is reflected in the behavior of $Z_{el+pn}T$ for both junctions, see Fig. 44(d), which is dictated by the electronic thermal conductance in the monomer case during the whole stretching process, while it is clearly limited by the phononic thermal conductance in the dimer junction. In other words, the main conclusion of the previous paragraph – that ZT values of dimer junctions are small due to phonon heat conduction – holds for the whole elongation process from the contact to the deep tunneling regime.

For completeness, let us now consider the role of the binding geometry. In particular, we now proceed to discuss the results for the equilibrium geometries shown in Fig. 45(a), where the molecules are bonded to both Au electrodes through atomically sharp tips. This kind of symmetric geometry is more likely to be realized in a break-junction configuration like that of Ref. [287]. The results for the different transport properties G, S, κ_{el} and κ_{pn} are qualitatively similar to those of the blunt-sharp geometries discussed above. All the room temperature values of these properties are summarized in Table 2 together with the derived $Z_{el}T$ and $Z_{el+pn}T$ values. The main difference to the blunt-sharp geometries is the fact that the electronic transmission does not follow a Lorentzian-like shape around the Fermi energy, see Fig. 45(b). This peculiar energy dependence is the result of a quantum interference and its origin has been explained in detail in Ref. [250]. This quantum interference leads to a rather steep transmission at the Fermi energy, which is in turn responsible for the particularly large values of the thermopower for these kind of binding geometries, see Fig. 45(d). The phononic thermal conductance in Fig. 45(e) is again determined by the transmission at energies below 10 meV, as visible in Fig. 45(c). Finally, κ_{el} in Fig. 45(e) is larger than κ_{pn} at $T = 300$ K for the monomer junction. This behavior is reversed for the dimer junction, where $\kappa_{pn} \gg \kappa_{el}$.

Thus, as in the case of the blunt-sharp geometries above, the room temperature thermal conductance is dominated by the electronic contribution in the monomer case, while phonon transport dictates the total value of the thermal conductance in the dimer case. This is reflected

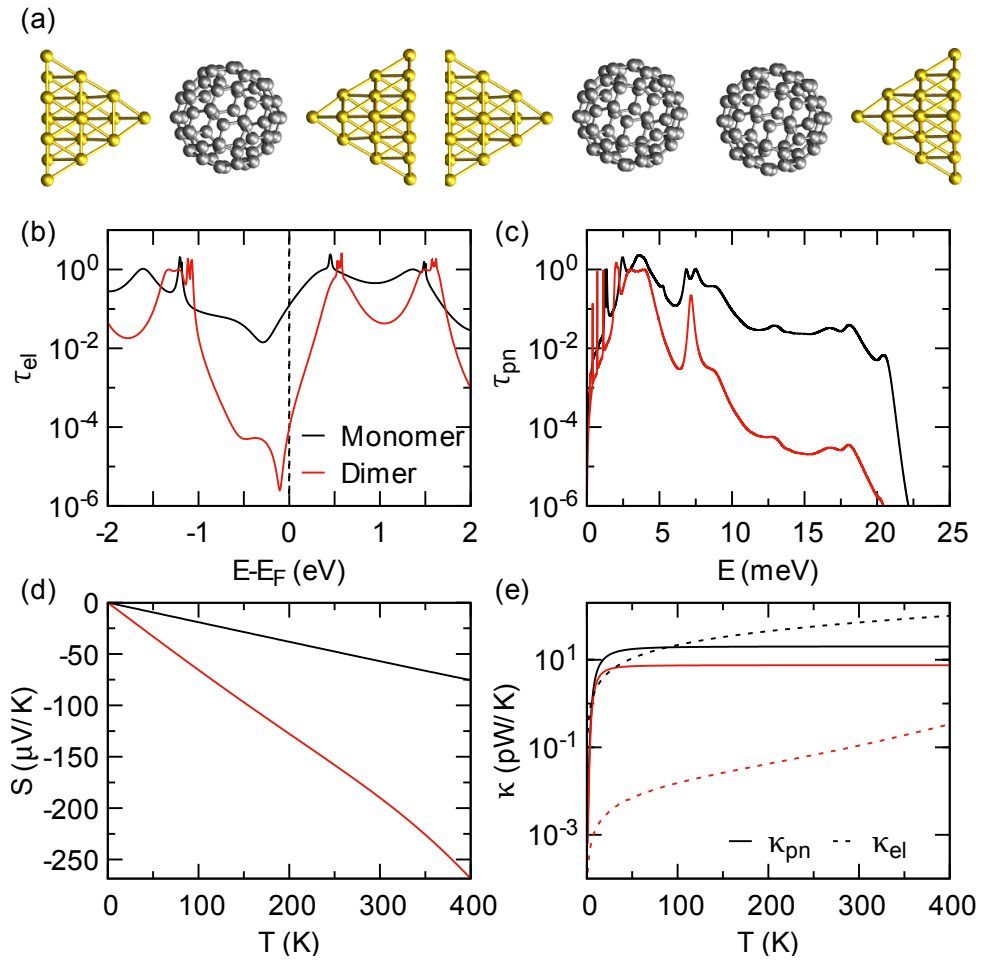

Figure 45. (a) Equilibrium geometries of a C_{60} monomer and a C_{60} dimer, bonded to both Au electrodes through atomically sharp tips. These geometries correspond to the minimum of the total energy with respect to the distance d between the electrodes, i.e. $d = d_0$. (b) Electronic transmission as a function of energy, measured with respect to the Fermi level, for the two geometries shown in panel (a). (c) Phonon transmissions as a function of energy. (d) Thermopower of the two junctions as a function of temperature. (e) Electronic and phononic contributions to the heat conductance for monomer and dimer junctions as a function of temperature. Data referring to the monomer is shown in black, those of the dimer in red.

in the $Z_{el}T$ and $Z_{el+pn}T$ values of these junctions, see Fig. 46. For the monomer $Z_{el}T$ and $Z_{el+pn}T$ are very similar in the whole temperature range, while $Z_{el+pn}T$ is 1-3 orders of magnitude smaller than $Z_{el}T$. As it is clear from the data listed in Table 2, at room temperature we find indeed $Z_{el+pn}T \approx Z_{el}T$ for the monomer, while for the dimer κ_{pn} reduces $Z_{el+pn}T$ as compared to $Z_{el}T$ by more than one order of magnitude. This illustrates once more the key role played by phonon transport in these dimer junctions.

In Figs. 47 and 48 we show results for yet another binding geometry, where in this case the molecules are bonded to both electrodes through blunt tips, see Fig. 47(a). The room temperature values of the different thermoelectric transport properties are summarized in Table 2. This binding geometry allows us to test our conclusions in a situation, where the metal-molecule coupling takes place through several Au atoms on both sides. As one can see in these two figures, the main conclusions of our discussions above are confirmed again. In particular, $Z_{el+pn}T$ is very similar to $Z_{el}T$ for the monomer, since κ_{pn} is negligible as compared to κ_{el}, while there is a strong reduction of $Z_{el+pn}T$ as compared to $Z_{el}T$ for the dimer since κ_{pn} dominates over κ_{el}.

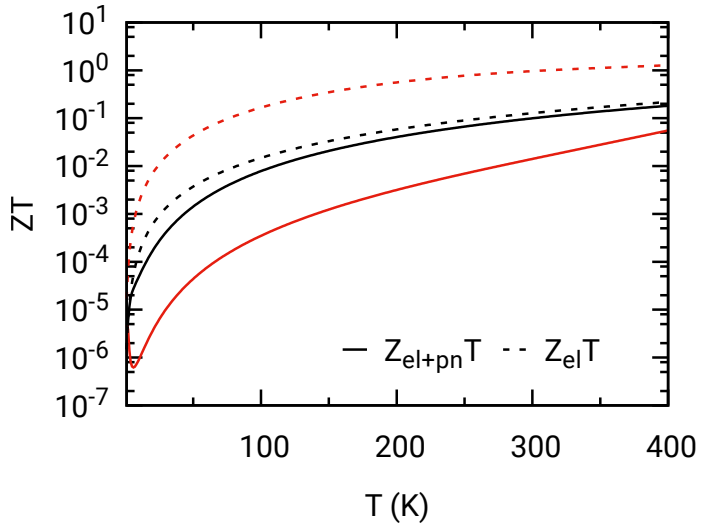

Figure 46. Figure of merit ZT as a function of temperature for the two geometries shown in Fig. 45(a). Black curves are for the monomer junction, while red ones are for the dimer. The solid lines correspond to $Z_{el+pn}T$, including both the electronic and phononic contributions to the heat conductance, $\kappa = \kappa_{el} + \kappa_{pn}$, while the dashed lines correspond to $Z_{el}T$, including only the electronic one, $\kappa = \kappa_{el}$.

A major difference of the blunt-blunt geometry with respect to the previous two types of geometries is the fact that the stronger electronic metal-molecule coupling leads to a rather high electronic transmission at the Fermi energy, which is reflected both in the electrical conductance and in the electronic contribution to the thermal conductance. As it is clear from Table 2, both G and κ_{el} increase monotonically for monomer and dimer junctions in the order of sharp-sharp, blunt-sharp, and blunt-blunt geometries. Let us emphasize that the metal-molecule binding geometry also limits the efficiency of phonon heat transfer in the monomer junctions, with the most efficient coupling for the blunt tips. Indeed we obtain a clear ordering of κ_{pn}, which increases from sharp-sharp to sharp-blunt and blunt-blunt junctions. However, the phonon thermal conductance of the dimer junctions is nearly insensitive to the metal-molecule coupling and limited by the weak molecule-molecule coupling.

Let us conclude this section by noting that we have also simulated the stretching of the sharp-sharp and blunt-blunt geometries (not shown here) and found that the main conclusions also apply there. In particular, we find in all of the cases that the phonon transport is very detrimental for the ZT values of the dimer junctions, while it plays a marginal role in the case of the monomer junctions.

4.3.3 Photon transport and thermoelectric figure of merit

The question that we want to address in this section is whether photon transport via thermal radiation can have an impact on the figure of merit of molecular junctions. Due to NFRHT the thermal conductance κ_{pt} can indeed largely exceed limits set by the by the Stefan-Boltzmann law for black bodies [279, 121]. We therefore put κ_{pt} in relation to κ_{el} and κ_{pn}, which were discussed before.

As described in Sec. 2.7, we use the formalism of fluctuational electrodynamics [120] to treat NFRHT. The results for the room temperature radiative heat conductance κ_{pt}, obtained with this procedure, are shown in Fig. 49 as a function of the gap size (or distance between the electrodes) Δ for (a) the tip-surface and (b) tip-tip geometries. We show these results in a relatively large gap-size range from 1 to 5 nm to provide an idea of the expectations for the photonic contribution

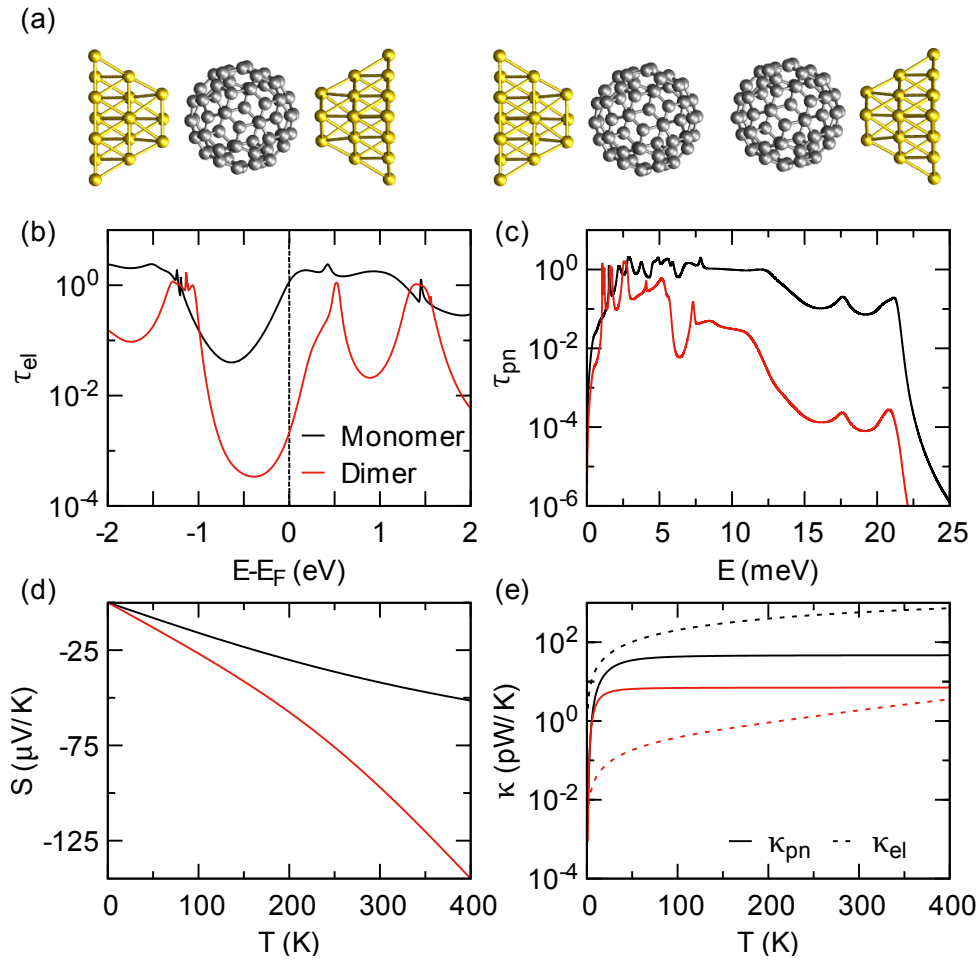

Figure 47. (a) Equilibrium geometries of a C_{60} monomer and a C_{60} dimer, bonded to both Au electrodes through blunt tips. These geometries correspond to the minimum of the total energy with respect to the distance d between the electrodes, i.e. $d = d_0$. (b) Electronic transmission as a function of energy, measured with respect to the Fermi level, for the two geometries shown in panel (a). (c) Phonon transmissions as a function of energy. (d) Thermopower of the two junctions as a function of temperature. (e) Electronic and phononic contributions to the heat conductance for monomer and dimer junctions as a function of temperature. Data referring to the monomer is shown in black, those of the dimer in red.

to the thermal conductance in a wide range of molecular junctions. Notice that the radiative heat conductance changes quite slowly with the gap size.

For our purposes, we can assume that κ_{pt} basically remains constant in the range of studied electrode-to-electrode distances Δ. Defined as shown in Figs. 43 and 49 and listed in Table 2, gap sizes Δ between the electrodes in our molecular junction geometries vary between 1 and 3 nm. Maximal elongations $d - d_0$, considered in Fig. 44, remain below 1 nm. The range of Δ, studied in Fig. 49, is thus compatible with the atomistic molecular junction models.

To relate κ_{pt} to κ_{el} and κ_{pn}, we consider again Table 2. The comparison of the listed thermal conductances with Fig. 49 shows that, depending on the radius of the tip used to model the electrodes, the photonic contribution to the thermal conductance can be comparable or larger than the phononic one in the contact regime. In some cases κ_{pt} can even exceed the electronic contribution κ_{el}. This happens for both types of nanogap configurations, i.e. tip-surface and tip-tip geometries. It is obvious that κ_{pt} is particularly important in the tunneling regime. There it dominates the thermal transport, if junctions are stretched just by a few Å, see Fig. 44.

To illustrate the impact of κ_{pt} on the figure of merit, we display in Fig. 50 the ZT values as a

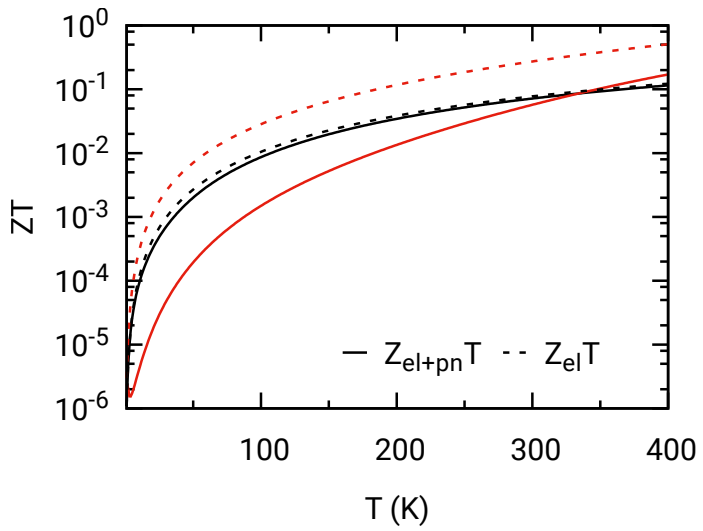

Figure 48. Figure of merit ZT as a function of temperature for the two geometries shown in Fig. 47(a). Black curves are for the monomer junction, while red ones are for the dimer. The solid lines correspond to $Z_{\mathrm{el+pn}}T$, including both the electronic and phononic contributions to the heat conductance, $\kappa = \kappa_{\mathrm{el}} + \kappa_{\mathrm{pn}}$, while the dashed lines correspond to $Z_{\mathrm{el}}T$, including only the electronic one, $\kappa = \kappa_{\mathrm{el}}$.

function of the displacement of the electrodes for the blunt-sharp junctions considered in Fig. 44. In particular, we show how the ZT values are modified by the photonic contribution for the tip-surface configuration and for various values of the tip radius. Notice that for elongations of the electrodes off the equilibrium by up to 2 Å, $Z_{\mathrm{el+pn+pt}}T$ with $\kappa = \kappa_{\mathrm{el}} + \kappa_{\mathrm{pn}} + \kappa_{\mathrm{pt}}$ for the monomer junction is similar to $Z_{\mathrm{el+pn}}T$ that considers only electronic and phononic contributions. But for larger separations, $Z_{\mathrm{el+pn+pt}}T$ breaks down dramatically. For the dimer junction, a suppression of $Z_{\mathrm{el+pn+pt}}T$ as compared to $Z_{\mathrm{el+pn}}T$ is obvious throughout the full range of elongations $d - d_0$ considered. Generally speaking, the detrimental influence of κ_{pt} on ZT is strongest in the tunneling regime for large electrode separations.

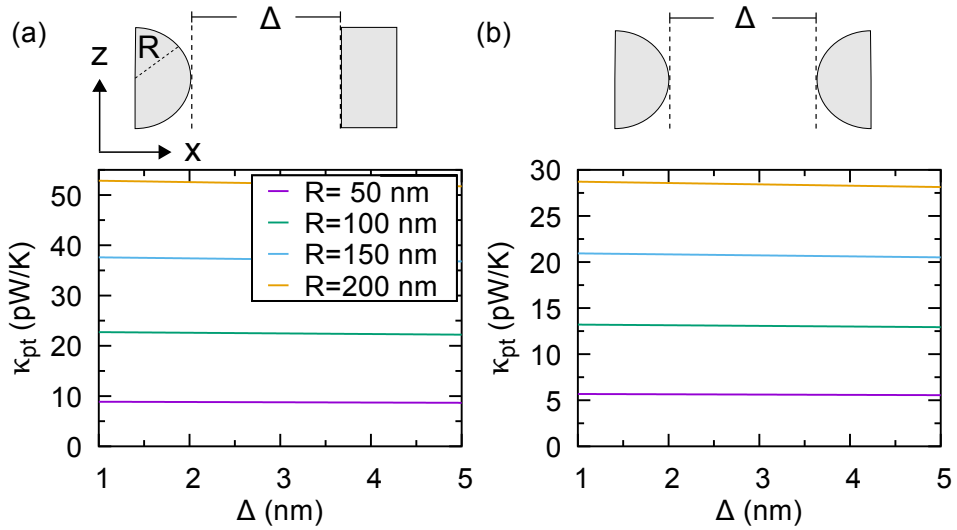

Figure 49. Room temperature radiative heat conductance as a function of the gap size for (a) a tip-surface geometry and (b) a tip-tip geometry. The different curves corresponds to different values of the radius of the spheres used to model the tips in both types of geometries.

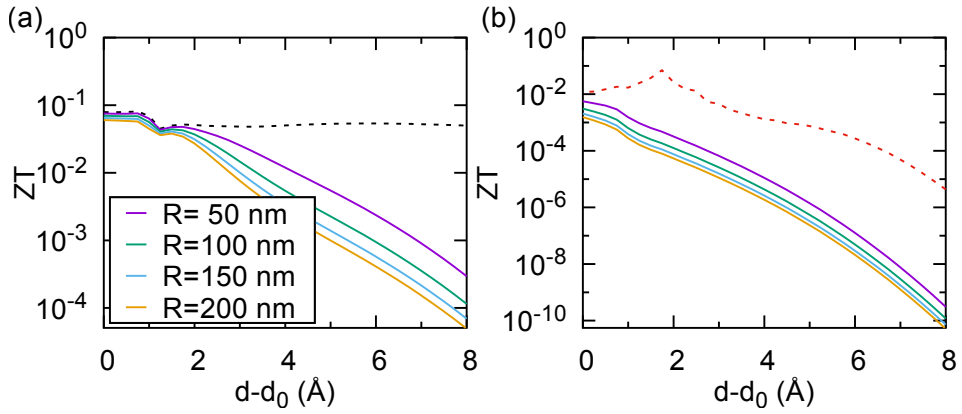

Figure 50. Comparison of the room temperature figure of merit $Z_{el+pn+pt}T$ (solid colored lines), including electronic, phononic and photonic contributions to the thermal conductance, with $Z_{el+pn}T$ (dashed lines), including only electronic and phononic parts, as a function of elongation for (a) the hollow-top monomer junction and (b) the hollow-top dimer junction. The dashed curves for $Z_{el+pn}T$ are identical to those shown in Fig. 44(d) and are reproduced to provide a reference. To determine the photonic heat conductance, the tip-surface geometry was assumed with tips of different radii R, as indicated by the legend.

5 Summary and outlook

This work presented the theoretical analysis of both charge and heat transport in nanoscale systems. To be more precise, we took into account several contributions from electrons, phonons, and photons, and looked at their influence on the different currents. Especially, our focus was set on the heat current in particular driven by phononic excitations.

In the first part of this thesis a theoretical model was developed, to look at a space or space-time representation of the phononic eigenchannels. These eigenchannels are known from the study of electronic transport, and we were able to transfer these ideas to phononic systems. The key issue was to connect the phononic scattering states with the transmission matrix in the NEGF framework. In the basis of these scattering states, we proposed a representation in terms of a static, and a time-dependent version, which helps to analyze the phononic transmission function. These ideas were demonstrated by the help of an analytical 1D model and various realistic examples that could be explored throughout this work.

Concerning an improvement of the theoretical transport modelling with the standard NEGF approach, we incorporated the, in the phononic community, well-known problem of the acoustic sum rule into a cluster-based transport description that allows different dimensionalities in certain subregions. In particular, we emphasized the importance of considering the alternating number of atomic neighbors for a surface atom compared to a bulk-crystal environment. By further correcting the on-site elements of these atoms in terms of a Dyson equation, for instance, due to a coupling to a molecule, we managed at least in principle to construct a system which perfectly fulfills the acoustic sum rule. The basic ideas were tested and verified in an analytical 1D model. Furthermore, we built a simplified model of 2D leads connected via a 1D wire with only 1 degree of freedom. There, we wanted to analyze the impact of the leads dimensionality on the phononic transmission function. In fact, we were able to reveal that, in contrast to the 1D model, a resonance at zero energy is suppressed due to the different behavior of the phononic density of states of the leads with respect to their spatial dimension. Finally, the method was tested for realistic examples, where the sum rule is on the one hand fulfilled for both Hessian and dynamical matrix and on the other hand only for the Hessian. We demonstrated here empirically that the inclusion of our method leads to an enhanced thermal conductance up to 22 %.

The second part of this work was related to metallic single-atom contacts. The main question we wanted to address was to check whether the macroscopic Wiedemann-Franz law is still applicable in these length scales. Herefore we looked at three different metals, namely gold, platinum, and aluminum, which differ in their chemical valence. In particular, we first analyzed a so-called atomic dimer configuration and discussed the specific electronic and phononic transmission functions for every metal, in terms of an eigenchannel representation, to quantify their relative contributions to the total heat current. We found out that, in contrast to the electronic transmission, or the number of electronic eigenchannels, that are mainly influenced by the chemical valence, for phonons the total number of eigenchannels are comparable, and the Debye energy sets an upper limit for the thermal conductance. In these examples, the Wiedemann-Franz law was still valid within a tolerance of 10% for gold and platinum, while for aluminum, due to an interplay of reduced electronic transmission and a higher Debye energy, a larger deviation of 32% occurred.

Furthermore, we investigated pulling and stretching curves with lead orientations in (111) and (100) directions for aluminum and gold contacts, to see whether these insights are robust against

different strain conditions and surface orientations. Consistent with the previous analysis, we found in all cases the phononic influence in aluminum higher compared to gold. For the gold contact, we saw additionally a plateau at twice the thermal conductance quantum before the junction breaks in both examples, while in aluminum no such precise plateau occurred. Again, we were able to explain this with the chemical valence of *s*-type for gold and *p*-type for aluminum. In total, we observed deviations for the Wiedemann-Franz law below 10% for gold, while we got larger deviations up to 40% for aluminum.

Besides the NEGF-based approach, we explored the validity of the assumed phase-coherent transport regime for the phononic system, as an example with gold and aluminum. Here we used NEMD simulations which take into account anharmonic effects in terms of phonon-phonon scattering. First of all, we calculated the impact of lattice expansion at finite temperatures on the phonon density of states, which can be summarized in a shift of the cut-off energy, relative to the zero temperature value. Moreover, we simulated the temperature-dependent phonon thermal conductance of an ideal monomer contact, to quantify the influence of anharmonicity. We found the mean conductance almost independent of temperature and due to the temperature only the variance increased. This enabled us to justify our assumption of a harmonic transport at room temperature. Additionally, we compared these results to the NEGF approach in the classical limit and discussed certain differences between these two models. Finally, we concluded that the phase-coherent transport regime is reasonable within the relative uncertainty of both methods.

At last, we performed a statistical analysis of different geometrical configurations by simulating multiple conductance traces. Here we combined the phononic description in the framework of NEMD with a tight-binding representation of the electronic system, to look also at the statistical validity of the Wiedemann-Franz law. For gold, the calculations are in qualitative agreement with the DFT-based approach and the mean influence of the phonons on the total thermal conductance is less than 10%. Further, we statistically verified the occurrence of the quantized thermal conductance at the value of twice the thermal conductance quantum. In the case of aluminium, however, we found an influence on possible geometric configurations as a result of temperature. It turned out that the dimer configuration is unstable at room temperature. Nevertheless, for the stable monomer configuration the contribution of the phonons was comparable to the DFT-based approach. In this metal statistically no quantized value for the thermal conductance appeared.

In summary, we could confirm the Wiedemann-Franz law in the gold and platinum contacts, while in some cases for aluminum larger deviations are possible. Our study reveals that not simply the phonons, but rather the interplay between electronic properties and phononic contributions is important for the question, whether this law is applicable. Furthermore, due to the excellent agreement between the DFT and NEGF results, we can identify elastic processes as the dominant scattering mechanism on these length scales.

The last part of this work was dedicated to molecular junctions, which was divided into three different sections. In these we addressed several topics like Fourier's law or the length dependence of the thermal conductance, the influence of phonon interference effect on the thermal conductance, and the impact of various heat carriers, like electrons, phonons, and photons, on the thermoelectric efficiency.

Starting the first section with the length dependence we studied in particular molecular junctions of various alkane derivatives. In the first part, we used comparable geometries of straight chains coupled to leads oriented in (111) direction and alternated the internal molecular degrees of freedom like anchoring groups and substituents. To be precise, we used thiolated, and amino-anchored alkane and fluoroalkane chains of length varying between 2 and 30 C units in steps of two. We found the thermal conductance at room-temperature of all investigated junctions to be nearly length independent and the relative efficiency to be mainly, although not exclusively, dictated by the metal-molecule coupling. We explained these results with the help of a 1D model, where the individual coupling elements were extracted from the corresponding DFT calculation, which showed that the coupling strength is smaller for amino-anchors in comparison

to the thiols. Furthermore, we calculated the electronic contributions in all the molecules, which demonstrated that in these systems, except for the smallest molecule with 2 C units, the total thermal conductance is dominated by the phononic contribution. Additionally, we related our calculations to existing experiments and calculations in the literature.

The next part of this section dealt with the variability of the phononic thermal conductance, due to variations in the lead orientation and bonding position, as well as the impact of geometric defects. Here we focused especially on the thiolated alkane chains of lengths ranging from 2 to 10 units. Regarding variations in the lead geometry, we could correlate the variance to the relative contributions coming from electrons and phonons, thus we found an increased variance for C2. Overall, conductance variations were obtained within a range of roughly 5 pW/K, while in the specific case of C2, due to electrons, these were roughly 10 pW/K. With respect to geometric defects, we considered for each molecule an arbitrary geometric configuration which holds at least one of these. Further, we simulated stretching curves with those, to look at their response to different lead distances. It turned out that all defects vanish upon stretching of the junction, so before rupture, all molecules were in a straight, defect-free configuration. In all cases we obtained consistently a reduced thermal conductance of the defective alkane chain with respect to the defect-free one. Our analysis in terms of the accumulated thermal conductance revealed, that we could not associate a particular set of vibrations in a specific energy range to this reduction.

At the end of this section, we looked again at temperature effects by means of NEMD simulations. In all calculations we could observe the thermally activated occurrence of geometric defects. Therefore, we concluded that at ambient temperature the thermal conductance must be averaged over several geometric configurations, including defect-containing as well as defect-free chains. Since the mean thermal conductance compared well with the one obtained for defective chains under the DFT approach, we provided a further justification for phase-coherent transport in such systems.

In the second section the influence of interference effects on the thermal conductance was analyzed. Here we considered molecular junctions of benzene derivatives. In particular, we investigated the impact of para vs. meta conjugation as well the effect of attaching substituents with different masses to the molecule. In the case of benzenediamine we found that due to the small maximum phonon energy in Au of around 20 meV, no destructive interference effects were visible in the phonon transmission function, irrespective of whether the molecule is contacted to Au in para or meta configuration. This leads to a room-temperature thermal conductance that is similar for the two contacting schemes. More importantly we showed that this situation can be changed by replacing a H atom of benzene by a halogen atom (F, Cl, Br, I). The substitution leaded to a reduction of the thermal conductance up to a factor of 1.7. A calculation of the accumulated thermal conductance revealed that this reduction can be attributed to an anti-resonance in the transmission function. Going further, we could relate the interference feature to two molecular vibrations, based on a symmetry argumentation. Since this effect is a molecular-internal one, we could demonstrate that it persists under different strain conditions. We also showed that by increasing the number of substituent atoms in the benzene molecule and depending on their precise position on the ring, one can induce additional reductions of the thermal conductance by a factor of 2.5. Finally, we also demonstrated that similar concepts apply to the case of OPE3 and, in particular, we found a clear difference between para- and meta-OPE3, where the central benzene ring is connected in para or meta position.

The last section dealt with molecular C_{60} junctions. Here we looked at the individual contributions from electrons, phonons, and photons and estimated their influence on the thermoelectric figure of merit. We calculated for a C_{60} monomer as well as a dimer junction all the contributions for contact geometries, hollow-hollow, hollow-top, and top-top. The photonic contributions were taken into account within the framework of fluctuational electrodynamics. Our results showed that the phonons play a minor role in the thermal conductance of the monomer junctions, while

they largely determine this property in dimer junctions. This fact resulted in a substantial reduction of the ZT values of the dimer junctions, as compared to the monomer junctions, in spite of the fact that phonons are transported less efficiently in the dimer case. In other words, our results showed that phonons severely limit the thermoelectric performance of dimer junctions. In addition, we provided in this work a critical analysis of the impact of thermal radiation on the ZT values of molecular junctions, a factor that has been overlooked so far in molecular electronics. We revealed, in particular, that the NFRHT between the metallic electrodes can indeed further reduce the figure of merit of molecular junctions. This effect was particularly pronounced in the tunneling regime. Overall, our work demonstrated the importance of taking into account both phonons and photons for a proper evaluation of the performance of molecular junctions as possible thermoelectric devices. Moreover, it provided valuable insights into the relative contribution of different heat carriers to the thermal conductance, namely electrons, phonons, and photons.

Let us close with a short outlook with respect to future projects. We have illustrated in this thesis at several examples, that the phase-coherent transport regime is justified in single-atomic contacts and molecular junctions with gold leads. Nevertheless, the physics of phonon heat conduction in systems related to applications is, in general, anharmonic, so it should be worthwhile to explore effects related to this topic. Simple systems for which the assumption of coherent transport is expected to break down, are those with a large miss-match between the Debye energies of the leads. Here the ballistic transport should underestimate the real conductance since anharmonic processes should be able to establish a connection between modes with energies below to modes with energies above the lowest Debye energy of the two materials. Further, molecular junctions with a reduced mismatch of the molecular vibrations to the phonons of the lead, for instance, alkane chains attached to graphene, or graphite, should also show higher anharmonic effects since it is known from bulk calculations that the anharmonicity scales with the energy as E^2. Henceforth due to the higher modes involved in the transport in these systems, an effect could be visible in terms of a reduced conductance. The key question which should be addressed is how can the molecular design influence the anharmonicity to either reduce or increase the effects. From a methodology point of view, an appealing strategy could be to combine recent advances in theories based on the quasi-harmonic approximation for the lead materials [158], where the change of the density of states of the phonon bath due to temperature can be considered consistent with our NEMD results, with more progressive ways of handling perturbative approaches based on NEGF-methods in the central part [306, 307, 308]. There, one calculates the current conserving Born series up to a certain degree and uses efficient resummation techniques to get convergent results.

Another interesting topic which emerged in recent years that is closely related to this thesis is the transition of the heat current between the contact and the tunneling regime. Motivated by the experiments in Ref. [282], the influence of phonon tunneling has been debated with various methods [309, 310, 311, 312], the actual role of this effect, however, is still under discussion and a clear ab-initio prediciton is missing, too. From a different perspective it has been shown that the whole story can be translated to the question of how the microscopic description of heat transfer mediated by phonons and electrons merges into the macroscopic theory based on fluctuational electrodynamics [313, 314, 315]. Combined with methods beyond DFT like Random-Phase-Approximation [316, 317] one could further contribute to this exciting research area by investigating these theories with material parameters obtained from first-principles.

A Phonon Green's function

In this appendix we calculate the Heisenberg equation of motion for a system of coupled harmonic oscillators and define some basic properties related to phonon Green's functions.

A.1 Quantum oscillator

For the quantum mechanical system of coupled harmonic oscillators the following commutators for the position and momentum operator $[q_{i\alpha}, q_{j\beta}] = 0 = [p_{i\alpha}, p_{j\beta}]$ and $[q_{i\alpha}, p_{j\beta}] = \delta_{ij}\delta_{\alpha\beta} i\hbar$ hold. Transforming the operators into the Heisenberg picture according to

$$q^H_{i\alpha}(t) = e^{iHt/\hbar} q_{i\alpha} e^{-iHt/\hbar}, \tag{A.1}$$

we can evaluate the dynamics of the system using the Heisenberg equation of motion

$$\frac{dq^H_{i\alpha}(t)}{dt} = \frac{1}{i\hbar}\left[q^H_{i\alpha}(t), H\right]. \tag{A.2}$$

If a Hamiltonian of the form Eq. 2.2 applies, we obtain

$$\frac{dq^H_{i\alpha}(t)}{dt} = \frac{1}{i\hbar} e^{iHt/\hbar}\left[q_{i\alpha}, H\right] e^{-iHt/\hbar} = \frac{1}{i\hbar} e^{iHt/\hbar}\left[q_{i\alpha}, \frac{p^2_{i\alpha}}{2}\right] e^{-iHt/\hbar} = \frac{1}{i\hbar} e^{iHt/\hbar}\frac{i\hbar p_{i\alpha}}{2} e^{-iHt/\hbar} = \frac{p^H_{i\alpha}(t)}{2} \tag{A.3}$$

and

$$\frac{dp^H_{i\alpha}(t)}{dt} = \frac{1}{i\hbar}\left[p^H_{i\alpha}(t), H\right] = \frac{1}{i\hbar} e^{iHt/\hbar}\sum_{j\beta}\left[p_{i\alpha}, q_{i\alpha}K_{i\alpha j\beta}q_{j\beta}\right] e^{-iHt/\hbar} = -\sum_{j\beta} K_{i\alpha j\beta} q^H_{j\beta}(t). \tag{A.4}$$

Finally, we get the following equation

$$\frac{d^2 q^H_{i\alpha}(t)}{dt^2} = -\sum_{j\beta} K_{i\alpha j\beta} q^H_{j\beta}(t). \tag{A.5}$$

A.2 Definition of phonon Green's function

We outline in this appendix the definitions of the Green's functions used in this work. The greater phonon Green's function is defined as

$$D^{>}(t,t') = -\frac{1}{\hbar}\langle q(t)q(t')\rangle. \tag{A.6}$$

Other functions are those of the lesser phonon Green's function

$$D^{<}(t,t') = -\frac{1}{\hbar}\langle q(t')q(t)\rangle, \tag{A.7}$$

the retarded phonon Green's function

$$D^{r}(t,t') = -\frac{1}{\hbar}\Theta(t-t')\langle[q(t), q(t')]\rangle, \tag{A.8}$$

where $\Theta(t)$ is the usual Theta function and the last one

$$D^a(t,t') = \frac{1}{\hbar}\Theta(t'-t)\langle[q(t),q(t')]\rangle, \tag{A.9}$$

the advanced phonon Green's function. These different quantities are connected according to

$$D^r(t,t') - D^a(t,t') = D^>(t,t') - D^<(t,t'). \tag{A.10}$$

A typical case in the transport calculations is the assumption of a stationary current. In this way, the respective functions can be calculated in energy space, with the Fourier transformation defined as

$$D(E) = \int_{-\infty}^{+\infty} D(t) e^{itE/\hbar} \mathrm{d}t \tag{A.11}$$

and

$$D(t) = \frac{\hbar}{2\pi} \int_{-\infty}^{+\infty} D(E) e^{itE/\hbar} \mathrm{d}E \tag{A.12}$$

for the inverse transformation.

B Transmission eigenchannels

We present in this appendix further results for the 1D-chain model discussed in Chap. 2.4.4. The idea is to cover the limiting cases that have not been discussed so far. For this purpose, we start with the case of a perfect chain $k_c = k_l$, see Fig. 51(a). The total transmission for this chain is constant and one over the whole energy range, as expected for the defect-free case. Therefore, the absolute values of the two individual components of the transmission eigenchannel are equal. The total one follows again the local density of states, which has the well-known van Hove singularity at the cut-off energy. As in the case $k_c < k_l$, atom $i = -1$ gains a phase equal to π when going from 0 energy to the cut-off energy of 20 meV.

Now we consider $k_c > k_l$ shown in Fig. 51(b) with $k_c = 2000\text{meV}^2$, we find that the absolute value of each component is almost the same, again. Note that in contrast to the example discussed in the Sec. 2.4.4, the absolute value is now slightly larger on the right atom $i = 0$. More interestingly, there is almost no phase difference between the two atoms. Here, due to the strong bonding between the two atoms, they behave like a rigid molecule.

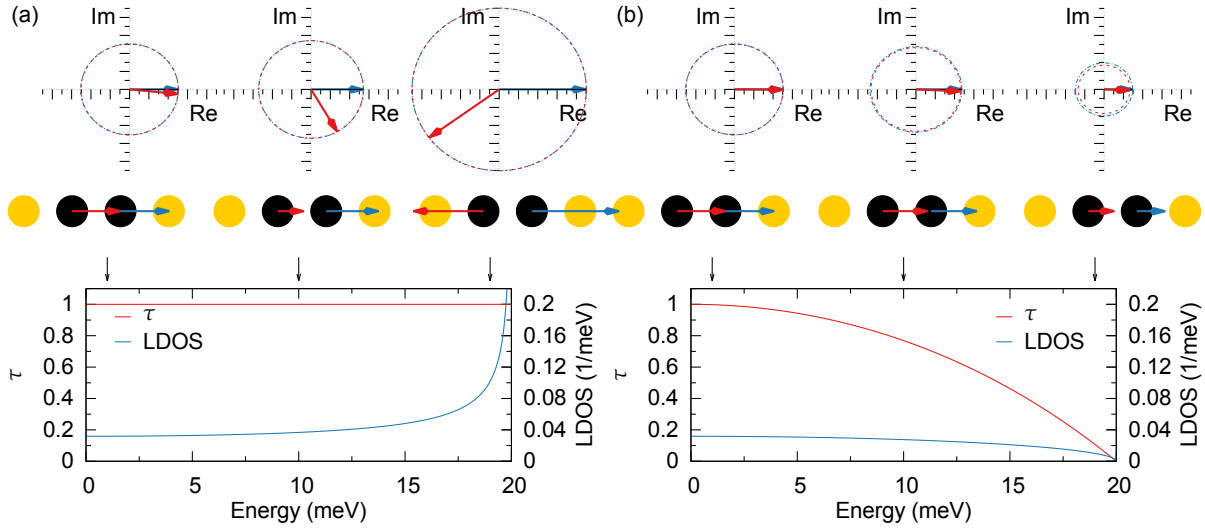

Figure 51. Same as Fig. 52 in the main manuscript, but with the parameters (a) $k_l = 100$ meV^2 and $k_c = 100$ meV^2, and (b) $k_l = 100$ meV^2 and $k_c = 2000$ meV^2.

For completeness we depict in Fig. 52 the components of $|\tilde{\chi}_1|$ (Eq. (2.63) in the main manuscript), which apart from the normalization with the local density of states is proportional to the transmission eigenchannel. In particular, we show this quantity for the energies 1, 10 and 19meV as a function of the coupling constant k_c. Notice that below k_l the absolute value on the left atom is bigger compared to the one of the right atom, whereas at k_l both are equal, and above one can see a transition to the "rigid molecule".

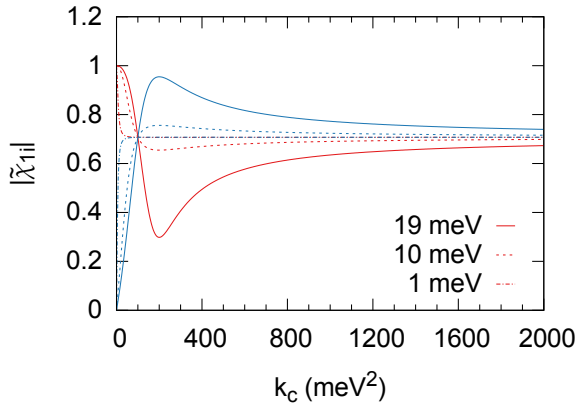

Figure 52. $|\tilde{\chi}_{1i}|$ as a function of the coupling constant k_c for the three different energies. The red color corresponds in all cases to the left atom $i = -1$, whereas the blue curves correspond to the right atom $i = 0$.

C Bulk parameters

In addition to the information about the contact geometry in single-atom or molecular junctions, it is necessary to find a suitable parametrization of the bulk parameters for the respective lead material, in order to get a realistic description of the whole junction. For all our electronic calculations, we extract these parameters from a finite cluster of 1415 atoms, using TURBOMOLE, as the coupling elements from the central atom to all its surroundings. This procedure is described in Ref. [64] and it enables a satisfiying description of the electronic band structure. However, for phononic systems, due to computational burdens within density functional perturbation theory, we are restricted to relative small clusters of around 300 atoms. For these sizes, the phonon dispersion relation is generally not converged. However, since the phonon basis is the Cartesian elongations of the atoms, parameters from different DFT codes are convertible. Henceforth, in order to achieve adequate parametrization, we use the plane-wave code QUANTUM ESPRESSO for some materials. In the following, we present all properties for materials related to this work, namely gold, platinum, and aluminum. Additionally, we investigate the convergence of the electronic transmission for metallic dimer junctions with respect to the number of atoms in the ECC.

C.1 Gold

For gold, we use the def-SV(P) basis set with the scalar relativistic core potential from Ref. [318]. The electronic bulk parameters are extracted from a gold cluster consisting of 1415 atoms. For the calculation we use an orbitalshift of 0.5, Fermi smearing with $T_{\mathsf{start}} = 50$, a start damping of 20.7, scftol 1e-14, and scfconv 6. A plot of the band structure with these parameters can be seen in Fig. 53(a) together with a periodic calculation using the riper module. The band structure of the cluster calculation is shifted by an amount $-E_F$ such that the two curves are on top of each other. In this way, we can estimate the Fermi energy of the material.

As is apparent, the shifted band structure fits quite well to the periodic calculation except for a few single points, for example in the vicinity of the W point. These points are caused by a poor k-point dependent conditioning of the basis due to the use of a finite k-point mesh. An increased number of k-points or a better-conditioned basis would resolve this issue. For the purpose of transport calculation, however, these parameters are sufficient since the density of states, which influences the transmission, is nearly unaffected from these single points. In Fig. 53(b) all coupling elements of the Fock matrix from the central atom to all its neighbours and all basis functions, as a function of the distance, are shown. Since we are looking at an ideal fcc lattice, points appear at discrete distance values. The maximum value decreases as a function of separation, however, only after the 7-th nearest neighbour, or beyond the distance of 8 Å, its value is in the meV range.

Inspired by this, we try to look at the convergence of the electronic transmission, with respect to the number of lead atoms inside the ECC. Here, we use the geometries depicted in Fig. 53(c). These consist of an idealized gold-dimer junction, build with a lattice constant of 4.08 Å. In every junction the central part is identical. The leads, in contrast, are varied so that every gold atom in the center is coupled to at least all possible 3,4,5,6, and 7 nearest neighbours. In this way, we get a systematic way of looking at a convergence of the electronic transmission function.

The corresponding transmissions are depicted in Fig. 53(d), where from top to bottom the

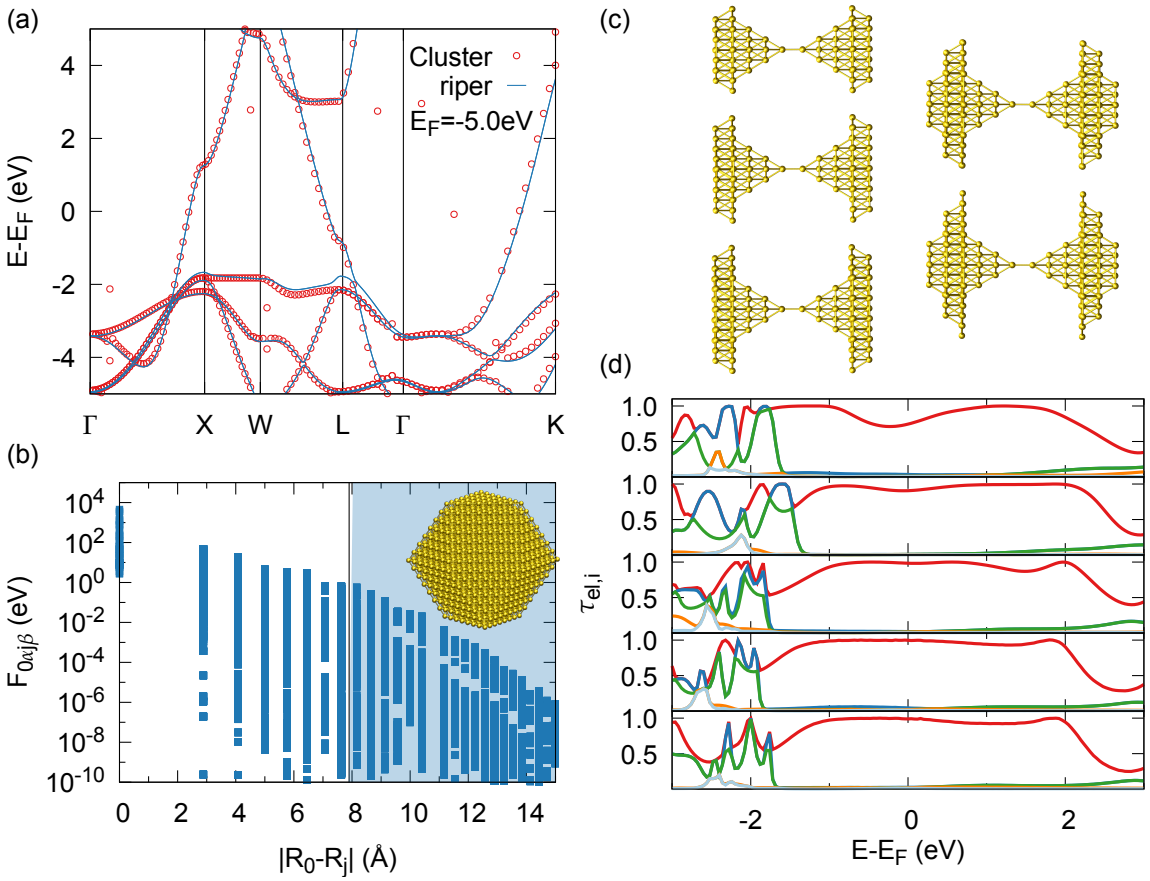

Figure 53. (a) Comparison of the electronic band structure obtained with cluster parameters to those of the riper module. (b) Fock matrix elements of the central cluster atom to all its neighbours and all basis functions. The inset shows a geometry of the cluster used in this calculation. (c) Geometries for the test of convergence with respect to leads-center coupling. The number of lead atoms increases from top to bottom and from left to right. (d) The corresponding eigenchannel resolved electronic transmission.

number of neighbours increases. Typical for this gold contact, only a single channel is present in the vicinity of the Fermi energy. Around -2 eV, and 2 eV, in all cases several channels show up, which are connected to the d-, and p- bands of the crystal. This illustrates the correspondence of the transmission eigenchannels to the electronic band structure. With respect to the cluster size, we see that while larger variations are visible for the smallest contacts, these are nearly negligible for the biggest ones.

For completeness, we also show the phonon band structure and the corresponding density of states for gold in Fig. 54. The dynamical matrix has been obtained with the cluster-based approach using a cluster size of 333 atoms and a comparison to the experimental density of states has already been published in Ref. [109]. We supplement this comparison by analyzing now, in addition, the agreement of the band structures. The measurement has been done at 300 K, and is taken from Ref. [319]. The shapes of the calculated, and the experimental curves are in a reasonable agreement to each other. However, the theoretical ones are shifted ≈ 3 meV to higher energies, with respect to the experiment. Under this circumstances, all calculated thermal conductances values in this thesis tend to be slightly overestimated.

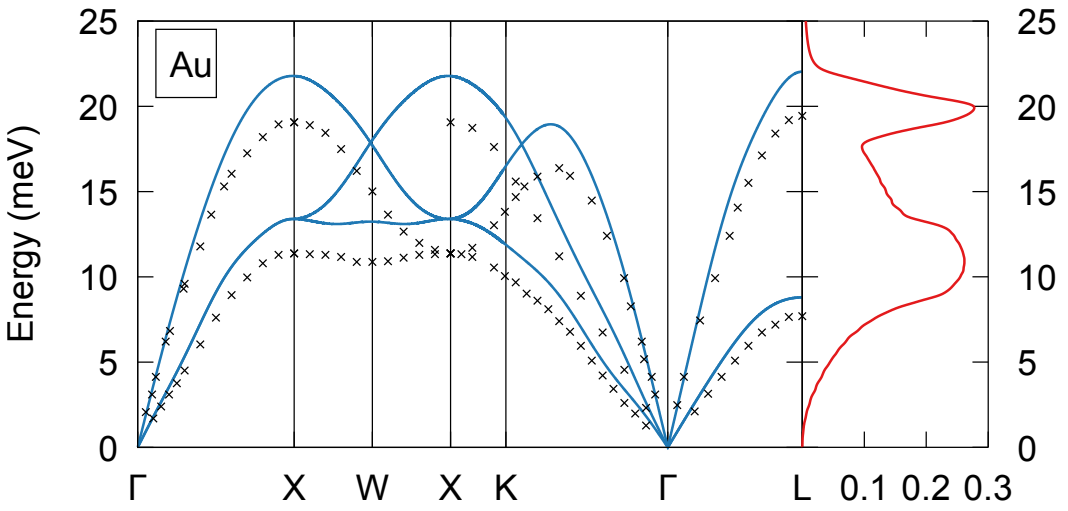

Figure 54. Comparison of the Au bulk parameters to the experiment at T=300 K taken from Ref. [319]. Additionally, the density of states is shown.

C.2 Platinum

As a further material we are considering platinum. Here, the standard basis sets are not compatible with bulk calculation, due to bad conditioning of these bases. For this reason, we build a basis derived from the def-TZVP basis of Ref. [320], by changing the exponent of the most diffusive *s* basis function from 0.04 a.u.$^{-2}$ to 0.07 a.u.$^{-2}$ and those of the most diffuse *p* function from 0.05 a.u.$^{-2}$ to 0.08 a.u.$^{-2}$. For the electronic bulk parameters, we use again a cluster of 1415 atoms with an automatic orbitalshift of 0.5, a start damping of 25.00, scftol 1e-14, scfconv 7, and marij with a precision of 0.1e-10. In Fig. 55(a) the obtained band structure is shown in comparison to a riper calculation. Here the agreement is satisfactory, too. The Fermi energy is -5.55 eV. Again, the Fock matrix elements of the bulk parameters decrease with increasing distance. This time already after the 5-th nearest neighbour, the maximum element is in the meV range. We proceed similar to gold and study the convergence of the transmission with respect to the lead-center coupling. The structures in Fig. 55(c) have been constructed with a lattice constant of 3.92 Å. Their transmission in Fig. 55(d) , ordered from top to bottom with an increasing electrode, shows a reasonable convergence.

For the calculation of the phononic bulk parameters, we use QUANTUMESPRESSO. As a pseudopotential, we use a PAW from the PsLibrary [321]. We employ a grid of 24 x 24 x 24 elec- tronic k-points, an energy cutoff of 100 Ry and a Marzari- Vanderbilt smearing of 0.07 Ry. The phonons are computed on a grid of 9 x 9 x 9 q-points. The resulting band structure and density of states can be seen in Fig. 56, with a comparison to experimental results from Ref. [319], measured at 90 K.

C.3 Aluminum

The last material is aluminum. For the electronic band structure, we use the def-TZVP with the corresponding coulomb fitting basis. The bulk properties, obtained with a cluster of 1415 atoms, are compared to the riper module in Fig. 57(a). Here we used an automatic orbitalshift of 0.2, scfconv 7, start damping of 15.000, and Fermi smearing with $T_{\text{start}} = 300$. Similar to Au, a non-physical point in the direction $\Gamma \rightarrow \mathrm{K}$ appears, due to a bad condition number of the basis set. The Fermi energy of this material is -4.1 eV. The maximum Fock element of the central atom to its neighbours in Fig. 57(b) decreases with increasing distance. The electronic

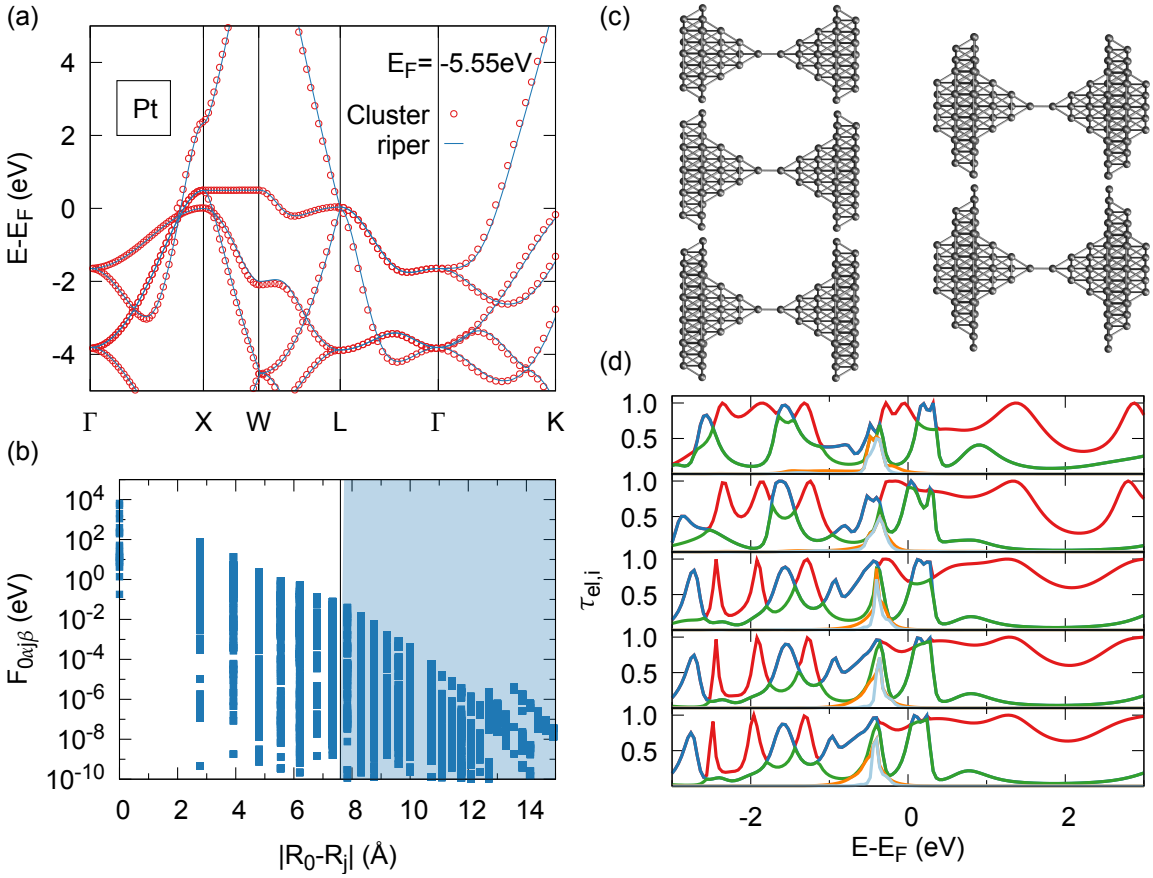

Figure 55. Same as Fig. 53 for a platinum contact.

transmission in Fig. 57(d), for the contacts displayed in Fig. 57(d), shows a good convergence around the Fermi energy after the inclusion of all atoms up to the 5-th nearest neighbour.

To complete, we calculate the phononic properties using QUANTUMESPRESSO, with a PAW pseudopotential taken from the PsLibrary [321]. For the calculation we utilize 24 x 24 x 24 k-points, an energy cutoff of 100 Ry, Marzari-Vanderbilt smearing of 0.1 Ry and a q-grid of 11 x 11 x 11. A comparison of the band structure with an experiment at 300 K is depicted in Fig. 58.

C.4 Lattice constant

In the DFT calculations for the ECCs, we always use fixed atomic positions equal to the experimental lattice sites for the parts belonging to the leads, while the positions of the atoms in the central parts are variable. In this way, we introduce artificial stress in our calculation. To estimate the discrepancy to the theoretical equilibrium lattice constant, we compute the energy of an ideal fcc structure with respect to the lattice parameter. For the calculation we use $24 \times 24 \times 24$ electronic k-points, epsbext 1e-10, a smearing of 0.005 a.u., scfconv 9, PBE functional, and the basis as described in the previous section. The results can be seen in Fig. 59. Apart from Al the difference in the experimental lattice constant and the calculated equilibrium position is in the order of 0.2 Å. This is partially attributed to the use of ECPs, which are not optimized for bulk calculations. Instead, they are built for molecular purposes. In order to reduce stress effects in the calculation we would need to find more sophisticating core potentials.

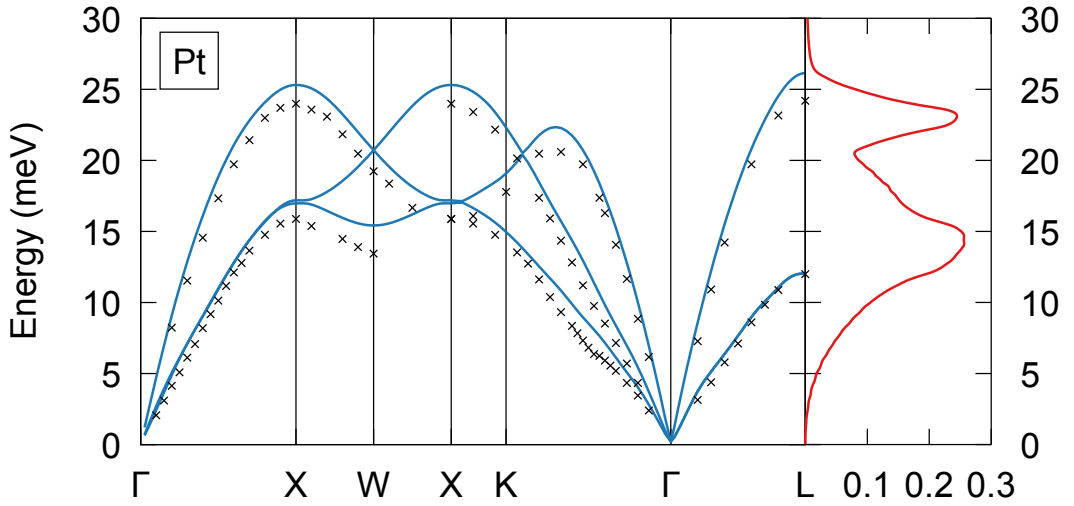

Figure 56. Same as Fig. 54 for a platinum contact. In the expirement T=90 K.

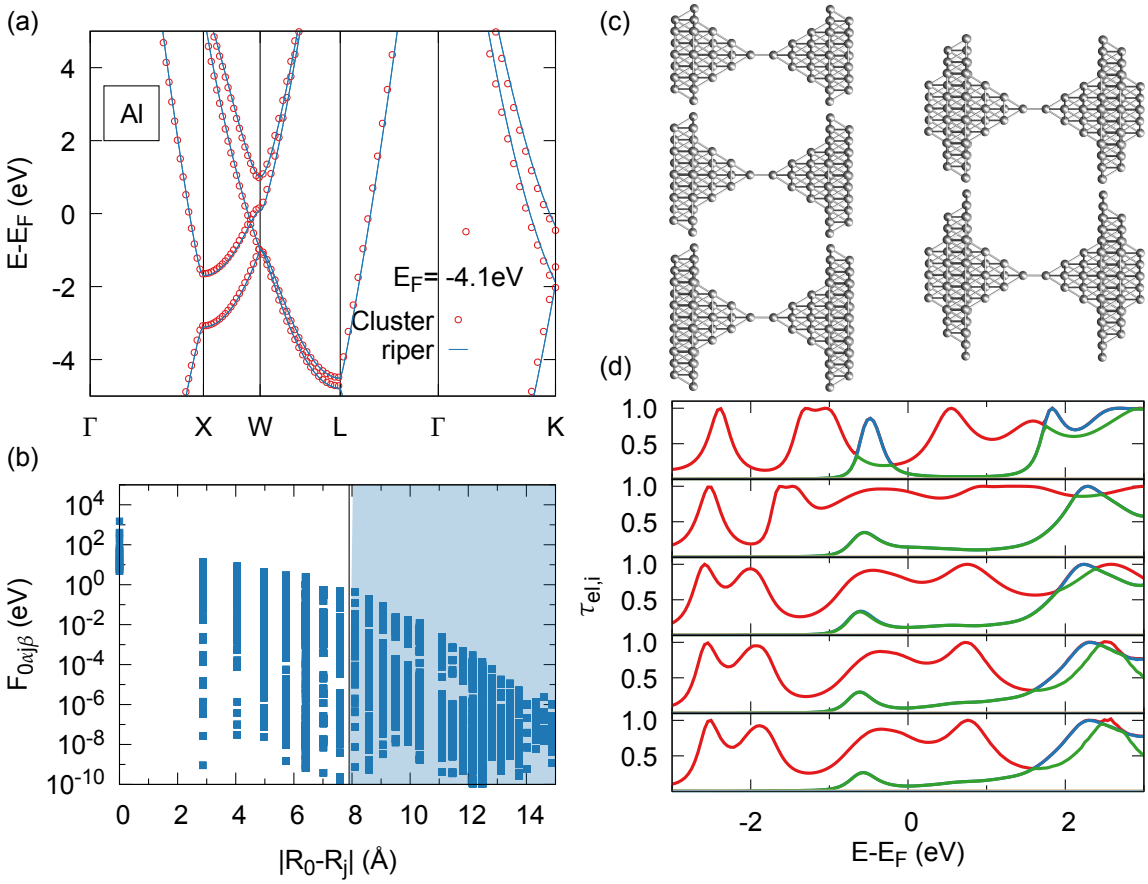

Figure 57. Same as Fig. 53 for an aluminum contact.

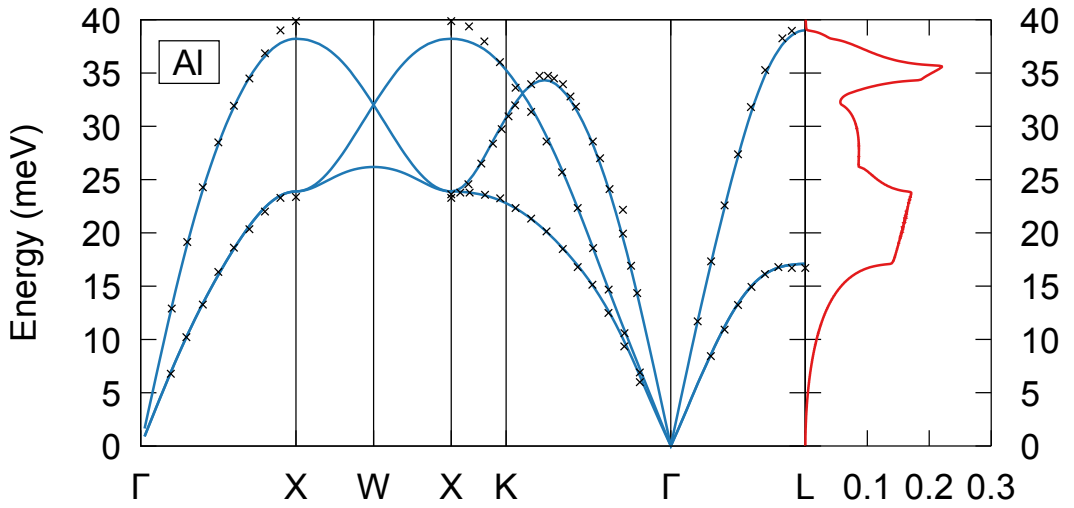

Figure 58. Same as Fig. 54 for an aluminum contact. The temperature in the experiment is 300 K.

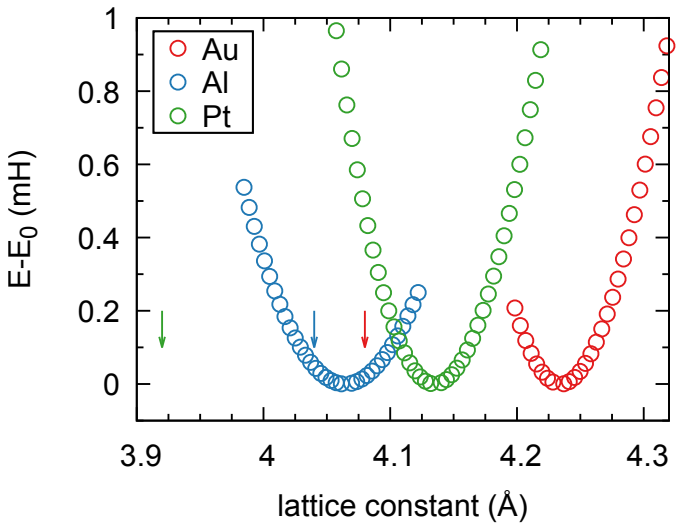

Figure 59. Calculated energy curve with respect to the lattice parameter. The arrow indicates the corresponding experimental lattice parameter used in the calculations.

D Alkanes

In this appendix, we consider the convergence of the transmission functions with respect to the lead-center coupling for a molecular junction as an example with a dithiolated alkane chain of 10 CH_2 segments. Therefore, we try to follow the same ideas as for the metallic contacts in App. C, and systematically increase the number of nearest neighbours of the gold atoms nearest to the surface. Here, we are also interested in the convergence of the phonon transmission function, so the junction has to be relaxed. However, this leads to unavoidable variations of the geometry in the center, which can influence the transmission and thus distort the comparison. In principle, two ways of looking at the convergence could be imagined. In a first way, one starts with a relaxed structure, builds a particular geometry in the usual manner by relaxing the molecule first on one lead and then attaching the second lead. If one increases the number of lead atoms afterwards, the distance between the leads stays unaltered. Another possibility would be to build each junction individually, thus allowing additionally for a variation in the lead distance.

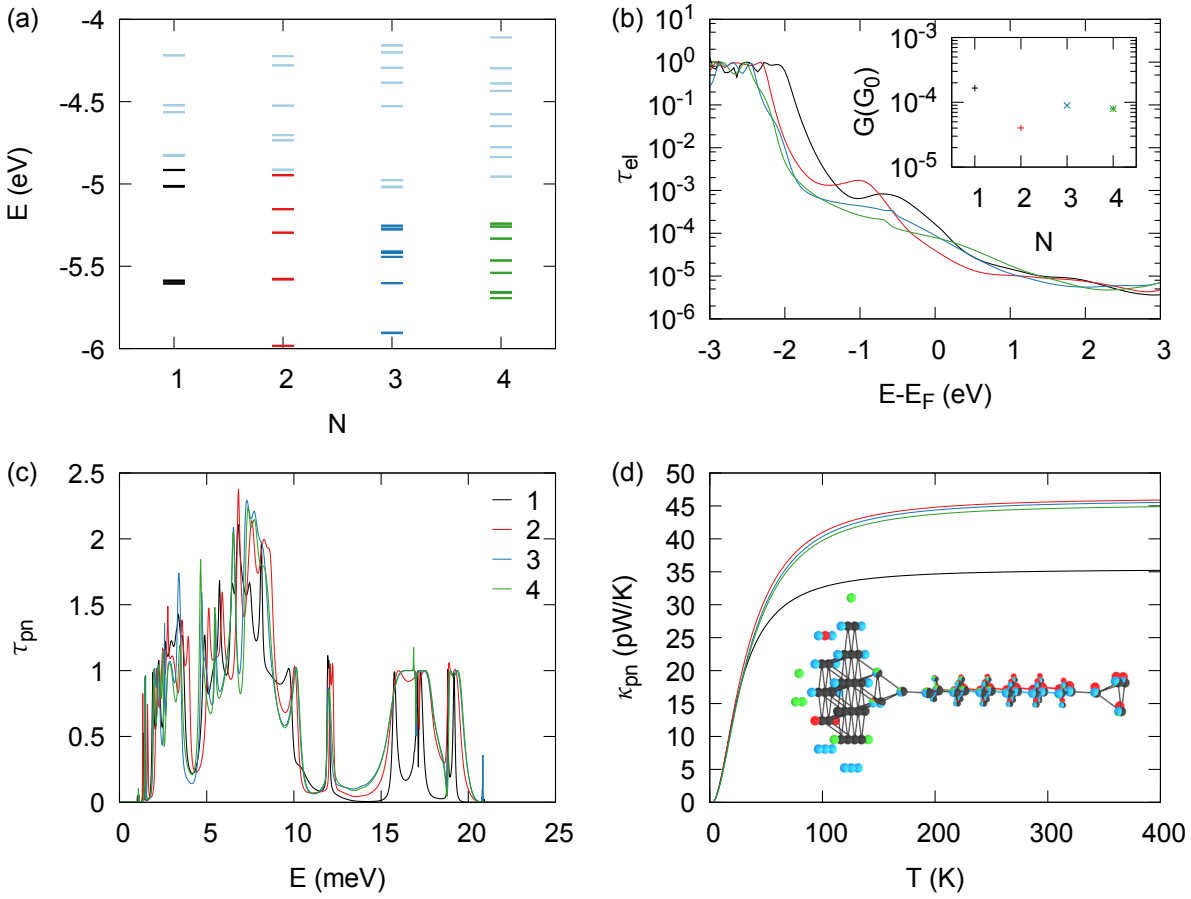

Figure 60. (a) Energy levels of the 4 systems shown in (d). With increasing N, The number of lead atoms increases. The occupied orbitals are colored in black, red, dark blue and green, and the lead orientation is in (111) direction. (b) Electronic transmission and corresponding electronic conductance. (c) Phononic transmission and (d) corresponding temperature-dependent phononic thermal conductance.

While the former one would give in general more comparable geometries, the latter one is more related to the general workflow in building a molecular junction. For this reason, we will always use the second approach to additionally reveal the differences in the starting geometries related to the modelling.

The results for the leads oriented along (111) direction will be presented in the following. In Fig. 60(a) we show the occupation of the different systems, where with increasing N the number of lead atoms increases. We show this plot to emphasize two things, first, the electronic structure alternates quite strong with respect to the chosen ECC structure, so the electronic levels differ in energy. Second, the band gap also strongly depends on the system size. In general, one would like to pick up an ECC which gives the largest band gap, since the band gap correlates with the behaviour of the scf-convergence and, in general, systems with a larger band gap behave better. The electronic transmission for these clusters are depicted in Fig. 60(b). Overall, the HOMO of the electronic transmission shifts to lower energies with increasing cluster size. The electronic conductance at zero temperature, in contrast, does not follow this monotonic behavior. However, the transmissions for the two biggest clusters compare well. Regarding the phononic transmission in Fig. 60(c), we find a reasonable convergence in all energy ranges, within the uncertainty and with respect to geometrical variations. In addition, the phononic thermal conductance in Fig. 60(d) is nearly equal for all cluster except the smallest.

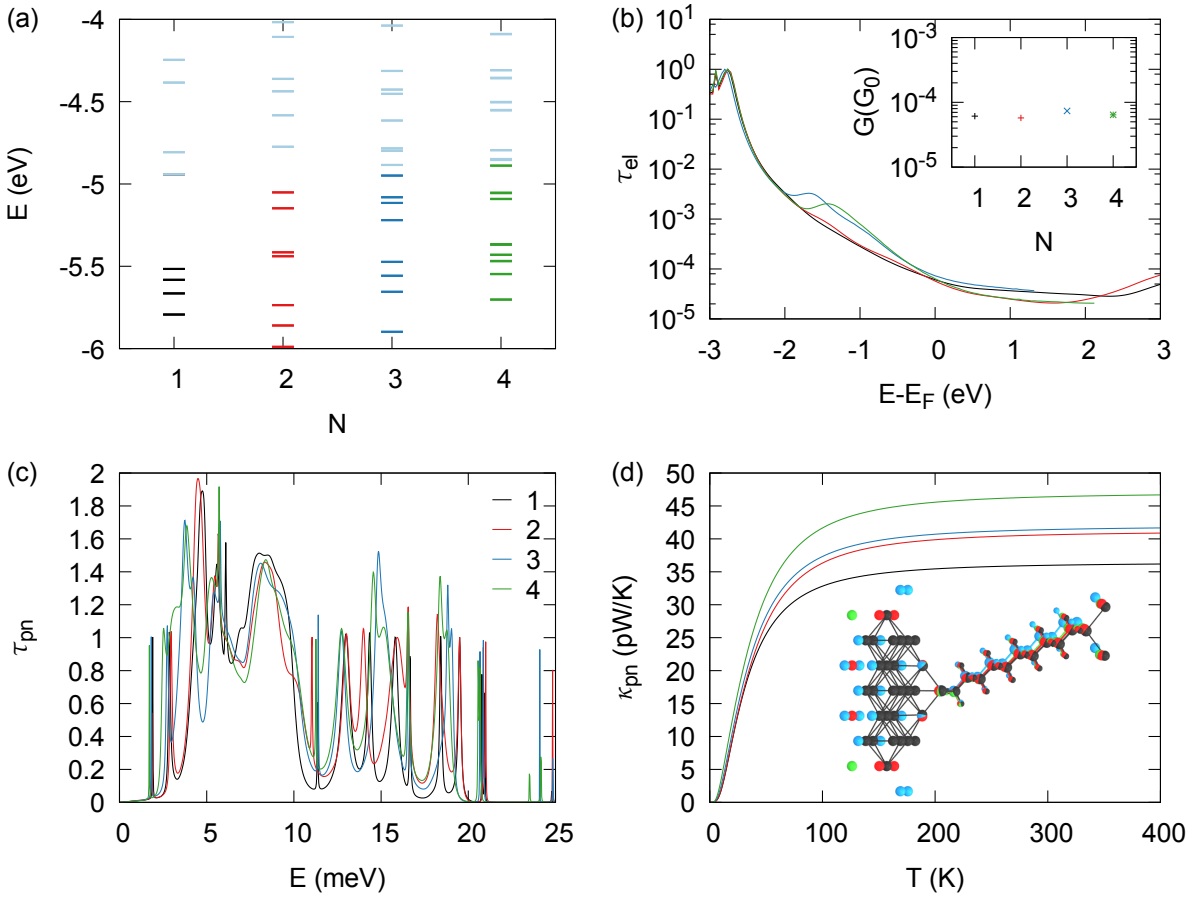

Figure 61. Same as Fig. 60 for a contact oriented along (110) direction.

Next, we look at ECCs with leads oriented along the (110) direction. The occupation is shown in Fig. 61(a). Except for the structure with N=2, almost degenerate levels at the energy of the highest occupied state appear. These unphysical, or unstable, situation is due to the finite size of the lead cluster and in general, can have an unwanted, and uncontrolled, influence on the force constant, which are evaluated in the framework of density functional perturbation theory. Nevertheless, in Fig. 61(b) the electronic transmission shows a nice convergence. The

phononic transmission alternates more compared to the (111) leads, although this variation can be partially explained due to the differences in the geometries. This time, the thermal conductance in Fig. 61(d) does not show a clear convergence.

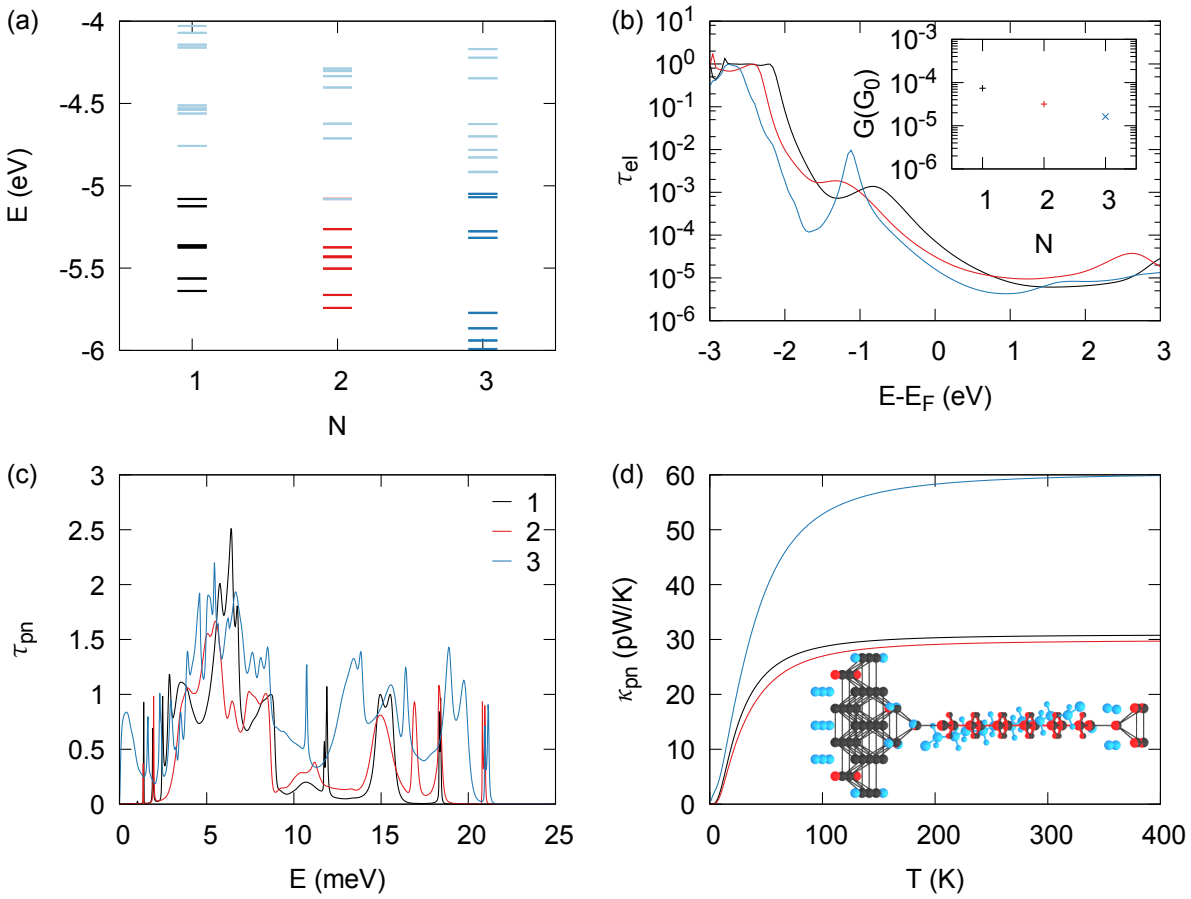

Figure 62. Same as Fig. 60 for a contact oriented along (100) direction.

At last, we show in Fig. 62(a) the occupation of the structure with a lead orientation in (100) direction. In all but the first structure, the levels at the energy of the HOMO are degenerate. The electronic transmission in Fig. 62(b) displays again a shift of the HOMO to lower energies with respect to the size of the clusters and the electronic conductance shows a monotonic trend towards convergence. However, the phononic thermal conductance of the biggest cluster, this time, strongly deviates in comparison to the smaller ones, which is due to a strong variation in the geometry.

E Benzene derivatives

In this appendix, we briefly discuss our results on the electronic contribution to the thermal conductance for the different molecular junctions investigated in Chap. 4.2. The aim is to show that the thermal transport in these junctions is dominated by phonons and that the interference effects predicted here should therefore be observable experimentally. We neglect contributions to the thermal conductance from NFRHT, whose significance can be controlled by the macroscopic shape of the electrodes, see Chap. 4.3.

As in the phononic case, we assume that the electronic transport is dominated by elastic tunneling processes. Thus, we compute the electronic contribution to the thermal conductance in the linear response regime within the Landauer-Büttiker formalism, as explained in Sec. 2.6.

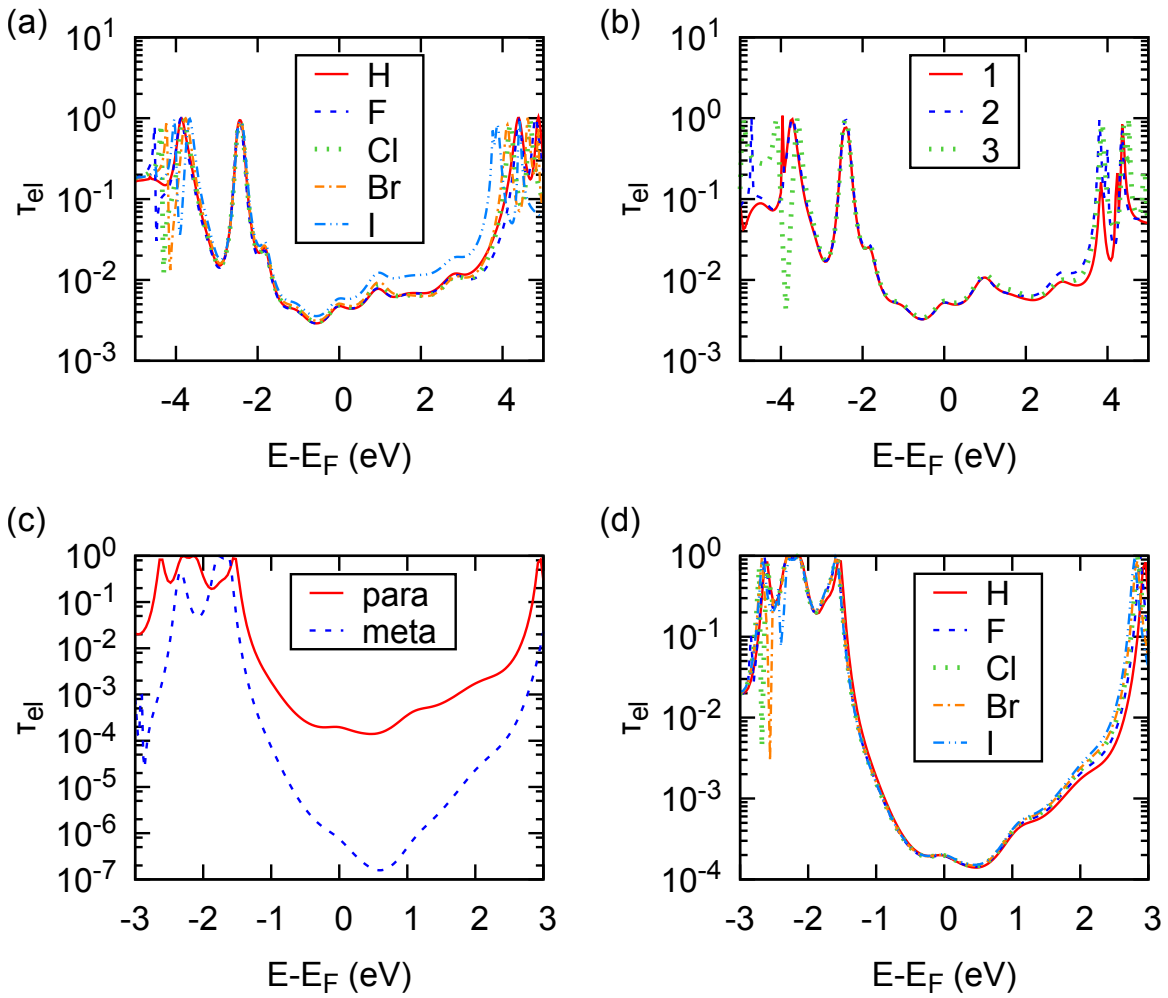

Figure 63. Electronic transmission as a function of energy, computed for (a) the molecular junctions of Fig. 36(b) based on benzene with a single halogen atom as substituent, (b) the junctions of Fig. 39 based on benzene with two Br atoms as substituents, (c) the para- and meta-bonded OPE3 junctions of Fig. 40(a) and (d) the OPE3-based junctions of Fig. 40(b) with a single substituent on the central benzene ring.

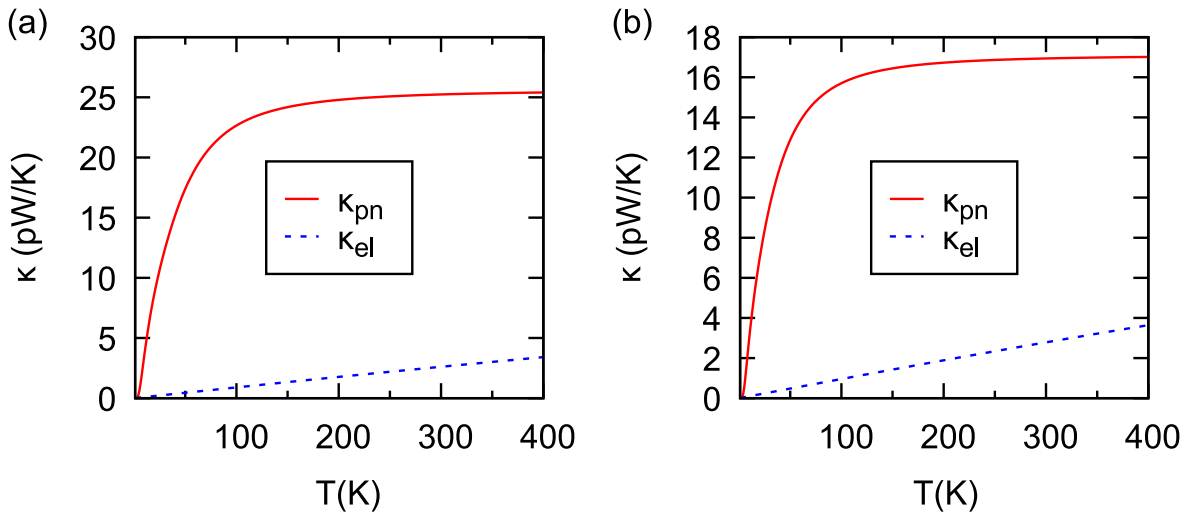

Figure 64. Temperature dependence of the phononic and electronic contribution to the thermal conductance for the (a) Au-1,4-diaminobenzene-Au and (b) Au-2-bromo-1,4-diaminobenzene-Au junctions of Fig. 36(b).

In Fig. 63 we show our results for the electronic transmission τ_{el} as a function of energy for all the junctions of Figs.39, and 40, based on both benzene and OPE3 derivatives. In all cases the electronic transport proceeds mainly through the tail of the HOMO of the molecule in an off-resonant situation. The results for the transport properties of these molecular junctions at room temperature are summarized in Table 3. We present there both the phononic and electronic thermal conductances κ_{pn} and κ_{el}, as well as the electrical conductance

$$G(T) = G_0 K_0(T), \tag{E.1}$$

with $G_0 = 2e^2/h$. Moreover, when available, we also report the experimental values for G. The electric conductance can be used together with the Wiedemann-Franz law $\kappa_{el} \approx L_0 G T$ with the Lorentz number $L_0 = (k_B/e)^2\pi^2/3$ to estimate the electronic thermal conductance. We find the Wiedemann-Franz law to be approximately fulfilled for our computed molecular junctions, and the comparison of experimental and theoretical electrical conductance values G can hence be used to estimate uncertainties in the theoretical κ_{el}.

The key point is that in all the studied cases the electronic thermal conductance is considerably smaller than the corresponding phononic thermal conductance. In particular, for the junctions based on the benzene derivatives the electronic contribution is at least 5 times smaller than the phononic one, while for the OPE3 compounds the electronic contribution is more than two orders of magnitude smaller. Due to their lower G the longer molecules are thus advantageous, if we want to exclude the contribution of electrons to heat transport.

Moreover, in order to illustrate that phonons dominate the thermal transport in these junctions for a wide temperature range, we show in Fig. 64 the temperature dependence of the phononic and electronic thermal conductances for the Au-1,4-diaminobenzene-Au and Au-2-bromo-1,4-diaminobenzene-Au junctions of Fig. 39. As one can see, the phononic contribution largely dominates at all temperatures between 10 and 400 K. Similar results hold for all the other molecular junctions.

To conclude, the results presented in this appendix confirm that the thermal transport in these molecular junctions is dominated by phonons. The predicted interference effects should, therefore, be visible in possible experiments.

Table 3. Computed room-temperature phononic thermal conductance κ_{pn}, electronic thermal conductance κ_{el} and electrical conductance G in units of the electrical conductance quantum $G_0 = 2e^2/h$ for the different molecular junctions investigated in this work. The last column shows, when available, the experimental value of the electrical conductance, as obtained from the peaks of conductance histograms. Experimental uncertainties due to broad distributions of conductance values have been omitted.

Molecule	κ_{pn} (pW/K)	κ_{el} (pW/K)	G (G_0) (theory)	G (G_0) (exp.)
1,4-diaminobenzene (para)	25.24	2.61	4.7×10^{-3}	6.4×10^{-3} [182]
2-fluoro-1,4-diaminobenzene	24.40	2.62	4.7×10^{-3}	5.8×10^{-3} [182]
2-chloro-1,4-diaminobenzene	22.17	2.70	4.9×10^{-3}	6.0×10^{-3} [182]
2-bromo-1,4-diaminobenzene	16.94	2.78	5.0×10^{-3}	6.1×10^{-3} [182]
2-iodo-1,4-diaminobenzene	15.24	3.25	5.8×10^{-3}	
2,5-dibromo-1,4-diaminobenzene	17.85	2.88	5.20×10^{-3}	
2,6-dibromo-1,4-diaminobenzene	10.46	2.88	5.19×10^{-3}	
2,3-dibromo-1,4-diaminobenzene	17.99	3.02	5.44×10^{-3}	
OPE3 (para)	24.57	0.11	1.94×10^{-4}	2.6×10^{-5} [322], 1.27×10^{-4} [323]
OPE3 (meta)	13.82	4.24×10^{-4}	7.53×10^{-7}	
F-OPE3	24.56	0.11	1.93×10^{-4}	
Cl-OPE3	23.12	0.11	1.96×10^{-4}	
Br-OPE3	19.62	0.11	1.97×10^{-4}	
I-OPE3	19.04	0.11	2.00×10^{-4}	

List of abbreviations

1D	One-dimensional
2D	Two-dimensional
3D	Three-dimensional
DFT	Density functional theory
DOS	Density of states
EAM	Embedded atom method
ECC	Extended central cluster
ECP	Effective core potential
HOMO	Highest occupied molecular orbital
LDOS	Local density of states
LUMO	Lowest unoccupied molecular orbital
MD	Molecular dynamics
NEGF	Non-equilibrium Green's function
NEMD	Non-equilibrium molecular dynamics
NFRHT	Near-field radiative heat transfer
OPE3	Oligo-phenylene-ethynylene
PBE	Perdew-Burke-Ernzerhof
PTFE	Polytetrafluoroethylene
REAXFF	Reactive force fields
SAM	Self-assembled monolayer
SThM	Scanning thermal microscope
STM	Scanning tunneling microscope

List of publications

Regular articles

- J. C. Klöckner, J. C. Cuevas, and F. Pauly. Transmission eigenchannels for coherent phonon transport. *Phys. Rev. B*, 97:155432, 2018
- J. C. Klöckner, J. C. Cuevas, and F. Pauly. Tuning the thermal conductance of molecular junctions with interference effects. *Phys. Rev. B*, 96:245419, 2017
- J. C. Klöckner, M. Matt, P. Nielaba, F. Pauly, and J. C. Cuevas. Thermal conductance of metallic atomic-size contacts: phonon transport and Wiedemann-Franz law. *Phys. Rev. B*, 96:205405, 2017
- J. C. Klöckner, R. Siebler, J. C. Cuevas, and F. Pauly. Thermal conductance and thermoelectric figure of merit of C60-based single-molecule junctions: Electrons, phonons, and photons. *Phys. Rev. B*, 95:245404, 2017
- L. Cui, W. Jeong, S. Hur, M. Matt, J. C. Klöckner, F. Pauly, P. Nielaba, J. C. Cuevas, E. Meyhofer, and P. Reddy. Quantized thermal transport in single-atom junctions. *Science*, 355:1192, 2017
- J. C. Klöckner, M. Bürkle, J. C. Cuevas, and F. Pauly. Length dependence of the thermal conductance of alkane-based single-molecule junctions: An ab-initio study. *Phys. Rev. B*, 94:205425, 2016

Bibliography

[1] J. C. Klöckner, J. C. Cuevas, and F. Pauly. Transmission eigenchannels for coherent phonon transport. *Phys. Rev. B*, 97:155432, 2018.

[2] L. Cui, W. Jeong, S. Hur, M. Matt, J. C. Klöckner, F. Pauly, P. Nielaba, J. C. Cuevas, E. Meyhofer, and P. Reddy. Quantized thermal transport in single-atom junctions. *Science*, 355(6330):1192–1195, 2017.

[3] J. C. Klöckner, M. Matt, P. Nielaba, F. Pauly, and J. C. Cuevas. Thermal conductance of metallic atomic-size contacts: Phonon transport and Wiedemann-Franz law. *Phys. Rev. B*, 96:205405, 2017.

[4] J. C. Klöckner, M. Bürkle, J. C. Cuevas, and F. Pauly. Length dependence of the thermal conductance of alkane-based single-molecule junctions: An ab initio study. *Phys. Rev. B*, 94:205425, 2016.

[5] J. C. Klöckner, J. C. Cuevas, and F. Pauly. Tuning the thermal conductance of molecular junctions with interference effects. *Phys. Rev. B*, 96:245419, 2017.

[6] J. C. Klöckner, R. Siebler, J. C. Cuevas, and F. Pauly. Thermal conductance and thermoelectric figure of merit of C_{60}-based single-molecule junctions: Electrons, phonons, and photons. *Phys. Rev. B*, 95:245404, 2017.

[7] G. Chen. *Nanoscale Energy Transport and Conversion: A Parallel Treatment of Electrons, Molecules, Phonons, and Photons*. MIT-Pappalardo Series in Mechanical Engineering. Oxford University Press, 2005.

[8] C. Kittel. *Introduction to Solid State Physics*. Wiley, Hoboken, 2004.

[9] P. Debye. Zur Theorie der spezifischen Wärmen. *Annalen der Physik*, 344(14):789–839, 1912.

[10] R.E. Peierls. *Quantum Theory of Solids*. International series of monographs on physics. Clarendon Press, Oxford, 1955.

[11] M. G. Holland. Analysis of lattice thermal conductivity. *Phys. Rev.*, 132:2461–2471, 1963.

[12] J. M. Ziman. *Electrons and phonons: the theory of transport phenomena in solids*. Clarendon Press, Oxford, 2007.

[13] D. A. Broido, M. Malorny, G. Birner, N. Mingo, and D. A. Stewart. Intrinsic lattice thermal conductivity of semiconductors from first principles. *Appl. Phys. Lett.*, 91(23):231922, 2007.

[14] L. Paulatto, F. Mauri, and M. Lazzeri. Anharmonic properties from a generalized third-order ab initio approach: Theory and applications to graphite and graphene. *Phys. Rev. B*, 87:214303, 2013.

[15] L. Lindsay, D. A. Broido, and T. L. Reinecke. First-principles determination of ultrahigh thermal conductivity of boron arsenide: A competitor for diamond? *Phys. Rev. Lett.*, 111:025901, 2013.

[16] G. A. S. Ribeiro, L. Paulatto, R. Bianco, I. Errea, F. Mauri, and M. Calandra. Strong anharmonicity in the phonon spectra of PbTe and SnTe from first principles. *Phys. Rev. B*, 97:014306, 2018.

[17] A. J. C. Ladd, B. Moran, and W. G. Hoover. Lattice thermal conductivity: A comparison

of molecular dynamics and anharmonic lattice dynamics. *Phys. Rev. B*, 34:5058–5064, 1986.

[18] A. J. H. McGaughey and M. Kaviany. Quantitative validation of the Boltzmann transport equation phonon thermal conductivity model under the single-mode relaxation time approximation. *Phys. Rev. B*, 69:094303, 2004.

[19] D. Donadio and G. Galli. Thermal conductivity of isolated and interacting carbon nanotubes: Comparing results from molecular dynamics and the Boltzmann transport equation. *Phys. Rev. Lett.*, 99:255502, 2007.

[20] J. M. Larkin, J. E. Turney, A. D. Massicotte, C. H. Amon, and A. J. H. McGaughey. Comparison and evaluation of spectral energy methods for predicting phonon properties. *J. Comput. Theor. Nanosci.*, 11(1):249–256, 2014.

[21] J. Rammer and H. Smith. Quantum field-theoretical methods in transport theory of metals. *Rev. Mod. Phys.*, 58:323–359, 1986.

[22] P. Chen, N. A. Katcho, J. P. Feser, W. Li, M. Glaser, O. G. Schmidt, D. G. Cahill, N. Mingo, and A. Rastelli. Role of surface-segregation-driven intermixing on the thermal transport through planar Si/Ge superlattices. *Phys. Rev. Lett.*, 111:115901, 2013.

[23] P. K. Schelling, S. R. Phillpot, and P. Keblinski. Comparison of atomic-level simulation methods for computing thermal conductivity. *Phys. Rev. B*, 65:144306, 2002.

[24] O. Delaire, J. Ma, K. Marty, A. F. May, M. A. McGuire, M.-H. Du, D. J. Singh, A. Podlesnyak, G. Ehlers, M. D. Lumsden, and B. C. Sales. Giant anharmonic phonon scattering in PbTe. *Nat. Mater.*, 10:614, 2011.

[25] L.-D. Zhao, S.-H. Lo, Y. Zhang, H. Sun, G. Tan, C. Uher, C. Wolverton, V. P. Dravid, and M. G. Kanatzidis. Ultralow thermal conductivity and high thermoelectric figure of merit in SnSe crystals. *Nature*, 508(7496):373–377, 2014.

[26] F. Tian, B. Song, X. Chen, N. K. Ravichandran, Y. Lv, K. Chen, S. Sullivan, J. Kim, Y. Zhou, T.-H. Liu, M. Goni, Z. Ding, J. Sun, G. A. G. Udalamatta Gamage, H. Sun, H. Ziyaee, S. Huyan, L. Deng, J. Zhou, A. J. Schmidt, S. Chen, C.-W. Chu, P. Y. Huang, D. Broido, L. Shi, G. Chen, and Z. Ren. Unusual high thermal conductivity in boron arsenide bulk crystals. *Science*, 361(6402):582–585, 2018.

[27] M. Maldovan. Sound and heat revolutions in phononics. *Nature*, 503(7475):209 – 217, 2013.

[28] M. Maldovan. Phonon wave interference and thermal bandgap materials. *Nat. Mater.*, 14(7):667–674, 2015.

[29] M. N. Luckyanova, J. Garg, K. Esfarjani, A. Jandl, M. T. Bulsara, A. J. Schmidt, A. J. Minnich, S. Chen, M. S. Dresselhaus, Z. Ren, E. A. Fitzgerald, and G. Chen. Coherent phonon heat conduction in superlattices. *Science*, 338(6109):936–939, 2012.

[30] C. W. Chang, D. Okawa, H. Garcia, A. Majumdar, and A. Zettl. Breakdown of Fourier's law in nanotube thermal conductors. *Phys. Rev. Lett.*, 101:075903, 2008.

[31] X. Xu, L. F. C. Pereira, Y. Wang, J. Wu, K. Zhang, X. Zhao, S. Bae, C. Tinh Bui, R. Xie, J. T. L. Thong, B. H. Hong, K. P. Loh, D. Donadio, B. Li, and B. Özyilmaz. Length-dependent thermal conductivity in suspended single-layer graphene. *Nat. Commun.*, 5:3689, 2014.

[32] A. Dhar. Heat transport in low-dimensional systems. *Adv. Phys.*, 57(5):PII 906324869, 2008.

[33] L. Wang, N. Li, and P. Hänggi. *Simulation of heat transport in low-dimensional oscillator lattices*, pages 239–274. Springer International Publishing, Cham, 2016.

[34] L. G. C. Rego and G. Kirczenow. Quantized thermal conductance of dielectric quantum wires. *Phys. Rev. Lett.*, 81:232–235, 1998.

[35] K. Schwab, E. A. Henriksen, J. M. Worlock, and M. L. Roukes. Measurement of the quantum of thermal conductance. *Nature*, 404:974, 2000.

[36] R. Anufriev, A. Ramiere, J. Maire, and M. Nomura. Heat guiding and focusing using ballistic phonon transport in phononic nanostructures. *Nat. Commun.*, 8:15505, 2017.

[37] M. Schmotz, J. Maier, E. Scheer, and P. Leiderer. A thermal diode using phonon rectification. *New J. Phys.*, 13(11):113027, 2011.

[38] S. I. Kim, K. H. Lee, H. A. Mun, H. S. Kim, S. W. Hwang, J. W. Roh, D. J. Yang, W. H. Shin, X. S. Li, Y. H. Lee, G. J. Snyder, and S. W. Kim. Dense dislocation arrays embedded in grain boundaries for high-performance bulk thermoelectrics. *Science*, 348(6230):109–114, 2015.

[39] J. C. Cuevas and F. J. García-Vidal. Radiative heat transfer. *ACS Photonics*, 5(10):3896–3915, 2018.

[40] E. Pop. Energy dissipation and transport in nanoscale devices. *Nano Res.*, 3(3):147–169, 2010.

[41] G. J. Snyder and E. S. Toberer. Complex thermoelectric materials. *Nat. Mater.*, 7(2):105–114, 2008.

[42] M. G. Kanatzidis. Nanostructured thermoelectrics: The new paradigm? *Chem. Mater.*, 22(3):648–659, 2010.

[43] B. Poudel, Q. Hao, Y. Ma, Y. Lan, A. Minnich, B. Yu, X. Yan, D. Wang, A. Muto, D. Vashaee, X. Chen, J. Liu, M. S. Dresselhaus, G. Chen, and Z. Ren. High-thermoelectric performance of nanostructured bismuth antimony telluride bulk alloys. *Science*, 320(5876):634–638, 2008.

[44] K. Biswas, J. He, I. D. Blum, C.-I. Wu, T. P. Hogan, D. N. Seidman, V. P. Dravid, and M. G. Kanatzidis. High-performance bulk thermoelectrics with all-scale hierarchical architectures. *Nature*, 489:414, 2012.

[45] J. Li, X. Zhang, Z. Chen, S. Lin, W. Li, J. Shen, I. T. Witting, A. Faghaninia, Y. Chen, A. Jain, L. Chen, G. J. Snyder, and Y. Pei. Low-symmetry rhombohedral GeTe thermoelectrics. *Joule*, 2(5):976 – 987, 2018.

[46] J. He and T. M. Tritt. Advances in thermoelectric materials research: Looking back and moving forward. *Science*, 357(6358), 2017.

[47] Y. Dubi and M. Di Ventra. *Colloquium* : Heat flow and thermoelectricity in atomic and molecular junctions. *Rev. Mod. Phys.*, 83:131–155, 2011.

[48] J.-S. Wang, J. Wang, and J. T. Lü. Quantum thermal transport in nanostructures. *Eur. Phys. J. B*, 62(4):381–404, 2008.

[49] J.S. Wang, B. Agarwalla, H. Li, and J. Thingna. Nonequilibrium Green's function method for quantum thermal transport. *Front. of Phys.*, 9(6):673–697, 2014.

[50] G. Stefanucci and R. van Leeuwen. *Nonequilibrium many-body theory of quantum systems: A modern introduction.* Cambridge University Press, Cambridge, 2013.

[51] J.-S. Wang, N. Zeng, J. Wang, and C. K. Gan. Nonequilibrium Green's function method for thermal transport in junctions. *Phys. Rev. E*, 75:061128, 2007.

[52] H. Haug and A.P. Jauho. *Quantum Kinetics in Transport and Optics of Semiconductors.* Springer Series in Solid-State Sciences. Springer, Berlin Heidelberg, 1998.

[53] H. Bruus and K. Flensberg. *Many-Body Quantum Theory in Condensed Matter Physics: An Introduction.* Oxford Graduate Texts. Oxford University Press, Oxford, 2004.

[54] J. C. Cuevas and E. Scheer. *Molecular Electronics: An Introduction to Theory and Experiment.* World Scientific, Singapore, 2nd edition edition, 2017.

[55] H. Li, B. K. Agarwalla, and J.-S. Wang. Generalized Caroli formula for the transmission coefficient with lead-lead coupling. *Phys. Rev. E*, 86:011141, 2012.

[56] N. Mingo and L. Yang. Phonon transport in nanowires coated with an amorphous material: An atomistic Green's function approach. *Phys. Rev. B*, 68:245406, 2003.

[57] J.-S. Wang, J. Wang, and N. Zeng. Nonequilibrium Green's function approach to mesoscopic thermal transport. *Phys. Rev. B*, 74:033408, 2006.

[58] C. Xiaobin, L. Yizhou, and D. Wenhui. Thermal engineering in low-dimensional quantum devices: A tutorial review of nonequilibrium Green's function methods. *Small Methods*, 2(6):1700343, 2018.

[59] T. Yamamoto and K. Watanabe. Nonequilibrium Green's function approach to phonon transport in defective carbon nanotubes. *Phys. Rev. Lett.*, 96:255503, 2006.

[60] G. Kirsanskas, Q. Li, K. Flensberg, G. C. Solomon, and M. Leijnse. Designing π-stacked molecular structures to control heat transport through molecular junctions. *Appl. Phys. Lett.*, 105(23), 2014.

[61] A. Szabo and N.S. Ostlund. *Modern quantum chemistry: Introduction to advanced electronic structure theory.* Dover Books on Chemistry. Dover Publications, Mineola New York, 1996.

[62] W. Koch and M.C. Holthausen. *A chemist's guide to density functional theory.* Wiley-VCH, Weinheim, 2000.

[63] T. Kizuka. Atomic configuration and mechanical and electrical properties of stable gold wires of single-atom width. *Phys. Rev. B*, 77:155401, 2008.

[64] F. Pauly, J. K. Viljas, U. Huniar, M. Haefner, S. Wohlthat, M. Buerkle, J. C. Cuevas, and G. Schoen. Cluster-based density-functional approach to quantum transport through molecular and atomic contacts. *New J. Phys.*, 10:125019, 2008.

[65] S. Datta. *Electronic transport in mesoscopic systems.* Cambridge Studies in Semiconductor Physics and Microelectronic Engineering. Cambridge University Press, Cambridge, 1997.

[66] J. P. Perdew and Y. Wang. Accurate and simple analytic representation of the electron-gas correlation-energy. *Phys. Rev. B*, 45(23):13244–13249, 1992.

[67] J. P. Perdew, K. Burke, and M. Ernzerhof. Generalized gradient approximation made simple. *Phys. Rev. Lett.*, 77(18):3865–3868, 1996.

[68] TURBOMOLE GmbH Karlsruhe, TURBOMOLE, http://www.turbomole.com. TURBOMOLE was a development of the University of Karlsruhe and Forschungszentrum Karlsruhe from 1989 to 2007, and development has been undertaken by TURBOMOLE GmbH since 2007.

[69] F. Weigend and R. Ahlrichs. Balanced basis sets of split valence, triple zeta valence and quadruple zeta valence quality for H to Rn: Design and assessment of accuracy. *Phys. Chem. Chem. Phys.*, 7(18):3297–3305, 2005.

[70] F. Weigend. Accurate Coulomb-fitting basis sets for H to Rn. *Phys. Chem. Chem. Phys.*, 8(9):1057–1065, 2006.

[71] P. Deglmann, F. Furche, and R. Ahlrichs. An efficient implementation of second analytical derivatives for density functional methods. *Chem. Phys. Lett.*, 362(5):511 – 518, 2002.

[72] P. Deglmann, K. May, F. Furche, and R. Ahlrichs. Nuclear second analytical derivative calculations using auxiliary basis set expansions. *Chem. Phys. Lett.*, 384(1):103 – 107, 2004.

[73] F. Guinea, C. Tejedor, F. Flores, and E. Louis. Effective two-dimensional Hamiltonian at surfaces. *Phys. Rev. B*, 28:4397–4402, 1983.

[74] F. Mueller-Plathe. A simple nonequilibrium molecular dynamics method for calculating the thermal conductivity. *J. Chem. Phys.*, 106(14):6082–6085, 1997.

[75] G. Ciccotti and A. Tenenbaum. Canonical ensemble and nonequilibrium states by molec-

ular dynamics. *J. Stat. Phys.*, 23(6):767–772, 1980.

[76] E. S. Landry and A. J. H. McGaughey. Thermal boundary resistance predictions from molecular dynamics simulations and theoretical calculations. *Phys. Rev. B*, 80:165304, 2009.

[77] Y. Chalopin, K. Esfarjani, A. Henry, S. Volz, and G. Chen. Thermal interface conductance in Si/Ge superlattices by equilibrium molecular dynamics. *Phys. Rev. B*, 85:195302, 2012.

[78] J.-L. Barrat and F. Chiaruttini. Kapitza resistance at the liquid-solid interface. *Mol. Phys.*, 101(11):1605–1610, 2003.

[79] S. Merabia and K. Termentzidis. Thermal conductance at the interface between crystals using equilibrium and nonequilibrium molecular dynamics. *Phys. Rev. B*, 86:094303, 2012.

[80] D. P. Sellan, E. S. Landry, J. E. Turney, A. J. H. McGaughey, and C. H. Amon. Size effects in molecular dynamics thermal conductivity predictions. *Phys. Rev. B*, 81:214305, 2010.

[81] Z. Liang and P. Keblinski. Finite-size effects on molecular dynamics interfacial thermal-resistance predictions. *Phys. Rev. B*, 90:075411, 2014.

[82] Z. Wang and X. Ruan. On the domain size effect of thermal conductivities from equilibrium and nonequilibrium molecular dynamics simulations. *J. Appl. Phys.*, 121(4):044301, 2017.

[83] S. Plimpton. Fast parallel algorithms for short-range molecular dynamics. *J. Comput. Phys.*, 117(1):1–19, 1995.

[84] W. C. Swope, H. C. Andersen, P. H. Berens, and K. R. Wilson. A computer simulation method for the calculation of equilibrium constants for the formation of physical clusters of molecules: Application to small water clusters. *J. Chem. Phys.*, 76(1):637–649, 1982.

[85] H. M. Flores Ruiz. *Modos vibracionales de baja frecuencia y su impacto en la formación de vidrios.* PhD thesis, Universidad nacional autonoma de Mexiko, 2012. pw:tesis.

[86] M. F. Russo and A. C. T. van Duin. Atomistic-scale simulations of chemical reactions: Bridging from quantum chemistry to engineering. *Nuc. Instr. Meth. Phys. Res. B*, 269(14):1549 – 1554, 2011.

[87] T. P. Senftle, S. Hong, M. M. Islam, S. B. Kylasa, Y. Zheng, Y. K. Shin, C. Junkermeier, R. Engel-Herbert, M. J. Janik, H. M. Aktulga, T. Verstraelen, A. Grama, and A. C. T. van Duin. The ReaxFF reactive force-field: development, applications and future directions. *NPJ Comput. Mater.*, 2:15011, 2016.

[88] W. J. Mortier, S. K. Ghosh, and S. Shankar. Electronegativity-equalization method for the calculation of atomic charges in molecules. *J. Am. Chem. Soc.*, 108(15):4315–4320, 1986.

[89] G. O. A. Janssens, B. G. Baekelandt, H. Toufar, W. J. Mortier, and R. A. Schoonheydt. Comparison of cluster and infinite crystal calculations on zeolites with the electronegativity equalization method (EEM). *J. Phys. Chem.*, 99(10):3251–3258, 1995.

[90] A. K. Rappe and W. A. Goddard. Charge equilibration for molecular dynamics simulations. *J. Phys. Chem.*, 95(8):3358–3363, 1991.

[91] K. Chenoweth, A. C. T. van Duin, and W. A. Goddard. ReaxFF reactive force field for molecular dynamics simulations of hydrocarbon oxidation. *J. Phys. Chem. A*, 112(5):1040–1053, 2008.

[92] Y. Tanaka, F. Yoshida, and S. Tamura. Lattice thermal conductance in nanowires at low temperatures: Breakdown and recovery of quantization. *Phys. Rev. B*, 71:205308, 2005.

[93] V. B. Antonyuk, M. Larsson, A. G. Mal'shukov, and K. A. Chao. Phonon transmission in III-V semiconductor superlattices and alloys. *Semicond. Sci. Technol.*, 20(5):347, 2005.

[94] P. G. Murphy and J. E. Moore. Coherent phonon scattering effects on thermal transport

in thin semiconductor nanowires. *Phys. Rev. B*, 76:155313, 2007.

[95] Z.-Y. Ong and G. Zhang. Efficient approach for modeling phonon transmission probability in nanoscale interfacial thermal transport. *Phys. Rev. B*, 91:174302, 2015.

[96] S. Sadasivam, U. V. Waghmare, and T. S. Fisher. Phonon-eigenspectrum-based formulation of the atomistic Green's function method. *Phys. Rev. B*, 96:174302, 2017.

[97] Z.-X. Xie, K.-Q. Chen, and W. Duan. Thermal transport by phonons in zigzag graphene nanoribbons with structural defects. *J. Phys. Condens. Matter*, 23(31):315302, 2011.

[98] J. Wang, L. Li, and J.-S. Wang. Tuning thermal transport in nanotubes with topological defects. *Appl. Phys. Lett.*, 99(9):091905, 2011.

[99] T. Ouyang, Y. Chen, L.-M. Liu, Y. Xie, X. Wei, and J. Zhong. Thermal transport in graphyne nanoribbons. *Phys. Rev. B*, 85:235436, 2012.

[100] X.-F. Peng and K.-Q. Chen. Thermal transport for flexural and in-plane phonons in graphene nanoribbons. *Carbon*, 77:360, 2014.

[101] M. Paulsson and M. Brandbyge. Transmission eigenchannels from nonequilibrium Green's functions. *Phys. Rev. B*, 76:115117, 2007.

[102] A. M. Kriman, N. C. Kluksdahl, and D. K. Ferry. Scattering states and distribution functions for microstructures. *Phys. Rev. B*, 36:5953–5959, 1987.

[103] M. Büttiker. Scattering theory of current and intensity noise correlations in conductors and wave guides. *Phys. Rev. B*, 46:12485–12507, 1992.

[104] J. E. G. Farina. *Quantum theory of scattering processes.* The international encyclopedia of physical chemistry and chemical physics. Topic 2: Classical and quantum mechanics, v. 4. Pergamon Press, Oxford, 1. ed. edition, 1973.

[105] N. Mingo. Anharmonic phonon flow through molecular-sized junctions. *Phys. Rev. B*, 74:125402, 2006.

[106] M. Bürkle, J. K. Viljas, D. Vonlanthen, A. Mishchenko, G. Schön, M. Mayor, T. Wandlowski, and F. Pauly. Conduction mechanisms in biphenyl dithiol single-molecule junctions. *Phys. Rev. B*, 85:075417, 2012.

[107] N. W. Ashcroft and N. Mermin. *Solid state physics.* Holt, Rinehart and Winston, New York, 1976.

[108] V. Lee, C.-H. Wu, Z.-X. Lou, W.-L. Lee, and C.-W. Chang. Divergent and ultrahigh thermal conductivity in millimeter-long nanotubes. *Phys. Rev. Lett.*, 118:135901, 2017.

[109] M. Buerkle, T. J. Hellmuth, F. Pauly, and Y. Asai. First-principles calculation of the thermoelectric figure of merit for [2,2]paracyclophane-based single-molecule junctions. *Phys. Rev. B*, 91(16):165419, 2015.

[110] J.-W. Jiang, B.-S. Wang, and J.-S. Wang. First principle study of the thermal conductance in graphene nanoribbon with vacancy and substitutional silicon defects. *Appl. Phys. Lett.*, 98(11):113114, 2011.

[111] N. Mingo, D. A. Stewart, D. A. Broido, and D. Srivastava. Phonon transmission through defects in carbon nanotubes from first principles. *Phys. Rev. B*, 77:033418, 2008.

[112] N. Mounet. Structural, vibrational and thermodynamic properties of carbon allotropes from first-principles : diamond, graphite, and nanotubes. Master's thesis, Massachusetts Institute of Technology, 2005.

[113] A. Chaudhuri, A. Kundu, D. Roy, A. Dhar, J. L. Lebowitz, and H. Spohn. Heat transport and phonon localization in mass-disordered harmonic crystals. *Phys. Rev. B*, 81:064301, 2010.

[114] U. Sivan and Y. Imry. Multichannel Landauer formula for thermoelectric transport with application to thermopower near the mobility edge. *Phys. Rev. B*, 33(1):551–558, 1986.

[115] S. Y. Quek, L. Venkataraman, H. J. Choi, S. G. Louie, M. S. Hybertsen, and J. B. Neaton. Amine-gold linked single-molecule circuits: Experiment and theory. *Nano Lett.*, 7(11):3477–3482, 2007.

[116] S. Y. Quek, H. J. Choi, S. G. Louie, and J. B. Neaton. Length dependence of conductance in aromatic single-molecule junctions. *Nano Lett.*, 9(11):3949–3953, 2009.

[117] S. Y. Quek, H. J. Choi, S. G. Louie, and J. B. Neaton. Thermopower of amine-gold-linked aromatic molecular junctions from first principles. *ACS Nano*, 5(1):551–557, 2011.

[118] L. A. Zotti, M. Bürkle, F. Pauly, W. Lee, K. Kim, W. Jeong, Y. Asai, P. Reddy, and J. C. Cuevas. Heat dissipation and its relation to thermopower in single-molecule junctions. *New J. Phys.*, 16(1):015004, 2014.

[119] J. B. Neaton, M. S. Hybertsen, and S. G. Louie. Renormalization of molecular electronic levels at metal-molecule interfaces. *Phys. Rev. Lett.*, 97:216405, 2006.

[120] S. M. Rytov, Y. A. Kravtsov, and V. I. Tatarskii. *Principles of statistical radiophysics 3: Elements of random fields.* Springer, Berlin, 1989.

[121] D. Polder and M. Van Hove. Theory of radiative heat transfer between closely spaced bodies. *Phys. Rev. B*, 4:3303–3314, 1971.

[122] M. A. Ordal, L. L. Long, R. J. Bell, S. E. Bell, R. R. Bell, R. W. Alexander, and C. A. Ward. Optical properties of the metals Al, Co, Cu, Au, Fe, Pb, Ni, Pd, Pt, Ag, Ti, and W in the infrared and far infrared. *Appl. Opt.*, 22(7):1099–1119, 1983.

[123] P.-O. Chapuis, S. Volz, C. Henkel, K. Joulain, and J.-J. Greffet. Effects of spatial dispersion in near-field radiative heat transfer between two parallel metallic surfaces. *Phys. Rev. B*, 77:035431, 2008.

[124] B. V. Derjaguin, I. I. Abrikosova, and E. M. Lifshitz. Direct measurement of molecular attraction between solids separated by a narrow gap. *Q. Rev. Chem. Soc.*, 10:295–329, 1956.

[125] K. Sasihithlu and A. Narayanaswamy. Proximity effects in radiative heat transfer. *Phys. Rev. B*, 83:161406, 2011.

[126] C. Otey and S. Fan. Numerically exact calculation of electromagnetic heat transfer between a dielectric sphere and plate. *Phys. Rev. B*, 84:245431, 2011.

[127] B. Song, Y. Ganjeh, S. Sadat, D. Thompson, A. Fiorino, V. Fernández-Hurtado, J. Feist, F. J. García-Vidal, J. C. Cuevas, P. Reddy, and E. Meyhofer. Enhancement of near-field radiative heat transfer using polar dielectric thin films. *Nat. Nanotechnol.*, 10(3):253–258, 2015.

[128] J. M. Krans, J. M. van Ruitenbeek, V. Fisun, I. Yanson, and L. J. de Jongh. The signature of conductance quantization in metallic point contacts. *Nature*, 375:767, 1995.

[129] E. Scheer, N. Agraït, J. C. Cuevas, A. L. Yeyati, B. Ludoph, A. Martin-Rodero, G. Rubio-Bollinger, J. M. van Ruitenbeek, and C. Urbina. The signature of chemical valence in the electrical conduction through a single-atom contact. *Nature*, 394(6689):154–157, 1998.

[130] H. E. van den Brom and J. M. van Ruitenbeek. Quantum suppression of shot noise in atom-size metallic contacts. *Phys. Rev. Lett.*, 82:1526, 1999.

[131] P. J. Wheeler, J. N. Russom, K. Evans, N. S. King, and D. Natelson. Shot noise suppression at room temperature in atomic-scale Au junctions. *Nano Lett.*, 10(4):1287–1292, 2010.

[132] R. Chen, P. J. Wheeler, and D. Natelson. Excess noise in STM-style break junctions at room temperature. *Phys. Rev. B*, 85:235455, 2012.

[133] R. Vardimon, M. Matt, P. Nielaba, J. C. Cuevas, and O. Tal. Orbital origin of the electrical conduction in ferromagnetic atomic-size contacts: Insights from shot noise measurements and theoretical simulations. *Phys. Rev. B*, 93:085439, 2016.

[134] D. C. Guhr, D. Rettinger, J. Boneberg, A. Erbe, P. Leiderer, and E. Scheer. Influence of laser light on electronic transport through atomic-size contacts. *Phys. Rev. Lett.*, 99:086801, 2007.

[135] J. K. Viljas and J. C. Cuevas. Role of electronic structure in photoassisted transport through atomic-sized contacts. *Phys. Rev. B*, 75:075406, 2007.

[136] N. Ittah, G. Noy, I. Yutsis, and Y. Selzer. Measurement of electronic transport through 1G0 gold contacts under laser irradiation. *Nano Lett.*, 9(4):1615–1620, 2009.

[137] D. R. Ward, F. Hüser, F. Pauly, J. C. Cuevas, and D. Natelson. Optical rectification and field enhancement in a plasmonic nanogap. *Nat. Nanotechnol.*, 5:732, 2010.

[138] B. Ludoph and J. M. van Ruitenbeek. Thermopower of atomic-size metallic contacts. *Phys. Rev. B*, 59:12290–12293, 1999.

[139] M. Tsutsui, T. Morikawa, A. Arima, and M. Taniguchi. Thermoelectricity in atom-sized junctions at room temperatures. *Sci. Rep.*, 3:3326, 2013.

[140] C. Evangeli, M. Matt, L. Rincón-García, F. Pauly, P. Nielaba, G. Rubio-Bollinger, J. C. Cuevas, and N. Agraït. Quantum thermopower of metallic atomic-size contacts at room temperature. *Nano Lett.*, 15(2):1006–1011, 2015.

[141] A. Ofarim, B. Kopp, T. Möller, L. Martin, J. Boneberg, P. Leiderer, and E. Scheer. Thermo-voltage measurements of atomic contacts at low temperature. *Beilstein J. Nanotechnol.*, 7:767–775, 2016.

[142] W. Lee, K. Kim, W. Jeong, L. A. Zotti, F. Pauly, J. C. Cuevas, and P. Reddy. Heat dissipation in atomic-scale junctions. *Nature*, 498(7453):209–212, 2013.

[143] L. Cui, R. Miao, C. Jiang, E. Meyhofer, and P. Reddy. Perspective: Thermal and thermoelectric transport in molecular junctions. *J. Chem. Phys.*, 146(9):092201, 2017.

[144] N. Mosso, U. Drechsler, F. Menges, P. Nirmalraj, S. Karg, H. Riel, and B. Gotsmann. Heat transport through atomic contacts. *Nat. Nanotechnol.*, 12:430, 2017.

[145] M. Dreher, F. Pauly, J. Heurich, J. C. Cuevas, E. Scheer, and P. Nielaba. Structure and conductance histogram of atomic-sized Au contacts. *Phys. Rev. B*, 72:075435, 2005.

[146] G. Rubio-Bollinger, C. de las Heras, E. Bascones, N. Agraït, F. Guinea, and S. Vieira. Single-channel transmission in gold one-atom contacts and chains. *Phys. Rev. B*, 67:121407, 2003.

[147] G. Rubio-Bollinger, S. R. Bahn, N. Agraït, K. W. Jacobsen, and S. Vieira. Mechanical properties and formation mechanisms of a wire of single gold atoms. *Phys. Rev. Lett.*, 87:026101, 2001.

[148] R. H. M. Smit, C. Untiedt, G. Rubio-Bollinger, R. C. Segers, and J. M. van Ruitenbeek. Observation of a parity oscillation in the conductance of atomic wires. *Phys. Rev. Lett.*, 91:076805, 2003.

[149] A. I. Yanson, G. Rubio-Bollinger, H. E. van den Brom, N. Agraït, and J. M. van Ruitenbeek. Formation and manipulation of a metallic wire of single gold atoms. *Nature*, 395:783, 1998.

[150] H. Ohnishi, Y. Kondo, and K. Takayanagi. Quantized conductance through individual rows of suspended gold atoms. *Nature*, 395:780, 1998.

[151] V. Rodrigues, T. Fuhrer, and D. Ugarte. Signature of atomic structure in the quantum conductance of gold nanowires. *Phys. Rev. Lett.*, 85:4124–4127, 2000.

[152] N. Agraït, A. Levy Yeyati, and J. M. van Ruitenbeek. Quantum properties of atomic-sized conductors. *Phys. Rep.*, 377(2):81 – 279, 2003.

[153] F. Pauly, M. Dreher, J. K. Viljas, M. Häfner, J. C. Cuevas, and P. Nielaba. Theoretical analysis of the conductance histograms and structural properties of Ag, Pt, and Ni nanocontacts. *Phys. Rev. B*, 74:235106, 2006.

[154] K. Sasikumar and P. Keblinski. Effect of chain conformation in the phonon transport across a Si-polyethylene single-molecule covalent junction. *J. Appl. Phys.*, 109(11):114307, 2011.

[155] M. Buerkle and Y. Asai. Thermal conductance of teflon and polyethylene: Insight from an atomistic, single-molecule level. *Sci. Rep.*, 7:41898, 2017.

[156] H. W. Sheng, M. J. Kramer, A. Cadien, T. Fujita, and M. W. Chen. Highly optimized embedded-atom-method potentials for fourteen fcc metals. *Phys. Rev. B*, 83:134118, 2011.

[157] L. Zhang, J. Thingna, D. He, J.-S. Wang, and B. Li. Nonlinearity enhanced interfacial thermal conductance and rectification. *EPL*, 103(6):64002, 2013.

[158] D. He, J. Thingna, J.-S. Wang, and B. Li. Quantum thermal transport through anharmonic systems: A self-consistent approach. *Phys. Rev. B*, 94:155411, 2016.

[159] J. Li, T. C. A. Yeung, C. H. Kam, Y. Peng, Q.-H. Chen, X. Zhao, and C. Q. Sun. Anharmonic phonon transport in atomic wire coupled by thermal contacts with surface bond reconstruction. *J. Appl. Phys.*, 106(1):014308, 2009.

[160] M. J. Mehl and D. A. Papaconstantopoulos. Applications of a tight-binding total-energy method for transition and noble metals: Elastic constants, vacancies, and surfaces of monatomic metals. *Phys. Rev. B*, 54:4519–4530, 1996.

[161] M. J. Mehl and D. A. Papaconstantopoulos. *Topics in computational materials science*. World Scientific, Singapore, 1998.

[162] C. Sirvent, J. G. Rodrigo, S. Vieira, L. Jurczyszyn, N. Mingo, and F. Flores. Conductance step for a single-atom contact in the scanning tunneling microscope: Noble and transition metals. *Phys. Rev. B*, 53:16086–16090, 1996.

[163] S. K. Nielsen, Y. Noat, M. Brandbyge, R. H. M. Smit, K. Hansen, L. Y. Chen, A. I. Yanson, F. Besenbacher, and J. M. van Ruitenbeek. Conductance of single-atom platinum contacts: Voltage dependence of the conductance histogram. *Phys. Rev. B*, 67:245411, 2003.

[164] F. Pauly, J. K. Viljas, M. Bürkle, M. Dreher, P. Nielaba, and J. C. Cuevas. Molecular dynamics study of the thermopower of Ag, Au, and Pt nanocontacts. *Phys. Rev. B*, 84:195420, 2011.

[165] E. Scheer, P. Joyez, D. Esteve, C. Urbina, and M. H. Devoret. Conduction channel transmissions of atomic-size aluminum contacts. *Phys. Rev. Lett.*, 78:3535–3538, 1997.

[166] J. C. Cuevas, A. Levy Yeyati, and A. Martín-Rodero. Microscopic origin of conducting channels in metallic atomic-size contacts. *Phys. Rev. Lett.*, 80:1066–1069, 1998.

[167] J. C. Cuevas, A. Levy Yeyati, A. Martín-Rodero, G. Rubio Bollinger, C. Untiedt, and N. Agraït. Evolution of conducting channels in metallic atomic contacts under elastic deformation. *Phys. Rev. Lett.*, 81:2990–2993, 1998.

[168] P. Jelínek, R. Pérez, J. Ortega, and F. Flores. First-principles simulations of the stretching and final breaking of Al nanowires: Mechanical properties and electrical conductance. *Phys. Rev. B*, 68:085403, 2003.

[169] C. Schirm, M. Matt, F. Pauly, J. C. Cuevas, P. Nielaba, and E. Scheer. A current-driven single-atom memory. *Nat. Nanotechnol.*, 8:645, 2013.

[170] N. Kobayashi, M. Brandbyge, and M. Tsukada. First-principles study of electron transport through monatomic Al and Na wires. *Phys. Rev. B*, 62:8430–8437, 2000.

[171] D. Sánchez-Portal, C. Untiedt, J. M. Soler, J. J. Sáenz, and N. Agraït. Nanocontacts: Probing electronic structure under extreme uniaxial strains. *Phys. Rev. Lett.*, 79:4198–4201, 1997.

[172] A. Hasmy, A. J. Pérez-Jiménez, J. J. Palacios, P. García-Mochales, J. L. Costa-Krämer, M. Díaz, E. Medina, and P. A. Serena. Ballistic resistivity in aluminum nanocontacts.

Phys. Rev. B, 72:245405, 2005.

[173] X.-Y. Liu, F. Ercolessi, and J. B. Adams. Aluminium interatomic potential from density functional theory calculations with improved stacking fault energy. *Modell. Simul. Mater. Sci. Eng.*, 12(4):665, 2004.

[174] M. Matt. *Theoretical study of the charge and energy transport in metallic atom-size contacts*. PhD thesis, University of Konstanz, 2017.

[175] A. Aviram and M. A. Ratner. Molecular rectifiers. *Chem. Phys. Lett.*, 29(2):277 – 283, 1974.

[176] C. Joachim, J. K. Gimzewski, and A. Aviram. Electronics using hybrid-molecular and mono-molecular devices. *Nature*, 408:541, 2000.

[177] R. H. M. Smit, Y. Noat, C. Untiedt, N. D. Lang, M. C. van Hemert, and J. M. van Ruitenbeek. Measurement of the conductance of a hydrogen molecule. *Nature*, 419:906, 2002.

[178] B. Xu and N. J. Tao. Measurement of single-molecule resistance by repeated formation of molecular junctions. *Science*, 301(5637):1221–1223, 2003.

[179] L. Venkataraman, J. E. Klare, C. Nuckolls, M. S. Hybertsen, and M. L. Steigerwald. Dependence of single-molecule junction conductance on molecular conformation. *Nature*, 442:904, 2006.

[180] Y. S. Park, A. C. Whalley, M. Kamenetska, M. L. Steigerwald, M. S. Hybertsen, C. Nuckolls, and L. Venkataraman. Contact chemistry and single-molecule conductance: A comparison of phosphines, methyl sulfides, and amines. *J. Am. Chem. Soc.*, 129(51):15768–15769, 2007.

[181] E. Leary, A. La Rosa, M. T. González, G. Rubio-Bollinger, N. Agraït, and N. Martín. Incorporating single molecules into electrical circuits. The role of the chemical anchoring group. *Chem. Soc. Rev.*, 44:920–942, 2015.

[182] L. Venkataraman, Y. S. Park, A. C. Whalley, C. Nuckolls, M. S. Hybertsen, and M. L. Steigerwald. Electronics and chemistry: Varying single-molecule junction conductance using chemical substituents. *Nano Lett.*, 7(2):502–506, 2007.

[183] J. Vacek, J. V. Chocholoušová, I. G. Stará, I. Starý, and Y. Dubi. Mechanical tuning of conductance and thermopower in helicene molecular junctions. *Nanoscale*, 7:8793–8802, 2015.

[184] D. Stefani, K. J. Weiland, M. Skripnik, C. Hsu, M. L. Perrin, M. Mayor, F. Pauly, and H. S. J. van der Zant. Large conductance variations in a mechanosensitive single-molecule junction. *Nano Lett.*, 18(9):5981–5988, 2018.

[185] C. Jia, A. Migliore, N. Xin, S. Huang, J. Wang, Q. Yang, S. Wang, H. Chen, D. Wang, B. Feng, Z. Liu, G. Zhang, D.-H. Qu, H. Tian, M. A. Ratner, H. Q. Xu, A. Nitzan, and X. Guo. Covalently bonded single-molecule junctions with stable and reversible photoswitched conductivity. *Science*, 352(6292):1443–1445, 2016.

[186] M. Frei, S. V. Aradhya, M. S. Hybertsen, and L. Venkataraman. Linker dependent bond rupture force measurements in single-molecule junctions. *J. Am. Chem. Soc.*, 134(9):4003–4006, 2012.

[187] M. S. Hybertsen and L. Venkataraman. Structure-property relationships in atomic-scale junctions: Histograms and beyond. *Acc. Chem. Res.*, 49(3):452–460, 2016.

[188] M. H. Garner, H. Li, Y. Chen, T. A. Su, Z. Shangguan, D. W. Paley, T. Liu, F. Ng, H. Li, S. Xiao, C. Nuckolls, L. Venkataraman, and G. C. Solomon. Comprehensive suppression of single-molecule conductance using destructive σ-interference. *Nature*, 2018.

[189] P. Reddy, S.-Y. Jang, R. A. Segalman, and A. Majumdar. Thermoelectricity in molecular junctions. *Science*, 315(5818):1568–1571, 2007.

[190] Y. Kim, W. Jeong, K. Kim, W. Lee, and P. Reddy. Electrostatic control of thermoelectricity in molecular junctions. *Nat. Nanotechnol.*, 9(11):881–885, 2014.

[191] L. Rincon-Garcia, C. Evangeli, G. Rubio-Bollinger, and N. Agrait. Thermopower measurements in molecular junctions. *Chem. Soc. Rev.*, 45(15):4285–4306, 2016.

[192] L. Cui, R. Miao, K. Wang, D. Thompson, L. A. Zotti, J. C. Cuevas, E. Meyhofer, and P. Reddy. Peltier cooling in molecular junctions. *Nat. Nanotechnol.*, 13(2):122–127, 2018.

[193] D. Segal and B. K. Agarwalla. Vibrational heat transport in molecular junctions. *Annu. Rev. Phys. Chem.*, 67(1):185, 2016.

[194] T. Luo and J. R. Lloyd. Non-equilibrium molecular dynamics study of thermal energy transport in Au-SAM-Au junctions. *Int. J. Heat Mass Transfer*, 53(1):1, 2010.

[195] J. C. Duda, C. B. Saltonstall, P. M. Norris, and P. E. Hopkins. Assessment and prediction of thermal transport at solid-self-assembled monolayer junctions. *J. Chem. Phys.*, 134(9):094704, 2011.

[196] S. Majumdar, J. A. Sierra-Suarez, S. N. Schiffres, W.-L. Ong, C. F. Higgs, A. J. H. McGaughey, and J. A. Malen. Vibrational mismatch of metal leads controls thermal conductance of self-assembled monolayer junctions. *Nano Lett.*, 15(5):2985, 2015.

[197] J. Liu and R. Yang. Length-dependent thermal conductivity of single extended polymer chains. *Phys. Rev. B*, 86:104307, 2012.

[198] J.-S. Wang, N. Zeng, J. Wang, and C. K. Gan. Nonequilibrium Green's function method for thermal transport in junctions. *Phys. Rev. E*, 75:061128, 2007.

[199] J. T. Gaskins, A. Bulusu, A. J. Giordano, J. C. Duda, S. Graham, and P. E. Hopkins. Thermal conductance across phosphonic acid molecules and interfaces: Ballistic versus diffusive vibrational transport in molecular monolayers. *J. Phys. Chem. C*, 119(36):20931–20939, 2015.

[200] P. J. O' Brien, S. Shenogin, J. Liu, P. K. Chow, D. Laurencin, P. H. Mutin, M. Yamaguchi, P. Keblinski, and G. Ramanath. Bonding-induced thermal conductance enhancement at inorganic heterointerfaces using nanomolecular monolayers. *Nat. Mater.*, 12:118, 2012.

[201] T. Meier, F. Menges, P. Nirmalraj, H. Hoelscher, H. Riel, and B. Gotsmann. Length-dependent thermal transport along molecular chains. *Phys. Rev. Lett.*, 113(6):060801, 2014.

[202] D. Segal, A. Nitzan, and P. Hanggi. Thermal conductance through molecular wires. *J. Chem. Phys.*, 119(13):6840–6855, 2003.

[203] Y. Asai. Nonequilibrium phonon effects on transport properties through atomic and molecular bridge junctions. *Phys. Rev. B*, 78:045434, 2008.

[204] L. Hu, L.and Zhang, M. Hu, J.-S. Wang, B. Li, and P. Keblinski. Phonon interference at self-assembled monolayer interfaces: Molecular dynamics simulations. *Phys. Rev. B*, 81:235427, 2010.

[205] Q. Li, I. Duchemin, S. Xiong, G. C. Solomon, and D. Donadio. Mechanical tuning of thermal transport in a molecular junction. *J. Phys. Chem. C*, 119(43):24636–24642, 2015.

[206] Q. Li, M. Strange, I. Duchemin, D. Donadio, and G. C. Solomon. A strategy to suppress phonon transport in molecular junctions using π-stacked systems. *J. Phys. Chem. C*, 121(13):7175, 2017.

[207] M. Royo, A. Antidormi, and R. Rurali. A thermal switch for coherent phonons based on a molecular junction. *J. Phys. Chem. C*, 121(19):10571–10576, 2017.

[208] R. Ranganathan, K. Sasikumar, and P. Keblinski. Realizing tunable molecular thermal devices based on photoisomerism? Is it possible? *J. Appl. Phys.*, 117(2):025305, 2015.

[209] H. Sadeghi, S. Sangtarash, and C. J. Lambert. Oligoyne molecular junctions for efficient room temperature thermoelectric power generation. *Nano Lett.*, 15(11):7467–7472, 2015.

[210] S. Lepri, R. Livi, and A. Politi. Thermal conduction in classical low-dimensional lattices. *Phys. Rep. Sec. Phys. Lett.*, 377(1):1–80, 2003.

[211] X. D. Cui, A. Primak, X. Zarate, J. Tomfohr, O. F. Sankey, A. L. Moore, T. A. Moore, D. Gust, G. Harris, and S. M. Lindsay. Reproducible measurement of single-molecule conductivity. *Science*, 294(5542):571–574, 2001.

[212] W. Y. Wang, T. Lee, and M. A. Reed. Mechanism of electron conduction in self-assembled alkanethiol monolayer devices. *Phys. Rev. B*, 68(3):035416, 2003.

[213] W. Haiss, R. J. Nichols, H. van Zalinge, S. J. Higgins, D. Bethell, and D. J. Schiffrin. Measurement of single molecule conductivity using the spontaneous formation of molecular wires. *Phys. Chem. Chem. Phys.*, 6(17):4330–4337, 2004.

[214] X. L. Li, J. He, J. Hihath, B. Q. Xu, S. M. Lindsay, and N. J. Tao. Conductance of single alkanedithiols: Conduction mechanism and effect of molecule-electrode contacts. *J. Am. Chem. Soc.*, 128(6):2135–2141, 2006.

[215] M. T. González, S. Wu, R. Huber, S. J. van der Molen, C. Schoenenberger, and M. Calame. Electrical conductance of molecular junctions by a robust statistical analysis. *Nano Lett.*, 6(10):2238–2242, 2006.

[216] M. Fujihira, M. Suzuki, S. Fujii, and A. Nishikawa. Currents through single molecular junction of Au/hexanedithiolate/Au measured by repeated formation of break junction in STM under UHV: Effects of conformational change in an alkylene chain from gauche to trans and binding sites of thiolates on gold. *Phys. Chem. Chem. Phys.*, 8(33):3876–3884, 2006.

[217] S.-Y. Jang, P. Reddy, A. Majumdar, and R. A. Segalman. Interpretation of stochastic events in single molecule conductance measurements. *Nano Lett.*, 6(10):2362–2367, 2006.

[218] F. Chen, X. Li, J. Hihath, Z. Huang, and N. Tao. Effect of anchoring groups on single-molecule conductance: Comparative study of thiol-, amine-, and carboxylic-acid-terminated molecules. *J. Am. Chem. Soc.*, 128(49):15874–15881, 2006.

[219] C. Li, I. Pobelov, T. Wandlowski, A. Bagrets, A. Arnold, and F. Evers. Charge transport in single Au vertical bar alkanedithiol vertical bar Au junctions: Coordination geometries and conformational degrees of freedom. *J. Am. Chem. Soc.*, 130(1):318–326, 2008.

[220] M. T. González, J. Brunner, R. Huber, S. Wu, C. Schoenenberger, and M. Calame. Conductance values of alkanedithiol molecular junctions. *New J. Phys.*, 10:065018, 2008.

[221] C. A. Martin, D. Ding, J. K. Sorensen, T. Bjornholm, J. M. van Ruitenbeek, and H. S. J. van der Zant. Fullerene-based anchoring groups for molecular electronics. *J. Am. Chem. Soc.*, 130(40):13198–13199, 2008.

[222] H. B. Akkerman and B. de Boer. Electrical conduction through single molecules and self-assembled monolayers. *J. Phys. Condens. Matt.*, 20(1):013001, 2008.

[223] M. D. Losego, M. E. Grady, N. R. Sottos, D. G. Cahill, and P. V. Braun. Effects of chemical bonding on heat transport across interfaces. *Nat. Mater.*, 11:502, 2012.

[224] M. Paulsson, C. Krag, T. Frederiksen, and M. Brandbyge. Conductance of alkanedithiol single-molecule junctions: A molecular dynamics study. *Nano Lett.*, 9(1):117–121, 2009.

[225] J. Soussi, S. Volz, B. Palpant, and Y. Chalopin. A detailed microscopic study of the heat transfer at a water gold interface coated with a polymer. *Appl. Phys. Lett.*, 106(9):093113, 2015.

[226] W.-L. Ong, S. Majumdar, J. A. Malen, and A. J. H. McGaughey. Coupling of organic and inorganic vibrational states and their thermal transport in nanocrystal arrays. *J. Phys. Chem. C*, 118(14):7288–7295, 2014.

[227] T. T. Järvi, A. C. T. van Duin, K. Nordlund, and W. A. Goddard. Development of interatomic ReaxFF potentials for Au-S-C-H systems. *J. Phys. Chem. A*, 115(37):10315–

10322, 2011.

[228] G.-T. Bae and C. M. Aikens. Improved ReaxFF force field parameters for Au-S-C-H systems. *J. Phys. Chem. A*, 117(40):10438–10446, 2013.

[229] J. Ravichandran, A. K. Yadav, R. Cheaito, P. B. Rossen, A. Soukiassian, S. J. Suresha, J. C. Duda, B. M. Foley, C.-H. Lee, Y. Zhu, A. W. Lichtenberger, J. E. Moore, D. A. Muller, D. G. Schlom, P. E. Hopkins, A. Majumdar, R. Ramesh, and M. A. Zurbuchen. Crossover from incoherent to coherent phonon scattering in epitaxial oxide superlattices. *Nat. Mater.*, 13(2):168–172, 2014.

[230] H. Han, L. G. Potyomina, A. A. Darinskii, S. Volz, and Y. A. Kosevich. Phonon interference and thermal conductance reduction in atomic-scale metamaterials. *Phys. Rev. B*, 89:180301, 2014.

[231] U. Fano. Effects of configuration interaction on intensities and phase shifts. *Phys. Rev.*, 124:1866–1878, 1961.

[232] A. E. Miroshnichenko, S. Flach, and Y. S. Kivshar. Fano resonances in nanoscale structures. *Rev. Mod. Phys.*, 82:2257–2298, 2010.

[233] B. Luk'yanchuk, N. I. Zheludev, S. A. Maier, N. J. Halas, P. Nordlander, H. Giessen, and C. T. Chong. The Fano resonance in plasmonic nanostructures and metamaterials. *Nat. Mater.*, 9(9):707–715, 2010.

[234] P. Fan, Z. Yu, S. Fan, and M. L. Brongersma. Optical Fano resonance of an individual semiconductor nanostructure. *Nat. Mater.*, 13(5):471–475, 2014.

[235] P. Sautet and C. Joachim. Electronic interference produced by a benzene embedded in a polyacetylene chain. *Chem. Phys. Lett.*, 153(6):511 – 516, 1988.

[236] E. G. Emberly and G. Kirczenow. Theoretical study of electrical conduction through a molecule connected to metallic nanocontacts. *Phys. Rev. B*, 58:10911–10920, 1998.

[237] R. Baer and D. Neuhauser. Phase coherent electronics: A molecular switch based on quantum interference. *J. Am. Chem. Soc.*, 124(16):4200–4201, 2002.

[238] R. Stadler, M. Forshaw, and C. Joachim. Modulation of electron transmission for molecular data storage. *Nanotechnology*, 14(2):138, 2003.

[239] D. Walter, D. Neuhauser, and R. Baer. Quantum interference in polycyclic hydrocarbon molecular wires. *Chem. Phys.*, 299(1):139 – 145, 2004.

[240] D. M. Cardamone, C. A. Stafford, and S. Mazumdar. Controlling quantum transport through a single molecule. *Nano Lett.*, 6(11):2422–2426, 2006.

[241] C. A. Stafford, D. M. Cardamone, and S. Mazumdar. The quantum interference effect transistor. *Nanotechnology*, 18(42):424014, 2007.

[242] S.-H. Ke, W. Yang, and H. U. Baranger. Quantum-interference-controlled molecular electronics. *Nano Lett.*, 8(10):3257–3261, 2008.

[243] D. Q. Andrews, G. C. Solomon, R. H. Goldsmith, T. Hansen, M. R. Wasielewski, R. P. van Duyne, and M. A. Ratner. Quantum interference: The structural dependence of electron transmission through model systems and cross-conjugated molecules. *J. Phys. Chem. C*, 112(43):16991–16998, 2008.

[244] G. C. Solomon, D. Q. Andrews, T. Hansen, R. H. Goldsmith, M. R. Wasielewski, R. P. van Duyne, and M. A. Ratner. Understanding quantum interference in coherent molecular conduction. *J. Chem. Phys.*, 129(5):054701, 2008.

[245] G. C. Solomon, D. Q. Andrews, R. H. Goldsmith, T. Hansen, M. R. Wasielewski, R. P. van Duyne, and M. A. Ratner. Quantum interference in acyclic systems: Conductance of cross-conjugated molecules. *J. Am. Chem. Soc.*, 130(51):17301–17308, 2008.

[246] D. Q. Andrews, G. C. Solomon, R. P. van Duyne, and M. A. Ratner. Single molecule electronics: Increasing dynamic range and switching speed using cross-conjugated species.

J. Am. Chem. Soc., 130(51):17309–17319, 2008.

[247] R. Stadler. Quantum interference effects in electron transport through nitrobenzene with pyridil anchor groups. *Phys. Rev. B*, 80:125401, 2009.

[248] G. C. Solomon, C. Herrmann, T. Hansen, V. Mujica, and M. A. Ratner. Exploring local currents in molecular junctions. *Nat. Chem.*, 2(3):223–228, 2010.

[249] T. Markussen, J. Schiøtz, and K. S. Thygesen. Electrochemical control of quantum interference in anthraquinone-based molecular switches. *J. Chem. Phys.*, 132(22):224104, 2010.

[250] G. Géranton, C. Seiler, A. Bagrets, L. Venkataraman, and F. Evers. Transport properties of individual C60-molecules. *J. Chem. Phys.*, 139(23):234701, 2013.

[251] L. A. Zotti, E. Leary, M. Soriano, J. C. Cuevas, and J. J. Palacios. A molecular platinum cluster junction: A single-molecule switch. *J. Am. Chem. Soc.*, 135(6):2052–2055, 2013.

[252] A. Grigoriev, J. Sköldberg, G. Wendin, and Ž. Crljen. Critical roles of metal-molecule contacts in electron transport through molecular-wire junctions. *Phys. Rev. B*, 74:045401, 2006.

[253] T. A. Papadopoulos, I. M. Grace, and C. J. Lambert. Control of electron transport through Fano resonances in molecular wires. *Phys. Rev. B*, 74:193306, 2006.

[254] M. Ernzerhof. A simple model of molecular electronic devices and its analytical solution. *J. Chem. Phys.*, 127(20):204709, 2007.

[255] X. Shi, Z. Dai, and Z. Zeng. Electron transport in self-assembled monolayers of thiolalkane: Symmetric $I - V$ curves and Fano resonance. *Phys. Rev. B*, 76:235412, 2007.

[256] C. M. Finch, V. M. García-Suárez, and C. J. Lambert. Giant thermopower and figure of merit in single-molecule devices. *Phys. Rev. B*, 79:033405, 2009.

[257] K. Yoshizawa, T. Tada, and A. Staykov. Orbital views of the electron transport in molecular devices. *J. Am. Chem. Soc.*, 130(29):9406–9413, 2008.

[258] T. Markussen, R. Stadler, and K. S. Thygesen. The relation between structure and quantum interference in single molecule junctions. *Nano Lett.*, 10(10):4260–4265, 2010.

[259] K. G. L. Pedersen, M. Strange, M. Leijnse, P. Hedegård, G. C. Solomon, and J. Paaske. Quantum interference in off-resonant transport through single molecules. *Phys. Rev. B*, 90:125413, 2014.

[260] M. H. Garner, G. C. Solomon, and M. Strange. Tuning conductance in aromatic molecules: Constructive and counteractive substituent effects. *J. Phys. Chem. C*, 120(17):9097–9103, 2016.

[261] M. Mayor, H. B. Weber, J. Reichert, M. Elbing, C. von Hänisch, D. Beckmann, and M. Fischer. Electric current through a molecular rod-relevance of the position of the anchor groups. *Angew. Chem., Int. Ed.*, 42(47):5834–5838, 2003.

[262] D. Fracasso, H. Valkenier, J. C. Hummelen, G. C. Solomon, and R. C. Chiechi. Evidence for quantum interference in SAMs of arylethynylene thiolates in tunneling junctions with eutectic Ga-In (EGaIn) top-contacts. *J. Am. Chem. Soc.*, 133(24):9556–9563, 2011.

[263] W. Hong, H. Li, S.-X. Liu, Y. Fu, J. Li, V. Kaliginedi, S. Decurtins, and T. Wandlowski. Trimethylsilyl-terminated oligo(phenylene ethynylene)s: An approach to single-molecule junctions with covalent Au-C σ-bonds. *J. Am. Chem. Soc.*, 134(47):19425–19431, 2012.

[264] C. M. Guedon, H. Valkenier, T. Markussen, K. S. Thygesen, J. C. Hummelen, and S. J. van der Molen. Observation of quantum interference in molecular charge transport. *Nat. Nanotechnol.*, 7(5):305–309, 2012.

[265] S. V. Aradhya, J. S. Meisner, M. Krikorian, S. Ahn, R. Parameswaran, M. L. Steigerwald, C. Nuckolls, and L. Venkataraman. Dissecting contact mechanics from quantum interference in single-molecule junctions of stilbene derivatives. *Nano Lett.*, 12(3):1643–1647,

2012.

[266] H. Vazquez, R. Skouta, S. Schneebeli, M. Kamenetska, R. Breslow, L. Venkataraman, and M.S. Hybertsen. Probing the conductance superposition law in single-molecule circuits with parallel paths. *Nat. Nanotech.*, 7(10):663–667, 2012.

[267] V. Rabache, J. Chaste, P. Petit, M. L. Della Rocca, P. Martin, J.-C. Lacroix, R. L. McCreery, and P. Lafarge. Direct observation of large quantum interference effect in anthraquinone solid-state junctions. *J. Am. Chem. Soc.*, 135(28):10218–10221, 2013.

[268] C. R. Arroyo, S. Tarkuc, R. Frisenda, J. S. Seldenthuis, C. H. M. Woerde, R. Eelkema, F. C. Grozema, and H. S. J. van der Zant. Signatures of quantum interference effects on charge transport through a single benzene ring. *Angew. Chem., Int. Ed.*, 52(11):3152–3155, 2013.

[269] C. R. Arroyo, R. Frisenda, K. Moth-Poulsen, J. S. Seldenthuis, T. Bjørnholm, and H. S. J. van der Zant. Quantum interference effects at room temperature in OPV-based single-molecule junctions. *Nanoscale Res. Lett.*, 8(1):234, 2013.

[270] J. Xia, B. Capozzi, S. Wei, M. Strange, A. Batra, J. R. Moreno, R. J. Amir, E. Amir, G. C. Solomon, L. Venkataraman, and L. M. Campos. Breakdown of interference rules in azulene, a nonalternant hydrocarbon. *Nano Lett.*, 14(5):2941–2945, 2014.

[271] D. Z. Manrique, C. Huang, M. Baghernejad, X. Zhao, O. A. Al-Owaedi, H. Sadeghi, V. Kaliginedi, W. Hong, M. Gulcur, T. Wandlowski, M. R. Bryce, and C. J. Lambert. A quantum circuit rule for interference effects in single-molecule electrical junctions. *Nat. Commun.*, 6:6389–, March 2015.

[272] R. Frisenda, V. A. E. C. Janssen, F. C. Grozema, H. S. J. van der Zant, and N. Renaud. Mechanically controlled quantum interference in individual π-stacked dimers. *Nat. Chem.*, 8(12):1099–1104, 2016.

[273] T. Markussen. Phonon interference effects in molecular junctions. *J. Chem. Phys.*, 139(24):244101, 2013.

[274] M. Famili, I. Grace, H. Sadeghi, and C. J. Lambert. Suppression of phonon transport in molecular Christmas trees. *Chem. Phys. Chem.*, 18(10):1234–1241, 2017.

[275] H.-W. Lee. Generic transmission zeros and in-phase resonances in time-reversal symmetric single channel transport. *Phys. Rev. Lett.*, 82:2358–2361, 1999.

[276] Y. S. Joe, A. M. Satanin, and C. S. Kim. Classical analogy of Fano resonances. *Phys. Scr.*, 74(2):259, 2006.

[277] M. T. González, X. Zhao, D. Z. Manrique, D. Miguel, E. Leary, M. Gulcur, A. S. Batsanov, G. Rubio-Bollinger, C. J. Lambert, M. R. Bryce, and N. Agraït. Structural versus electrical functionalization of oligo(phenylene ethynylene) diamine molecular junctions. *J. Phys. Chem. C*, 118(37):21655–21662, 2014.

[278] H. J. Goldsmid. *Introduction to thermoelectricity*. Springer, Berlin, 2016.

[279] B. Song, A. Fiorino, E. Meyhofer, and P. Reddy. Near-field radiative thermal transport: From theory to experiment. *AIP Adv.*, 5(5):053503, 2015.

[280] A. Kittel, W. Müller-Hirsch, J. Parisi, S.-A. Biehs, D. Reddig, and M. Holthaus. Near-field heat transfer in a scanning thermal microscope. *Phys. Rev. Lett.*, 95:224301, 2005.

[281] L. Worbes, D. Hellmann, and A. Kittel. Enhanced near-field heat flow of a monolayer dielectric island. *Phys. Rev. Lett.*, 110:134302, 2013.

[282] K. Kloppstech, N. Könne, S.-A. Biehs, A. W. Rodriguez, L. Worbes, D. Hellmann, and A. Kittel. Giant heat transfer in the crossover regime between conduction and radiation. *Nat. Commun.*, 8:14475, 2017.

[283] L. Cui, W. Jeong, V. Fernández-Hurtado, J. Feist, F. J. García-Vidal, J. C. Cuevas, E. Meyhofer, and P. Reddy. Study of radiative heat transfer in ångström- and nanometre-

sized gaps. *Nat. Commun.*, 8:14479, 2017.

[284] C. Joachim, J. K. Gimzewski, R. R. Schlittler, and C. Chavy. Electronic transparence of a single C_{60} molecule. *Phys. Rev. Lett.*, 74:2102–2105, 1995.

[285] H. Park, J. Park, A. K. L. Lim, E. H. Anderson, A. P. Alivisatos, and P. L. McEuen. Nanomechanical oscillations in a single-C60 transistor. *Nature*, 407(6800):57–60, 2000.

[286] J. J. Parks, A. R. Champagne, G. R. Hutchison, S. Flores-Torres, H. D. Abruña, and D. C. Ralph. Tuning the Kondo effect with a mechanically controllable break junction. *Phys. Rev. Lett.*, 99:026601, 2007.

[287] T. Böhler, A. Edtbauer, and E. Scheer. Conductance of individual C_{60} molecules measured with controllable gold electrodes. *Phys. Rev. B*, 76:125432, 2007.

[288] N. Néel, J. Kröger, L. Limot, T. Frederiksen, M. Brandbyge, and R. Berndt. Controlled contact to a C_{60} molecule. *Phys. Rev. Lett.*, 98:065502, 2007.

[289] M. Kiguchi. Electrical conductance of single C60 and benzene molecules bridging between Pt electrode. *Appl. Phys. Lett.*, 95(7):073301, 2009.

[290] G. Schull, T. Frederiksen, M. Brandbyge, and R. Berndt. Passing current through touching molecules. *Phys. Rev. Lett.*, 103:206803, 2009.

[291] G. Schull, T. Frederiksen, A. Arnau, D. Sanchez-Portal, and R. Berndt. Atomic-scale engineering of electrodes for single-molecule contacts. *Nat. Nanotechnol.*, 6(1):23–27, 2011.

[292] G. Schull, Y. J. Dappe, C. González, H. Bulou, and R. Berndt. Charge injection through single and double carbon bonds. *Nano Lett.*, 11(8):3142–3146, 2011.

[293] J. J. Palacios, A. J. Pérez-Jiménez, E. Louis, and J. A. Vergés. Fullerene-based molecular nanobridges: A first-principles study. *Phys. Rev. B*, 64:115411, 2001.

[294] J. J. Palacios, A. J. Pérez-Jiménez, E. Louis, and J. A. Vergés. Electronic transport through C 60 molecules. *Nanotechnology*, 12(2):160, 2001.

[295] R. Stadler, S. Kubatkin, and T. Bjørnholm. An ab initio study of the field-induced position change of a C 60 molecule adsorbed on a gold tip. *Nanotechnology*, 18(16):165501, 2007.

[296] T. Ono and K. Hirose. First-principles study of electron-conduction properties of C_{60} bridges. *Phys. Rev. Lett.*, 98:026804, 2007.

[297] M. K. Shukla, M. Dubey, and J. Leszczynski. Theoretical investigation of electronic structures and properties of C60 gold nanocontacts. *ACS Nano*, 2(2):227–234, 2008.

[298] X. Zheng, Z. Dai, and Z. Zeng. The size effects of electrodes in molecular devices: an ab initio study on the transport properties of C 60. *J. Phys. Condens. Matter*, 21(14):145502, 2009.

[299] E. Abad, C. González, J. Ortega, and F. Flores. Charging energy, self-interaction correction and transport energy gap for a nanogap organic molecular junction. *Org. Electron.*, 11(2):332 – 337, 2010.

[300] E. Abad, J. I. Martínez, J. Ortega, and F. Flores. Barrier formation and charging energy for a variable nanogap organic molecular junction: a tip/C_{60}/Au(111) configuration. *J. Phys. Condens. Matter*, 22(30):304007, 2010.

[301] S. Bilan, L. A. Zotti, F. Pauly, and J. C. Cuevas. Theoretical study of the charge transport through C_{60}-based single-molecule junctions. *Phys. Rev. B*, 85(20):205403, 2012.

[302] S. K. Yee, J. A. Malen, A. Majumdar, and R. A. Segalman. Thermoelectricity in fullerene-metal heterojunctions. *Nano Lett.*, 11(10):4089–4094, 2011.

[303] C. Evangeli, K. Gillemot, E. Leary, M. T. González, G. Rubio-Bollinger, C. J. Lambert, and N. Agraït. Engineering the thermopower of C60 molecular junctions. *Nano Lett.*, 13(5):2141–2145, 2013.

[304] S. K. Lee, T. Ohto, R. Yamada, and H. Tada. Thermopower of benzenedithiol and C60 molecular junctions with Ni and Au electrodes. *Nano Lett.*, 14(9):5276–5280, 2014.

[305] F. Pauly, J. K. Viljas, and J. C. Cuevas. Length-dependent conductance and thermopower in single-molecule junctions of dithiolated oligophenylene derivatives: A density functional study. *Phys. Rev. B*, 78:035315, 2008.

[306] H. Mera, M. Lannoo, N. Cavassilas, and M. Bescond. Nanoscale device modeling using a conserving analytic continuation technique. *Phys. Rev. B*, 88:075147, 2013.

[307] H. Mera, T. G. Pedersen, and B. K. Nikolić. Hypergeometric resummation of self-consistent sunset diagrams for steady-state electron-boson quantum many-body systems out of equilibrium. *Phys. Rev. B*, 94:165429, 2016.

[308] Y. Lee, M. Bescond, D. Logoteta, N. Cavassilas, M. Lannoo, and M. Luisier. Anharmonic phonon-phonon scattering modeling of three-dimensional atomistic transport: An efficient quantum treatment. *Phys. Rev. B*, 97:205447, 2018.

[309] I. Altfeder, A. A. Voevodin, and A. K. Roy. Vacuum phonon tunneling. *Phys. Rev. Lett.*, 105:166101, 2010.

[310] B. V. Budaev and D. B. Bogy. On the role of acoustic waves (phonons) in equilibrium heat exchange across a vacuum gap. *Appl. Phys. Lett.*, 99(5):053109, 2011.

[311] G. D. Mahan. The tunneling of heat. *Appl. Phys. Lett.*, 98(13):132106, 2011.

[312] D. P. Sellan, E. S. Landry, K. Sasihithlu, A. Narayanaswamy, A. J. H. McGaughey, and C. H. Amon. Phonon transport across a vacuum gap. *Phys. Rev. B*, 85:024118, 2012.

[313] G. D. Mahan. Tunneling of heat between metals. *Phys. Rev. B*, 95:115427, 2017.

[314] Z.-Q. Zhang, J.-T. Lü, and J.-S. Wang. Energy transfer between two vacuum-gapped metal plates: Coulomb fluctuations and electron tunneling. *Phys. Rev. B*, 97:195450, 2018.

[315] J.-S. Wang, Z.-Q. Zhang, and J.-T. Lü. Coulomb-force-mediated heat transfer in the near field: Geometric effect. *Phys. Rev. E*, 98:012118, 2018.

[316] X. Ren, P. Rinke, C. Joas, and M. Scheffler. Random-phase approximation and its applications in computational chemistry and materials science. *Journal of Materials Science*, 47(21):7447–7471, 2012.

[317] B. Ramberger, T. Schäfer, and G. Kresse. Analytic interatomic forces in the random phase approximation. *Phys. Rev. Lett.*, 118:106403, 2017.

[318] D. Andrae, U. Häußermann, M. Dolg, H. Stoll, and H. Preuß. Energy-adjusted ab initio pseudopotentials for the second and third row transition elements. *Theor. Chim. Acta*, 77(2):123–141, 1990.

[319] H. R. Schober and P. H. Dederichs. *Phonon states of elements. Electron states and Fermi surfaces of alloys.* Springer-Verlag, Berlin, 1981.

[320] A. Schäfer, C. Huber, and R. Ahlrichs. Fully optimized contracted Gaussian basis sets of triple zeta valence quality for atoms Li to Kr. *J. Chem. Phys.*, 100(8):5829–5835, 1994.

[321] PsLibrary. https://github.com/dalcorso/pslibrary (accessed on 28.08.2017).

[322] M. T. González, A. Díaz, E. Leary, R. García, M. Á. Herranz, G. Rubio-Bollinger, N. Martín, and N. Agraït. Stability of single- and few-molecule junctions of conjugated diamines. *J. Am. Chem. Soc.*, 135(14):5420–5426, 2013.

[323] Q. Lu, K. Liu, H. Zhang, Z. Du, X. Wang, and F. Wang. From tunneling to hopping: A comprehensive investigation of charge transport mechanism in molecular junctions based on oligo(p-phenylene ethynylene)s. *ACS Nano*, 3(12):3861–3868, 2009.